AFRL-RX-WP-TR-2017-0027

DYNAMIC MULTIVARIATE ACCELERATED CORROSION TEST PROTOCOL

Douglas C. Hansen

University of Dayton Research Institute

1 OCTOBER 2014
Final Report

Distribution Statement A.
Approved for public release: distribution unlimited.

(STINFO COPY)

AIR FORCE RESEARCH LABORATORY
MATERIALS AND MANUFACTURING DIRECTORATE
WRIGHT-PATTERSON AIR FORCE BASE, OH 45433-7750
AIR FORCE MATERIEL COMMAND
UNITED STATES AIR FORCE

NOTICE AND SIGNATURE PAGE

Using Government drawings, specifications, or other data included in this document for any purpose other than Government procurement does not in any way obligate the U.S. Government. The fact that the Government formulated or supplied the drawings, specifications, or other data does not license the holder or any other person or corporation; or convey any rights or permission to manufacture, use, or sell any patented invention that may relate to them.

This report was cleared for public release by the USAF 88th Air Base Wing (88 ABW) Public Affairs Office (PAO) and is available to the general public, including foreign nationals.

Copies may be obtained from the Defense Technical Information Center (DTIC) (http://www.dtic.mil).

AFRL-RX-WP-TR-2017-0027 HAS BEEN REVIEWED AND IS APPROVED FOR PUBLICATION IN ACCORDANCE WITH ASSIGNED DISTRIBUTION STATEMENT.

//SIGNATURE//_____
CHAD N. HUNTER
Project Engineer
Acquisition Systems Support Branch
Systems Support Division
Materials and Manufacturing Directorate

//SIGNATURE//_____
MATTHEW J. QUINTON
Acting Branch Chief
Acquisition Systems Support Branch
Systems Support Division
Materials and Manufacturing Directorate

This report is published in the interest of scientific and technical information exchange, and its publication does not constitute the Government's approval or disapproval of its ideas or findings.

REPORT DOCUMENTATION PAGE

Form Approved
OMB No. 0704-0188

The public reporting burden for this collection of information is estimated to average 1 hour per response, including the time for reviewing instructions, searching existing data sources, gathering and maintaining the data needed, and completing and reviewing the collection of information. Send comments regarding this burden estimate or any other aspect of this collection of information, including suggestions for reducing this burden, to Department of Defense, Washington Headquarters Services, Directorate for Information Operations and Reports (0704-0188), 1215 Jefferson Davis Highway, Suite 1204, Arlington, VA 22202-4302. Respondents should be aware that notwithstanding any other provision of law, no person shall be subject to any penalty for failing to comply with a collection of information if it does not display a currently valid OMB control number. **PLEASE DO NOT RETURN YOUR FORM TO THE ABOVE ADDRESS**.

1. REPORT DATE ***(DD-MM-YY)*** 1 October 2014	**2. REPORT TYPE** Final	**3. DATES COVERED** ***(From - To)*** 28 January 2013 – 30 September 2014
4. TITLE AND SUBTITLE DYNAMIC MULTIVARIATE ACCELERATED CORROSION TEST PROTOCOL		**5a. CONTRACT NUMBER** FA8601-06-D-0013
		5b. GRANT NUMBER
		5c. PROGRAM ELEMENT NUMBER 62102F
6. AUTHOR(S) Douglas C. Hansen		**5d. PROJECT NUMBER** 4349
		5e. TASK NUMBER
		5f. WORK UNIT NUMBER X0KW
7. PERFORMING ORGANIZATION NAME(S) AND ADDRESS(ES) University of Dayton Research Institute 300 College Park Dayton, OH 45469-0054		**8. PERFORMING ORGANIZATION REPORT NUMBER** SERDP PROJECT: WP-1674
9. SPONSORING/MONITORING AGENCY NAME(S) AND ADDRESS(ES) Air Force Research Laboratory Materials and Manufacturing Directorate Wright-Patterson Air Force Base, OH 45433-7750 Air Force Materiel Command United States Air Force		**10. SPONSORING/MONITORING AGENCY ACRONYM(S)** AFRL/RXSC
		11. SPONSORING/MONITORING AGENCY REPORT NUMBER(S) AFRL-RX-WP-TR-2017-0027

12. DISTRIBUTION/AVAILABILITY STATEMENT
Distribution Statement A. Approved for public release: distribution unlimited.

13. SUPPLEMENTARY NOTES
PA Case Number: 88ABW-2016-6386; Clearance Date: 09 Dec 2016. This document contains color.

14. ABSTRACT ***(Maximum 200 words)***

The objective of this effort was to develop a comprehensive test protocol to accurately predict all aspects of the performance lifetime of Department of Defense (DoD) coatings and alloys. This test protocol was to be comprised of a test methodology which would include the development of a test chamber, modified to include the synergistic effects of UV and ozone and the exposure of bare and coated samples to yield an accelerated corrosion test. This test would result in not only accelerated corrosion rates for the bare metals, but also similar corrosion chemistries on the surface of the exposure test coupons as were found on the field exposed samples. If this could be replicated, then the test chamber environment would be applied to coated samples as well. Indeed, DoD service environments are variable in nature (e.g., beachfront vs. desert) and therefore the intent of the test protocol was to be either specific to a particular service environment or dynamically "tunable" to match the particular service environment in which the coating or alloy substrate is intended to be used in service. Finally, the test protocol was to allow a reasonable prediction of performance lifetime based upon a relatively short timeframe accelerated test.

15. SUBJECT TERMS
Corrosion, ozone, ultraviolet, atmospheric, accelerated, AA2024-T3, AA6061-T6, AA7075-T3, 1010 steel, AgCl, rare earth conversion coat, magnesium rich primer, polyurethane, Eyring, Monte Carlo, cumulative damage, model.

16. SECURITY CLASSIFICATION OF:			**17. LIMITATION OF ABSTRACT:**	**18. NUMBER OF PAGES**	**19a. NAME OF RESPONSIBLE PERSON** (Monitor)
a. REPORT Unclassified	**b. ABSTRACT** Unclassified	**c. THIS PAGE** Unclassified	SAR	970	Chad Hunter **19b. TELEPHONE NUMBER** *(Include Area Code)* (937) 713-7719

Standard Form 298 (Rev. 8-98)
Prescribed by ANSI Std. Z39-18

Abstract

Objectives

The objective of this effort was to develop a comprehensive test protocol to accurately predict all aspects of the performance lifetime of Department of Defense (DoD) coatings and alloys. This test protocol was to be comprised of a test methodology which would include the development of a test chamber, modified to include the synergistic effects of UV and ozone and the exposure of bare and coated samples to yield an accelerated corrosion test. This test would result in not only accelerated corrosion rates for the bare metals, but also similar corrosion chemistries on the surface of the exposure test coupons as were found on the field exposed samples. If this could be replicated, then the test chamber environment would be applied to coated samples as well. Indeed, DoD service environments are variable in nature (e.g., beachfront vs. desert) and therefore the intent of the test protocol was to be either specific to a particular service environment or dynamically "tunable" to match the particular service environment in which the coating or alloy substrate is intended to be used in service. Finally, the test protocol was to allow a reasonable prediction of performance lifetime based upon a relatively short timeframe accelerated test.

Technical Approach

Coupon panels of bare aluminum alloys AA2024-T3, AA6061-T6, AA7075-T6, and 1010 steel, pure silver and pure copper were exposed to eight atmospheric test site environments and within two laboratory corrosion test chambers. One of the laboratory corrosion test chambers operated in 5% NaCl salt fog in accordance with ASTM B117, and the other was modified to allow concurrent exposure of ultraviolet (UV) light, ozone, and 5% NaCl salt fog in accordance with ASTM B117. Various analyses (mass loss determinations, corrosion morphology and elemental analysis by scanning electron microscopy-energy dispersive spectroscopy (SEM-EDS) and electrochemical determinations of corrosion product thickness) were performed in order to investigate a possible correlation between corrosion behavior of the panels exposed at the outdoor sites and those in the laboratory tests. The atmospheric test site environments were: Wright-Patterson AFB, Kirtland AFB, Tyndall AFB, Hickam AFB, Pt. Judith, RI and Daytona, FL. There were two additional sites located on University National Oceanographic Laboratory Ships. A second set of panels consisting of AA2024-T3 and 1010 steel substrates coated with various organic coating systems (both chromate-containing and chromate-free), and an AA2024-T3 lap joint ensemble with Cd-plated steel fasteners, were exposed at the eight atmospheric sites and the two laboratory corrosion test chambers. The coated panels were mounted on racks adjacent to the bare metal samples at each exposure location. Qualitative coating system (performance rankings) and quantitative coating system determinations (SEM-EDS, FTIR) on the coated substrates and lap joint samples were made and compared after the 1 and 2 year exposure cycles. Bare sample coupons were retrieved at 3 month intervals over two years and the coated panels were retrieved at 1 year intervals. Weather data over the 2 year exposure period was either recorded on deployed weather monitoring systems at each exposure site (temperature, relative humidity, total UV irradiation and ozone levels) or downloaded from nearby EPA monitoring sites. The cumulative frequencies of the four weathering parameters (UV, ozone, temperature and RH) measured were determined for the exposure sites, which allowed comparison to mass loss data and provided input to the cumulative damage model. Analysis of the agreement between deployed weather monitoring systems and EPA monitoring sites was performed, where applicable. Additionally, a proof of concept model for predicting atmospheric corrosion rates of 1010 steel was developed, using a cumulative damage non-linear modeling and simulation approach. The model used inputs from weather data including time dependent temperature, relative humidity (%RH) and atmospheric contaminant (SO_2 and ozone) levels and chloride deposition rate (mass per unit volume of rainwater).

Results

Coupon panels exposed at atmospheric sites and in the laboratory chambers were analyzed and several important trends were discovered. It was determined that the amount of corrosion experienced by

the coated panels in outdoor environments, including lap joint specimens, correlated more strongly to elevated temperature and %RH than other parameters measured. In addition, comprehensive analysis suggests that the cumulative amount of time that a coated sample was exposed to damaging environments (as measured by temperature, %RH, ozone, UV, Cl, and SO_2) was a dominant factor in determining the severity of corrosion that occurred. It was found that even short exposures to "elevated" UV and ozone levels under constant salt fog in the laboratory study resulted in an accelerated corrosion phenomenon in the scribe and that was more severe than similar exposure time to salt fog alone, or after 2 years of exposure at the most aggressive sites in the field. Other observations: degradation of the coating system was also evident in the FT-IR analysis; degradation of the components of the high performance polyurethane coatings exposed in the UV/ozone chamber were more pronounced than when exposed in the B117 chamber; and the degradation of the Mg-rich coating system in the UV/ozone chamber was more like the degradation seen at two exposure sites after 2 years. For the full chromate coating system, the degradation of the coating in the B117 chamber was similar in appearance to 2 of the outdoor test sites but did not resemble the appearance of coated panels exposed in the UV/ozone chamber. These results suggest that it may be possible to tailor the chamber conditions to yield coating component degradation to replicate field exposures.

In examining the data from the laboratory tests and the outdoor environments for the bare metal coupons, elevated levels of UV and ozone significantly increased corrosion of the three aluminum alloys and pure copper in the laboratory, but increased corrosion was not observed in the coupons exposed in the outdoor environments with high UV and ozone. This discrepancy is likely due to the fact that the modified ASTM B117 test performed in this evaluation is much more aggressive than natural outdoor environments and does not contain all factors of influence- for example, other atmospheric contaminants such as SO_2, wet/dry cycles with dilute electrolytes, temperature and humidity cycling, mechanical stress, etc. Elevated levels of UV and ozone in the modified salt fog test resulted in lower corrosion rates for 1010 steel than those observed for the low UV/low ozone levels. Of the three aluminum alloys studied, AA2024-T3 exhibited the greatest corrosion rate when subjected to the high UV/high ozone conditions, which is consistent with the observed increase in corrosion rate that the high UV/high ozone condition had on pure copper, since AA2024-T3 alloy has the highest weight percent of copper in its composition of the three aluminum alloys. Accelerated formation of AgCl films was demonstrated, with the film formation rate greater in the B117/UV/ozone chamber than in the B117 chamber over time. Correlation of the AgCl film thickness with hours of exposure time in the B117/UV/ozone chamber to similar thicknesses in the field exposures was achieved, indicating that it may be possible to replicate the parameters required for the formation of the AgCl film thicknesses seen in the field at various exposure sites.

The cumulative damage corrosion model was developed to predict mass loss on 1010 steel due to atmospheric corrosion using inputs of temperature, relative humidity, ozone and SO_2 concentration, and deposition rate (mass per unit volume of rainwater) of chloride. The R^2 values for the calibration and validation data sets, comprised of the 8 atmospheric test sites in the study, were 0.96 and 0.86 respectively. The accuracy of this model exceeded any atmospheric corrosion rate prediction models published in the literature to date.

Benefits

This project and other similar efforts have laid the groundwork for research program investments in multiple DoD laboratories (e.g. AFRL, NAVAIR) that are developing and implementing new accelerated test methodologies for management of weapon systems. DoD laboratory activities in accelerated test methodology and other technology development are now coordinated via the science and technology working integrated product team (S&T WIPT) which meet 3 times a year as part of the DoD Corrosion Forum which are sponsored by the Office of Secretary of Defense (OSD) Office of Corrosion Policy and Oversight (CPO).

Table of Contents

Section **Page**

List of Figures iii

List of Tables.... viii

Key Words ix

Acknowledgements x

I. Objective 1

II. Background 1

III. Materials and Methods 4

IV. Results and Discussion 18

V. Conclusions and Implications for Future Research/Implementation 81

1. Systematic and Comprehensive Evaluation of Field Exposed Bare Metal and Coated Substrates 82
2. Measurement and Correlation of Environmental data at Land Based Field Exposure Sites with Environmental Protection Agency (EPA) Monitoring Sites 82
3. Correlation of Ultraviolet Radiation and Ozone Levels in the Field to Corrosion Behavior of Bare and Coated Exposure Samples 82
4. Modification of a Salt Fog Exposure Chamber to include UV Radiation and Ozone to Accelerate Corrosion of Bare and Coated Metal Substrates 82
5. Development of a Synergistic Corrosion Model utilizing a Cumulative Damage Approach 83
6. Development of a Dynamic Multivariate Accelerated Corrosion Test Protocol 84
7. Benefits and Implications for Future Research/Technology Transition…….. 84

Literature Cited 85

Distribution Statement A. Approved for public release.

Table of Contents (continued)

Section **Page**

Appendices:

Appendix A: Weather Data 87

Appendix B: Scanning Electron Microscopy Images (Daytona Beach, FL) 124

Appendix C: Scanning Electron Microscopy Images (Pt. Judith, RI) 164

Appendix D: Scanning Electron Microscopy Images (East Coast Ship, DE) 204

Appendix E: Scanning Electron Microscopy Images (West Coast Ship, WA) 257

Appendix F: Scanning Electron Microscopy Images (Hickam AFB, HI) 310

Appendix G: Scanning Electron Microscopy Images (Tyndall AFB, FL) 363

Appendix H: Scanning Electron Microscopy Images (Wright-Patterson AFB, OH) 416

Appendix I: Scanning Electron Microscopy Images (Kirtland AFB, NM) 469

Appendix J: EDS Data for All Outdoor Exposure Sites 521

Appendix K: Optical Images of Coated 1010 Steel and 2024-T3 Aluminum Substrates and Lap Joint Assemblies From Field Exposures After 1 and 2 Years 573

Appendix L: EDS Data for All field Exposures of Coated AA2024-T3 Panels Locations 1 and 3 600

Appendix M: Scanning Electron Microscopy Images (High UV and High Ozone Chamber) 612

Appendix N: Scanning Electron Microscopy Images (High UV and Low Ozone Chamber) 679

Appendix O: Scanning Electron Microscopy Images Bare Coupons (Low UV and Low Ozone Chamber) 742

Appendix P: Scanning Electron Microscopy Images Bare Coupons (Low UV and High Ozone Chamber) 809

Appendix Q: EDS Data for All Chamber Exposures (Modified and B117) Bare Metal Coupons 875

Appendix R: Optical Images of 2024-T3 Aluminum Substrates Exposed in B117 and Modified UV/Ozone Salt Fog Chamber Tests 909

Appendix S: EDS Data for All Chamber Exposures (Modified and B117) Coated Panels 921

Appendix T: List of Scientific/Technical Publications 938

Appendix U: Dynamic Multivariate Accelerated Corrosion Test Protocol 940

Appendix V: Cumulative Predictions for Model Calibration and Validation Sites 946

Distribution Statement A. Approved for public release.

List of Figures

Figure **Page**

1. Bare coupons mounted on exposure card 5
2. Bare coupons mounted in exposure picture frame.....5
3. Shipboard exposure rack of 1 set of coated samples as described in Table 1 5
4. (Left) Image of weather monitoring station mounted on railing above pilot deck on the West Coast ship, R/V Thomas G. Thompson, showing the location of the UV sensor. (Right) Image showing ozone measurement and data logging instrumentation inside monitoring station.....7
5. Images of the modified exposure chamber exposure system.....8
6. Map of UV-A irradiance levels in chamber based upon location on exposure racks....9
7. Cumulative corrosion damage model features.....13
8. Construction of the temperature – relative humidity shape functions 14
9. Illustration of the temperature – relative humidity shape functions 15
10. Illustration of how the temperature – contaminant shape functions are constructed (illustration is for the chloride shape function, others are similar 16
11. Illustration of the temperature – contaminant shape functions (assumes a value of C_{max} = 1.0) 17
12. Representative data of monitored concentration of ozone at Kirtland AFB.....20
13. Plots of ozone, UV-A and %RH levels as a function of temperature at Kirtland AFB during 1 – 7 June 2010; data was recorded hourly and is presented over 24 hour intervals. 20
14. Cumulative frequency plots of (a) ozone and (b) UV levels monitored hourly over a 2 year period at the field exposure sites.....21
15. Cumulative frequency plots of (a) temperature and (b) %RH levels monitored hourly over a 2 year period at the field exposure sites 22
16. Mass loss of (a) AA7075-T6, (b) AA2024-T3 and (c) AA6061-T6 at all exposure sites. 26
17. Mass loss determinations for AA6061-T6, AA7075-T3 and 2024-T3 as a function of exposure locations over a 2 year period. 27
18. Mass loss for 1010 steel at all exposure sites over a two year period. EOL = end of lifetime for sample material.....28
19. Mass loss for pure copper at all exposure sites over a two year period.....28
20. AgCl film thickness on pure silver coupons as a function of time over a two year period at all exposure sites 30

Distribution Statement A. Approved for public release.

List of Figures (Continued)

Figure **Page**

21. EDS spectra of the pure silver coupons exposed at Dayton Beach, FL.....31
22. SEM images of the (a) 3 months, (b) 6 months, (c) 9 months, (d) 12 months, (e) 18 months and (f) 24 months exposure of pure silver coupons at Daytona Beach, FL(1000x magnification). 32
23. EDS spectra of the pure silver coupons exposed at Kirtland AFB, NM.....32
24. SEM images of (a) 3 months, (b) 6 months, (c) 9 months, (d) 12 months, (e) 15 months and (f) 21 months exposure of pure silver coupons at Kirtland AFB, NM (500x magnification). 33
25. Cl/Ag ratio on pure silver coupons as a function of exposure time at the eight exposure locations.....34
26. EDS analysis of AA7075-T6 samples retrieved over a two year exposure period from Daytona Beach FL.....35
27. EDS analysis of 2024-T3 samples retrieved over a two year exposure period from (a) Daytona Beach, FL and (b) Kirtland AFB, NM exposure sites.....36
28. EDS analysis of 2024-T3 samples retrieved over a two year exposure period from (a) the East Coast ship (DE) and (b) Kirtland AFB, NM exposure sites. 37
29. EDS analysis of 2024-T3 samples retrieved over a two year exposure period from (a) the East Coast ship (DE) and (b) Kirtland AFB, NM exposure sites 38
30. SEM images of AA7075-T6 samples retrieved from Kirtland AFB, NM exposure site after (a) 3 months, (b) 6 months, (c) 9 months, (d) 12 months, (e) 15 months, (f) 18 months, (g) 21 months and (h) 24 months.....39
31. SEM images of AA7075-T6 samples retrieved from Kirtland AFB, NM exposure site after (a) 3 months, (b) 6 months, (c) 9 months, (d) 12 months, (e) 15 months, (f) 18 months, (g) 21 months and (h) 24 months.....40
32. SEM images of AA2024-T3 samples retrieved from Daytona Beach, FL exposure site after (a) 3 months, (b) 6 months, (c) 9 months, (d) 12 months, (e) 18 months and (f) 24 months.....41
33. SEM images of AA2024-T3 samples retrieved from Kirtland AFB, NM exposure site after (a) 3 months, (b) 6 months, (c) 9 months, (d) 12 months, (e) 15 months, (f) 18 months, (g) 21 months and (h) 24 months.....42
34. SEM images of AA6061-T6 samples retrieved from the East Coast ship (DE) exposure site after (a) 3 months, (b) 6 months, (c) 9 months, (d) 12 months, (e) 15 months, (f) 18 months, (g) 21 months and (h) 24 months.....43
35. SEM images of AA6061-T6 samples retrieved from Kirtland AFB, NM exposure site after (a) 3 months, (b) 6 months, (c) 9 months, (d) 12 months, (e) 15 months, (f) 18 months, (g) 21 months and (h) 24 months 44

Distribution Statement A. Approved for public release.

List of Figures (Continued)

Figure **Page**

36. EDS analysis of AA7075-T6 retrieved from Tyndall AFB at 24 months, Daytona Beach at 3 months, Pt. Judith at 3 months, East Coast ship at 3 months, and West Coast ship at 3 months. 45

37. SEM images of AA7075-T6 samples retrieved from (a) Tyndall AFB at 24 months, (b) Daytona Beach at 3 months, (c) Pt. Judith at 3 months, (d) East Coast ship at 3 months, and (e) west Coast ship at 3 months.....46

38. EDS analysis of AA2024-T3 retrieved from Daytona Beach at 6 months, Pt. Judith at 9 months, the East Coast ship at 12 months and the West Coast ship at 18 months 47

39. SEM images of 2024-T3 samples retrieved from (a) Daytona Beach at 6 months, (b) Pt. Judith at 9 months, (c) the East Coast ship at 12 months, and (d) the West Coast ship at 18 months. 48

40. Images of coated panels retrieved from the Pt. Judith, RI exposure site after 1 year (Top) and 2 years (Bottom) exposure. Coating designations are: A1A, coating system A; A1E, coating system E; A1F, coating system F; A1G, coating system G; and A1I, coating system I 50

41. Images of lap joint samples from 1 year (Top) and 2 year (Bottom) exposure at Pt. Judith, RI exposure site.....51

42. Example of EDS analysis locations on interior surface of a lap joint sample 52

43. Plot of relative weight percent of elemental composition of locations 1, 2 and 3 within lap joint samples retrieved from the field sites after 1 year of exposure.....52

44. Representative plot of relative weight percent of elemental composition of locations 1 and 2 within lap joint samples retrieved from the ship sites after 1 year of exposure.....53

45. Example image of coated panel retrieved from a field exposure site indicating areas of interrogation by EDS: Loc 1, location 1 within the intersection of scribe marks; Loc 2, location 2 within scribe mark above intersection; Loc 3, location 3 below intersection away from scribe marks; and Loc 4, location 4 above intersection away from scribe marks. 54

46. EDS spectrum of coating system A baseline measurement.....54

47. EDS relative weight percent spectra of 1 and 2 year exposures for coating system ...55

48. EDS spectrum of coating system G baseline measurement.....56

49. EDS relative weight percent spectra of 1 and 2 year exposures for coating system G taken at location 3 on the coated panels.....57

Distribution Statement A. Approved for public release.

List of Figures (Continued)

Figure **Page**

50. Plots of mass loss for AA7075-T6, AA2024-T3, AA6061-T6, 1010 Steel and pure copper over 1000 hours of exposure at each of four UV-A and ozone combinations. 58

51. AgCl film thickness measurements on pure silver coupons as a function of exposure condition (UV/ozone) over 1000 hours in the modified exposure chamber 59

52. AgCl film thickness on the front (Left) and the back (Right) of pure silver coupons as a function of exposure condition (UV/ozone) over 1000 hours in the modified exposure chamber 60

53. AgCl film thickness measurements on pure silver coupons as a function of exposure condition (UV/ozone) over 1000 hours in the modified exposure chamber and the B117 test chamber 61

54. Comparison of mass loss of AA7076-T6, A2024-T3 and AA6061-T6 over 1000 hours exposure in the modified chamber versus the B117 test chamber 61

55. Comparison of mass loss of 1010 steel alloy coupons over 1000 hours exposure in the modified chamber versus the B117 test chamber. 62

56. Corrosion rates of AA7075-T6 at the field exposure sites in comparison to the corrosion rates determined for identical coupons exposed in the modified and B117 chambers 62

57. SEM images of AA7075-T6 coupon surfaces at (a) Daytona Beach, 12 months; (b) high UV/high ozone, 500 hours; (c) low UV/low ozone, 500 hours; B117 test, 600 hours; and (e) EDS analysis of the respective A7075-T6 surfaces 64

58. Comparison of 2 year exposures of the full chromate coating system (top) at the West Coast ship and Pt. Judith exposure sites to (bottom) 400 hours exposure of the same coating system in either the modified UV/ozone or B117 chambers 66

59. Comparison of 2 year exposures of the magnesium rich coating system (top) at the West Coast ship and Pt. Judith exposure sites to (bottom) 400 hours exposure of the same coating system in either the modified UV/ozone or B117 chambers 67

60. Side-by-side chamber exposure comparison of the three coating systems on AA2024-T3 panels at (top) 400 hours and (bottom) 2000 hours exposure in the modified UV/ozone and B117 chambers, respectively. 68

61. EDS analysis of fully chromated coating system (location 3) exposure panels from (top) modified UV/ozone chamber and (bottom) B117 chamber. 69

62. EDS analysis of magnesium rich coating system (location 3) exposure panels from (top) modified UV/ozone chamber and (bottom) B117 chamber. 70

Distribution Statement A. Approved for public release.

List of Figures (Continued)

Figure **Page**

63. EDS analysis of rare earth conversion coating system (location 3) exposure panels from (top) modified UV/ozone chamber and (bottom) B117 chamber.....71
64. FT-IR ATR % reflectance spectra of the magnesium rich coating system baseline sample and the B117 2000 hour exposure sample. Major absorbance peaks are designated by their wave number. 73
65. FT-IR ATR % reflectance spectra of the magnesium rich coating system baseline sample and the B117 2000 hour exposure sample, the UV/ozone 2000 hour modified chamber sample, the Pt. Judith and the West Coast ship 2 year exposed sample. 73
66. FT-IR ATR % reflectance spectra of the full chromate coating system baseline sample and the B117 2000 hour exposure sample. Major absorbance peaks are designated by their wave number.....74
67. FT-IR ATR % reflectance spectra of the full chromate coating system baseline sample and the B117 2000 hour exposure sample, the UV/ozone 2000 hour modified chamber sample, the Pt. Judith and the West Coast ship 2 year exposed sample. 74
68. Comparison of Predictions to Test Results (calibration sites).....76
69. AISI 1010 Steel Hourly Corrosion Rate Predictions for Kennedy Space Center, FL (midnight 12-13-05 to midnight 12-14-05).....77
70. AISI 1010 Steel Cumulative Weight Loss Predictions (midnight 12-13-05 to midnight 12-14-05). 77
71. Comparison of AISI 1010 Steel Corrosion Test Points and Associated Predictions (Arrow indicates approximate time period of cumulative predictions illustrated in Figure 12).....78
72. Comparison of Predictions to Test Results (validation sites) 80

Distribution Statement A. Approved for public release.

List of Tables

Table **Page**

I Summary of substrates and coating systems deploy 6

II Matrix of exposure sites and number of bare coupons (Cards or Picture Frames) and coated panels 6

III Definition of the Variables and Coefficients used in Equation 2 12

IV Average weather parameter values monitored at the field exposure sites over a 2 year period 23

V Mass loss for the bare metal coupons for each location and retrieval interval over the two year exposure period 24

VI Thickness of the AgCl film on pure silver coupons from all exposure sites over a two year exposure period 29

VII Elemental composition of AA7075, AA2024, AA6061 and 1010 Steel 34

VIII Summary Table of coating systems and substrates analyzed from field exposures 49

IX Summary of rankings of coating performance of the coated AA2024-T3 panels retrieved after a two year exposure 49

X Summary table of coating systems tested in the modified and B117 exposure chambers 65

XI Summary of rankings of coating performance for the three coating systems exposed in the modified and B117 test exposure chambers 65

XII Summary of peak assignments for coating systems analyzed from field and chamber exposures 75

XIII Validation Test Sites and Associated Climate Zones 79

Distribution Statement A. Approved for public release.

Key Words

Corrosion, ozone, ultraviolet, atmospheric, accelerated, AA2024-T3, AA6061-T6, AA7075-T3, 1010 steel, AgCl, rare earth conversion coat, magnesium rich primer, polyurethane, Eyring, Monte Carlo, cumulative damage, model.

Distribution Statement A. Approved for public release.

Acknowledgements

This work was sponsored by the SERDP-ESTCP Program under contract FA8601-06-D-0013, Dr. Bruce Sartwell, Program Manager, Weapons Systems and Platforms. Special thanks to Mr. James Postel (Univ. Washington, R/V Thomas G. Thompson), Capt. William Byam (Univ. of Delaware, R/V Hugh R. Sharp), Lt. Col. P. Legendre (Kirtland AFB, NM), Mr. John Puu (Hickam AFB, HI), Mr. P. V. Mitchell (AFRL, Tyndall AFB, FL) and Dr. J. Moran (ALCOA) for outdoor exposure placement and retrieval of the sample coupons and weather monitoring systems. The authors would also like to thank the Coatings Technologies Integration Office (CTIO) at the Air Force Research Laboratory (AFRL) Wright-Patterson Air Force Base (WPAFB) Ohio for sample preparation, especially Mr. William Culhane, Mr. Chris Josephs, and Dr. Scott Hayes; the AF Weather Agency, Det 3, 16 WS and Maj. John Crane, Mr. Kirk Lehneis and Mr. Paul Gehred for their assistance with weather monitoring instrumentation and coordination with weather monitoring sites and database mining; and Mr. Corey Bliss and Mr. Jeremy Angel, who served as the government principle investigators during the project. Scanning electron microscopy and energy dispersive spectroscopy characterization was performed at the Nanoscale Engineering Science and Technology (NEST) Laboratory located on the University of Dayton campus.

Distribution Statement A. Approved for public release.

I. OBJECTIVE

The objective of this effort was to develop a comprehensive test protocol to accurately predict all aspects of the performance lifetime of Department of Defense (DoD) coatings and alloys. This test protocol was to be comprised of a test methodology which would include the development of a test chamber, modified to include the synergistic effects of UV and ozone and the exposure of bare and coated samples to yield an accelerated corrosion test. The incorporation of temperature, relative humidity, UV and ozone would be regulated to mimic or exceed those monitored in the field. This test would result in not only accelerated corrosion rates for the bare metals, but also similar corrosion chemistries on the surface of the exposure test coupons as were found on the field exposed samples. If this could be replicated, then the test chamber environment would be applied to coated samples as well. The DoD has an urgent need for environmentally friendly coatings that have minimal or no toxic compounds (e.g., hexavalent chromium), volatile organic compounds (VOCs), and hazardous air pollutants (HAPs). Qualification of new coatings is usually an exceedingly long process that often requires in-service performance evaluation for a significant length of time. While advances have been made in accelerated testing of coatings regarding the aesthetic properties, there still is no reliable accelerated method to predict the performance of coatings regarding corrosion protection. Indeed, DoD service environments are variable in nature (e.g., beachfront vs. desert) and therefore the intent of the test protocol was to be either specific to a particular service environment or dynamically "tunable" to match the particular service environment in which the coating or alloy substrate is intended to be used in service. Another objective was that the test protocol developed should also provide accurate results for particular material configurations, such as fasteners, lap joints, etc. which can create concentration cells and galvanic couples. Finally, the test protocol was to allow a reasonable prediction of performance lifetime based upon a relatively short timeframe accelerated test.

II. BACKGROUND

Over the last few decades the analytical characterization of bare and coated surfaces undergoing atmospheric corrosion have improved, resulting in a more complete understanding and consideration of environmental parameters, corrosion layers, and degradation of polymeric coatings. However, the corrosion processes involved and the role that the environmental parameters play in what is a multiphase system is rather complex involving chemical reactions and equilibria, ionic transport phenomena, and gaseous, aqueous and solid phases [1]. Various corrosion products, specific to the metallic (or polymeric) substrates in the system, and the corrosive species present (anions, cations, acidic and basic salts, particulates, etc.) which interact with each other all vary in amounts and residence time. For the purposes of atmospheric corrosion, the electrochemical nature of the corrosion process requires the presence of an electrolyte, provided by the atmospheric precipitation or adsorption of water molecules on the surface of the metal or polymeric coating. Adsorbed water layers, which can range from 15 to 90 layers thick depending upon the relative humidity, plays a central role in supporting the electrochemical process [2]. Indeed, the presence of corrosive species and corrosion products, which are hygroscopic, can attract water vapor above a critical relative humidity and solubilize, further catalyzing the corrosion process. Indeed, a study by W.H.J. Vernon in 1935 established that for iron and steel, oxidation of the metal surface did not commence until a relative humidity of 70% was attained [3]. However, other researchers have reported on the role of atmospheric contaminants and the critical %RH required for atmospheric corrosion to occur on several metal

Distribution Statement A. Approved for public release.

substrates [4]. This critical relative humidity therefore depends upon the type of metal surface, the type of corrosion products or species and particulates/pollutants that are present in the system. Also, atmospheric constituents found on metal surfaces are a function of the atmosphere itself, with sulfates, nitrates, nitrites, chlorides, carbonates, hydrogen ions, ammonium, metal ions, particulates and organic compounds commonly found in electrolyte chemistries or corrosion layers. Each of these have an effect on the corrosion processes on exposed surfaces [5]. These result either directly from the deposition processes or from aqueous phase reactions of the deposited atmospheric constituents, whereas sulfates, nitrates and nitrites originate either directly from the wet deposition process, from particle deposition or from reactions of the gaseous air pollutants in the aqueous phase of the adsorbed electrolyte [1]. Atmospheric oxidizing agents such as ozone and hydrogen peroxide, and hydroxyl radicals are also important reactants on the surface, facilitating the formation of numerous organic compounds.

Many investigations have been performed in order to clarify the role of environmental and climatic factors in the atmospheric corrosion of commonly used structural metals and coatings as well as to simulate in the laboratory their observed corrosion behavior in the field [6]. Nearly every coatings test and qualification organization has documented instances where the corrosion performance of a series of coating systems in accelerated tests (such as ASTM B117) do not correlate with the rank order of performance in an outdoor exposure environment [7] [8]. This disparity has become more pronounced with the introduction of non-chromate based corrosion inhibitors, since the B117 protocols were developed around quality control of chromate systems [9]. Previous work has documented cases in which uncoated metal substrates do not show the same corrosion products in laboratory tests compared to outdoor exposure [7] [10] [11] [12]. Clearly, there are fundamental chemical and thermodynamic differences between these two environments. The first step towards developing better accelerated test methods is to analyze and accurately reproduce these environments in a laboratory setting. The second step in this process is to accelerate the kinetics of the simulated environment to enable performance evaluation in a reasonably short period of time to predict long term outdoor performance. Properly accelerating the kinetics involves knowledge of both the interaction of corrosive species as well as the effects within the polymeric coating system. These effects are specifically related to the diffusion rate of electrolyte into primer which contains inhibitor species, dissolution rate of the inhibitor, and transport phenomena and kinetics of inhibitor ions to suppress corrosion in damage/scribe sites. The method used to accelerate total corrosion performance must equally accelerate all of these factors; otherwise both false positives and false negatives are possible. A successful accelerated test method would provide accurate predictable results for any substrate with any type of protective coating present.

Prior to the effort described in this report, the synergistic effects of ozone, UV, and atmospheric chlorides were suggested to be a factor in the formation of transient chlorine gas which can rapidly react with metallic surfaces. This theory gained attention due to the formation of silver chloride films on bare silver coupons exposed outdoors, while no apparent reaction occurs in B117 exposure [8] [13] [14]. These proposed synergistic effects were investigated in a preliminary study at AFRL in 2007 and it was concluded that both the theory and explanation of corrosion products presented in the literature were incomplete. In that preliminary study, AFRL developed and exposed both bare silver and AA2024-T3 coupons in a custom exposure chamber which provides ozone, UV, and electrolyte exposure simultaneously and the results of that work demonstrated that corrosion is accelerated dramatically with the presence of a synergistic ozone

Distribution Statement A. Approved for public release.

+ aqueous environment. Therefore, for any accelerated corrosion exposure test to be directly correlated with results observed on field exposed samples, it would be critical to reproduce the presence of silver chloride films on any chamber exposed silver coupons. In addition to silver coupons, a comprehensive understanding of the role of environmental conditions and atmospheric contaminants on the corrosion of aluminum alloys used in aerospace applications such as AA2024, AA6061 and AA7075 as well as 1010 steel are required to meet the demand for reliable accelerated corrosion testing of widely used structural metal substrates for DoD applications. Finally, the interaction of pure copper with environmental atmospheric contaminants is of interest, since its corrosion behavior in standardized accelerated atmospheric corrosion tests has also demonstrated a disparity with what is observed in the field [15].

Past atmospheric corrosion modeling efforts most commonly employed statistical power-law or regression approaches that predicted corrosion as a linear or simple nonlinear process. Such models are incapable of considering how rapid changes to environmental factors result in highly variable corrosion rates. Some of these legacy models can be highly accurate but only when making predictions for those locations where corrosion test results and environmental data was collected for use during calibration. When these same models are applied to data for independent locations with different environmental conditions (e.g., validation locations), their accuracy is uncertain.

Environmental corrosivity is influenced by temperature, relative humidity, chloride aerosols, sulfur dioxide, ozone, and other potential factors. The actual levels of most, if not all of these factors can vary significantly over short periods of time. Thus, a model intended to attain a high level of accuracy must consider variability resulting from the combined effects of diurnal and seasonal temperature cycles, related changes to humidity levels, and stochastic changes to atmospheric contaminants. A corrosion model that directly considers such variability would be analogous to variable amplitude fatigue models. As such, the successful implementation of such a cumulative damage methodology could enable a new paradigm in product design and sustainment. The data collected from this effort was used in part to develop a corrosion damage model.

It was proposed that a matrix of bare coupons (for baseline corrosion kinetics and corrosion product composition and morphology), coated coupons (for baseline coating performance evaluation) and coated galvanic couple lap joint (2024 aluminum with steel fasteners) specimens would be exposed at various geographic locations in order to understand the role of atmospheric contaminants and environmental conditions on the corrosion and degradation of bare and coated substrates, respectively. The database generated from these field exposures was to then be the basis for the design and testing of an accelerated corrosion test protocol on identical bare and coated specimens using a laboratory atmospheric exposure chamber; surface and chemical analyses of both field- and chamber-exposed substrates would be compared to determine if similar corrosion behavior (corrosion product and surface morphology) could be obtained under accelerated conditions.

Distribution Statement A. Approved for public release.

III. MATERIALS AND METHODS

Preparation and Analysis of Substrates

Bare Coupons: Coupons of aluminum alloys AA2024-T6, AA6061-T3, AA7075-T6; 1010 steel, 99.99% silver and 99.99% copper were either mounted on corrosion "Exposure Cards" or "Exposure Picture Frames." The Exposure Cards are FR4 pc board material and the coupons are mounted on nylon standoffs (Figure 1) for land-based exposure racks and the Exposure Picture Frame is a Lucite frame (bolted together with stainless steel nuts and bolts which do not come in contact with the sample coupons held within the frame) for ship-board exposure racks (Figure 2). The coupons were 1/2 x 3 x 1/16 inches in dimension. Coupons were used as received from Battelle (Columbus, Ohio) already mounted in their respective mounts. Duplicate cards or frames of coupon sets were retrieved at 3 month intervals over a 2 year period for a total of 8 sets of coupons per exposure site. Upon receipt of the duplicate sets of bare coupons, one set was delivered to Dr. William Abbott at Battelle Laboratory in Columbus, OH where they were cleaned and the mass of each coupon determined to the nearest 10 microgram (0.00001 g) as per ASTM G1 [16]. The other set of identical coupons were analyzed at UDRI for chemical composition and morphology using a Zeiss EVO-50XVP environmental scanning electron microscope (ESEM) equipped with an EDAX Genesis 2000 energy dispersive spectroscopy (EDS) system. This X-ray microanalysis system could detect all elements with an atomic number greater than or equal to 5. The microscope was operated in high vacuum mode using an electron acceleration voltage of 25 kV. The working distance was nominally 15 mm. Magnification varied according to the sample and location being analyzed. An aluminum-copper (Al-Cu) standard was used to calibrate the X-ray system prior to analysis.

Silver chloride (AgCl) Film Formation Determination on Pure Silver Coupons: For the pure silver coupons, cathodic reduction was performed to determine the presence and thickness of the AgCl film on the silver substrate exposed at the various exposure sites over a two year period as an indication of corrosion rate and kinetics of film formation. This information is critical towards determining what is required for film formation on silver coupons in future chamber exposures as well as determine a relationship between environmental factors and geographical location and the corrosion of the silver coupons.

Coulometric reduction on a silver coupon after the field exposure was carried out to measure the AgCl film thickness by Dr. William Abbott at Battelle Laboratory in Columbus OH [17]. The electrolyte used for the experiment was 0.1 M Na2SO4, with the pH adjusted to 10.0 with sodium hydroxide and deaerated for 1 hour with argon. A mercury/mercury sulfate reference electrode was used to avoid chloride contamination. The silver samples were exposed to a constant cathodic current of and the potential was recorded as a function of time. The amount of time to reduce the silver at each potential is related to total charge at a constant current, which can be used to measure the AgCl film thickness using the Faraday constant, the equivalent weight and density of the compound being reduced.

Distribution Statement A. Approved for public release.

Coated Panels: Samples of 10 separate coating systems on either 2024-T3 or 1010 steel substrates were processed as described in Table 1. The lap joint specimens are highlighted in green to signify them as different from the other coating systems. The coated panels (Figure 3) were deployed (in triplicate, except for shipboard exposures) as two sample sets to be retrieved at 12 month intervals over 2 years. Upon receipt of the coated panel samples and lap joint specimens, the surface of the scribed panels and interior faying surface of the lap joints were analyzed for chemical composition and morphology using the ESEM/EDS system described previously.

Further analysis of the coated samples from the field exposures as well as samples exposed in the accelerated chamber were performed using Fourier Transform Infrared (FT-IR) Attenuated Total Reflectance (ATR) [18] on a Nicolet Model 4700 spectrometer with a potassium bromide (KBr) Mid-IR detector using Omnic spectroscopy software.

Figure 1. Bare coupons mounted on Exposure Card.

Figure 2. Bare coupons mounted in Exposure Picture frame.

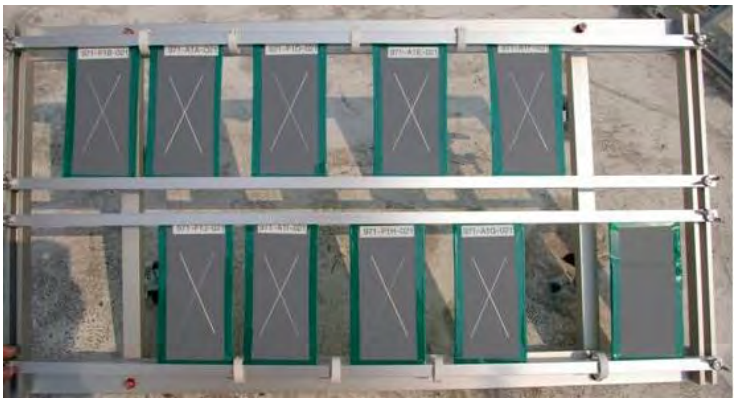

Figure 3. Shipboard exposure rack of 1 set of coated samples as described in Table I.

Distribution Statement A. Approved for public release.

Table I. Summary of substrates and coating systems deployed. Lap joint specimens are highlighted in green.

System	Substrate / Code	Pre Clean	Clean/Wash	De-Ox	Conversion Coat	Primer 0.6 - 0.9 Mils	Topcoat 1.7 - 2.3 Mils	Panel ID #s (12"x12" 8UP)
A	2024-T3 Bare .032"	Standard CTIO Prep			Alodine 1600	Deft 02-Y-40	Deft 99-GY-001	971-A1A-001 .. 040
B	1010 Steel 0.030"	Solvent Wipe and Alkaline Clean			None	MIL-PRF-26915 Zinc Rich Primer		971-F1B-001 .. 040
C	2024-T3 Bare .063" Lap Joints assembled with Hy-Loks	Standard CTIO Prep			Alodine 1600	Deft 02-Y-40		971-A1C001 .. 144 **12up .. 3x4s before assembly**
D	1010 Steel 0.030"					Deft 02-Y-40		971-F1D-001 .. 040
E	2024-T3 Bare .032"					Deft 02-GN-084		971-A1E-001 .. 040
F	2024-T3 Bare .032"				Alodine 5200	SICO 577-630 or alternate product	Akzo Nobel Aerodur 5000	971-A1F-001 .. 040
G	2024-T3 Bare .032"	Prekote				Akzo Nobel 2100 Mg-Rich 1.0-1.4 mils		971-A1G-001 .. 040
H	1010 Steel 0.030"							971-F1H-001 .. 040
I	2024-T3 Bare .032"					Negative Primer	Deft 99-GY-001	971-A1I-001 .. 040
J	1010 Steel 0.030"							971-F1J-001 .. 040

Exposure of Bare Coupons and Coated Panels at Outdoor Sites

Bare coupons and coated panels were deployed to 8 sites, (6 land-based and 2 ship-based, Table II).

Table II. Matrix of exposure sites and number of bare coupons (Cards or Picture Frames) and coated panels.

Site	Bare	# Cards/Picture Frames	Coated	# panels*	size panels
Daytona Beach, FL	x	16 Cards	x	60	3" x 6"
East Coast Ship, DE	x	16 Picture Frames	x	20	3" x 4"
Pt. Judith, RI	x	16 Cards	x	60	3" x 6"
Kirtland AFB, NM	x	16 Cards	x	60	3" x 6"
Tyndall AFB, FL	x	16 Cards	x	60	3" x 6"
Hickam AFB, HI	x	16 Cards	x	60	3" x 6"
Wright-Pat AFB, OH	x	16 Cards	x	60	3" x 6"
West Coast Ship, WA	x	16 Picture Frames	x	20	3" x 4"

* sites with 20 panels had 10 coating systems returned at 1-year point and 2-year point

* sites with 60 panels had 10 coating systems in triplicate, each set of 3 returned at year 1 and year 2 time points.

Collection of Weather Data at Outdoor Sites:

Weather monitoring stations capable of measuring total ultraviolet (UV), relative humidity (RH), ozone and temperature (°F) were deployed at six of the eight locations. These six locations were: East Coast Ship (DE), Wright-Patterson AFB, Kirtland AFB, Tyndall AFB, Pt. Judith, and the West Coast Ship (WA). The weather data was collected using a HOBO U23 Pro v2 external temperature/relative humidity data logger (Onset Computer Corporation, Pocasset, MA), a Series 130 ozone transmitter (Aeroqual Ltd., Auckland, NZ), and an SU-100 UV Sensor (Apogee Instruments, Inc., Logan, UT). The data was recorded on an hourly basis and

Distribution Statement A. Approved for public release.

downloaded approximately every 3 months using a HOBO U12 4 channel external data logger and HOBO U-DT-1 Shuttle Data Transporter. An image of a deployed weather monitoring instrumentation station is presented in Figure 4. Collection of weather data was designed to be coordinated with the retrieval of exposed cards and panels. The collective data for each parameter at each site are presented in Appendix A. A weather monitoring station was not deployed at the Daytona Beach Battelle site since they already have a monitoring station there; a system was also not deployed at the Hickam AFB, HI site since there was not a reliable power supply in close proximity to the exposure site.

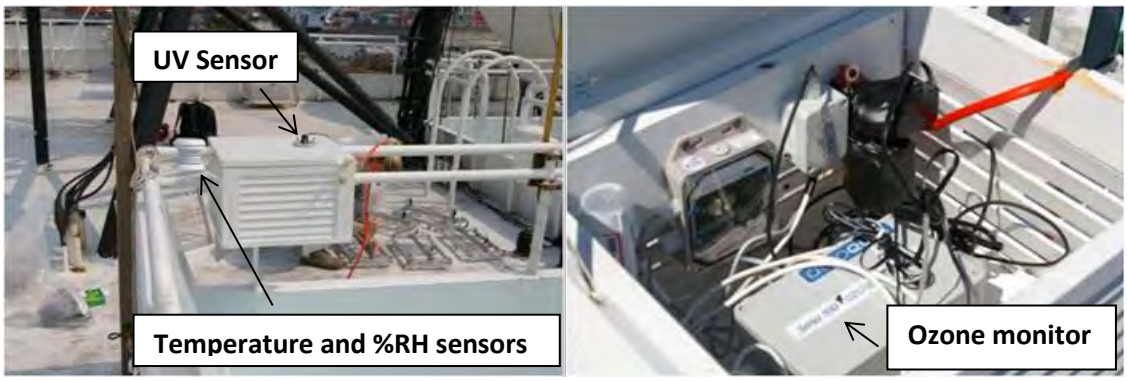

Figure 4. (Left) Image of weather monitoring station mounted on railing above pilot deck on the West Coast ship, R/V Thomas G. Thompson, showing the location of the UV sensor. (Right) Image showing ozone measurement and data logging instrumentation inside monitoring station.

Modification of Exposure Test Chamber:

In order to investigate the role of environmental and climatic factors in the field exposure sites, a standard corrosion test chamber (Q-Lab Corporation, OH) capable of conducting ASTM B117 exposure tests was modified with the introduction of both ultraviolet A (UV-A) illumination and ozone gas. The UV-A lamps (Q-Lab Corporation, OH) were installed on the exterior of the chamber lid and illuminated the coupons within the chamber through quartz windows. A commercial ozone generator (Pacific Ozone Model L11, CA), ozone monitor (Teledyne Model M450, CA) and a proportional-integral-derivative (PID) controller with microprocessor (Love Controls 2600 Series, IN) were put in line and plumbed into the exposure chamber to provide and control ozone levels. The ozone level within the chamber as a function of time and under continuous salt spray conditions was monitored during the exposures. The exhaust effluent gas from the chamber was passed through a graham condenser to remove the majority of the salt from the flow stream and the effluent gas was measured for ozone concentration. The ozone monitor was wired in a signal feedback loop to the PID controller microprocessor which actuated a control valve regulating the flow of ozone into the chamber. The UV-A irradiance levels as a function of distance from the light fixtures and location within the chamber were measured and mapped. Placement of the replicate test bare coupons and coated panels were randomly distributed within the chamber to ensure that UV irradiance levels could be accurately correlated with each sample. Therefore, using this modified exposure chamber, the effect of UV and ozone on the corrosion behavior of bare metal coupons and coated panels, which are identical to the samples deployed at the eight

Distribution Statement A. Approved for public release.

exposure sites, was investigated. The image of a modified exposure chamber system is shown in Figure 5. The map diagram of UV-A intensities as a function of location within the chamber is presented in Figure 6. The maximum irradiance level for the illumination fixtures was approximately 46.80 W/m^2.

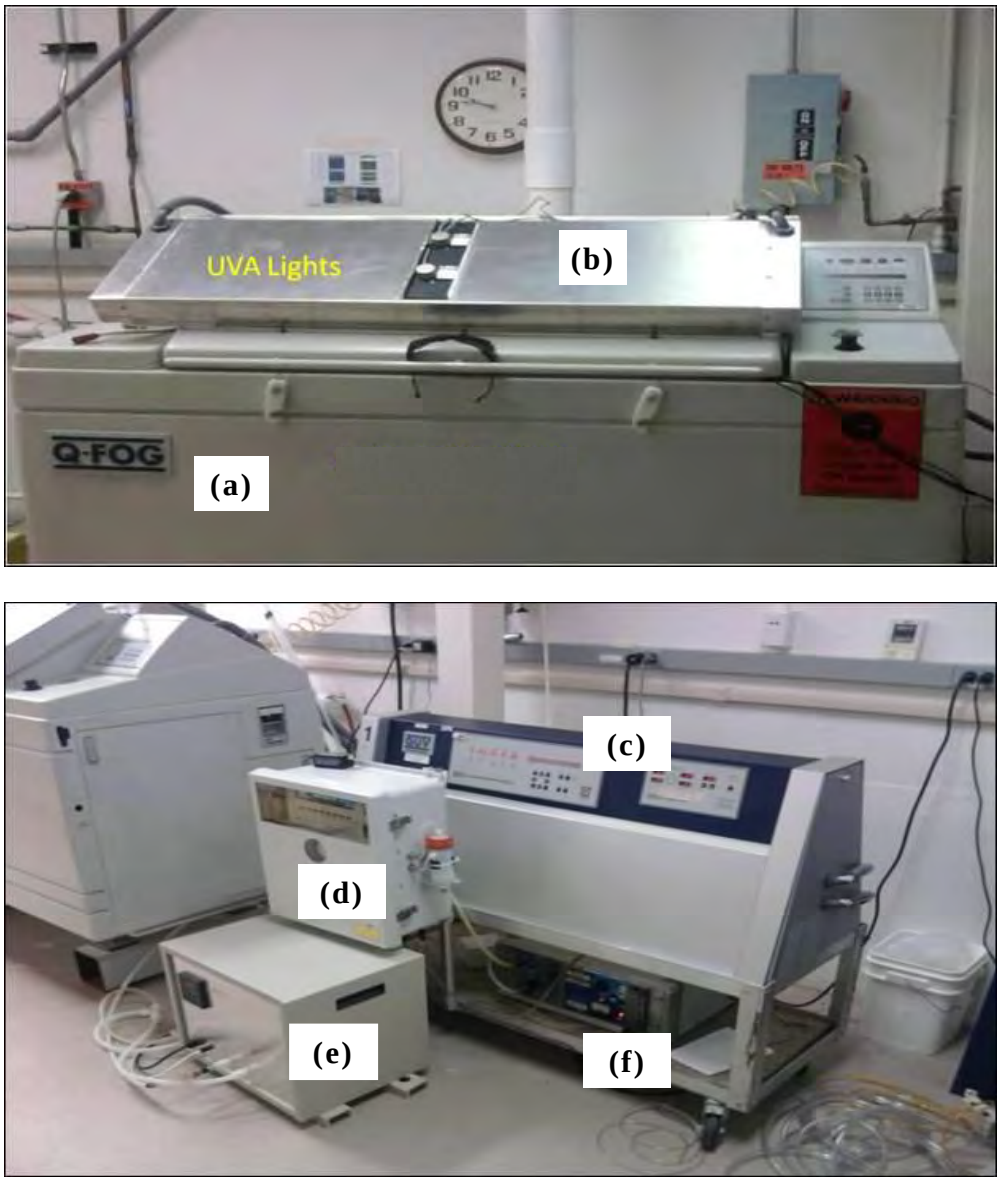

Figure 5. Images of the modified exposure chamber exposure system. (a) Q-Fog salt spray chamber, (b) UV-A light fixtures, (c) QUV accelerated weathering tester, (d) Teledyne ozone monitor, (e) PID and microprocessor control system and (f) ozone generator

Figure 1. Images of a modified exposure chamber system. (a) Q-fog salt chamber, (b) UVA lights, (c) QUV accelerated weathering tester, (d) Teledyne ozone monitor, (e) microprocessor control system and (f) ozone generator.

Distribution Statement A. Approved for public release.

25.03	15.24	**26.67**		**25.03**	9.80	17.96
26.67	25.03	31.56		31.56	25.58	25.58
23.40	28.30	28.84		28.30	28.30	21.77
23.94	31.56	27.21		28.30	27.75	21.77
31.02	37.55	32.65		33.20	34.83	28.30
31.02	36.46	32.65		34.28	38.09	30.48

3.81	2.72	**4.35**		**4.35**	2.18	2.72
3.81	3.81	4.35		4.35	3.27	3.27
3.27	4.35	4.35		3.81	3.81	3.27
3.81	4.35	3.81		3.81	3.81	2.72
4.35	4.35	4.35		3.81	4.35	3.81
3.81	4.90	4.90		4.35	4.35	3.81

Figure 6. Map of UV-A irradiance levels in chamber based upon location on exposure racks. (Top) Irradiance levels when light fixtures set at maximum illumination power (46.80 W/m^2). (Bottom) Irradiance levels when light fixtures set at minimum illumination power (5.44 W/m^2). Yellow areas indicate restricted exposure sites where illumination is obstructed due light fixture configuration and geometry of chamber lid and hinge points.

Based upon the maximum and minimum levels of irradiance of the UV-A light fixtures and the levels of ozone that the system was capable of controlling with precision, the exposure chamber test levels for the bare and coated samples were:

- Low Ozone (100 ppb) / Low UV-A (3.87 W/m^2)
- Low Ozone (100 ppb) / High UV-A (27.93 W/m^2)
- High Ozone (800 ppb) / Low UV-A (3.87 W/m^2)
- High Ozone (800 ppb) / High UV-A (27.93 W/m^2)

Distribution Statement A. Approved for public release.

Each condition was run for 1000 hours for the bare coupons; to expedite chamber testing of the coated panels, it was determined to expose the coated panels under high ozone / low UV-A conditions for 1000 hours immediately followed by low ozone / high UV-A conditions for an additional 1000 hours for a total of 2000 hours exposure testing. The coated panels were removed at 400 hour intervals and analyzed and compared with identical coated samples exposed for 1 and 2 years in the field, as well as identical samples exposed for 1000 hours in the B117 test chamber.

Cumulative Corrosion Damage Modeling Approach

The cumulative corrosion damage model described here was developed using an iterative inverse modeling approach [19]. During this process, 268 specific models based upon 16 different linear and nonlinear formulations were calibrated and statistically tested by comparing them to test measurements. During this process, nearly 150 billion Monte Carlo simulations were employed in a systematic and repetitive optimization process used to identify the most accurate model formulation. Predictions were made during each simulation run by applying a large group of candidate models (e.g., 1.5 million similar models) to large amounts of training data representing hourly environmental conditions at multiple calibration sites where actual corrosion tests were conducted. The predictions from each model were then statistically compared to test measurements and the most accurate model out of the group was identified. The modeling coefficient values pertaining to that model were then used to help set the parameters for the next run of simulations. Semi-automated analyses conducted during the simulation processes were employed that enabled convergence to the most accurate model and associated coefficients. Final formulations were then validated by applying the most accurate model to independent test and environmental characterization data for numerous other locations not used for calibration. The final proof-of-concept model is quite accurate and forms the basis for improved future models.

Model Formulation: Cumulative damage modeling refers to approaches where small increments of predicted damage are calculated for small increments of time and the individual results are then added together to make long-term predictions. Such an approach is used in certain types of random amplitude fatigue models, whereby individual damage increments are assumed to be identical if the applied loading during each cycle remains constant or the individual damage increments can vary in magnitude in response to variable cyclic loading. This current effort is the first to implement such an approach in the area of atmospheric corrosion prediction. The process is illustrated by Equation 1, whereby hourly increments of corrosion damage (indicated by the independent “Ki" variables) are added together to make long-term (i.e., annual) corrosion rate predictions, K.

$$K = \sum_{i=1}^{n} \mathrm{K_i} = K_1 + K_2 + K_3 + \ldots + K_{n-1} + K_n \tag{1}$$

Distribution Statement A. Approved for public release.

Equation 2 describes the final notional model developed under the current program. The basis of this cumulative corrosion damage model is a tailored form of the Eyring equation, which was originally developed to predict the kinetic rates of chemical reactions based upon changes to the levels of acceleration factors that contribute to the reaction [20].

$$K_i = \exp\left(\frac{\Delta H}{kT}\right)[A_{CL}T^{\alpha CL} f_{Cl}(T,RH) f(T,Cl) + A_{SO2}T^{\alpha SO2} f_{SO2}(T,RH) f(T,SO_2) + A_{O3}T^{\alpha O3} f_{O3}(T,RH) f(T,O_3) \tag{2}$$

Distribution Statement A. Approved for public release.

Table III. Definition of the Variables and Coefficients used in Equation 2

Model Component	Description	Units
K_i	Hourly corrosion rate	$\mu g/cm^2$
A_{Cl}	Scaling factor for the chloride reaction	$\mu g/cm^2$
A_{SO2}	Scaling factor for the SO_2 reaction	$\mu g/cm^2$
A_{O3}	Scaling factor for the ozone reaction	$\mu g/cm^2$
αCl	Temperature adjustment exponent used for the chloride reaction	nondimensional
αSO_2	Temperature adjustment exponent used for the SO_2 reaction	nondimensional
αO_3	Temperature adjustment exponent used for the ozone reaction	nondimensional
T	Temperature	Kelvin (K)
ΔH	Activation energy for the single activation energy formulation	eV/K
K	Boltzmann constant (=8.6173 x 10^{-5} eV/K)	eV/K
$f_{Cl}(T,RH)$	Temperature-Relative Humidity shape function for the chloride reaction.	nondimensional
$f_{SO2}(T,RH)$	Temperature-Relative Humidity shape function for the SO_2 reaction.	nondimensional
$f_{O3}(T,RH)$	Temperature-Relative Humidity shape function for the ozone reaction.	nondimensional
$f_{Cl}(T,Cl)$	Temperature-Contaminant shape function for the chloride reaction. Calibrated using chloride deposition measurements (mass per unit volume of rainwater*)	nondimensional
$f_{SO2}(T,SO_2)$	Temperature-Contaminant shape function for the SO_2 reaction. Calibrated using hourly gaseous measurements (ppm) measured by automated air pollution monitoring systems.	nondimensional
$f_{O3}(T,O_3)$	Temperature-Contaminant shape function for the ozone reaction. Calibrated using hourly gaseous measurements (ppm) measured by automated air pollution monitoring systems.	nondimensional

*Chloride data used was mass concentration measurements (mg/L of rainwater) made under the National Atmospheric Deposition Program (NADP).

Table III contains descriptions and related units for the variables, coefficients, and functions used in the notional cumulative corrosion damage model shown by Equation 2. As seen in the equation, three different Temperature-Relative Humidity shape functions are paired with three associated Temperature-Contaminant shape functions. This was done in order to calculate three nondimensional numerical indices proportional to the portion of the overall corrosion rate that results from the interaction between temperature, relative humidity, and each

Distribution Statement A. Approved for public release.

of the individual atmospheric contaminants considered by the model. Hourly corrosion rates result when these indices are appropriately combined with the kinetic terms (i.e., the activation energy and Boltzmann constant) as well as the requisite scaling and temperature adjustment factors.

The cumulative corrosion model described here is implemented using the piecewise function shown by Equation 3. This equation results in nonzero corrosion rates only when the temperature exceeds the freezing point, Tf, and the relative humidity (RH) levels exceed the 60% RH threshold (RHTH) established (for iron and steel) by Vernon in 1935 [3]. The nonzero function seen in Equation 3 is the same function shown in Equation 2. Figure 7 illustrates how the corrosion model was designed to calculate independent reactions based upon the specific combination of temperature and relative humidity levels in combination with the three contaminants assumed to be responsible for corrosive reactions.

$$Ki = \begin{cases} f(T, RH, Cl^-, SO_2, O_3), & RH > RH_{TH} \text{ and } T > T_f \\ 0, & RH \le RH_{TH} \text{ or } T \le T_f \end{cases} \tag{3}$$

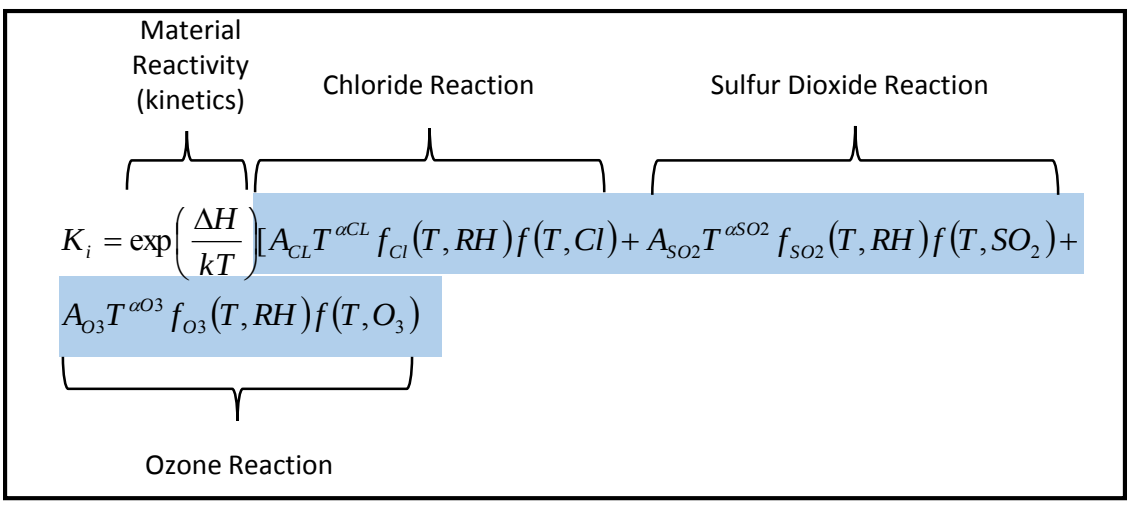

Figure 7. Cumulative Corrosion Damage Model Features

There are other atmospheric pollutants (e.g., nitrogen compounds) that when combined with suitable moisture and temperature levels are known to initiate and sustain corrosive reactions. However, for this proof-of-concept effort, it was assumed that sufficient prediction accuracy results from limiting consideration to the three contaminants employed by the above models. Another assumption made during the construction of this model was the proportion of the total corrosion rate due to each individual contaminant could be quantified using shape functions calibrated to account for different types of environmental characterization data including gaseous measurements (ppm) for air pollutant (i.e., SO2 and ozone) adsorption and concentration measurements (mass per unit volume of rainwater) for chloride aerosol particle deposition. Furthermore, it was assumed that gaseous SO2 levels were proportional to the total

Distribution Statement A. Approved for public release.

amount of all sulfur-based contaminants in the atmospheric environment including H2S, SO42- (sulphate), H2SO4 (acid rain), etc. This assumption enabled the construction of a single, properly calibrated shape function based upon SO2 measurements that was used to calculate the portion of the corrosion rate resulting from adsorption and deposition of all sulfur-based atmospheric contaminants. Similarly, it was assumed that wet chloride deposition measurements were proportional to the total amount of chloride deposition (i.e., wet and dry deposition) so that a single shape function could account for both processes.

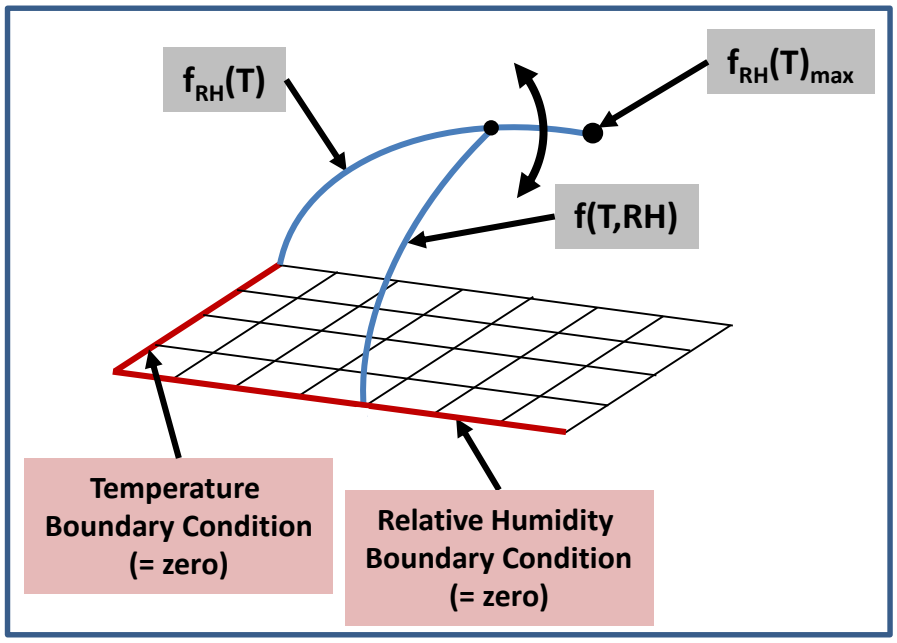

Figure 8. Construction of the Temperature – Relative Humidity Shape Functions

Figure 8 illustrates how the three Temperature-Relative Humidity shape functions shown in Equation 2 and described in Table III were constructed. For this proof-of-concept effort, the final shape functions examined via simulations were limited to those constructed from parabolic functions. Equation 4 describes how each of the three temperature functions used to define the three Temperature – Relative Humidity Shape functions (Equation 5) are constructed. The derivations for these functions, and those for the associated Temperature –Contaminant shape functions described later, are quite lengthy. The reader is referred to the complete Ph.D. dissertation for details concerning these derivations [19].

Distribution Statement A. Approved for public release.

$$f(T) = \frac{\sqrt{[\frac{-188}{(\mathrm{f_{RH}(T)_{max}})^2}](273.15 - T)}}{\frac{94}{(\mathrm{f_{RH}(T)_{max}})^2}} \tag{4}$$

$$f(T, RH) = \frac{\sqrt{-4[\frac{1 - RH_{TH}}{\mathrm{f(T)}^2}](RH_{TH} - RH)}}{2[\frac{1 - RH_{TH}}{\mathrm{f(T)}^2}]} \tag{5}$$

Figure 9 illustrates the Temperature – Relative Humidity shape functions that formed the basis for the final model. This shape function, which is similar to all three such functions, was constructed from two parabolic functions defined by Equations 4 and 5. There are three unique unknown values for fRH(T)max as shown on the figure, one for each of the three related Temperature-Relative Humidity shape functions used by the model described in Equation 2. Values for these three coefficients (along with the other unknowns) are determined via simulations.

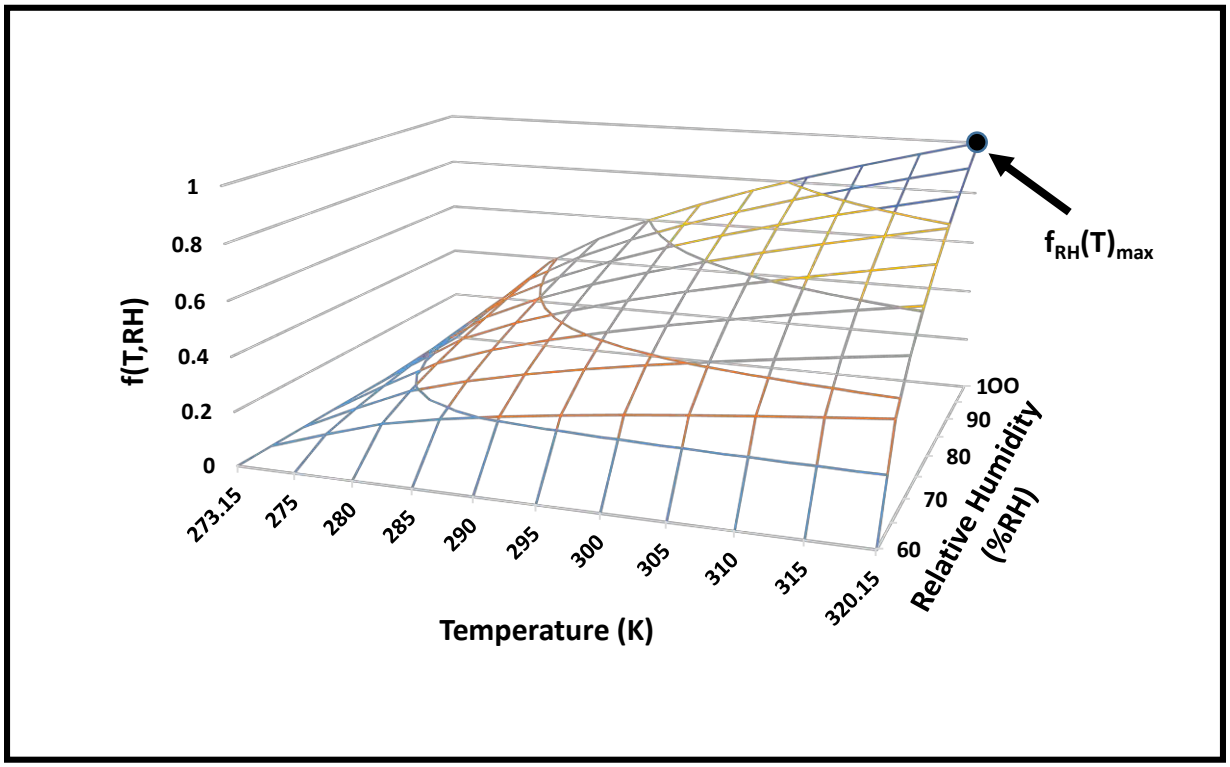

Figure 9. Illustration of the Temperature – Relative Humidity Shape Functions (assumes a value of $f_{RH}(T)_{max}$=1.0)

Distribution Statement A. Approved for public release.

Figure 10 illustrates how the three Temperature - Contaminant shape functions are constructed using upward-curvature parabolic functions. The temperature functions are constructed using Equations 6-9 while the subsequent Temperature – Contaminant shape functions are determined via Equation 10.

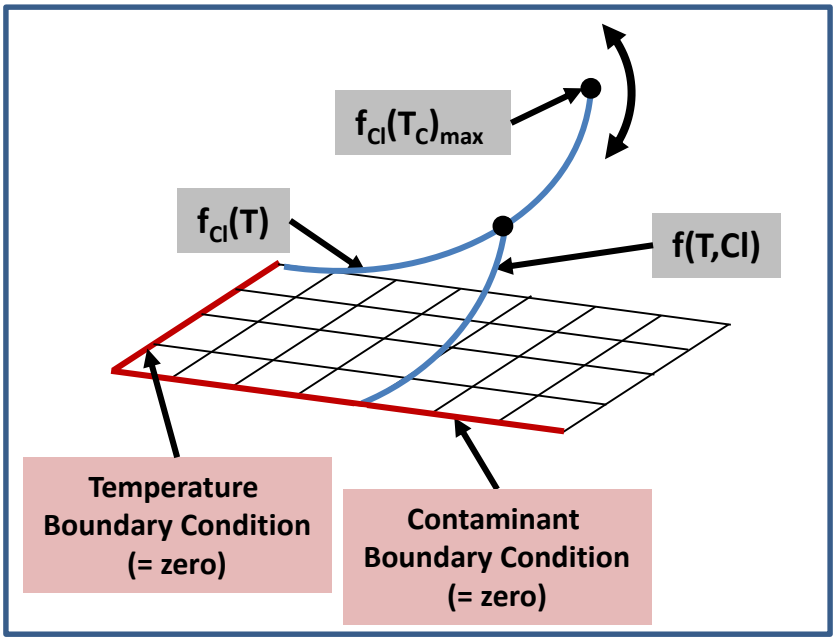

Figure 10. Illustration of How the Temperature – Contaminant Shape Functions are Constructed (illustration is for the chloride shape function, others are similar)

$$f_C(T) = aT^2 + bT + c \tag{6}$$

$$a = \frac{f_C(T)_{\max} - c - 320.15b}{(320.15)^2} \tag{7}$$

$$b = \frac{[\frac{(226.15^2)}{(320.15)^2} - 1]}{[226.15 - \frac{(226.15^2)}{320.15}]}(c - f_C(T)_{\max}) \tag{8}$$

Distribution Statement A. Approved for public release.

$$c = \frac{-\frac{(273.15)^2 f_C(T)_{\max}}{(320.15)^2} - [\frac{(273.15)^2[\frac{(226.15)^2}{(320.15)^2} - 1] f_C(T)_{\max}}{[226.15 - \frac{(226.15)^2}{320.15}](320.15)}] + 273.15 \frac{[\frac{(226.15)^2}{(320.15)^2} - 1] f_C(T)_{\max}}{226.15 - \frac{(226.15)^2}{320.15}}}{[-\frac{(273.15)^2}{(320.15)^2} - [\frac{(273.15)^2[\frac{(226.15)^2}{(320.15)^2} - 1]}{[226.15 - \frac{(226.15)^2}{320.15}](320.15)}] + 273.15 \frac{[\frac{(226.15)^2}{(320.15)^2} - 1]}{226.15 - \frac{(226.15)^2}{320.15}} + 1]} \tag{9}$$

$$f(T,C) = \frac{f(T_C)}{C_{\max}^2} C^2 \tag{10}$$

The three Temperature-Contaminant shape functions defined in Equation 2 and Table III are illustrated by Figure 11. As before, these functions are defined by the maximum values of the three associated temperature functions (i.e., f(Tc)max) used in their construction. In addition to the six total unknown maximum values for the temperature function (one for each shape function), there are other unknown coefficients employed by the model. These include the various scaling and temperature adjustment factors seen in the model (ACl, ASO2, AO3, αCl, αSO2, αO3) as well as the activation energy, ΔH. Thus there were 13 unknown variables that were determined via Monte Carlo simulations conducted on a massively parallel computing system.

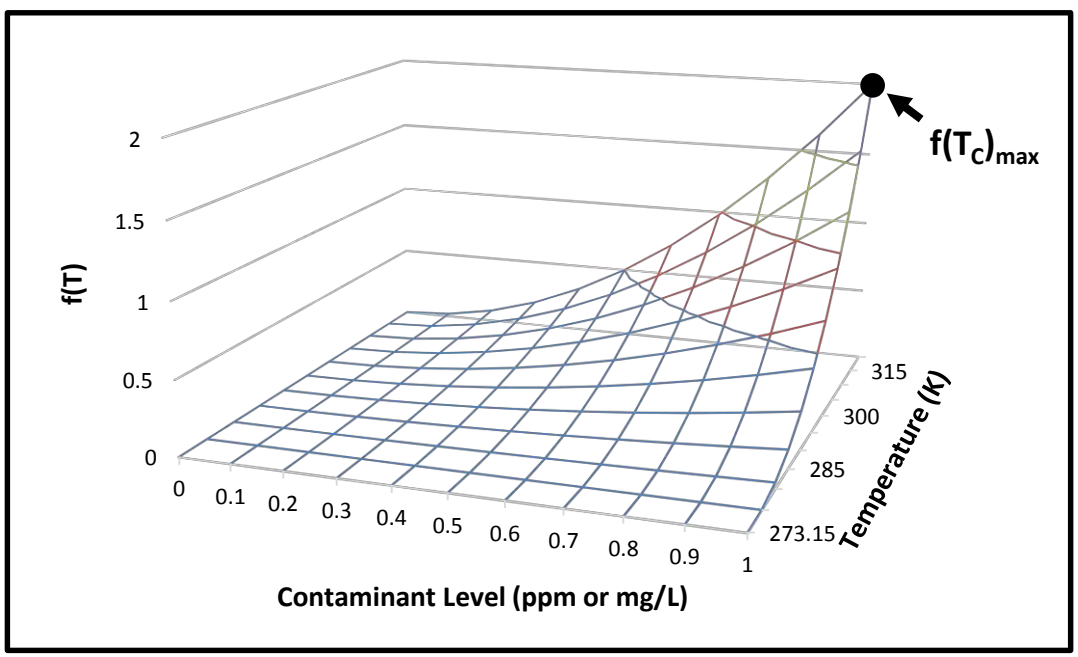

Figure 11. Illustration of the Temperature - Contaminant Shape Functions (assumes a value of C_{max} = 1.0)

Distribution Statement A. Approved for public release.

Model Calibration: Corrosion test data measured by Battelle [21] at three corrosion test sites with diverse environmental conditions was used to calibrate the final proof-of-concept model. These sites include Kennedy Space Center, Florida (five miles from the coast); Rock Island, IL; and Fort Drum, NY. The environmental severities for each site are quite different due to their differences with respect to climate zones and proximities to coastal surf areas and urban pollution sources. Such differences were needed so that high and low levels of hourly temperature, humidity, chlorides, SO2, and ozone levels were considered during calibration.

Proxy environmental data (data measured elsewhere for other purposes) was used to infer conditions at the time and place where the corrosion tests were conducted. This hourly data was applied to each candidate model and the results were statistically compared to test measurements to ascertain error.

A structured process using Monte Carlo simulations was used to iteratively evolve values for the numerous unknown modeling coefficients in order to identify the most accurate model formulation. This process applied each candidate to the proxy environmental data for a full year at each calibration site. Hourly temperature and relative humidity values measured at the nearest 24/7 National Weather Service or military base weather office were used during this process. Such data was combined with hourly air pollutant data (SO_2 and ozone) measured at the nearest pollution monitors (obtained from the EPA's Air Quality System database [22]) combined with longer-term average (e.g., monthly) wet chloride deposition data measured at the nearest National Atmospheric Deposition Program (NADP) monitor site [23].

IV. RESULTS AND DISCUSSION

Weather Monitoring Data

The weather data monitored at the field exposure sites are UV, ozone, temperature and % relative humidity (%RH). A complete set of data plots for the weather data monitored at the exposure sites are presented in Appendix A. Ozone levels monitored at the land-based exposure sites were in good agreement with the local EPA monitoring sites. Figure 12 shows the daily and yearly ozone level between Kirtland AFB and local EPA site, as a representative example of how well the monitoring system on site agreed with a local EPA monitoring site. As can be seen in Figure 12a the daily fluctuations of the ozone level during the winter time ranged from 0 to 40 ppb from 1 – 7 December 2009. The yearly pattern in Figure 12b shows the more visible seasonal pattern over the two years the site monitor was operational. During the summer months, the ozone levels reached as high as 80 ppb. Figure 13 shows a representative relationship between the following parameters: temperature, ozone, UV and relative humidity at hourly intervals from 1 – 7 June 2010, again at Kirtland AFB. Despite daily variability of the weather condition, typical daily patterns were found. Ozone concentration, UV and temperature are correlated positively while %RH has a negative relationship with ozone concentration, UV and temperature over daily pattern. Figures 14 and 15 show the distribution of cumulative frequency of Ozone concentration, UV, temperature and RH at the exposed locations. Ozone concentration, temperature and %RH at Daytona Beach, FL were utilized from Battelle's weather monitoring system. The weather monitoring station was not deployed at Hickam AFB, HI. For both of the ship based exposure sites, the East Coast Ship and West Coast Ship weather data, good agreement was observed between coastal EPA sites (when available) and the monitoring system

Distribution Statement A. Approved for public release.

contained on the ships. For the cumulative frequency of the weather parameters from all field exposure locations that had monitoring capability (Figures 14 and 15), the ozone levels ranged from 50 – 80 ppb for 99% of the time (Figure 14 a); for the UV levels, there was a range of 55 – 85 W/m^2 for all locations at a cumulative frequency of 99% (Figure 14b); In terms of temperature, there was a fairly close range of 82 – 98°F for the 99% cumulative frequency (Figure 15a); and in terms of RH, for 99% of the cumulative frequency all of the exposure sites exhibited 100% RH except for the Kirtland AFB, which was much lower at approximately 90% RH (Figure 15b). The average values for the four weather parameters monitored at the sites are presented in Table IV.

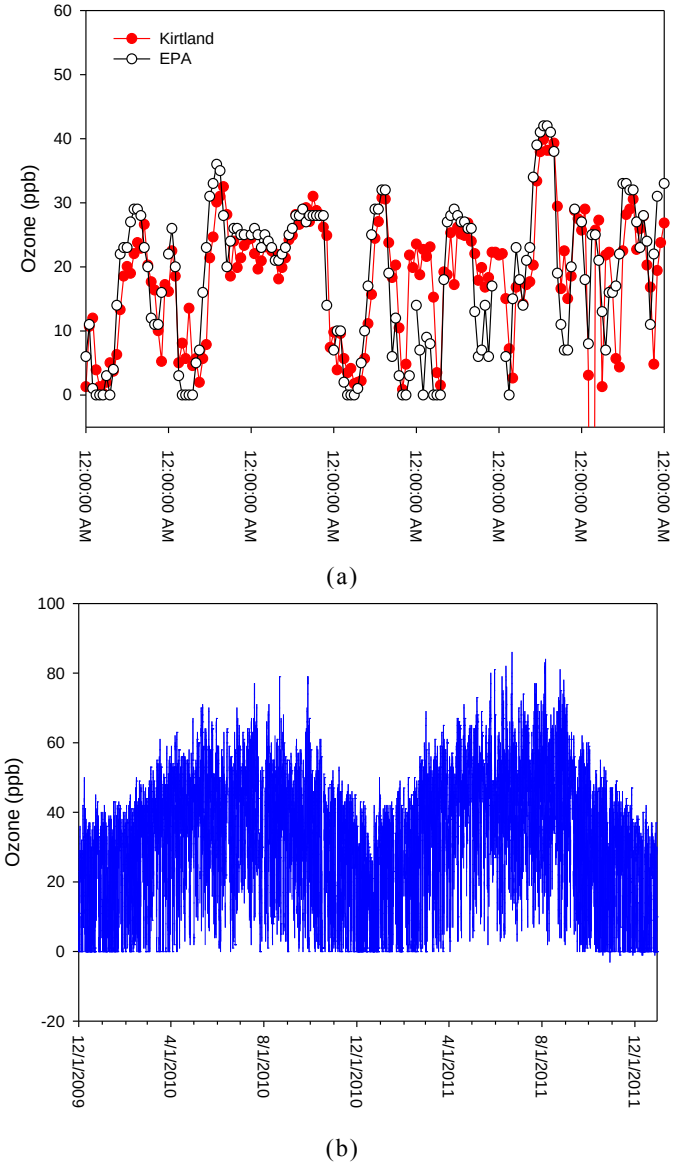

Figure 1. Concentration of ozone at Kirtland AFB. (a) Daily pattern with comparison to local EPA site (1–7 Dec. 2009). (b) Yearly pattern over two years.

Figure 12. Representative data of monitored concentration of ozone at Kirtland AFB. (a) Daily pattern with comparison to local EPA site for 1-7 December 2009. (b) Plot of ozone levels monitored hourly over two years.

Distribution Statement A. Approved for public release.

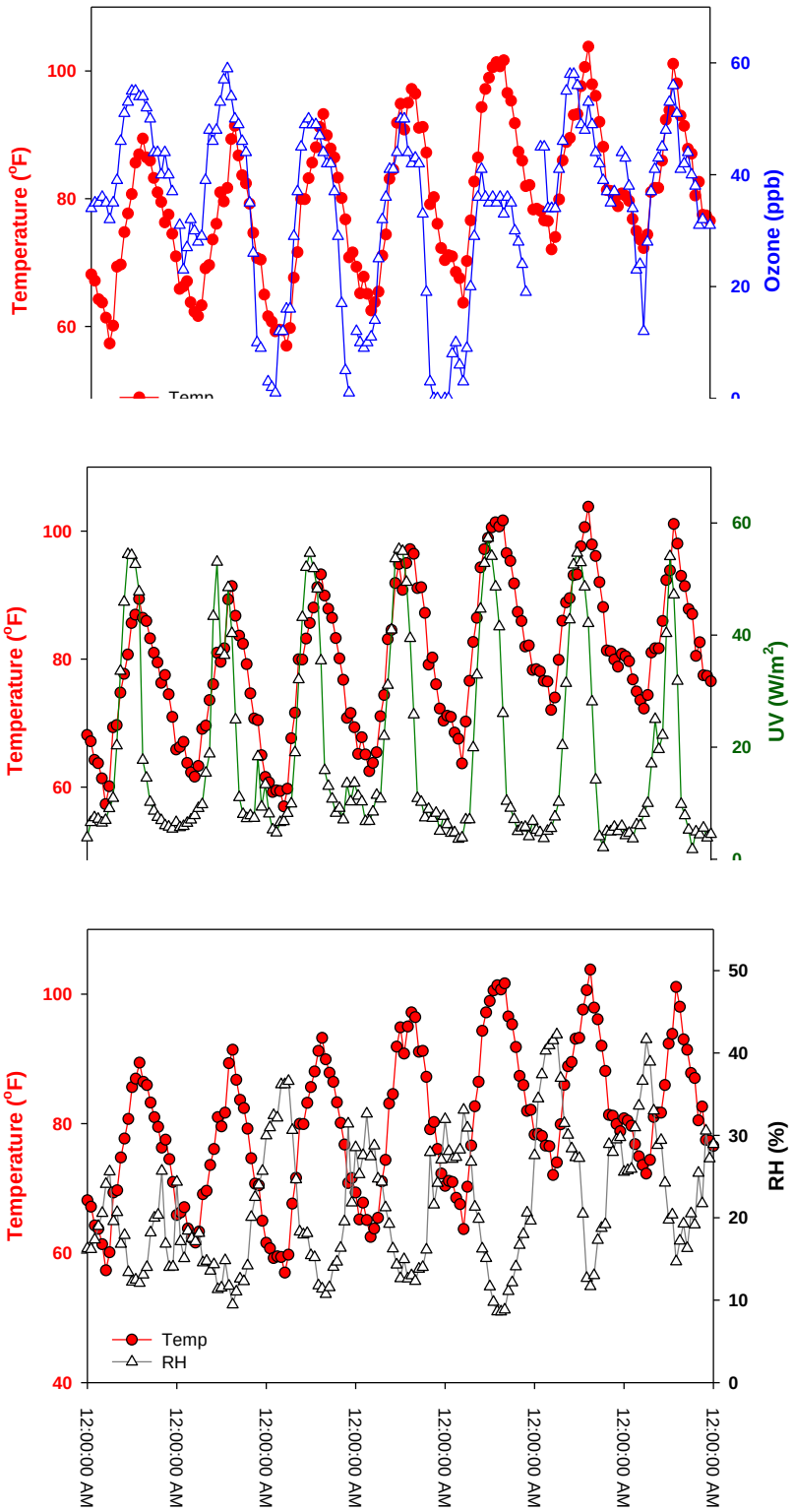

Figure 1. Temperature, ozone, UV and RH at Kirtland AFB from 1 to 7 June 2010

Figure 13. Plots of ozone, UV-A and %RH levels as a function of temperature at Kirtland AFB during 1 – 7 June 2010; data was recorded hourly and is presented over 24 hour intervals.

Distribution Statement A. Approved for public release.

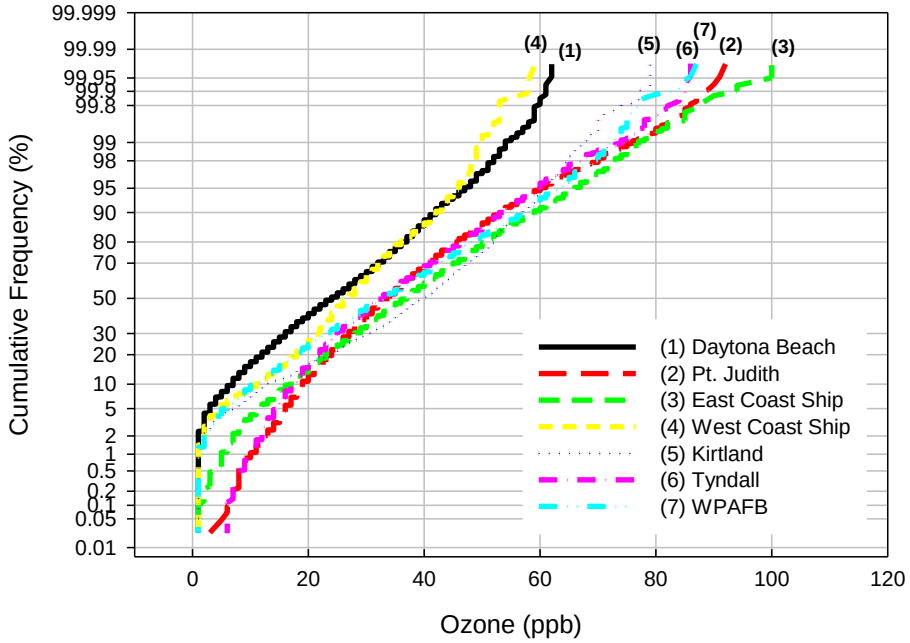

(a)

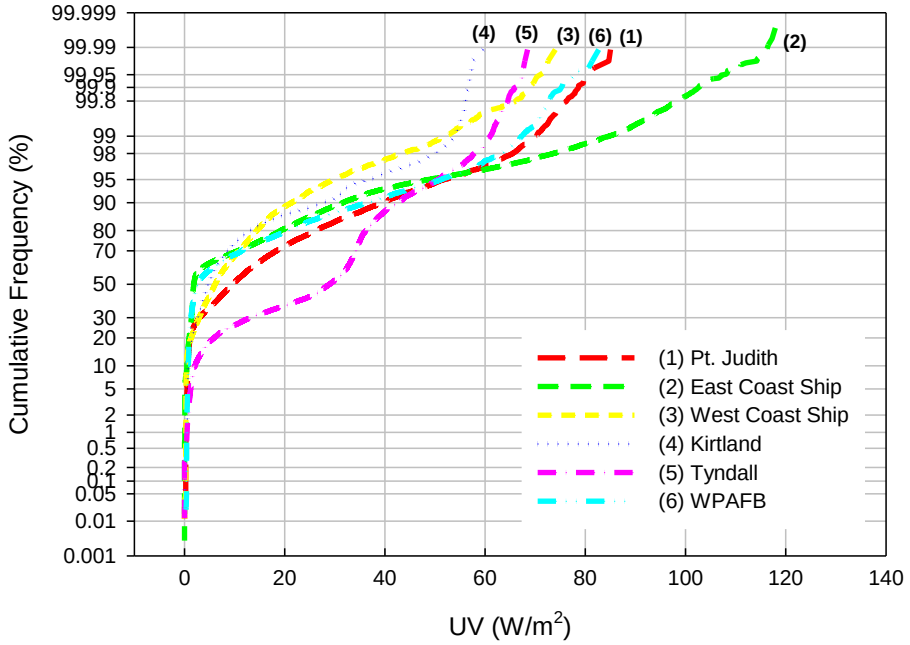

(b)

Figure 14. Cumulative frequency plots of (a) ozone and (b) UV levels monitored hourly over a 2 year period at the field exposure sites.

Distribution Statement A. Approved for public release.

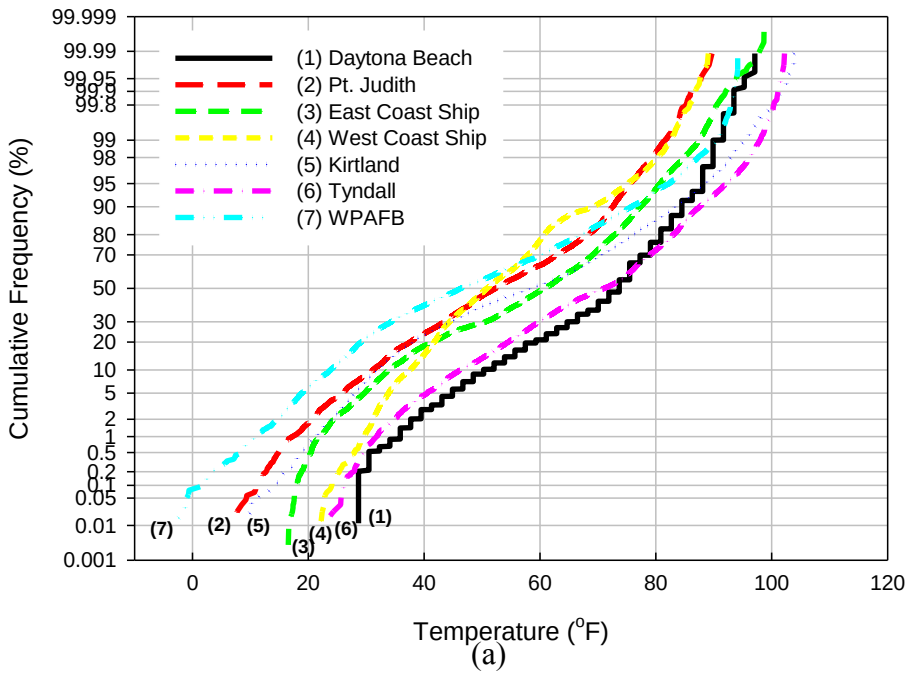

(a)

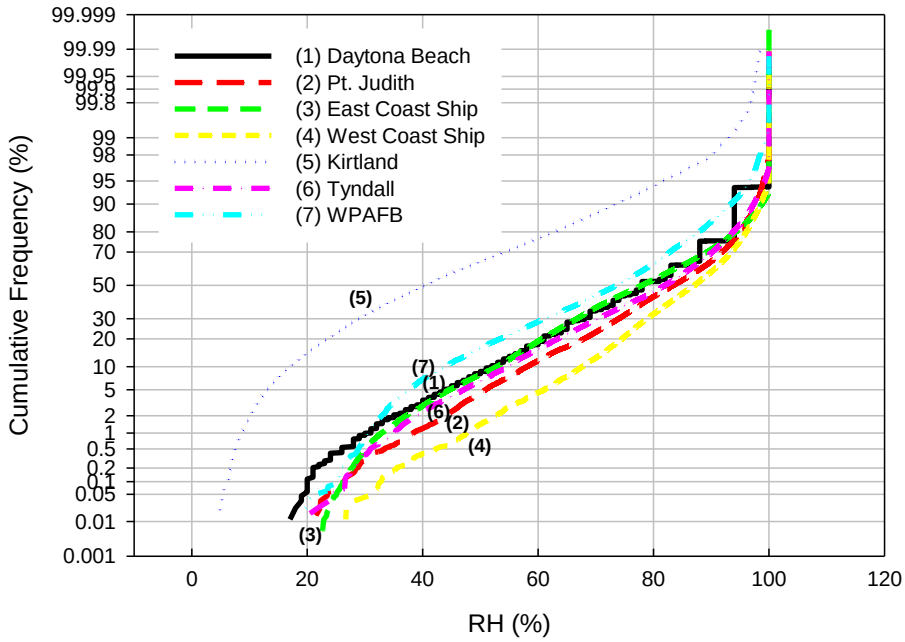

(b)

Figure 1. Distribution of cumulative frequency of (a) ozone, (b) UV, (c) temperature and (d) RH plots of (a) temperature and (b) %RH levels monitored hourly over a 2 year period at the field exposure sites.

Figure 15. Cumulative frequency plots of (a) temperature and (b) %RH levels monitored hourly over a 2 year period at the field exposure sites.

Distribution Statement A. Approved for public release.

Table IV. Average weather parameter values monitored at the field exposure sites over a 2 year period.

Site	Temperature (^oF)	Relative Humidity (%)	Ozone (ppb)	UV (W/m^2)
Daytona Beach, FL	70.2	75.9	26.7	*
Pt. Judith, RI	52.3	80.5	35.2	15.1
East Coast Ship, DE	58.1	76.4	37.4	10.8
West Coast Ship, WA	51.9	84.5	26.7	9.2
Kirtland AFB, NM	57.7	43.1	37.7	9.2
Tyndall AFB, FL	68.7	78.4	34.3	24.8
Wright-Pat AFB, OH	48.0	70.7	33.3	11.4

* No UV monitoring system at Daytona Beach (FL)
** No weather monitoring station at the Hickam AFB (HI) due to no power supply

Corrosion Rate/Mass Loss of Field Exposed Bare Coupons

The bare coupons containing AA7075-T6, AA2024-T3, AA6061-T6, 1010 Steel and pure copper were evaluated via gravimetric measurement, i.e., the corrosion rates were determined by weighing the coupons before exposure and after removal of the corrosion products using a standard cleaning method [16]. Mass loss data for the bare coupons at different exposure sites are given in Table V.

Aluminum and Steel Alloys: Mass losses of AA7075-T6, AA2024-T3 and AA6061-T6 at all locations during the 2 year exposure are shown in Figure 16. Remarkable differences between different exposure sites were observed: AA7075-T6 and AA2024-T3 exhibited the highest mass losses, and therefore the highest corrosion rates occurring at Daytona Beach with a cluster of the next highest rates occurring at Pt. Judith and both ship exposure sites as evident in Figures 16 (a) and (b). When the weather parameters measured for the exposure sites are reviewed, it is interesting to note that the ozone levels for Daytona Beach and the West Coast ship are the lowest values for the exposure sites over the 2 year period (Figure 14(a)). As UV data was not available at the Daytona Beach site, no direct correlation can be made between the possible interaction of UV and ozone for being responsible for the high mass loss observed on AA7075-T6 and AA2024-T3 at that location. However, when looking at the sites of Pt Judith, and both the West Coast ship and East Coast ship exhibiting the next highest corrosion rates for AA7075-T6 and AA2024-T3, all of which have UV and ozone data available. These exposure sites appear to present a correlation (although no statistical analysis of the data was performed) between the higher levels of UV and ozone for the East Coast ship and Pt. Judith and the elevated mass loss values in comparison to the remaining exposure sites. When the West Coast ship mass loss data and UV/ozone levels are considered, there appears to be similar mass loss and corrosion rates for AA7075-T6 and AA2024-T3 as compared to the other two sites (East Coast ship and Pt. Judith) but with relatively lower values of UV and ozone. This apparent difference may be due to different wet/dry exposure cycles, although for all sites except Kirtland AFB, 99% of the time the cumulative RH was 100%. The temperature ranges observed for Daytona Beach and the East Coast ship are very similar, with Pt. Judith and the West Coast ship exhibiting the lowest temperature ranges. Therefore, it is clear that other factors besides ozone, UV levels, temperature

Distribution Statement A. Approved for public release.

and RH may be responsible for the different ranges of mass losses (and therefore corrosion rates) observed. For example, surface chemistry and atmospheric contaminants present at the different sites may play a crucial role in the corrosion behavior of the aluminum alloys (discussed later).

Table V. Mass loss for the bare metal coupons for each location and retrieval interval over the two year exposure period.

($\mu g/cm^2$)

		3m	6m	9m	12m	15m	18m	21m	24m
Daytona Beach, FL	AA7075	590	1338	1630	2296	X	2363	X	3407
	AA2024	518	1380	2968	3669	X	4794	X	5561
	AA6061	62	140	173	210	X	469	X	690
	Steel	28626	68157	90335	*EOL				
Pt. Judith, RI	AA7075	496	871	865	1076	X	1193	X	1699
	AA2024	459	946	1077	1588	X	1670	X	2342
	AA6061	94	149	197	263	X	274	X	352
	Steel	24767	47885	67116	81671	X	97420	X	*EOL
East Coast Ship	AA7075	677	756	901	995	1251	951	1553	1428
	AA2024	615	944	749	1277	987	1046	1304	1405
	AA6061	352	410	423	580	713	773	782	816
	Steel	26986	41048	61504	79429	84662	94079	96097	100186
West Coast Ship	AA7075	544	783	1032	1163	1233	1279	1292	1657
	AA2024	463	730	944	1095	1181	1352	1499	1656
	AA6061	181	277	577	518	592	780	779	1005
	Steel	33639	46942	55740	68789	65995	76839	96138	107979
Kirtland AFB, NM	AA7075	21	10	1	5	4	2	0	X
	AA2024	14	13	5	4	0	2	0	X
	AA6061	16	12	7	2	3	5	0	X
	Steel	674	1575	1849	3256	3553	4580	12676	X
Hickam AFB, HI	AA7075	69	127	150	168	172	181	237	245
	AA2024	78	113	120	131	155	164	176	177
	AA6061	32	60	61	76	67	72	80	89
	Steel	8555	10323	16016	21821	23539	32655	38766	45398
Tyndall AFB, FL	AA7075	222	207	340	356	367	420	527	659
	AA2024	97	105	111	116	115	132	149	453
	AA6061	38	47	56	58	61	66	75	X
	Steel	7970	12652	16972	21001	23292	33709	32729	38983
WPAFB, OH	AA7075	25	26	76	81	88	89	91	102
	AA2024	13	26	51	54	59	43	60	72
	AA6061	29	17	47	52	52	36	58	64
	Steel	5833	9893	10111	14450	14813	18003	19905	23467

*EOL: End of life
X: not available

Mass losses of AA6061-T6 for both the East Coast Ship and West Coast Ship sites exhibited higher values than those at Daytona Beach and Pt. Judith. Mass losses of all three aluminum alloys at Tyndall AFB, Hickam, WPAFB and Kirtland AFB were the lowest, as exhibited in Figure 16 (a-c). Of special note is the mass loss of the alloys measured at Kirtland AFB, which were less than 20 $\mu g/cm^2$, which could be regarded as being equivalent to

Distribution Statement A. Approved for public release.

experiencing no mass loss during the 2 year exposure period. Based on the mass loss data, AA6061-T6 exhibits a much lower corrosion rate than AA7075-T6 and AA2024-T3 at all locations (Figure 17).

Corrosion rates of 1010 Steel at all exposure sites during 2 year exposure are also shown in Figure 18. As can be seen in Figures 16 and 17, the mass losses of the aluminum alloys were much lower than those of the 1010 steel, which indicates that the aluminum alloys have more corrosion resistance than the steel and also the steel could be used as a corrosion sensor material due to its high sensitivity to corrosive environments [13]. The highest corrosion rate of the steel coupon occurred at the Daytona Beach exposure site (Figure 18). After 12 months exposure, the steel coupon was totally corroded and disintegrated, and therefore designated to be at its "end of life" (EOL). The second highest corrosion rate of the steel coupon was observed at Pt. Judith and experienced as EOL after 18 months exposure. Following the Daytona Beach and Pt. Judith sites, the East Coast Ship and West Coast Ship both exhibited higher mass losses without experiencing EOL during the 2 year exposure. Again, UV data was not available at the Daytona Beach site, so there can be no direct correlation between the possible interaction of UV and ozone for being responsible for the high corrosion rate observed on 1010 Steel at that location; however, when looking at the sites of Pt Judith, West Coast ship and East Coast ship exhibiting the next highest mass losses for 1010 Steel, there appears to be a connection between the higher levels of UV and ozone for the Pt. Judith, East Coast ship and West Coast ship. This result suggests that a connection exists between mass loss and the exposure site in terms of its cumulative corrosion severity for the 1010 Steel coupons [13].

Copper: The bare copper coupons exhibited the highest mass loss at all of the exposure locations after the 1010 steel substrates (Table V). Not surprisingly, the location demonstrating the greatest mass loss for copper over the two year exposure period is Daytona Beach, followed by Pt. Judith (Figure 19). The corrosion of copper is sensitive to the presence of sulfur dioxide (SO_2) nitrogen dioxide (NO_2), ozone (O_3), ammonium ions (NH^{4+}) sulfate ions (SO_4^{-2}) and chloride ions (Cl^-) [24], [25] and therefore it is not surprising to see that the corrosion rate of the copper coupons at WPAFB and Kirtland AFB is similar after one year to that of other coastal exposure sites such as the East and West Coast ships, Hickam AFB and Tyndall AFB.

Steel: As can be seen in Figure 18, there were two distinct groupings of corrosion rates relative to each other within the eight field exposure sites: four exposure sites [Daytona Beach, FL, Pt. Judith, RI, the East Coast ship (DE) and the West Coast ship (WA)] where the recorded values were clearly higher than those with exhibiting lower corrosion rates [Hickam AFB, HI, Tyndall AFB, FL, Kirtland AFB, NM and WPAFB, OH]. What is surprising is the inclusion of the Tyndall AFB within the lower corrosion rate group, since the sites with the higher corrosion rates were all coastal or ship borne sites. It is not known at this time what makes the Tyndall exposure location so different in the lower corrosion rates for the steel samples. When the weather parameters are reviewed (see Figures 14 and 15) and compared to the other sites, there does not appear to be a specific combination of weather data that would explain a lower corrosion rate. However, it is clear that at sites where splash zone and aerosol spray occurs (Daytona Beach, FL and Pt. Judith, RI), the steel coupons experienced the highest mass loss and corrosion rate where the coupons, after 12 and 21 month exposures, literally crumbled and disintegrated, preventing any further mass loss or SEM/EDS analysis.

Distribution Statement A. Approved for public release.

Overall, as can be clearly seen from the plots, the Daytona Beach exposure site results in the highest corrosion rate for two of the three aluminum alloys, the 1010 steel alloy and the pure copper substrates than any of the other locations, while experiencing only temperatures in the middle of the range and lower ozone levels than the other exposure sites for 99% of the time.

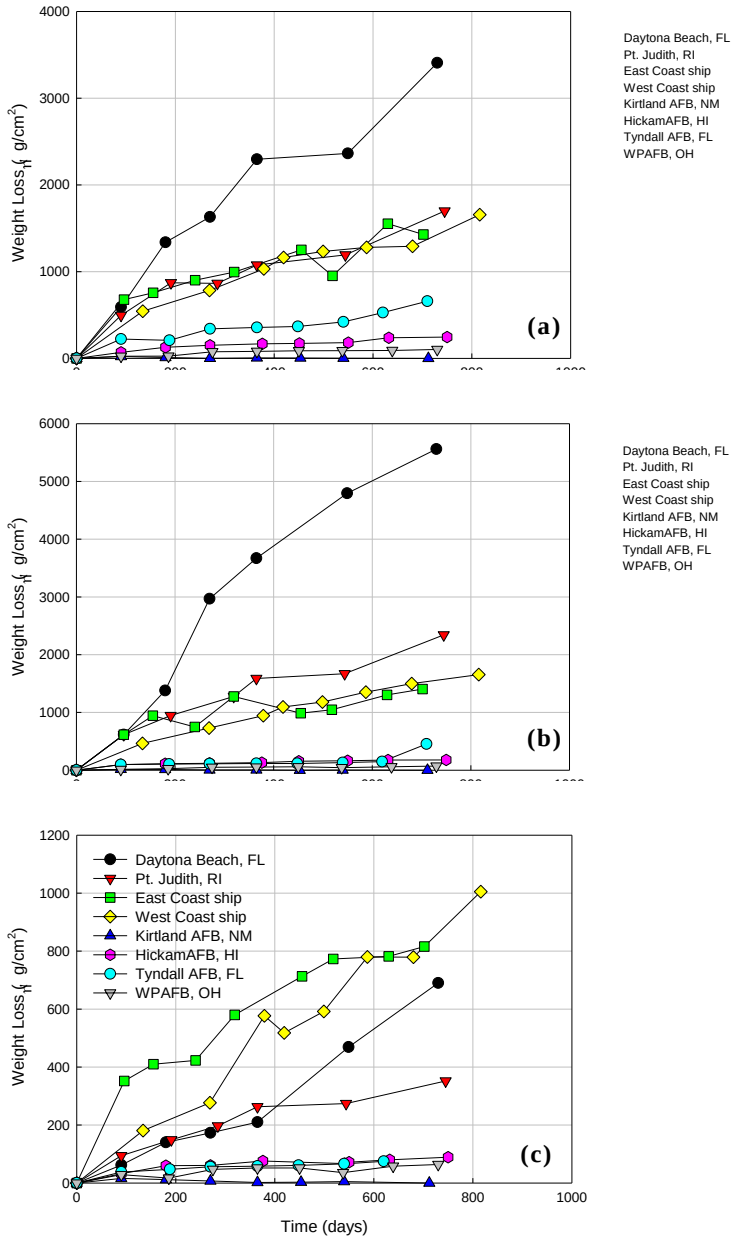

Figure 1. Weight loss of (a) AA7075-T6, (b) AA2024-T3 and (c) AA6061-T6 at all exposure sites

Figure 16. Mass loss of (a) AA7075-T6, (b) AA2024-T3 and (c) AA6061-T6 at all exposure sites.

Distribution Statement A. Approved for public release.

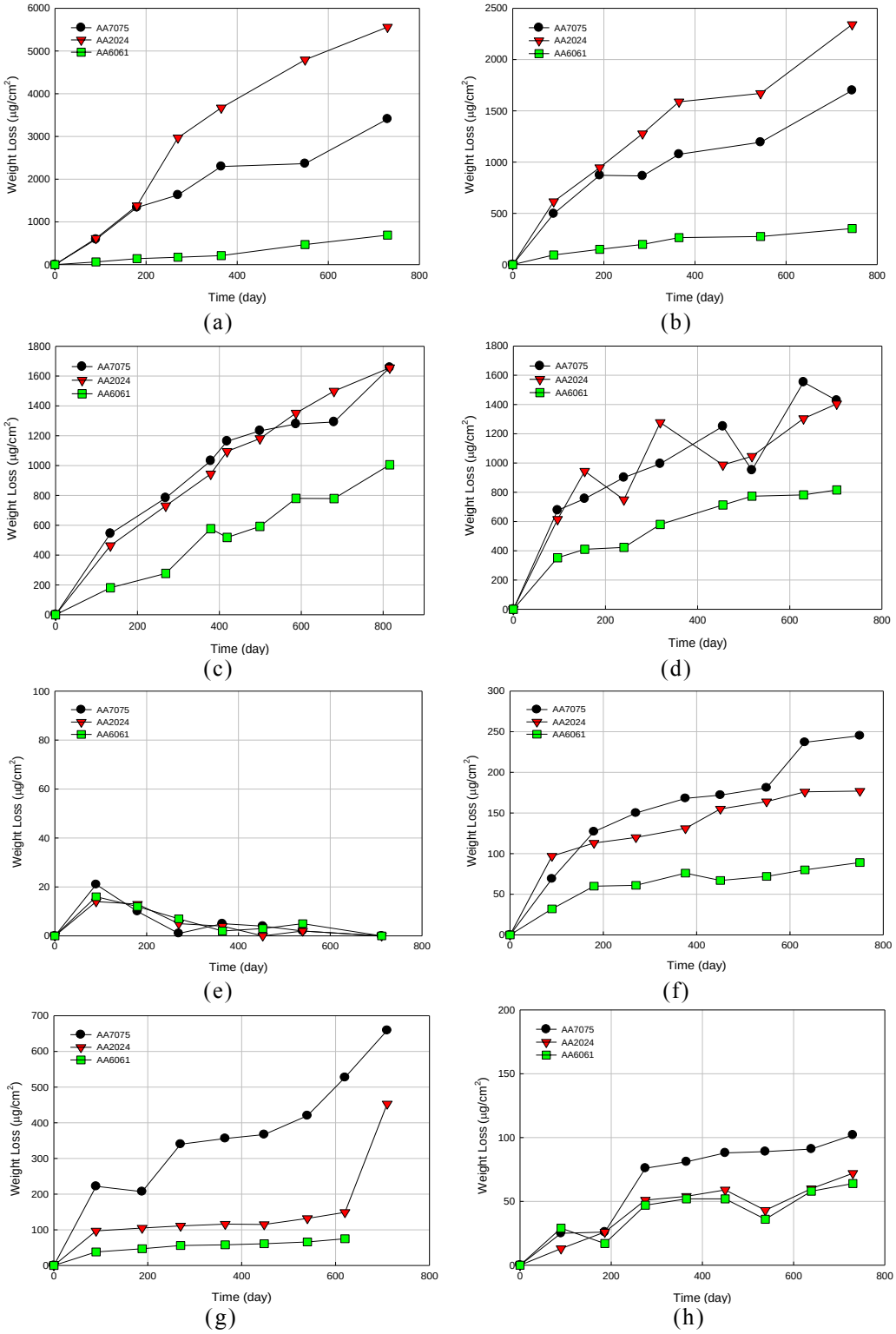

Figure 1. Weight loss determinations for AA6061-T6 compared to AA7075-T6 and AA2024-T3 at all exposure sites over a 2 year exposure period. (a) Daytona Beach, (b) Pt. Judith, (c) East Coast ship, (d) West Coast ship, (e) Kirtland AFB, (f) Eglin AFB, (g) Tyndall AFB and (h) Wright-Patterson AFB

Figure 17. Mass loss determinations for AA6061-T6, AA7075-T3 and 2024-T3 as a function of exposure locations over a 2 year period. (a) Daytona Beach, (b) Pt. Judith, (c) East Coast ship, (d) West Coast ship, (e) Kirtland AFB, (f) Eglin AFB, (g) Tyndall AFB and (h) Wright-Patterson AFB

Distribution Statement A. Approved for public release.

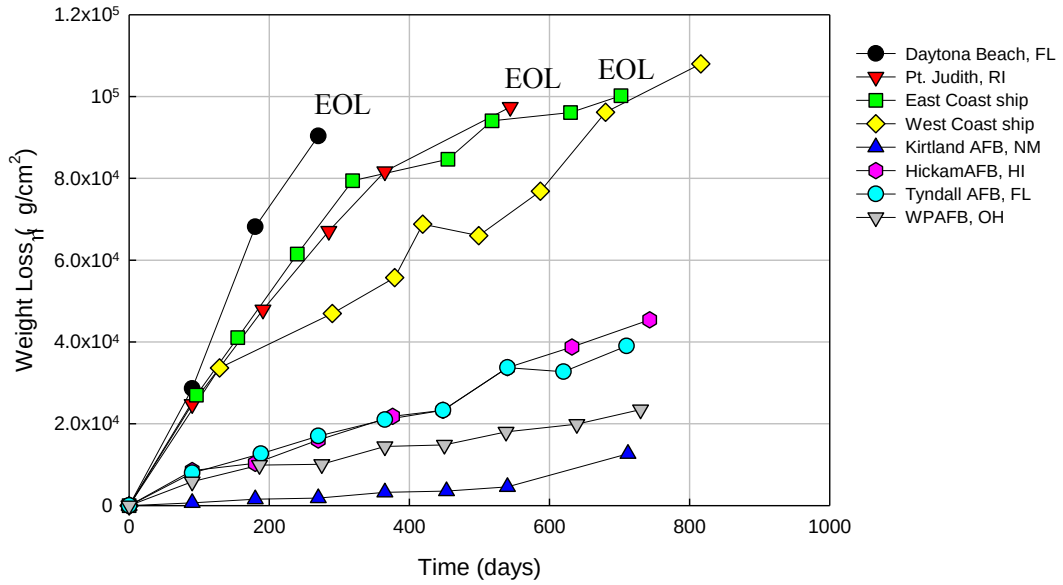

Figure 1. Weight losses of 1010 Steel at all exposure sites.

Figure 18. Mass loss for 1010 steel at all exposure sites over a two year period. EOL = end of lifetime for sample material.

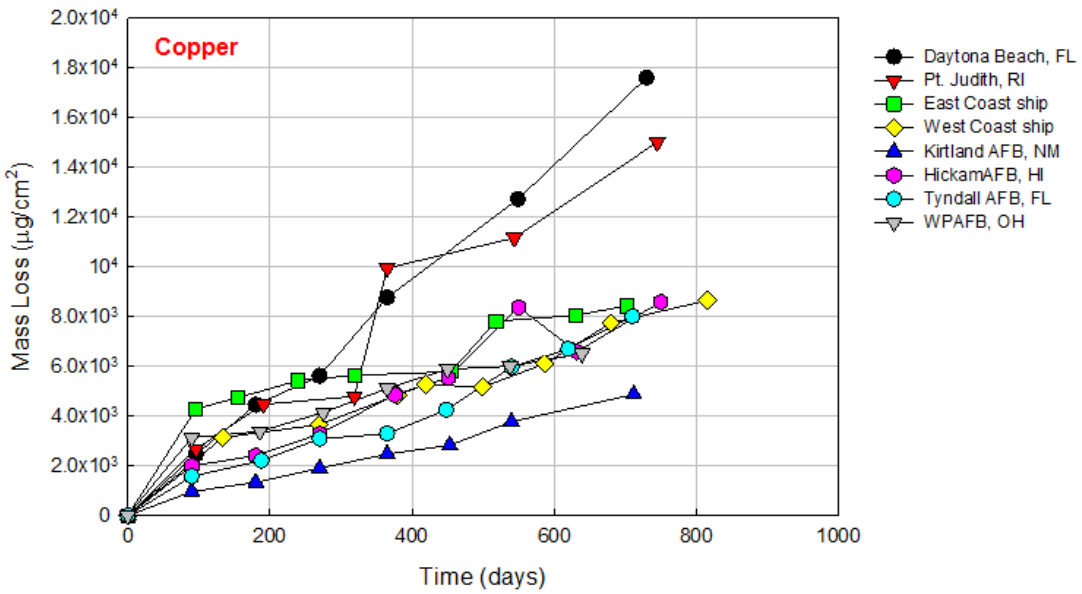

Figure 19. Mass loss for pure copper at all exposure sites over a two year period.

Silver Chloride Film Formation: The bare coupons of pure silver retrieved from the field exposure sites were evaluated by coulometric to measure the thickness of the AgCl present. The coulometric reduction is based on the cathodic reduction of a AgCl film, which forms on the silver surface during exposure in the field. These measurements were made by Dr. William Abbott at Battelle Laboratory (Columbus, OH). A quantitative value of AgCl formation could be indicative of the cumulative chloride deposition levels at the exposure sites. AgCl film thickness data for the pure silver coupons at all exposure sites are given in Table VI. Figure 20 shows the

Distribution Statement A. Approved for public release.

thickness of the AgCl film on pure silver coupons at all locations during the 2 year exposure. As can be seen, silver coupons at Daytona Beach, the East Coast Ship and West Coast Ship sites exhibited higher AgCl film thicknesses than the Pt. Judith site, which is different from the observed corrosion behavior for the aluminum alloys, 1010 steel and pure copper coupons. Again, when the cumulative frequency of the environmental parameters measured at the exposure sites are taken into account, the Daytona site experiences one of the lower levels of ozone at 99% of the time, whereas the second thickest AgCl films are found on coupons exposed on the East Coast ship, which experienced one of the highest ozone levels and the highest UV levels 99% of the time. The third thickest AgCl film levels are found on the West Coast ship, which experienced low ozone levels (similar to Daytona Beach) and the lowest UV levels of all the exposure sites 99% of the time. These results clearly do not point to a clear trend as to the role of UV and ozone in the growth of the AgCl film, but their involvement cannot be discounted.

Table VI. Thickness of the AgCl film on pure silver coupons from all exposure sites over a two year exposure period.

(Å/cm^2)

	3m	6m	9m	12m	15m	18m	21m	24m
Daytona Beach, FL	3546	12020	15645	28019	X	36251	X	43426
Pt. Judith, RI	2758	5357	7950	10461	X	14345	X	16951
East Coast Ship	7703	12105	15829	20824	25903	27807	35461	41076
West Coast Ship	4655	9226	17173	19173	25522	29763	31014	36862
Kirtland AFB, NM	306	486	1348	2158	2292	3656	6047	6396
Hickam AFB, HI	2285	4923	5872	7364	9078	10123	13205	15237
Tyndall AFB, FL	1417	3703	5713	6113	8570	9523	9629	10856
WPAFB, OH	2222	5460	6190	6525	4825	3174	5712	

X: non-measurement

Distribution Statement A. Approved for public release.

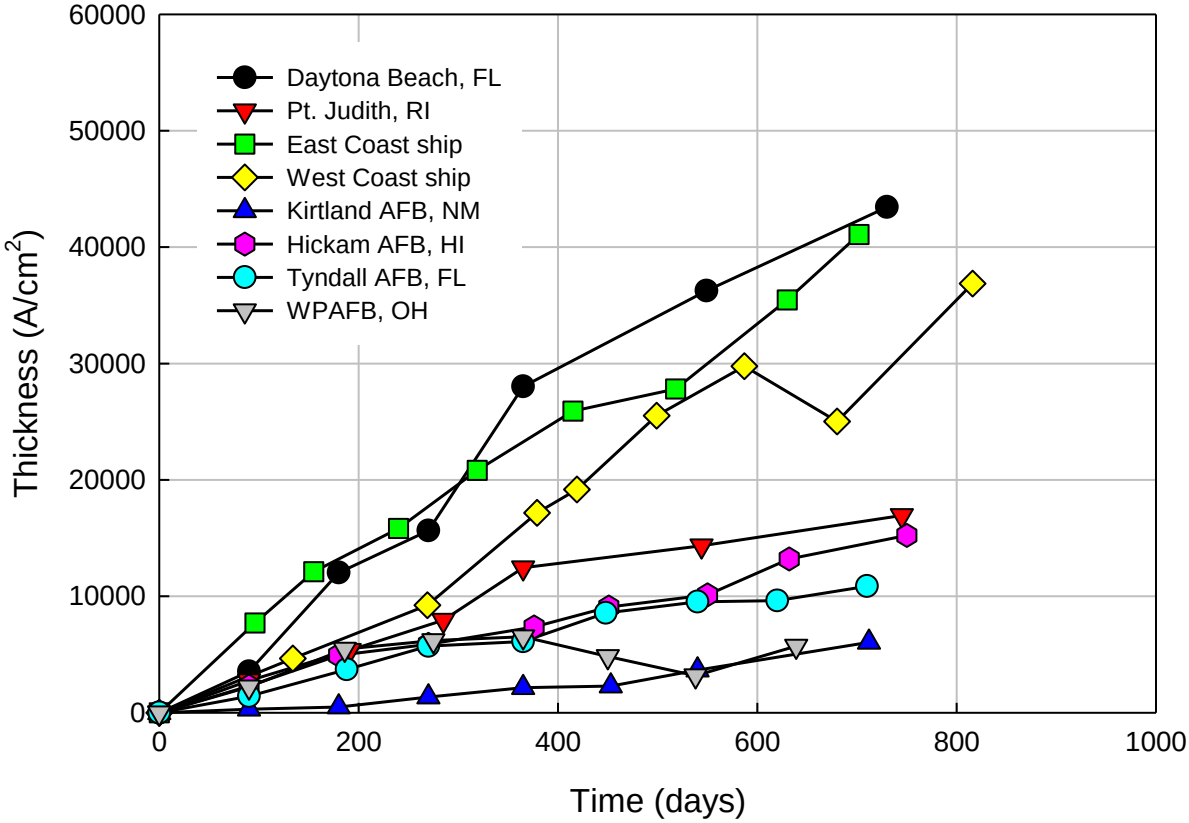

Figure 20. AgCl film thickness on pure silver coupons as a function of time over a two year period at all exposure sites.

Elemental Analysis and Surface Morphology of Field Exposed Bare Metal Coupons

The complete data set for the SEM and EDS analysis of all the bare coupons from the field exposure sites are presented in Appendices B – J.

Bare Pure Silver Coupons: Figures 21 and 22 show the EDS and SEM images of the pure silver coupons exposed at the Daytona Beach (FL) site over the 24 month period. Before being exposed in the field, only pure silver was detected on the surface by coulombic reduction. After field exposure, the silver samples contained Cl and O elements after 3 months of exposure and after longer exposure times O, Na, Mg, Al, Si as well as Cl were also detected. As can be seen in Figure 19, the morphology of the corrosion products were not uniform across the surface. The particles present on the surface were found to contain Ag and Cl elements as well as a small amount of Na element, as detected by EDS.

Similarly, Figure 23 and Figure 24 show the EDS and SEM images of a pure silver coupon exposed at Kirtland (NM), respectively. Relatively small amounts of Cl and O elements were detected on the Kirtland sample(s) compared to Daytona Beach. SEM images in Figure 24 show the scratch marks from sample processing still discernable on the surface after exposure up to 21 months at Kirtland AFB, which indicates that the corrosion product had not fully covered the Ag surface.

Distribution Statement A. Approved for public release.

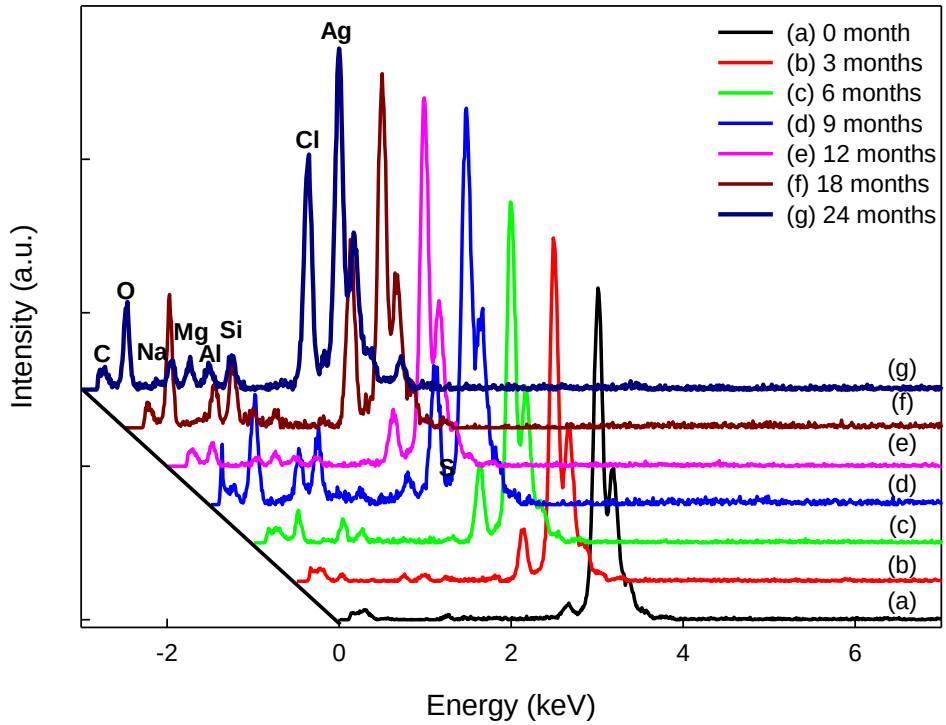

Figure 21. EDS spectra of the pure silver coupons exposed at Daytona Beach, FL.

Figure 25 shows the Cl/Ag ratios as a function of exposure time on the Ag coupons at 8 different exposure locations. The Cl/Ag ratio was calculated from the normalization of the Cl element with the Ag element. As can be seen for the Cl/Ag ratios on the Ag samples, Daytona Beach (FL), West Coast Ship, and East Coast Ship had high Cl/Ag ratios while Wright-Pat AFB (OH) and Kirtland AFB (NM) had low Cl/Ag ratios. The Cl/Ag ratios of Ag at Pt. Judith (RI), Hickam AFB (HI) and Tyndall AFB (FL) were intermediate between the other two groups. This trend of the Cl/Ag ratio being higher on the Ag coupon surfaces at Pt. Judith, Daytona Beach, the East Coast ship and the West Coast ship than at Kirtland AFB, Hickam AFB, Tyndall AFB, or WPAFB is similar to that observed for AgCl film thicknesses calculated from the coulometric reduction of Ag surface film as a function of exposure site location, as presented in Figure 25.

Distribution Statement A. Approved for public release.

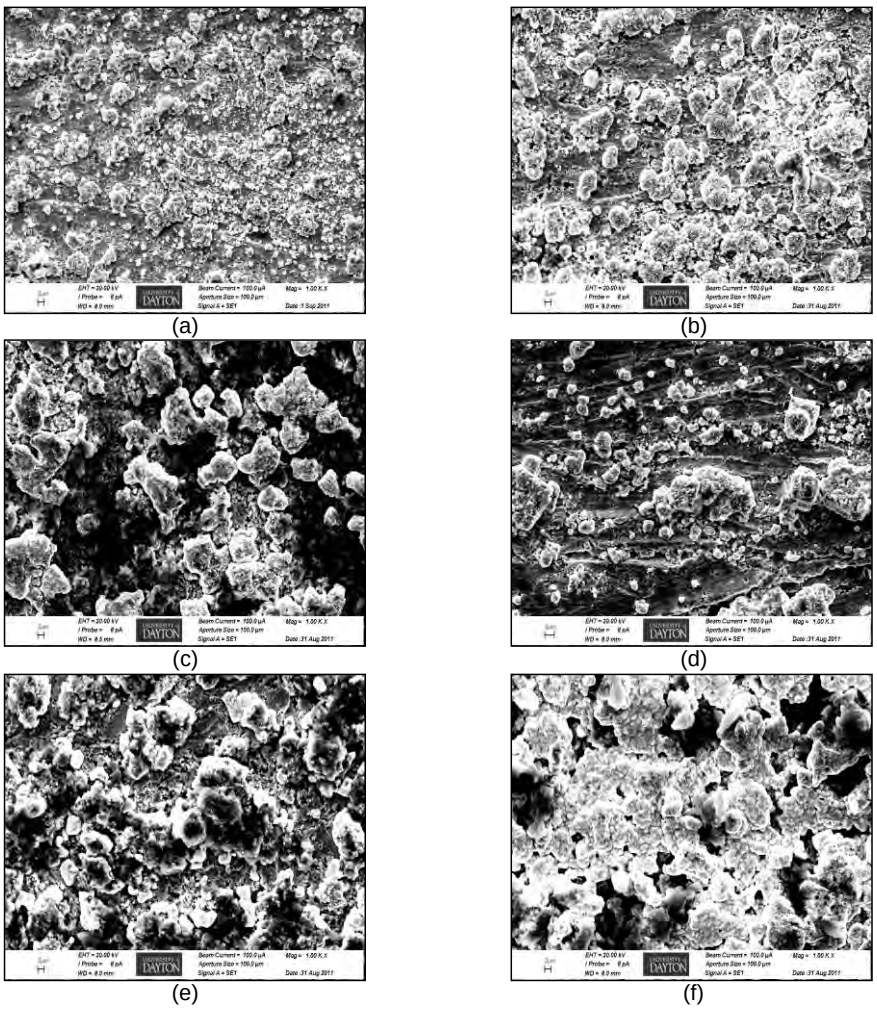

Figure 3. SEM images of the (a) 3 months, (b) 6 months, (c) 9 months, (d) 12 months, (e) 18 months and (f) 24 months pure silver exposed in Daytona Beach, FL (1000X Magnification)

Figure 22. SEM images of the (a) 3 months, (b) 6 months, (c) 9 months, (d) 12 months, (e) 18 months and (f) 2 ch, FL (1000x magnification).

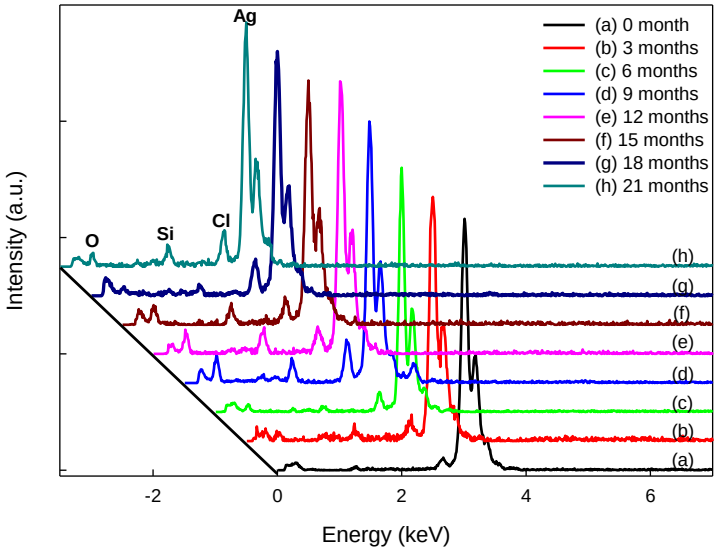

Figure 23. EDS spectra of the pure silver coupons exposed at Kirtland AFB, NM.

Distribution Statement A. Approved for public release.

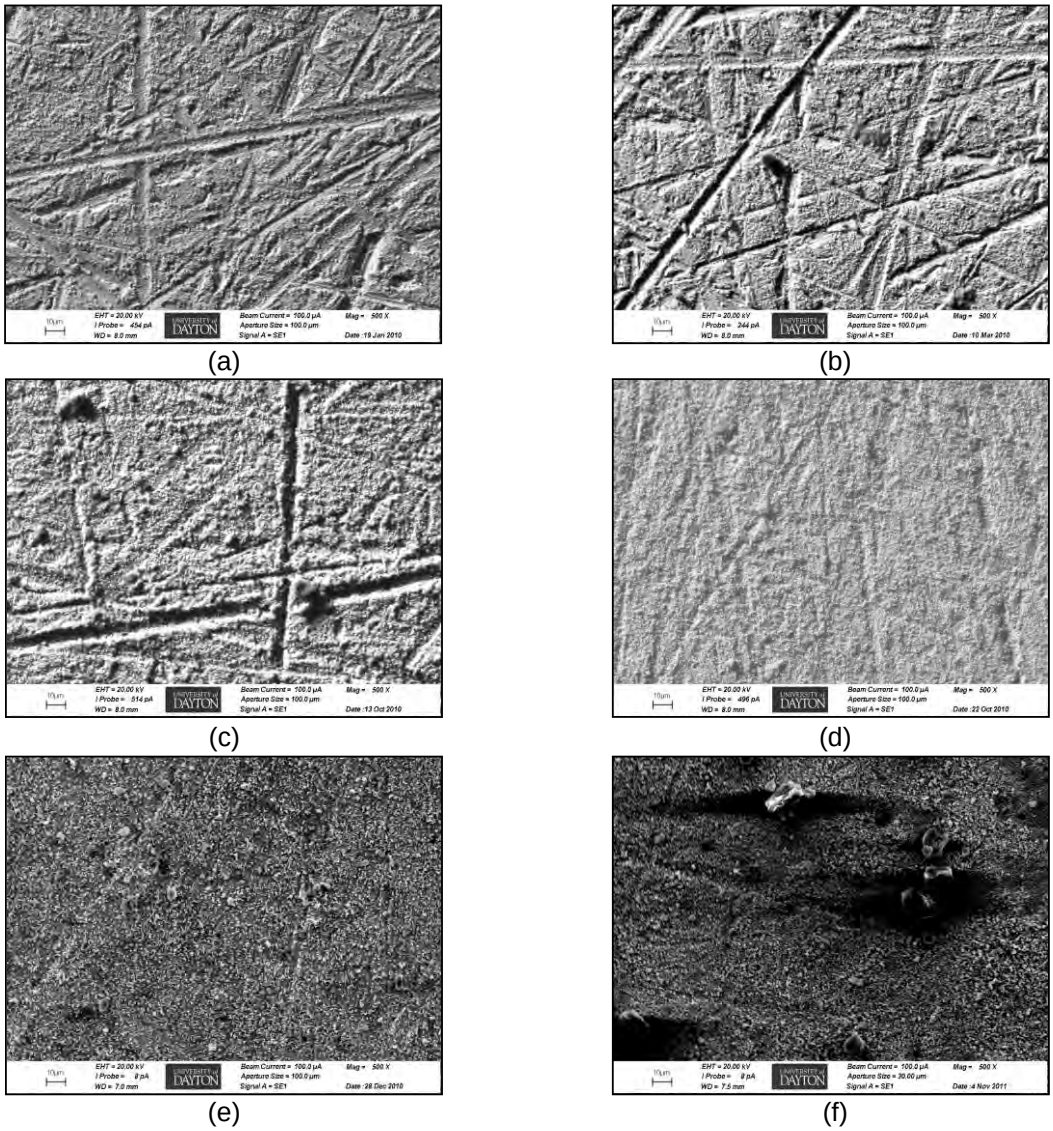

Figure 5. SEM images of the (a) 3 months, (b) 6 months, (c) 9 months, (d) 12 months, (e) 15

Figure 24. SEM images of (a) 3 months, (b) 6 months, (c) 9 months, (d) 12 months, (e) 15 months and (f) 21 months exposure of pure silver coupons at Kirtland AFB, NM (500x magnification).

Distribution Statement A. Approved for public release.

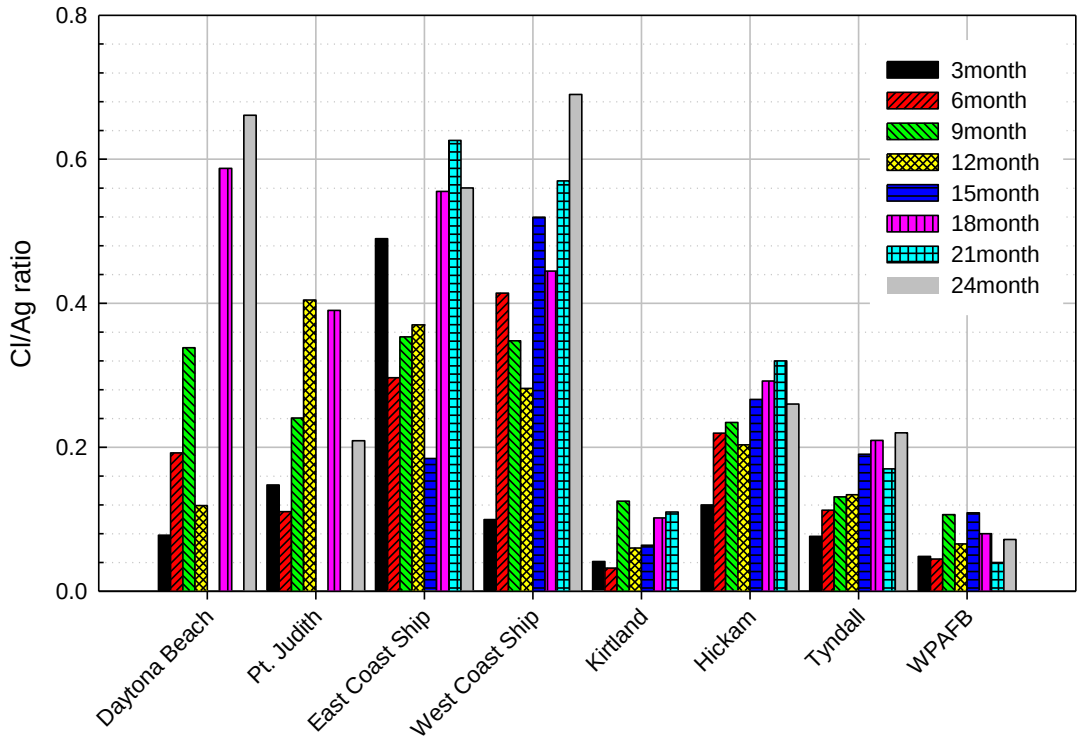

Figure 25. Cl/Ag ratio on pure silver coupons as a function of exposure time at the eight exposure locations.

Bare AA7075-T6, AA6061-T3 and AA2024-T3: This discussion will focus on differences between sites exhibiting the highest mass loss and the lowest mass loss for each metal alloy. For AA7075-T6, the most aggressive field location in terms of weight loss was Daytona Beach, FL for virtually all of the time exposure intervals (Figure 16a). An EDS analysis of the samples retrieved from the Daytona Beach exposure site every 3 months is shown in Figure 26. As can be seen in the plot, the presence of elements in trace amounts that are not contained in the nominal composition in Table VII are indicative of environmental contaminants such as Ca, Cl, S and Na. In addition, the presence of magnesium on the surface of the sample may have two origins: the alloy itself and the environment of seawater near the exposure site as the coupons were exposed to aerosols from sea spray and wind action. In addition, Ca, Cl, S and

Table VII. Elemental composition of AA7075, AA2024, AA6061 and 1010 Steel.

Table IV. Compositions of AA7075, AA2024, AA6061 and 1010 Steel

Alloy	Alloying elements (wt%)										
	Si	Cu	C	Mn	P	S	Mg	Cr	Zn	Al	Fe
AA7075		1.6					2.5	0.23	5.6	bal	
AA2024		4.4		0.6			1.5			bal	
AA6061	0.6	0.28					1.0	0.2		bal	
1010 Steel			0.10	0.45	<0.04	<0.05					bal

Distribution Statement A. Approved for public release.

Na could originate from seawater as well. Sulfur could also be an airborne contaminant arising from the coal fired power plants within the state of Florida [19] or simply from diesel exhaust derived from road traffic. Also, Si may be present on the surface from airborne dust/sand particles originating from the surrounding beach area, in addition to being a nominal trace composition element of the alloy; in reality, since the Si in the composition is a very small trace amount, the relatively high percentage of Si in the signal from the sample surface suggests it is probably derived from the environment as a surface contaminant. From the EDS analysis, it is clear that at time zero, the surface is composed mostly of aluminum, zinc and magnesium, which are the three most prevalent compositional elements of the alloy. It is only after the 3 month interval that other elements begin to appear on the sample surfaces, indicating the influence of the environmental exposure and possible surface contamination has on the corrosion behavior of the alloy. This corrosion behavior is evidenced by the decreasing aluminum signal and increasingly high oxygen signal present on the alloy surface as a function of exposure time, indicating the formation of aluminum oxide corrosion product.

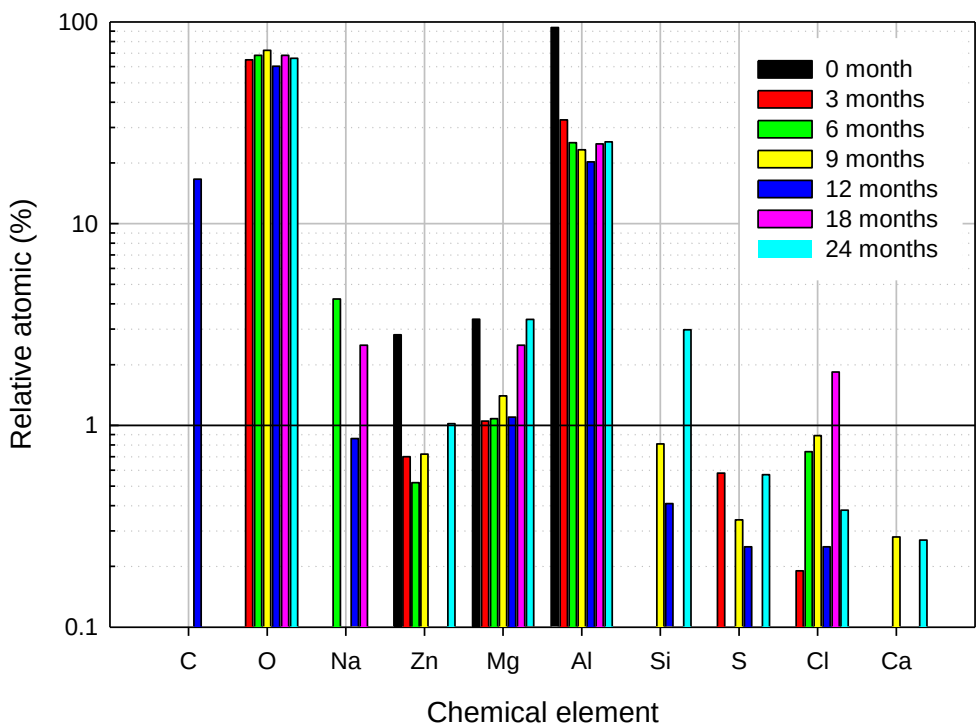

Figure 26. EDS analysis of AA7075-T6 samples retrieved over a two year exposure period from Daytona Beach FL.

In comparison, the EDS analysis of AA7075-T6 from the Kirtland AFB exposure site is presented in Figure 27. This site exhibited the lowest corrosion rate for this alloy; EDS analysis of the sample indicates that Na and Cl are absent from the surface as compared to the Daytona Beach exposure site where these elements were present. However, Ca is also present on the

Distribution Statement A. Approved for public release.

Kirtland AFB sample on 9 months exposure, most probably environmentally derived from the gypsum sand present in the area, which is a salt of calcium sulfate [26]. Gypsum is water soluble mineral, so it is possible that a significant amount of the material was removed due to isolated rain events over the 2 years exposure period. Silica sand is also present in the Kirtland area, which may explain the persistent elevated amount of Si present on the sample surface [26]. Otherwise, there is no decreasing trend of aluminum and also a relatively lower amount of oxygen signal present on the alloy surface over time for the Kirtland samples as was observed for the Daytona Beach samples, and therefore agreeing with the observed lower weight loss data for the Kirtland AFB site. This result indicates the formation of aluminum oxide corrosion product over time for the Kirtland AFB site was much slower than Daytona Beach site.

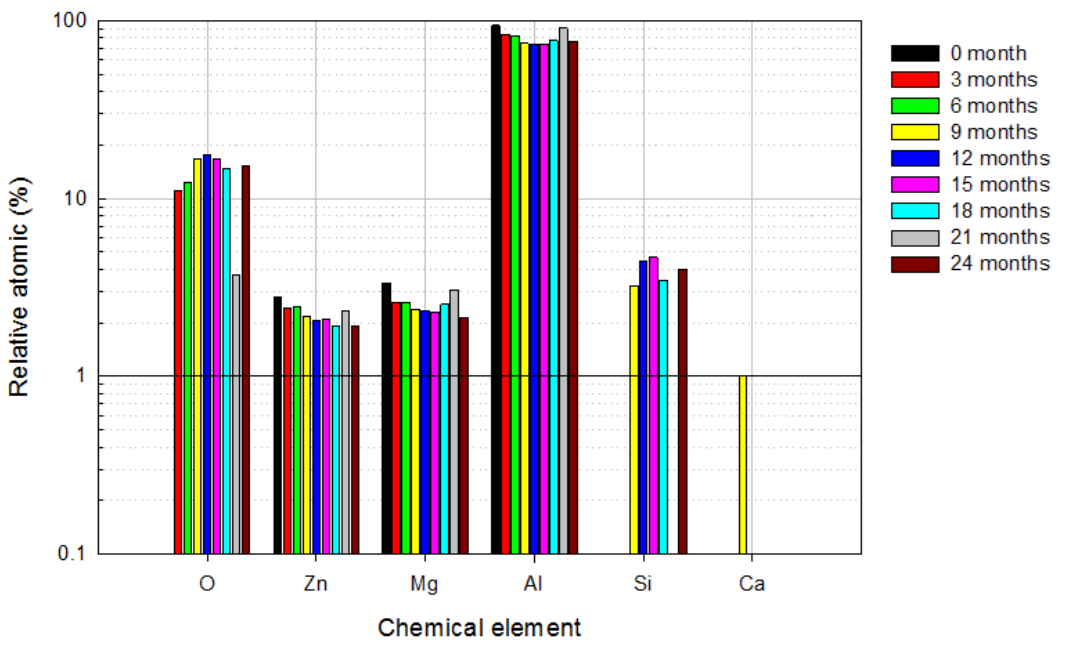

Figure 27. EDS analysis of AA7075-T6 samples retrieved over a two year exposure period from Kirtland AFB, NM.

For AA2024-T3, similar corrosion behavior to AA7075-T6 was observed, with the highest weight loss at the Daytona Beach site, followed by the Pt. Judith, East Coast ship and West Coast ship (Figure 16b). EDS analysis of the samples from the Daytona Beach exposure site is shown in Figure 28a. The results are very similar in terms of which elements are present on the alloy surface, except for the case of Zn and Cu. Since there is no Zn in the composition of AA2024-T3, this should not be a surprise, versus Cu, which is evident due to its presence in the composition of the alloy. It is interesting to note the decreasing trend of the Al and Cu elements such as Ca and S is much lower on AA2024-T3 than that observed on AA7075-T6 sample from the same exposure sites. EDS analysis of the samples from the Kirtland AFB exposure site is shown in Figure 28b. Similar elemental contaminations such as Ca and Si can be seen on this sample as was observed on AA7075-T6 samples. The occurrence of Ca at the same time interval leads one to believe that a wind event or dry period may have resulted in the presence of Ca on the surface on the AA2024-T3 and AA7075-T6 samples at Kirtland AFB.

Distribution Statement A. Approved for public release.

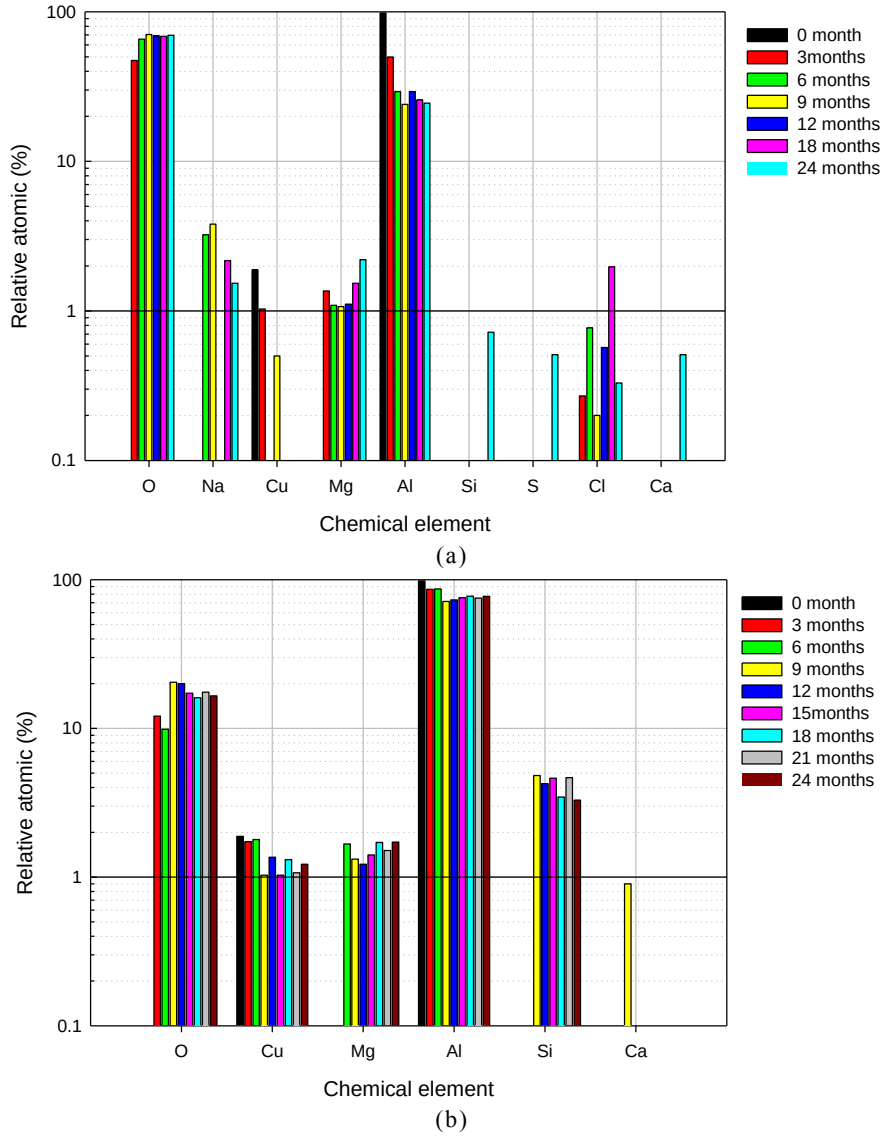

Figure 1. EDS analysis of AA2024-T3 samples retrieved from (a) Daytona Beach, FL and (b) Kirtland AFB, NM exposure sites.

Figure 28. EDS analysis of 2024-T3 samples retrieved over a two year exposure period from (a) Daytona Beach, FL and (b) Kirtland AFB, NM exposure sites.

AA6061-T6 alloy samples exhibited the lowest mass loss of the three aluminum alloys at all of the exposure sites, with a maximum of 1000 μg/cm^2 after two years exposure on the West Coast ship, closely followed by the East Coast ship and Daytona Beach exposure sites (Figure 16c). The Pt. Judith site exhibited intermediate mass loss and the remaining sites of Kirtland AFB, Tyndall AFB, Hickam AFB and WPAFB exhibiting the lowest mass loss. Considering that ocean water aerosols and ocean spray can occur on ships transecting the littoral zone, it is not a surprise that the mass losses of the two ship exposure sites on all three aluminum alloys are similar. The difference in mass loss between the Pt. Judith and Daytona Beach sites is less easily explained; similar corrosion rates are observed at both sites up until approximately 12 months, after which the corrosion rate at Daytona Beach is almost double that of Pt. Judith. Clearly, the

Distribution Statement A. Approved for public release.

difference in corrosion rates observed between these two sites warrants further investigation and comparison of environmental factors. However, it is instructional to compare the surface chemistries of AA6061-T6 samples from two distinctly different locations in terms of weight loss: the East Coast ship and Kirtland AFB. Figure 29 shows EDS analysis of AA6061-T6 samples from the East Coast ship and Kirtland AFB exposure sites, respectively. This result also indicates that the corrosion behavior of AA6061-T6 at both sites is evidenced by the decreasing aluminum signal and increasing high oxygen signal present on the alloy surface as a function of exposure time.

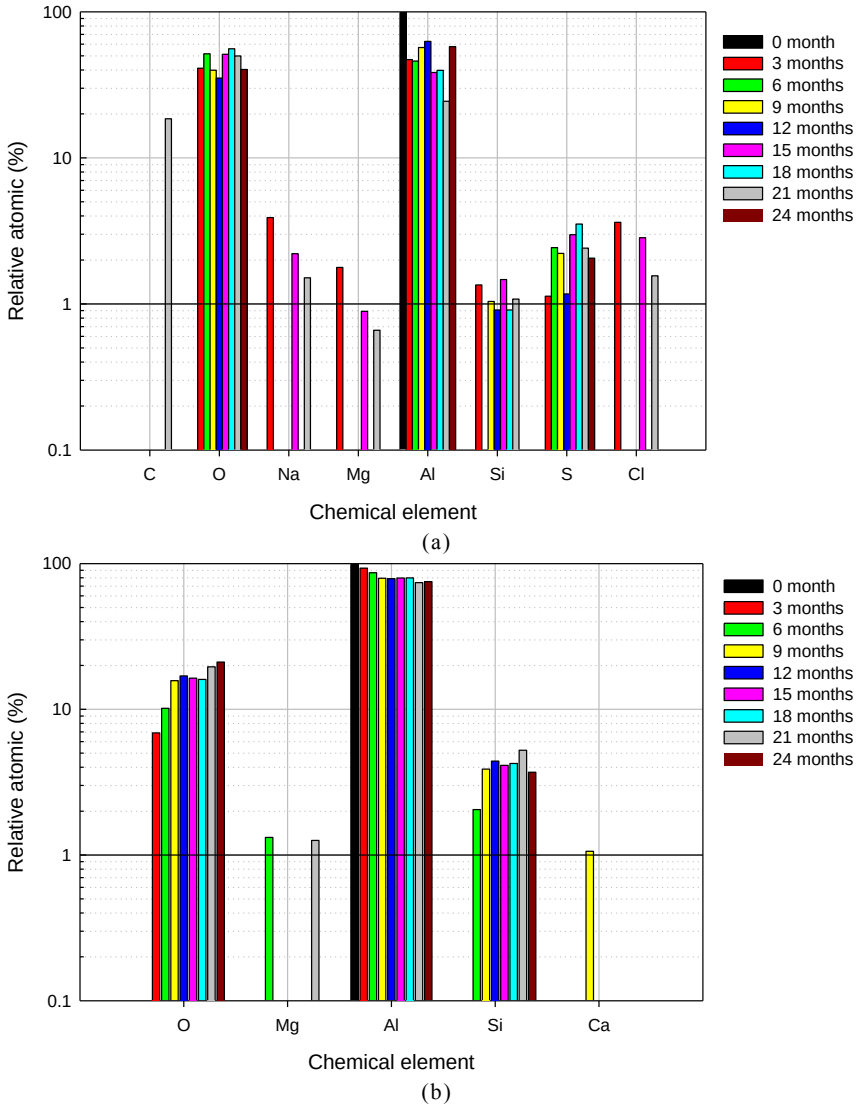

Figure 29. EDS analysis of 2024-T3 samples retrieved over a two year exposure period from (a) the East Coast ship (DE) and (b) Kirtland AFB, NM exposure sites.

As with the corrosion product analysis, this discussion of the surface morphology analysis will focus on differences between sites exhibiting the highest mass loss and the lowest mass loss for the aluminum alloys only, as they are of the greatest interest in terms of developing an accelerated corrosion protocol for DoD assets. While it is recognized that current standardized

Distribution Statement A. Approved for public release.

accelerated corrosion tests focus on the corrosion rate (which is measured by mass loss determinations) of substrates exposed in atmospheric chambers as a function of time, it is the results discussed in the following section that indicate this approach is misleading and can lead to erroneous results.

While the surface elemental analysis and mass loss is different between the sites for all 3 aluminum alloy samples, another aspect to be considered is the surface morphology of the corrosion products present on the samples. Figure 30 shows a series of SEM images of AA7075-T6 samples from the Daytona Beach exposure site and it is evident that the surface morphology and incorporated corrosion products reach a quasi-steady state after 6 months exposure. This is in contrast to the samples retrieved from the Kirtland AFB exposure sites, where grinding scratches from the sample preparation are still visible on all of the samples out to two years exposure (Figure 31).

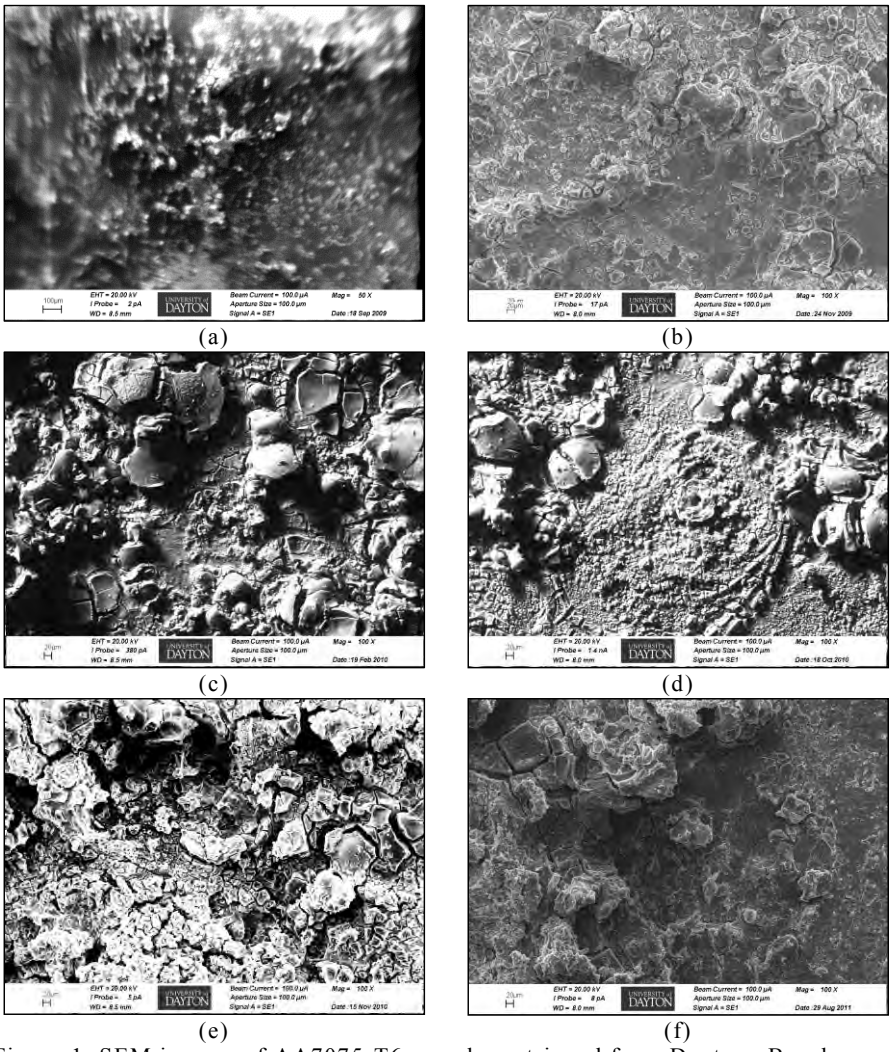

Figure 1. SEM images of AA7075-T6 samples retrieved from Daytona Beach exposure site after (a) 3 months, (b) 6 months, (c) 9 months, (d) 12 months, (e) 18 months and (f) 24 months.

Figure 30. SEM images of AA7075-T6 samples retrieved from Daytona Beach, FL exposure site after (a) 3 months, (b) 6 months, (c) 9 months, (d) 12 months, (e) 18 months and (f) 24 months.

Distribution Statement A. Approved for public release.

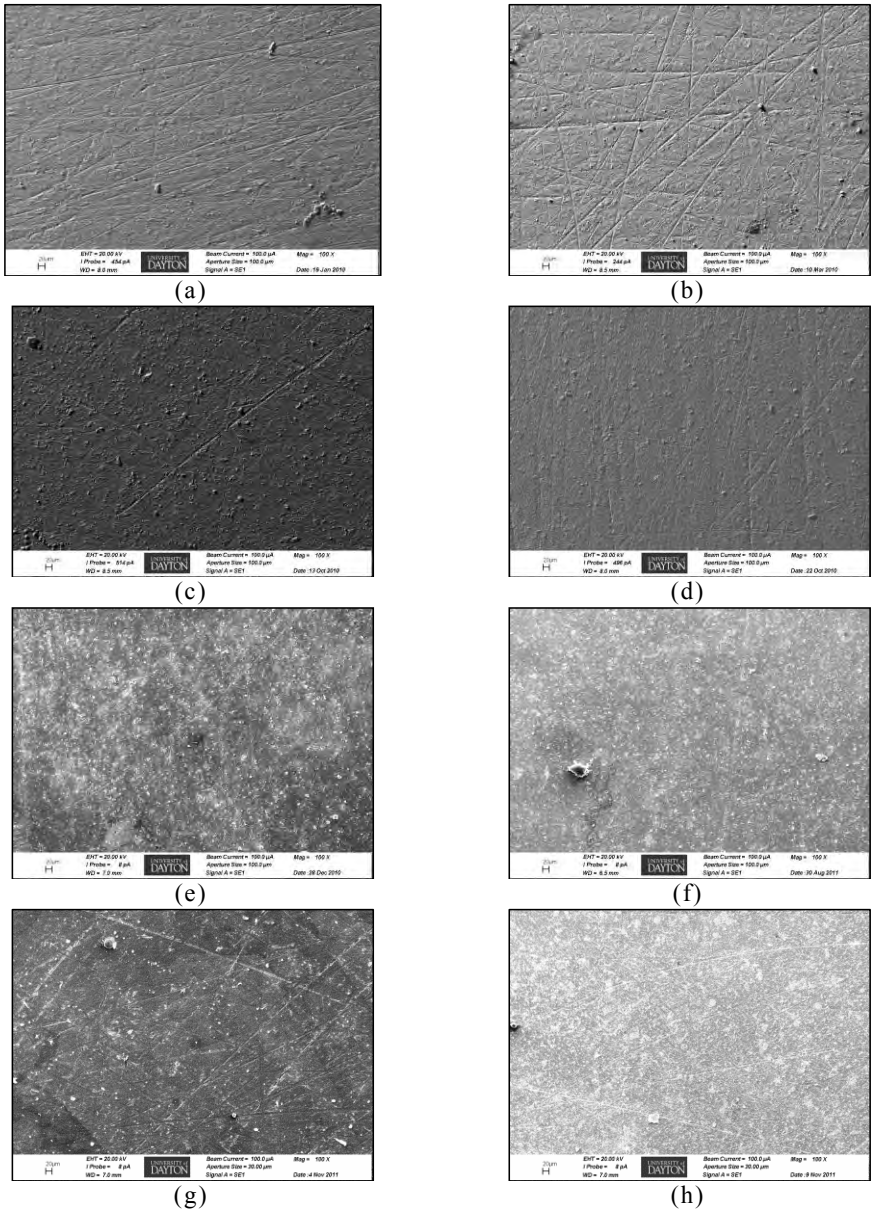

Figure 1. SEM images of AA7075-T6 samples retrieved from Kirtland AFB exposure site. (a) 3 months, (b) 6 months, (c) 9 months, (d) 12 months, (e) 15 months, (f) 18 months, (g) 21 months and (h) 24 months.

Figure 31. SEM images of AA7075-T6 samples retrieved from Kirtland AFB, NM exposure site after (a) 3 months, (b) 6 months, (c) 9 months, (d) 12 months, (e) 15 months, (f) 18 months, (g) 21 months and (h) 24 months.

Distribution Statement A. Approved for public release.

For AA2024-T3, the surface of the alloy after 6 months in Daytona Beach appears to reach a quasi-steady state in terms of surface morphology (Figure 32) and is quite similar to the behavior of the AA7075-T6 at that location. Not surprisingly, In Figure 33, AA2024-T3 exhibits similar surface morphology to AA7075-T6 exposed at Kirtland AFB. Scratch marks are still visible on the surface even after 24 months exposure, indicating very little corrosion product build up.

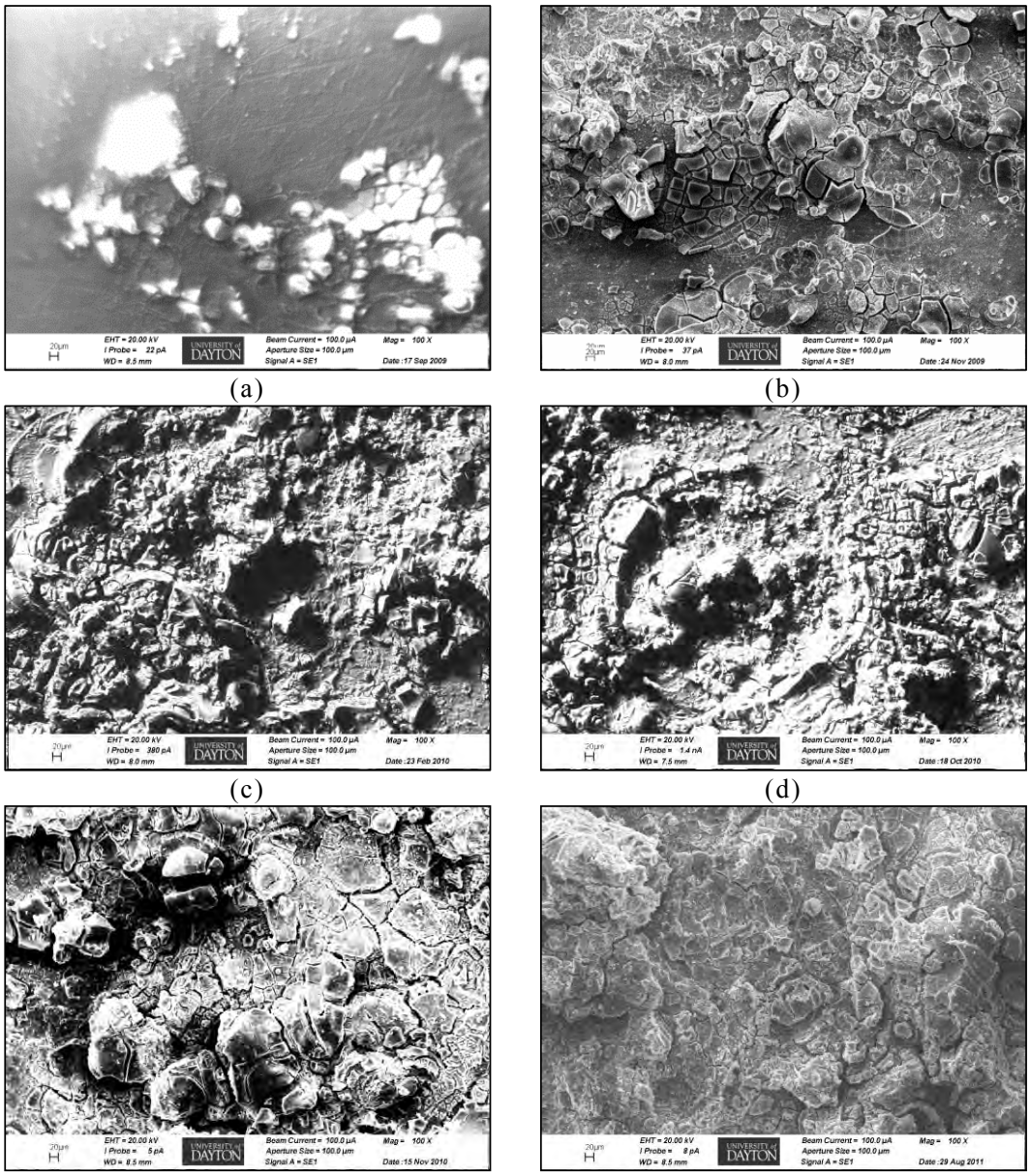

Figure 1. SEM images of AA2024-T3 samples retrieved from Daytona Beach exposure site. (a) 3 months, (b) 6 months, (c) 9 months, (d) 12 months, (e) 18 months and (f) 24 months

Figure 32. SEM images of AA2024-T3 samples retrieved from Daytona Beach, FL exposure site after (a) 3 months, (b) 6 months, (c) 9 months, (d) 12 months, (e) 18 months and (f) 24 months.

Distribution Statement A. Approved for public release.

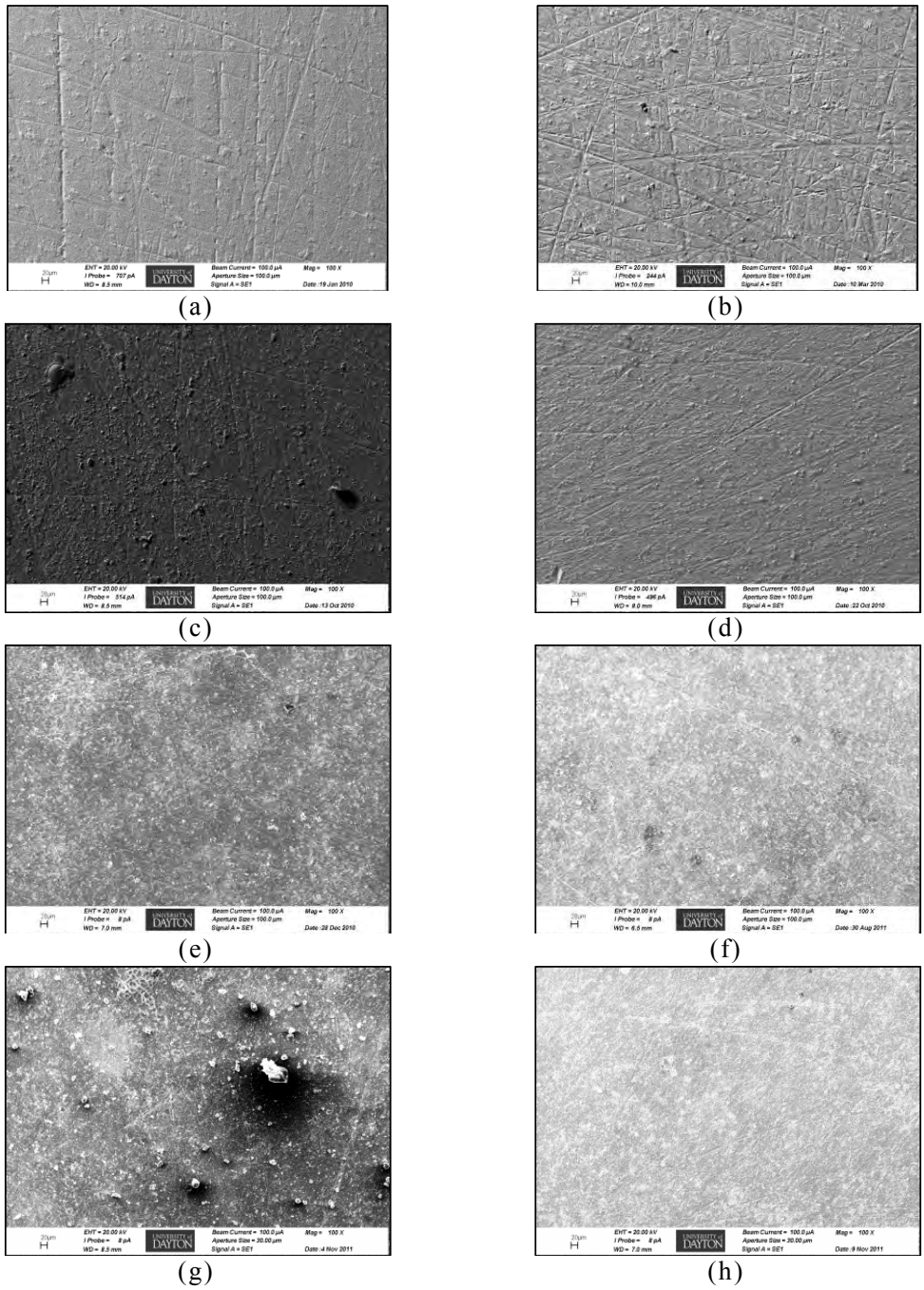

Figure 1. SEM images of AA2024-T3 samples retrieved from Kirtland AFB exposure site. (a) 3 months, (b) 6 months, (c) 9 months, (d) 12 months, (e) 15 months, (f) 18 months, (g) 21 months and (h) 24 months

Figure 33. SEM images of AA2024-T3 samples retrieved from Kirtland AFB, NM exposure site after (a) 3 months, (b) 6 months, (c) 9 months, (d) 12 months, (e) 15 months, (f) 18 months, (g) 21 months and (h) 24 months

Distribution Statement A. Approved for public release.

The corrosion behavior of AA6061-T6 was markedly different from AA7075-T6 and AA2024-T3 in that it exhibited much lower mass loss over time; consequently the surface morphology as shown in Figure 34 for the East Coast ship exposure exhibits a much lower amount of corrosion product and a smoother surface than seen on AA7075-T6 and AA2024-T3 at Daytona Beach site. Again, as expected, the surface morphology of AA6061-T6 samples from Kirtland AFB were similar to the other aluminum alloys exposed there as well in Figure 35, with thin corrosion products and surface scratches still visible after 2 years exposure.

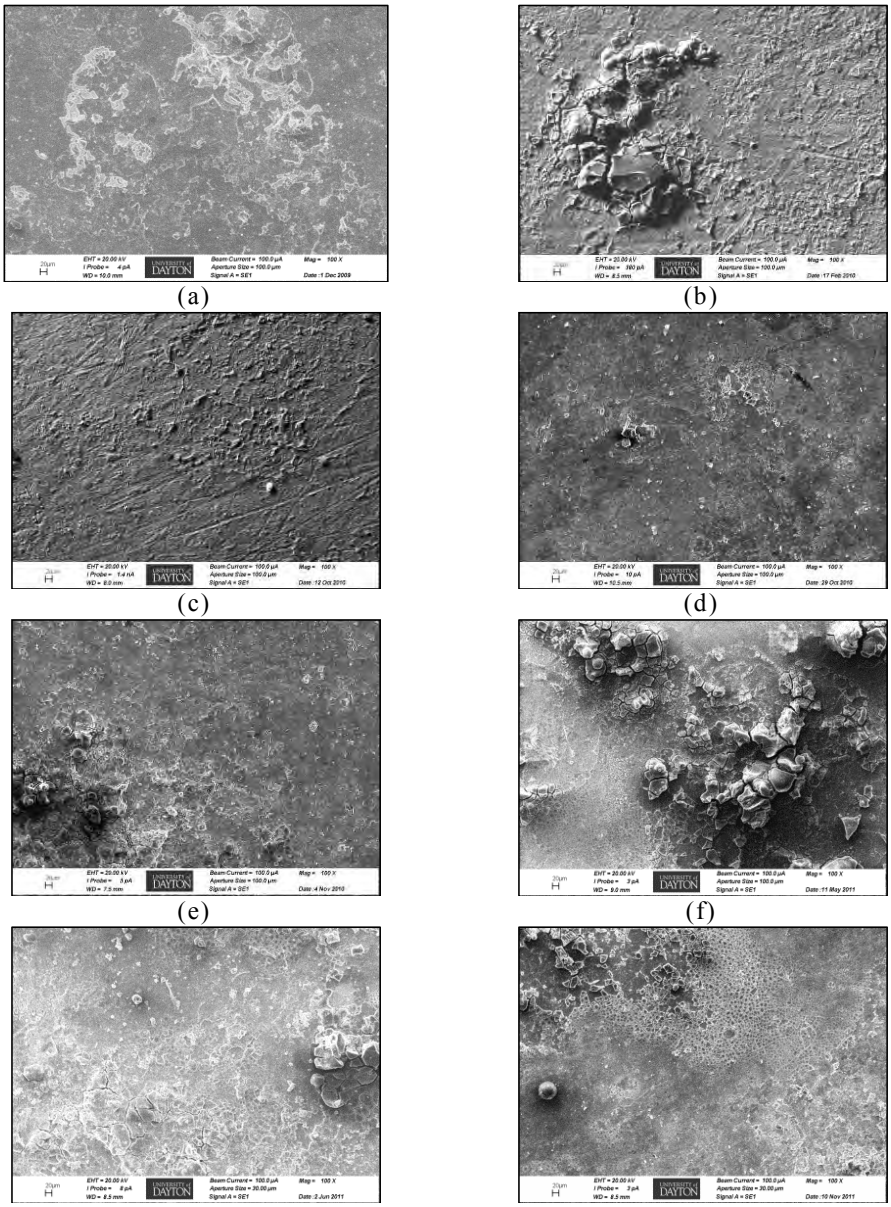

Figure 1. SEM images of AA6061-T6 samples retrieved from East Coast ship site (a) 3 months, (b) 6 months, (c) 9 months, (d) 12 months, (e) 15 months, (f) 18 months, (g) 21 months and (h) 24 months

Figure 34. SEM images of AA6061-T6 samples retrieved from the East Coast ship (DE) exposure site after (a) 3 months, (b) 6 months, (c) 9 months, (d) 12 months, (e) 15 months, (f) 18 months, (g) 21 months and (h) 24 months

Distribution Statement A. Approved for public release.

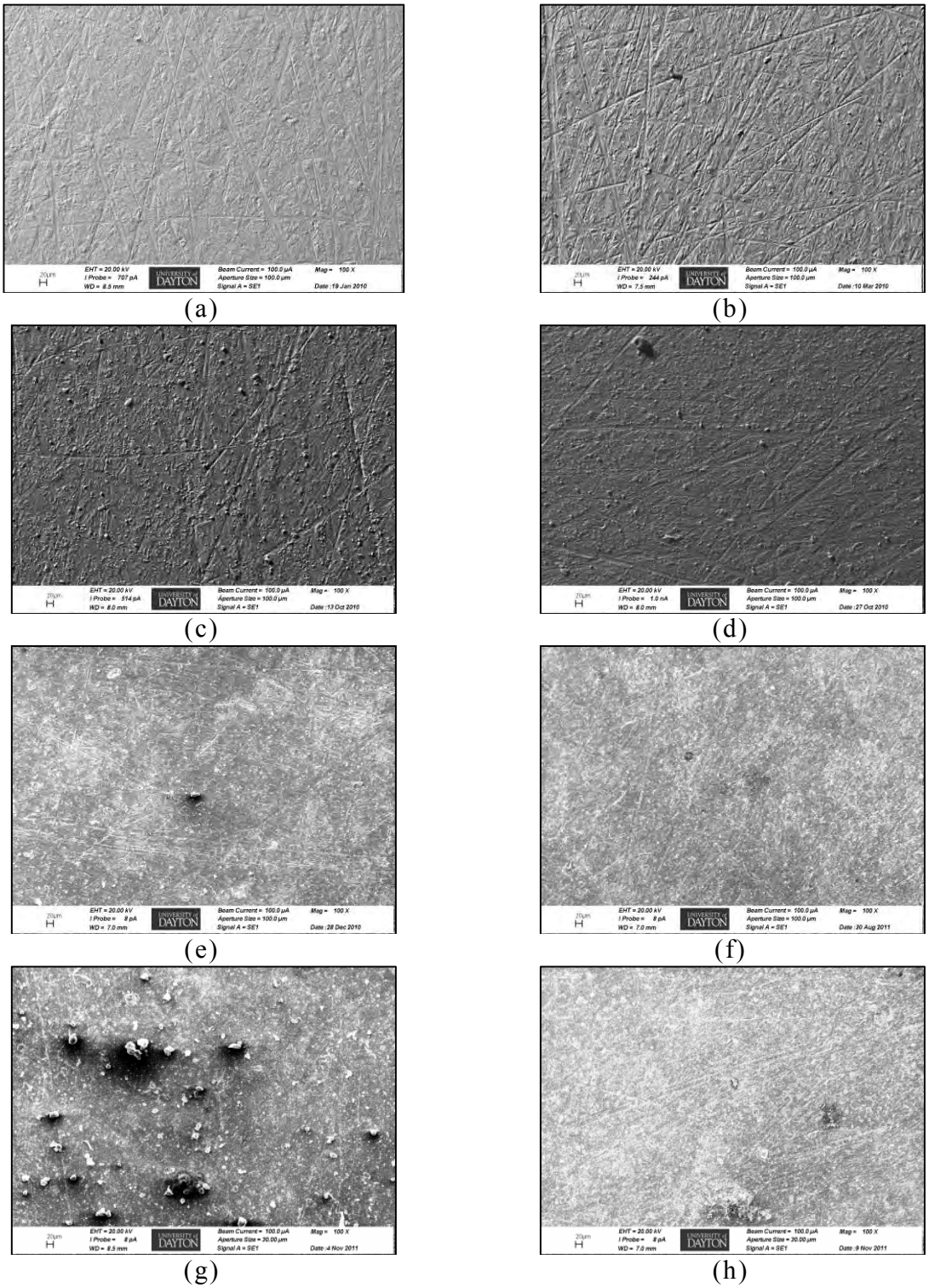

Figure 35. SEM images of AA6061-T6 samples retrieved from Kirtland AFB, NM exposure site after (a) 3 months, (b) 6 months, (c) 9 months, (d) 12 months, (e) 15 months, (f) 18 months, (g) 21 months and (h) 24 months

Distribution Statement A. Approved for public release.

It becomes clear from the mass loss data for the bare metal substrates at the various locations that similar mass losses can occur at various locations but at different time intervals. For example, in the case of the AA7075-T6 alloy in Figure 16a and Table V, similar mass losses occur after 3 months of exposure at Pt. Judith, RI, Daytona Beach, FL, the East Coast ship (DE), the West Coast ship (WA) and 24 months at Tyndall AFB, FL. A conclusion from these observations would be that indeed the corrosion rates are different; but what is more important is that the morphology and elemental analysis of the alloy substrates are different. This is demonstrated in Figures 36 and 37, which shows the difference in the elemental analysis of the AA7075-T6 alloy coupons experiencing similar mass loss from the various sites, and the difference in surface morphology. The same can be seen on AA2024-T3 in Figures 38 and 39, where similar mass loss at different locations at different time intervals again result in different elemental analysis and surface morphologies. While this might seem self-evident, since the substrates are being exposed at different locations and hence different environmental conditions, it is also important in the accelerated test protocols, where similar mass loss is observed at an accelerated rate in the modified chamber versus the field exposures, but the surface morphology of the substrates exposed in the chamber look markedly different from the substrates in the field (discussed in detail later). Therefore, it is important to note that if a metal substrate is undergoing corrosion, it may be more informative to consider the elemental composition and morphology of the corroded surface in addition to the mass loss, rather than rely on mass loss alone, since it appears that the morphology and composition of the corroding surface can have an effect on the kinetics of the corrosion process (or vice versa).

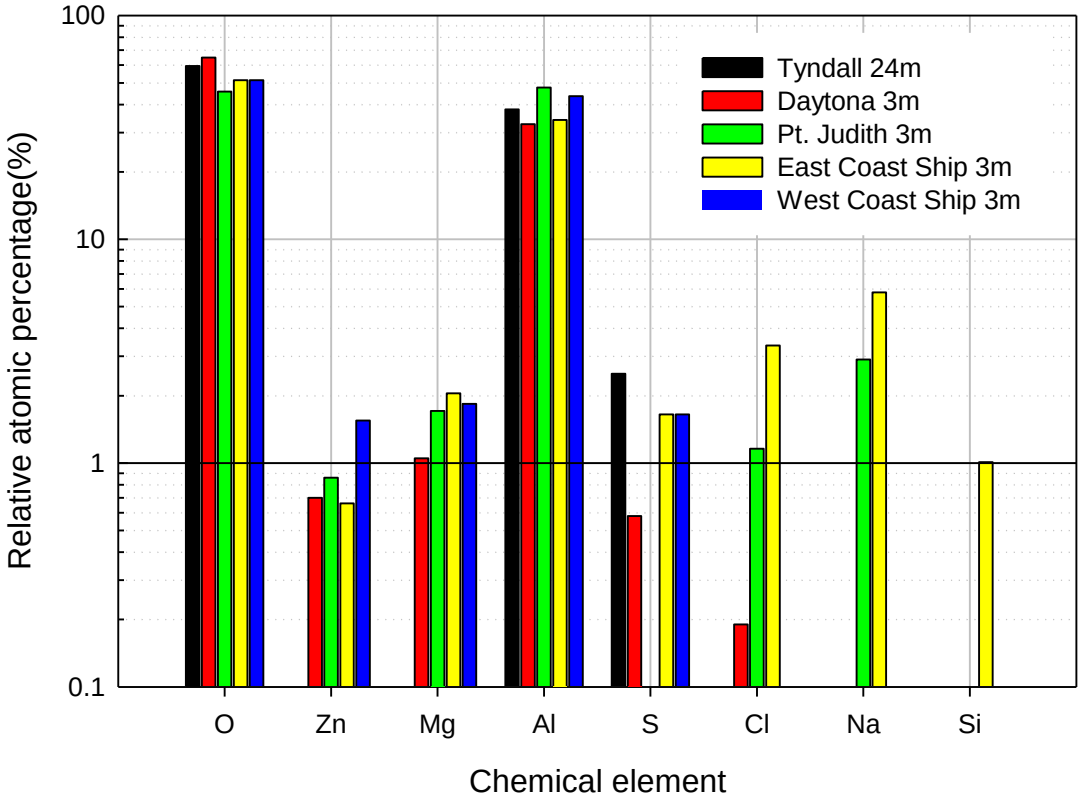

Figure 36. EDS analysis of AA7075-T6 retrieved from Tyndall AFB at 24 months, Daytona Beach at 3 months, Pt. Judith at 3 months, East Coast ship at 3 months, and West Coast ship at 3 months.

Distribution Statement A. Approved for public release.

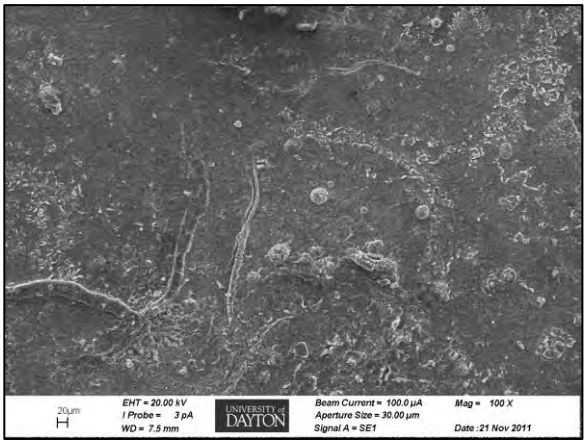

(a)

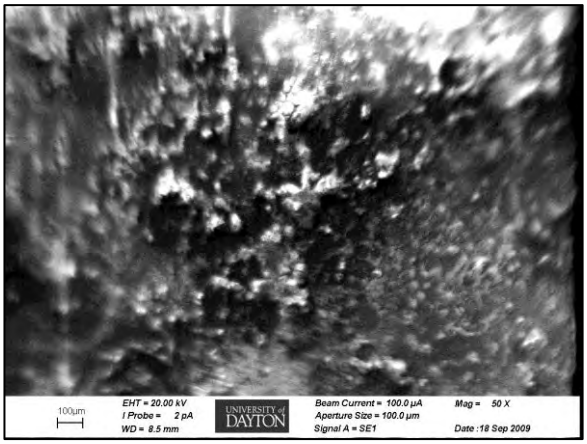

(b)

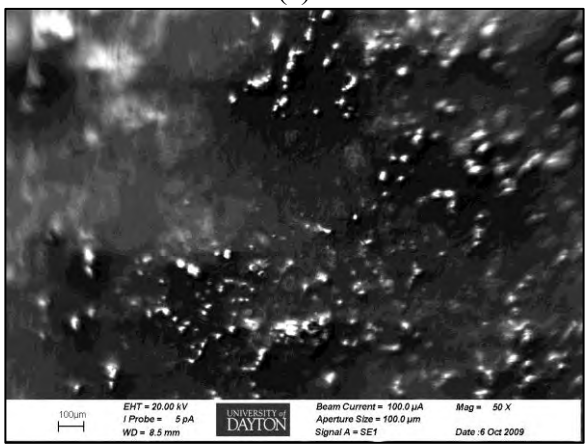

(c)

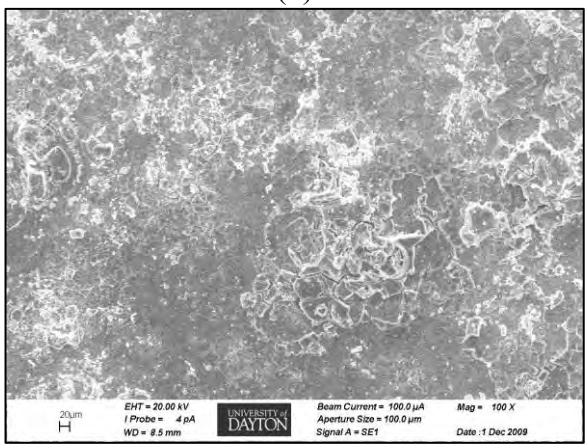

(d)

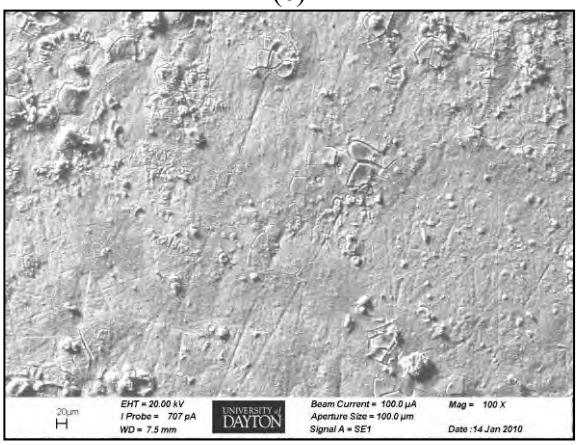

(e)

Figure 32. SEM images of AA 7075-T6 samples retrieved from (a) Tyndall AFB at 24 months, (b) Daytona Beach at 3 months, (c) Port Judith at 3 months, (d) East Coast ship at 3 months, and (e) West Coast ship at 3 months.

Distribution Statement A. Approved for public release.

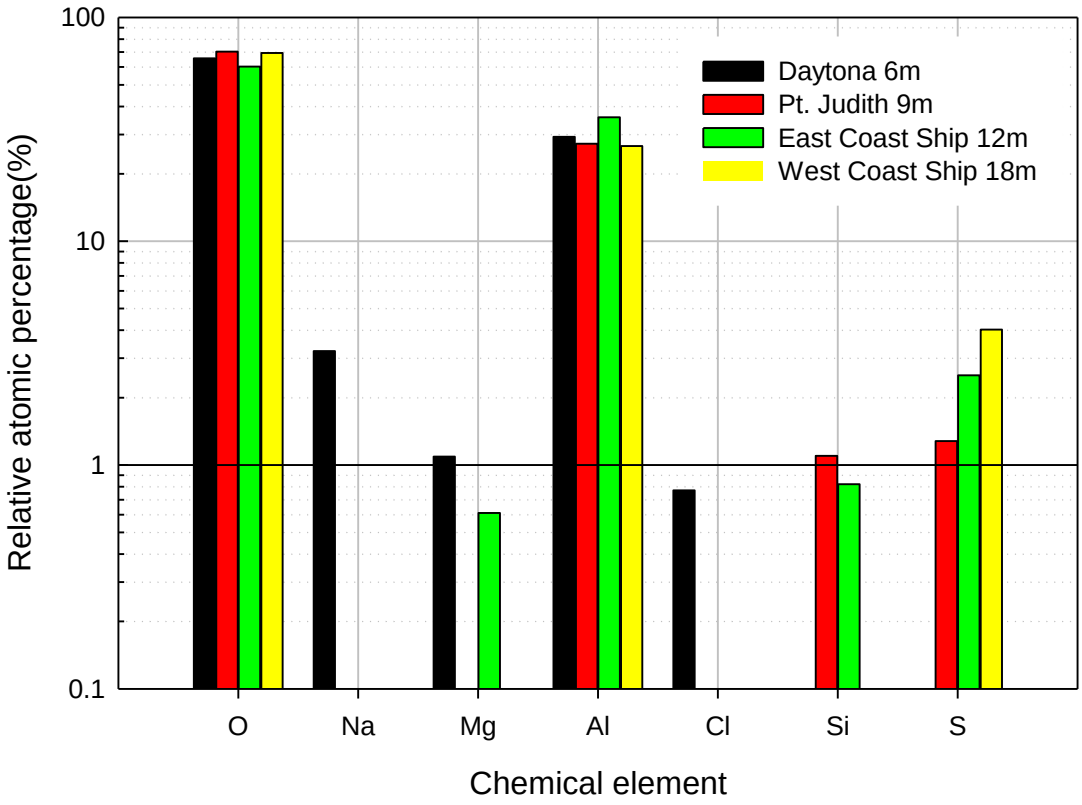

Figure 38. EDS analysis of AA2024-T3 retrieved from Daytona Beach at 6 months, Pt. Judith at 9 months, the East Coast ship at 12 months and the West Coast ship at 18 months.

Distribution Statement A. Approved for public release.

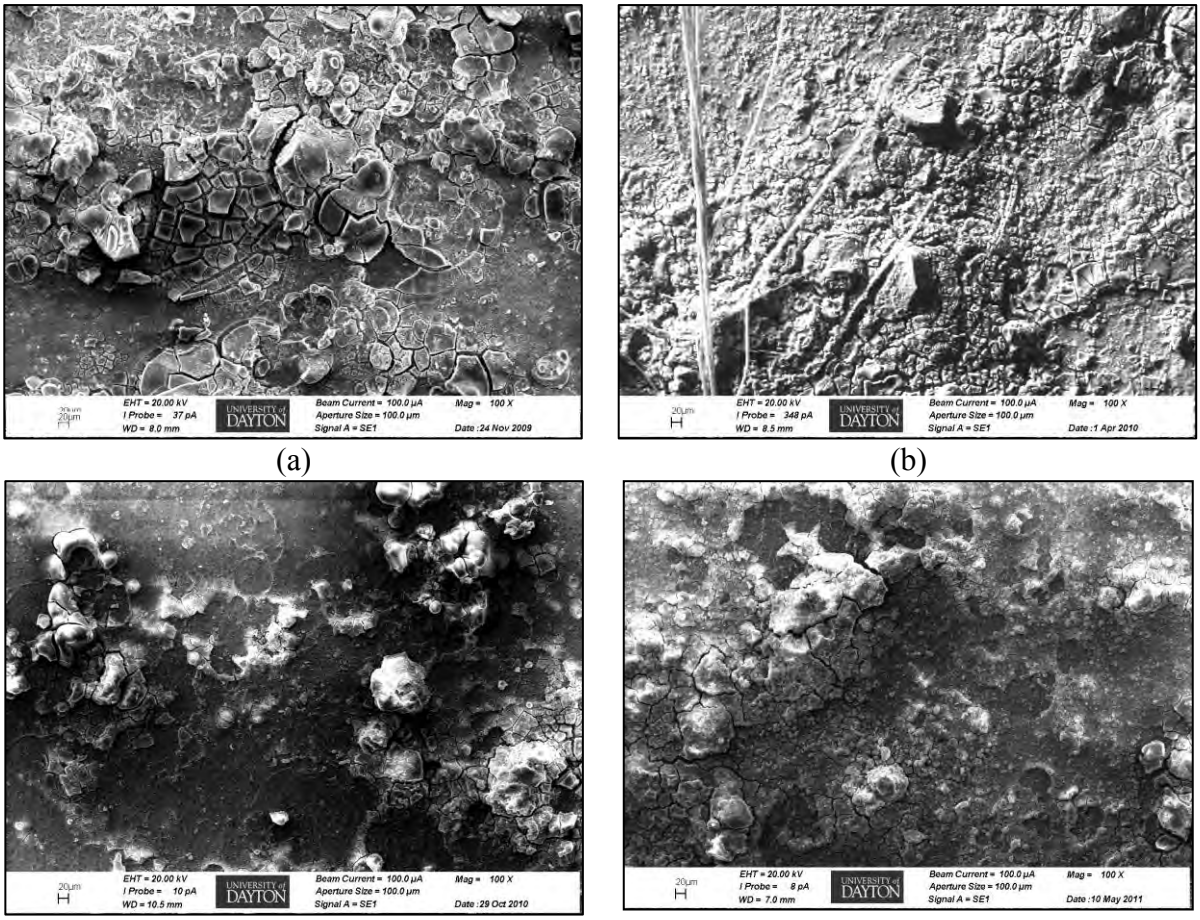

Figure 39. SEM images of 2024-T3 samples retrieved from (a) Daytona Beach at 6 months, (b) Pt. Judith at 9 months, (c) the East Coast ship at 12 months, and (d) the West Coast ship at 18 months.

Coating Performance Ranking, Elemental Analysis and Surface Morphology of Field Exposed Coated Aluminum Alloy Panels and Lap Joint Samples

As discussed in the previous sections, the analysis of the field exposed coated panels will focus on the coated aluminum alloy panels, as they are of the greatest interest in terms of developing an accelerated corrosion protocol for DoD assets. A complete set of representative optical images of the coated panels (steel and aluminum substrates and lap joints) are presented in Appendix K.

Table VIII lists the coating systems and substrates that were retrieved and analyzed from the field exposures. It is clear that the coating systems listed in Table VIII are the same as the coating systems listed in Table I. Coating systems A and C are designated as “full chrome” systems (both Alodine 1600 and Deft 02-Y-040 contain chromate); coating E is a “partial chrome” system (Alodine 1600 only); coating systems F and G are designated as “non-chrome” systems: coating system F contains a non-chromate primer; coating system G is chrome-free, but has a magnesium rich primer as a corrosion inhibitor; and coating system I was designated as a

Distribution Statement A. Approved for public release.

"negative control," where there were no corrosion inhibitors in the primer used, nor any corrosion inhibitors were present in the coating system.

Table VIII. Summary Table of coating systems and substrate analyzed from field exposures.

Coating System	Substrate	Pretreatment	Primer	Topcoat	Notes
A	AA2024 Panel	Alodine 1600	Deft 02-Y-040	Deft 99-GY-001	Full Cr
C	AA2024 Lap Joint	Alodine 1600	Deft 02-Y-040	Deft 99-GY-001	Full Cr
E	AA2024 Panel	Alodine 1600	Deft 02-GN-084	Deft 99-GY-001	Partial Cr
F	AA2024 Panel	Alodine 5200	SICO 577-630	ANAC Aerodur 5000	NonCr
G	AA2024 Panel	Prekote	ANAC 2100	ANAC Aerodur 5000	NonCr - MRP
I	AA2024 Panel	Prekote	Non-inhibitor primer	Deft 99-GY-001	Negative Conrtrol

MRP: Magnesium Rich Primer

Ranking of coating system performance: The coated panels retrieved from the field at the two year interval were ranked on the coating performance based upon a ranking system developed by the Coatings Technology Integration Office (CTIO) at WPAFB, integrating the amount of corrosion present within the scribe, the amount of undercutting and a blister scale (due to time and funding constraints, the coating systems from the one year interval were not ranked). These rankings are presented in Table IX, with a ranking of 1 = best performance and 5= worst performance. Note that the samples from WPAFB are missing due to them being lost inexplicably sometime during the second year of exposure on site. Figure 40 has images of all the exposed coated panels from Pt. Judith as an example; there is a clear difference in the performance of the coatings between year 1 and year 2, particularly for coating systems F, G, and I where blistering and corrosion product run-off form the scribe is clearly visible in the 2 year exposure samples. A complete set of representative images of the coated panels from all of the exposure sites are presented in Appendix K. Also note that the coating system C samples are lap joint specimens and are considered separately (see analysis of lap joint samples, page 51).

Table IX. Summary of rankings of coating performance of the coated AA2024-T3 panels retrieved after a two year exposure.

System	Pt. Judith	Daytona Beach	Hickam AFB HI	Tyndall AFB FL	Kirtland AFB NM	West Coast Ship	East Coast Ship
A: Deft 02-Y-40/Deft 99-GY-001	1	1	1	1	1	1	1
E: Deft 02-GN-084/Deft 99-GY-001 (Partial Cr system)	2	1	1	1	1	1	2
F: SICO 577-630/Aerodur 5000	5	5	5	1	1	4	5
G: Akzo Nobel 2100 Mg Rich/Aerodur 5000 (Non-Cr/Mg Rich Primer)	3	3	1	5	5	1	2
I: Negative Primer/Deft 99-GY-001 (Non-inhibitor Primer)	4	4	1	1	1	4	4

Distribution Statement A. Approved for public release.

As can be seen by the rankings in Table IX, the fully chromated coating system (A) and partially chromated system (E) performed the best of the tested coatings at all of the exposure sites after 2 years. For the non-chrome systems (F and G), the performance depended on what exposure location is being considered, with the SICO 577-630/Aerodur 5000 system outperforming the Mg rich primer/Aerodur 5000 system at both Kirtland and Tyndall sites, and the Mg rich primer system outperforming the non-chromate SICO system on both of the ship exposure sites. Based upon these rankings, if a mean value is calculated for each site in terms of coatings performance, it appears that Pt. Judith is the most aggressive (i.e. having the highest average for poor performance ranking) and follows in decreasing order of the East Coast ship, Daytona Beach, the West Coast ship and then Hickam, Tyndall and Kirtland all being the least aggressive.

If the coatings performance is ranked in terms of visible corrosion within the scribe, then the ranking is somewhat similar to what was observed for the bare 2024-T3 exposures (see Figure 16b), with Pt Judith and the West Coast ship sites resulting in the highest amount of corrosion within the scribe.

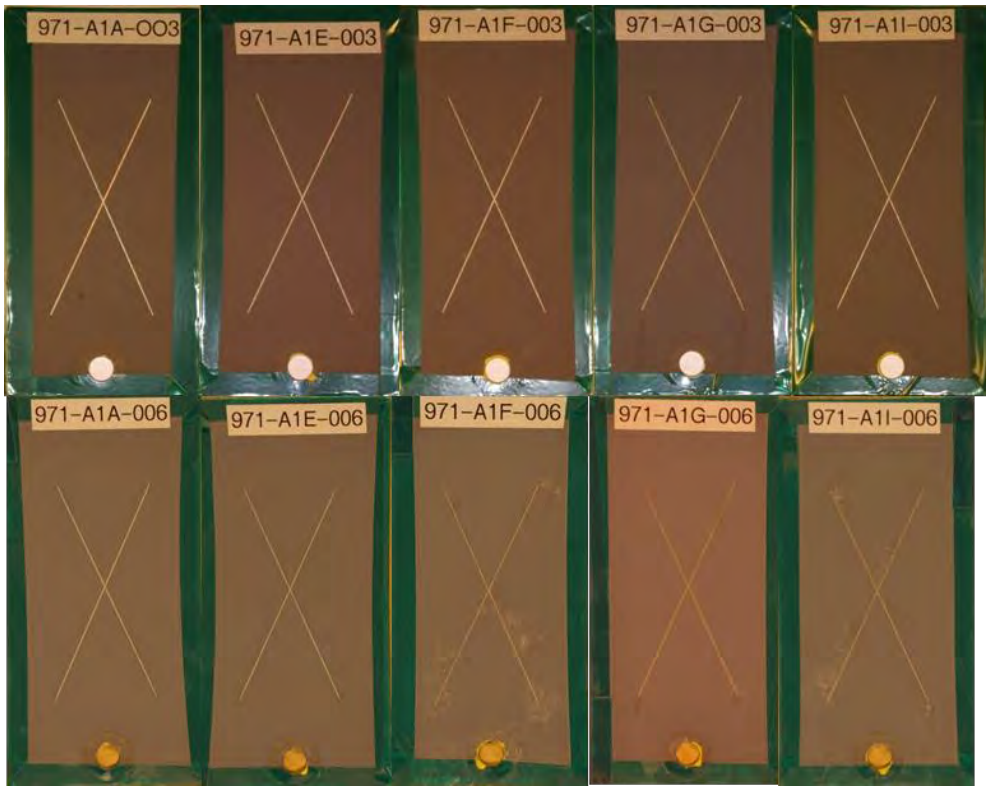

Figure 40. Images of coated panels retrieved from the Pt. Judith, RI exposure site after 1 year (Top) and 2 years (Bottom) exposure. Coating designations are: A1A, coating system A; A1E, coating system E; A1F, coating system F; A1G, coating system G; and A1I, coating system I.

Distribution Statement A. Approved for public release.

These rankings and observations are important in they served as a field exposure baseline for comparison of three coating systems tested in the modified exposure chamber as well as the B117 exposure chamber.

Analysis of Lap Joint Samples: Corrosion (pitting) within the lap joints after 1 year exposure was evident in samples retrieved from (in order of decreasing severity) Pt Judith~ Daytona Beach, the West Coast ship and Hickam AFB. For the 2 year exposures, corrosion (pitting) was evident in samples retrieved from (in order of decreasing severity) Daytona Beach ≈ Pt. Judith, the East Coast ship, the West Coast ship, Tyndall AFB and Hickam AFB. For those exposure sites not listed, no pitting or loss of metal was observed. Figure 41 contains images of the 1 and 2 year lap joint exposure samples from Pt. Judith as an example. The full chromate coating system was used on these lap joint specimens, which is identical to coating system A. A complete set of images of the lap joint samples from all of the exposure sites are presented in Appendix K. Also note that the coating system C samples are lap joint specimens and are considered separately (see analysis of lap joint samples, page 47).

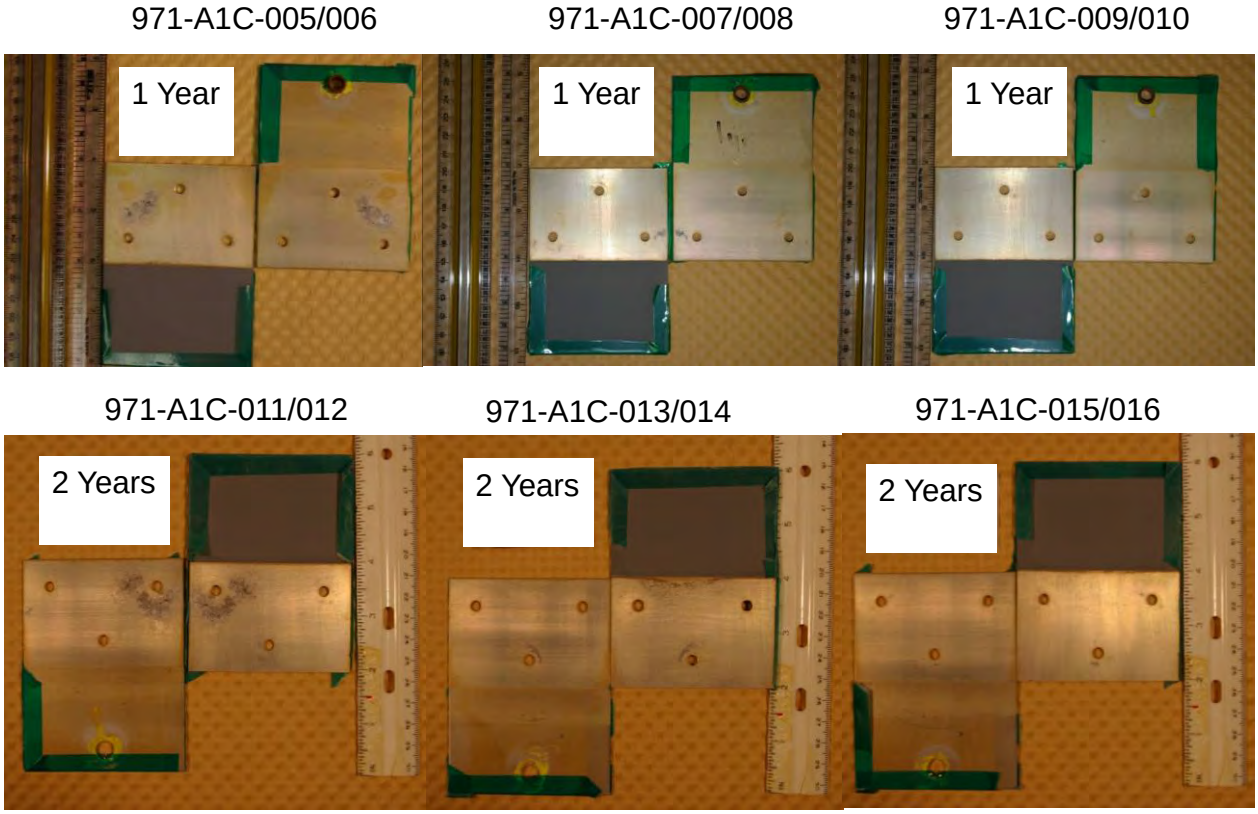

Figure 41. Images of lap joint samples from 1 year (Top) and 2 year (Bottom) exposure at Pt. Judith, RI exposure site. The coating designation A1C is identical to coating system A, the full chromate coating system.

Severe pitting can be seen on the interior surfaces of the lap joints, especially near the fastener holes.

Distribution Statement A. Approved for public release.

Elemental Analysis of Lap Joints and Coated Panels from Field Exposure Sites: EDS analysis of the interior surface of the lap joints allowed for the identification of corrosion products and surface contaminants. There were three locations analyzed by EDS within the lap joint upon opening of the joint; an image of the locations is presented in Figure 42

As evidenced by the EDS data, the two most aggressive land based field sites resulting in corrosion within the lap joint are Pt. Judith and Daytona Beach. This is clearly shown in the relative weight percent of aluminum present in areas analyzed within the lap joints being lowest for these two exposure locations after 1 year of exposure (Figure 43), followed by the two ship based exposure sites (Figure 44).

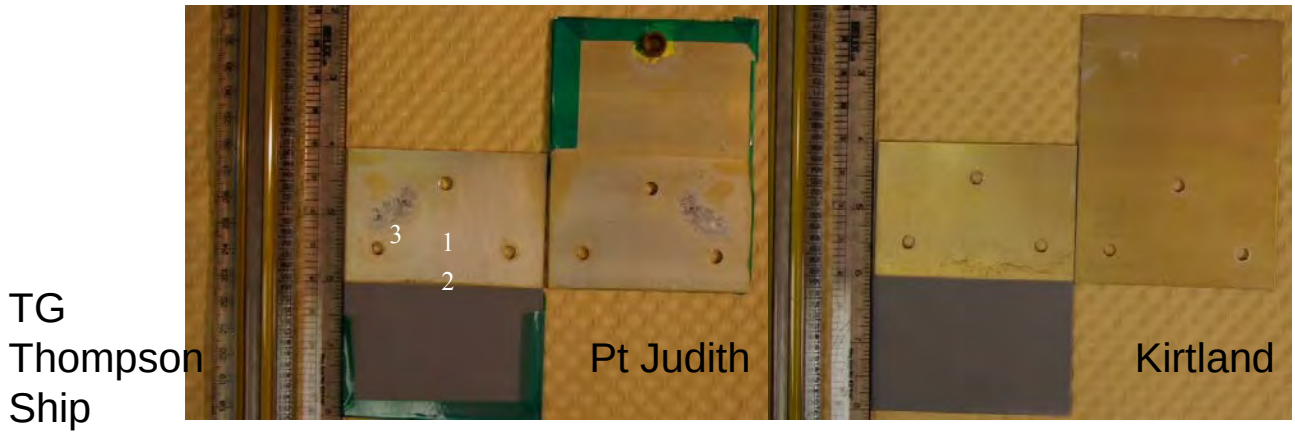

Figure 42. Example of EDS analysis locations on interior surface of a lap joint sample. The bottom plate of the lap joint was always the surface that was analyzed.

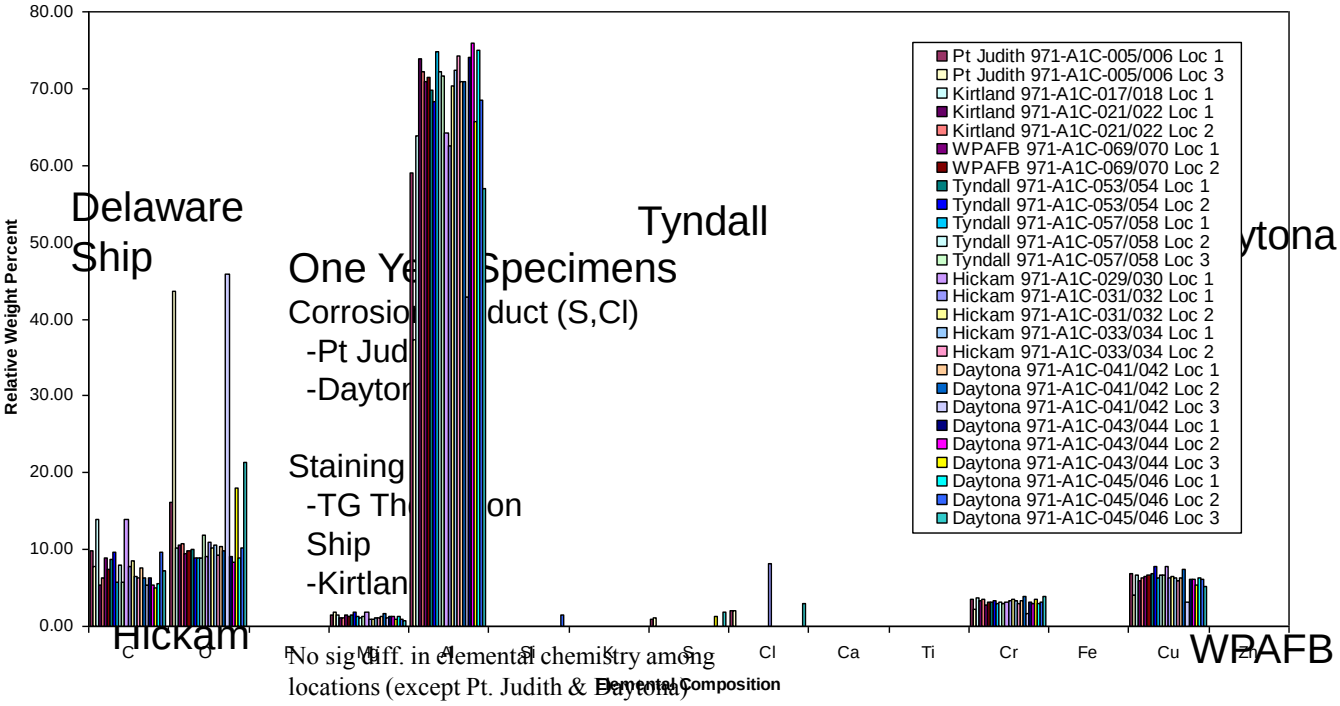

Figure 43. Plot of relative weight percent of elemental composition of locations 1, 2 and 3 within lap joint samples retrieved from the field sites after 1 year of exposure.

Distribution Statement A. Approved for public release.

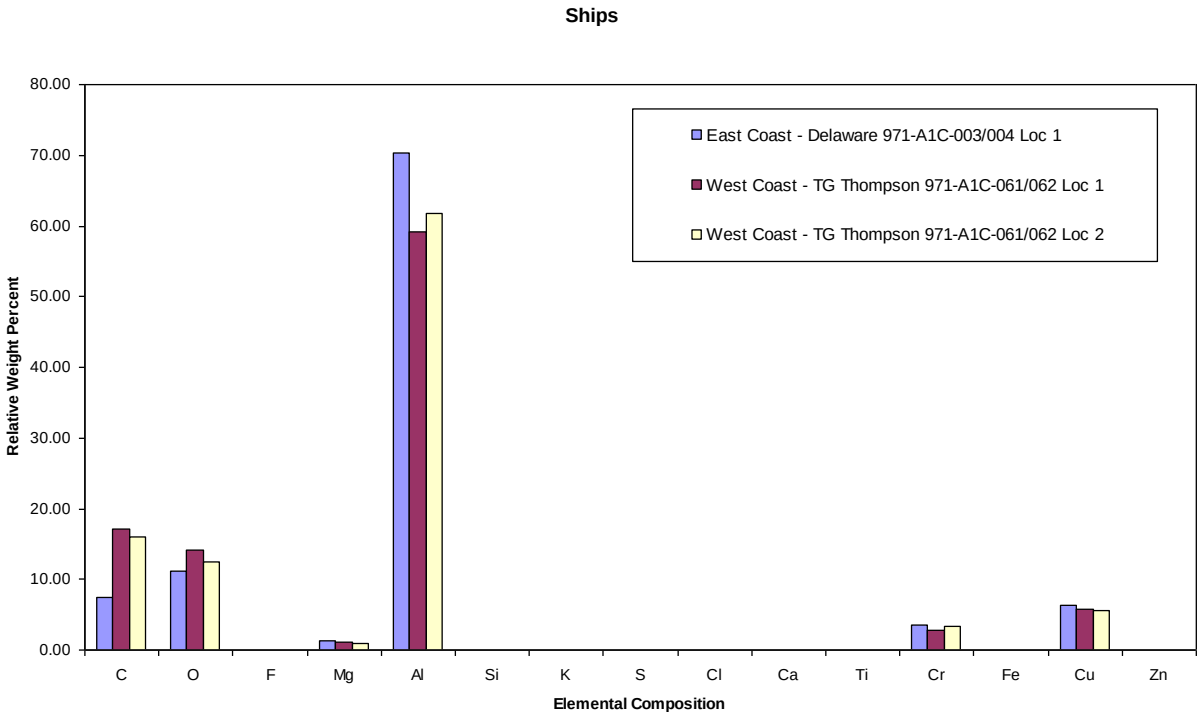

Figure 44. Representative plot of relative weight percent of elemental composition of locations 1 and 2 within lap joint samples retrieved from the ship sites after 1 year of exposure.

EDS analysis of the coated panels retrieved from the field after 1 and 2 years exposure were performed on 4 different locations on each retrieved panel. Figure 45 is an image illustrating the locations analyzed. For purposes of this discussion, EDS analysis results for location 3 will be presented, as it is the location farthest away from any potential contamination from corrosion product derived from the scribe mark during the field exposures. Also, for the purposes of comparison to the coating systems exposed in the modified and B117 chambers, coating systems A (full chromate system) and G (Mg rich primer system) will be discussed here. A complete set of EDS composition plots of the coating systems on 2024-T3 from all of the exposure sites are presented in Appendix L.

An EDS spectrum of a baseline coating system A is presented in Figure 46. This sample was coated at the same time as the field exposure panels, but was never deployed and was analyzed at the same time as the 1 and 2 year retrieval intervals of the coated panels. Figure 47 contains the EDS relative weight percent spectra of 1 and 2 year exposures for coating system A taken at location 3 on the coated panels. The increase in weight percent of Si and Ti between the baseline and the 1 and 2 year exposures are indicative of coating breakdown, since the coating resin is becoming more enriched in pigment particles at the coating surface and are associated with coating system degradation over time. Using that rationale, it appears that after the first year, the East Coast ship sample exhibits the most degradation, followed closely by the West Coast ship and Pt. Judith sites. The high values for Si at the Kirtland site is presumably due to silicate contamination from the surrounding gypsum and silica sands in the surrounding areas [27]. After the second year, Pt. Judith exhibits the highest levels of Si and Ti (again, discounting the levels measured at Kirtland as evidence of surface contamination), followed by Tyndall AFB.

Distribution Statement A. Approved for public release.

For the coating system G, again a baseline EDS spectrum is presented in Figure 48. It was identical to the sample panels deployed at the exposure sites, and was analyzed at the same time as the 1 and 2 year retrieval intervals of the coated panels. Figure 49 contains the plots of the EDS relative weight percent spectra of 1 and 2 year exposures for coating system G taken at location 3 on the coated panels.

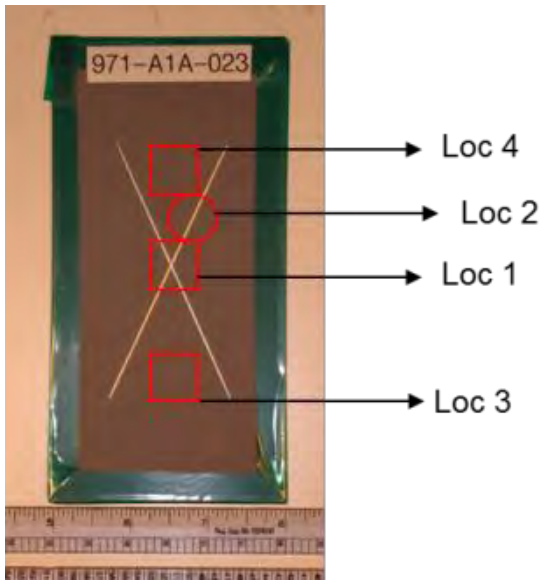

Figure 45. Example image of coated panel retrieved from a field exposure site indicating areas of interrogation by EDS: Loc 1, location 1 within the intersection of scribe marks; Loc 2, location 2 within scribe mark above intersection; Loc 3, location 3 below intersection away from scribe marks; and Loc 4, location 4 above intersection away from scribe marks.

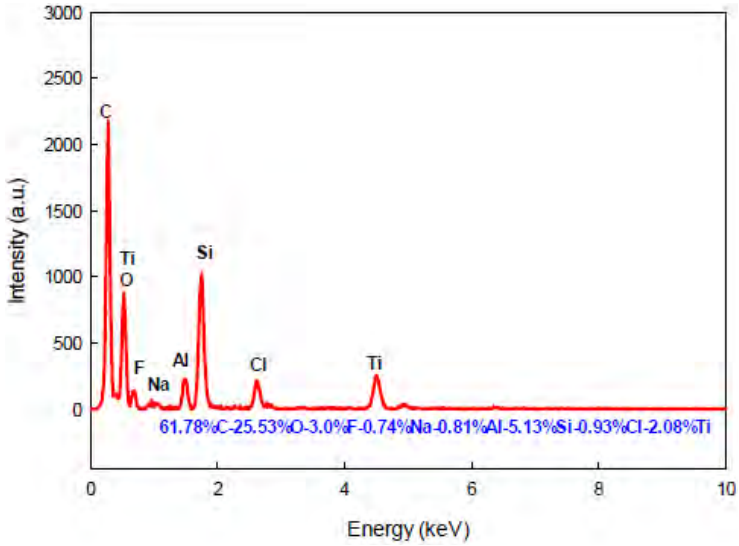

Figure 46. EDS spectrum of coating system A baseline measurement.

Distribution Statement A. Approved for public release.

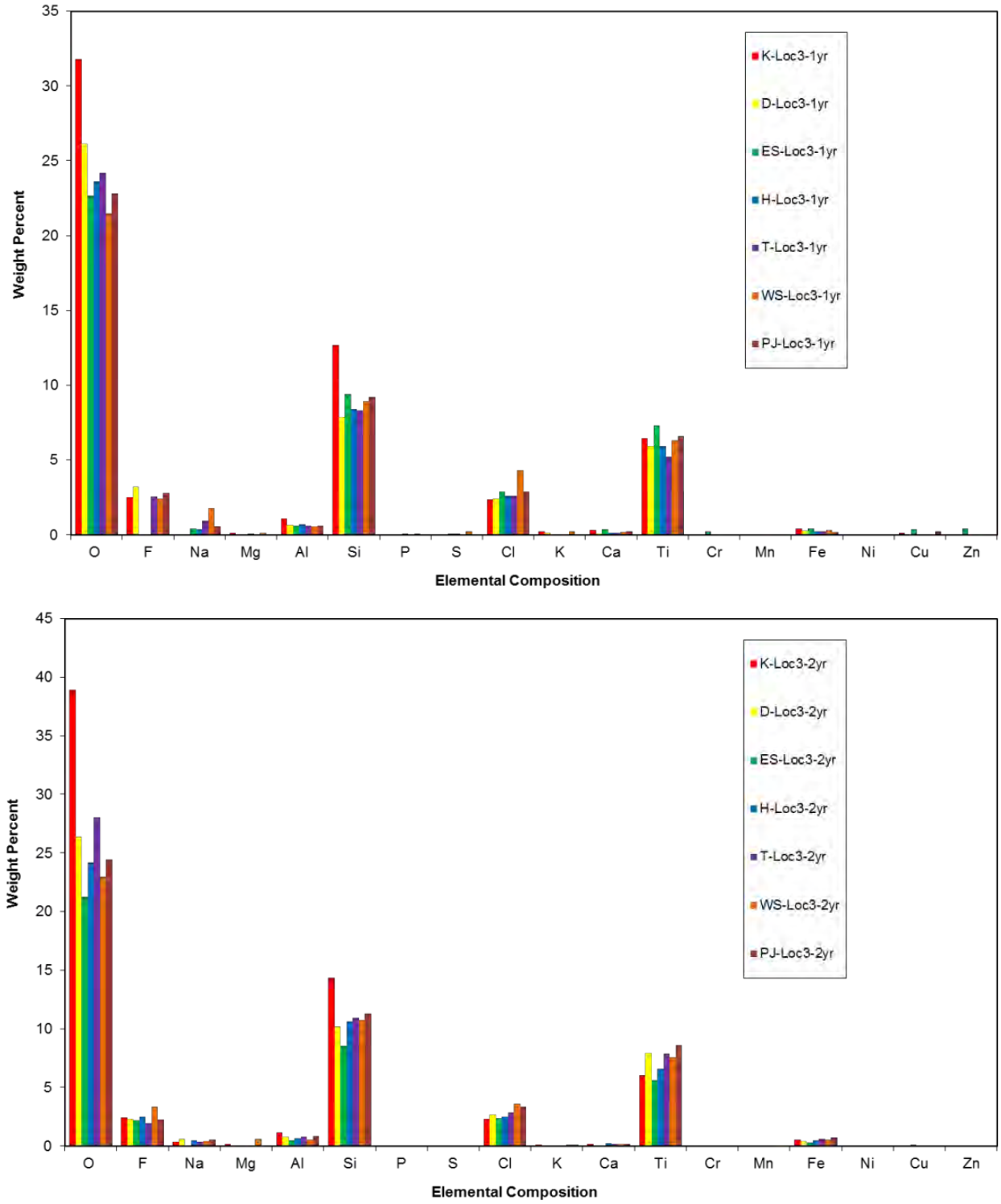

Figure 47. EDS relative weight percent spectra of 1 and 2 year exposures for coating system A taken at location 3 on the coated panels. Location key: K, Kirtland AFB; D, Daytona Beach; ES, East Coast ship; H, Hickam AFB; T, Tyndall AFB; WS, West Coast ship; PJ, Pt. Judith.

Distribution Statement A. Approved for public release.

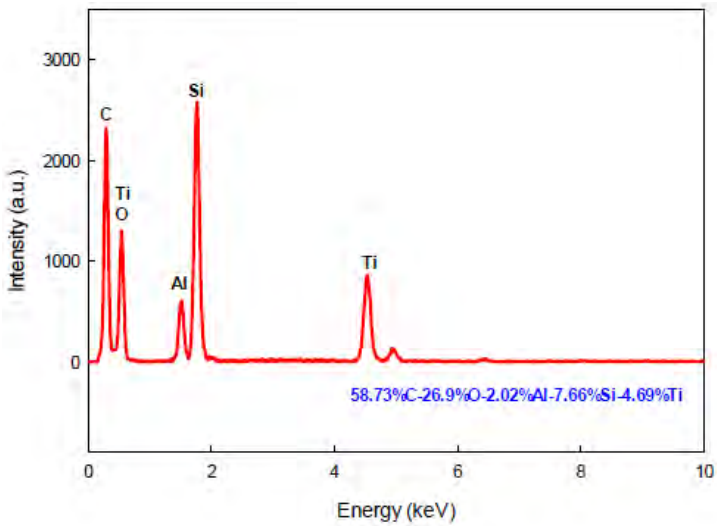

Figure 48. EDS spectrum of coating system G baseline measurement.

The presence of Mg in the EDS spectrum in location 3 on the coated panels (Figure 49) gives a strong indication that the coating has degraded, allowing for the primer pigment of migrate to the surface. This interpretation is strengthened by the fact that there is no Mg signal in the baseline spectrum for the Mg rich primer coating system (Figure 48). In addition, using the same rationale as before, the increasing proportion of the Si and Ti peaks in the 1 and 2 year exposures over the baseline contributes also supports the evidence of coating degradation with time at the various exposure locations. For coating system G after 1 year, the Ti relative weight percent values are higher than the baseline, whereas the Si values appear similar to the baseline. The Daytona Beach site exhibits the highest value, followed by Pt. Judith and the West Coast ship. After 2 years of exposure, both Si and Ti values increase; again, Pt. Judith, the West Coast ship, Tyndall and Daytona exhibit high values. This observation, along with the increased Mg values for the sample retrieved from the West Coast ship (for both 1 and 2 year exposures), give a strong indication that coating system G experiences breakdown on the West Coast ship greater than at the other locations.

Distribution Statement A. Approved for public release.

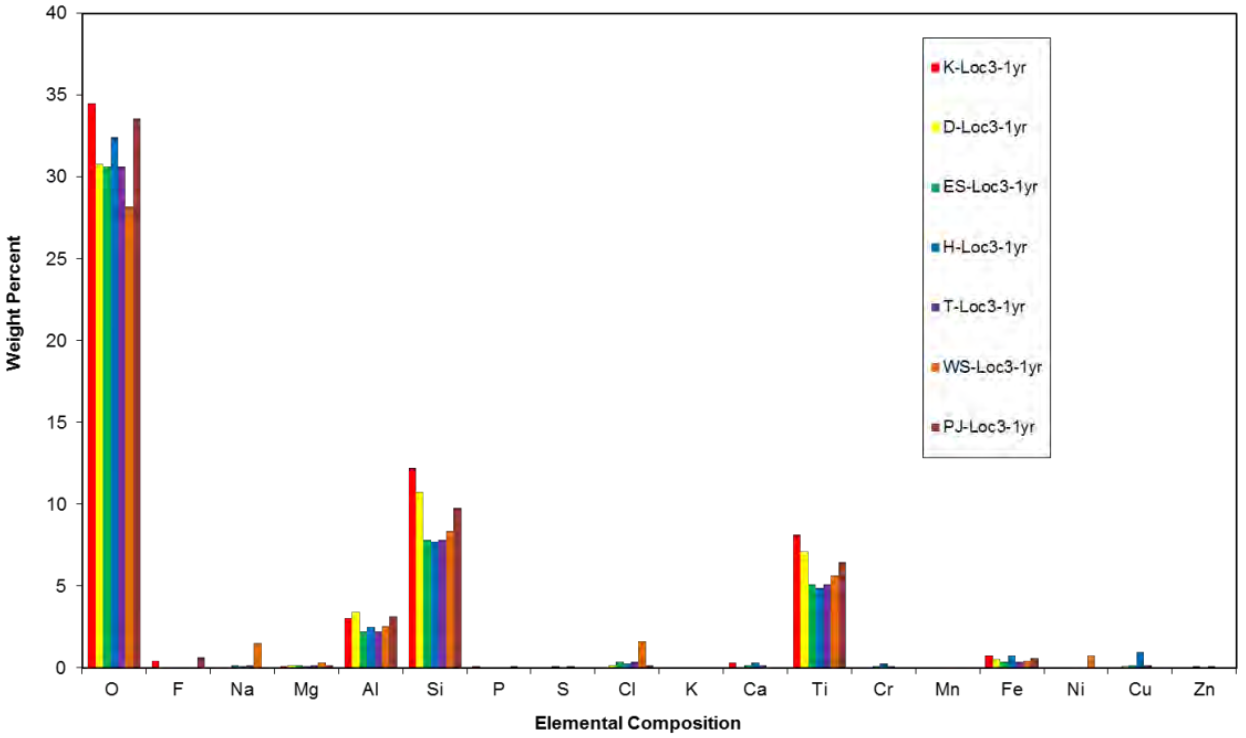

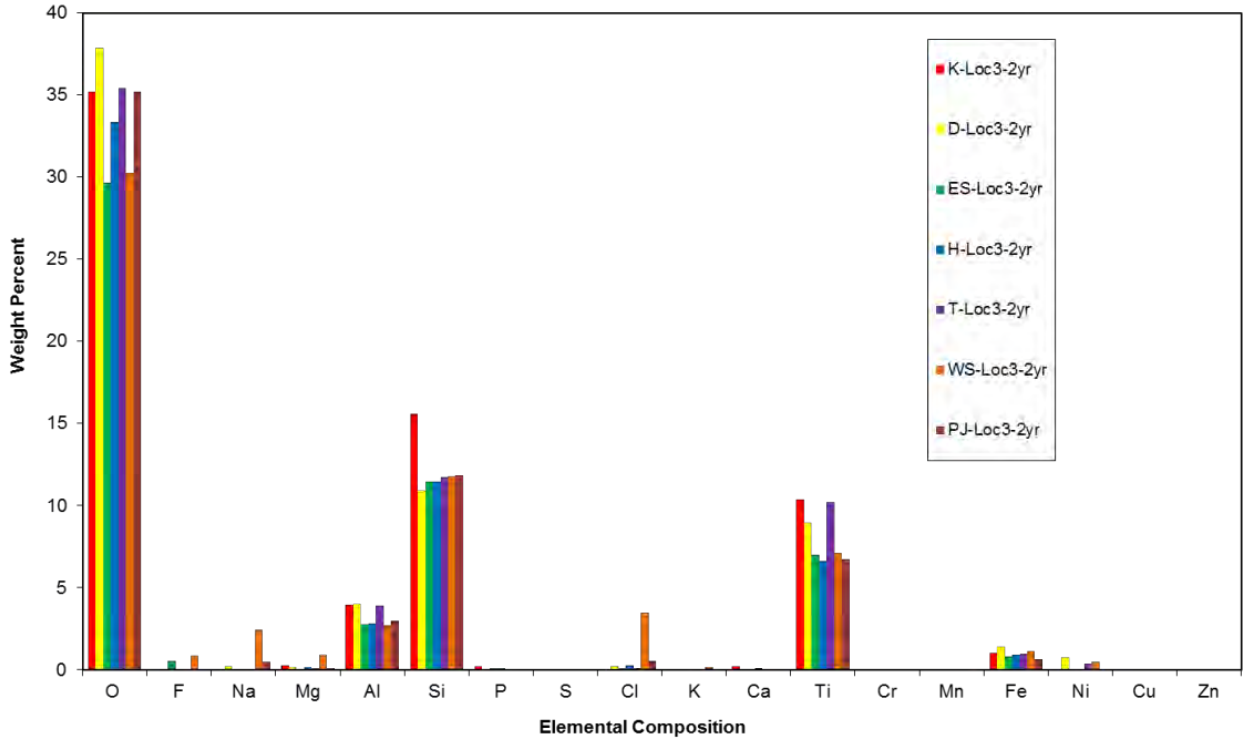

Figure 49. EDS relative weight percent spectra of 1 and 2 year exposures for coating system G taken at location 3 on the coated panels. Location key: K, Kirtland AFB; D, Daytona Beach; ES, East Coast ship; H, Hickam AFB; T, Tyndall AFB; WS, West Coast ship; PJ, Pt. Judith.

Distribution Statement A. Approved for public release.

Test Exposures in Modified and B117 Corrosion Chambers

<u>Bare Metal Coupons</u>**:** Mass loss values for the aluminum alloy, steel, and pure copper coupons exposed for 1000 hours under the four modified chamber conditions are presented in Figure 50.

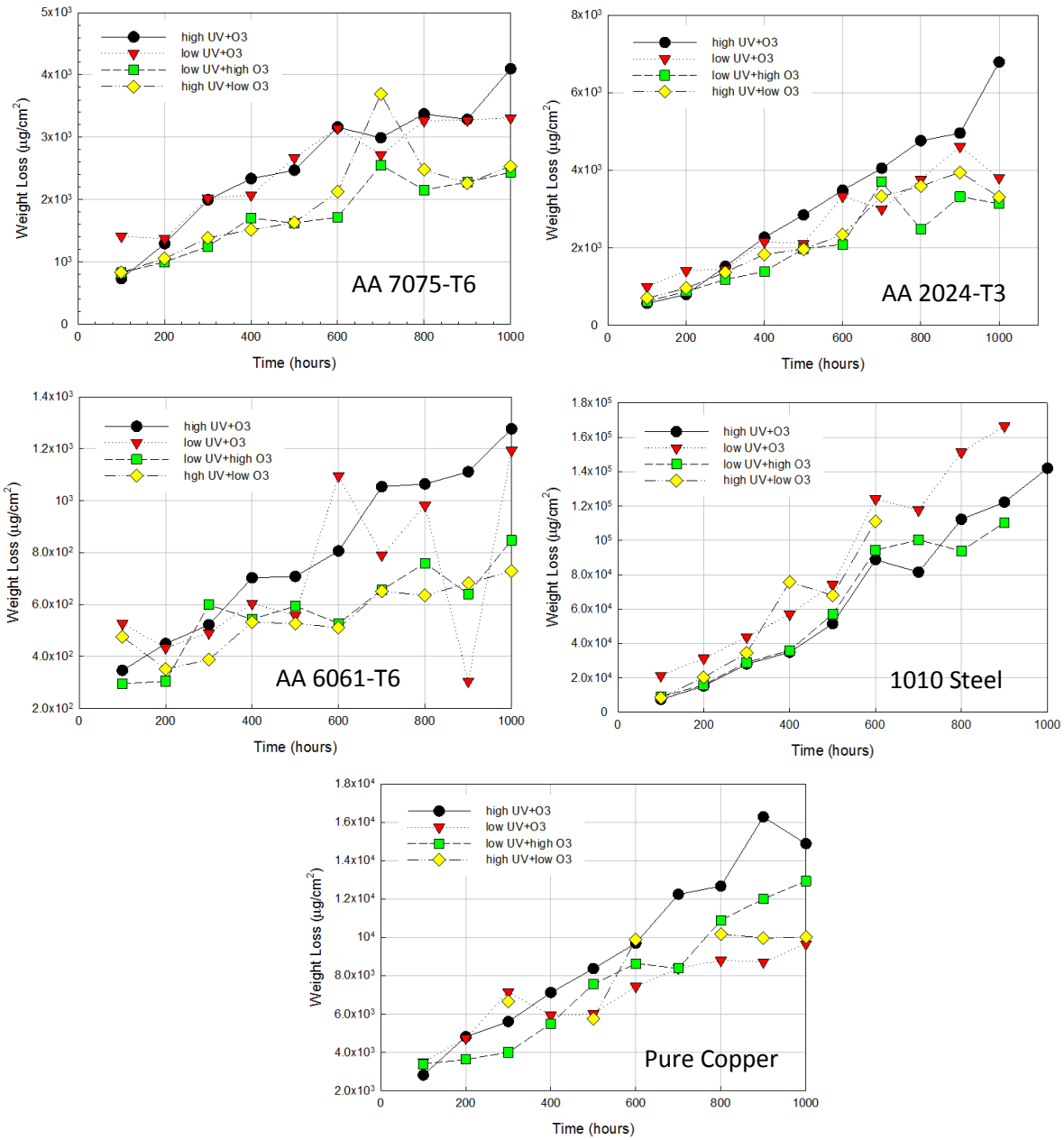

Figure 50. Plots of mass loss for AA7075-T6, AA2024-T3, AA6061-T6, 1010 Steel and pure copper over 1000 hours of exposure at each of four UV-A and ozone combinations.

In general, for the aluminum alloys it is the high UV/high ozone condition that results in the greatest mass loss, with the low UV/low ozone exhibiting a very similar corrosion rate (i.e. mass loss/unit time), more so than the other 2 conditions (low UV/high ozone and high UV/low ozone). These results strongly suggest that there is a synergistic effect in having both a high UV

Distribution Statement A. Approved for public release.

and high ozone exposure condition, with the other parameters (5% NaCl spray and temperature) kept constant. The aluminum results are in contrast to the mass loss (i.e. corrosion rate) for that of 1010 steel, where the low UV/low ozone exhibited the higher rate over time, with the high UV/high ozone condition exhibiting a somewhat lower corrosion rate, very similar to the low UV/high ozone condition. For copper, again the high UV/high ozone resulted in the highest corrosion rate with the low UV/high ozone condition corrosion rate approaching that of the high UV/high ozone condition. It is interesting to note that the high UV/high ozone condition does not result in the highest corrosion rate for 1010 steel. This suggests that the kinetics and oxidation mechanisms may be affected by the highly elevated level of ozone (800 ppb), since both conditions with low ozone (100 ppb) result in higher corrosion rates. However, the low ozone level is still much higher than the average ozone levels measured at the exposure sites (Table III), but the UV levels are much lower than the average UV levels measured at the exposure sites as well. Therefore, one conclusion from these tests can be that UV levels may not be as important in the acceleration of the corrosion rate of the bare metal substrates as ozone levels.

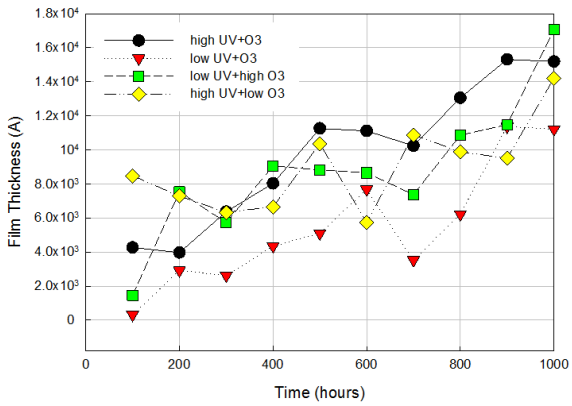

Figure 51. AgCl film thickness measurements on pure silver coupons as a function of exposure condition (UV/ozone) over 1000 hours in the modified exposure chamber.

This effect is further demonstrated when one looks at the AgCl film thickness measurements on pure silver coupons as a function of exposure conditions in the modified chamber (Figure 51). The high UV/high ozone conditions, in general, yields the thickest AgCl film on the pure silver coupons over time until the end of the test, where the low UV/high ozone condition exhibits a larger thickness value, with the low UV/low ozone condition showing a high degree of variability over time with thickness values close to those of the high UV/high ozone and low UV/high ozone. The low UV/low ozone level has a consistent trend with the lowest thickness values over time. The conclusion from these measurements would be that either the high UV or high ozone levels are required for yielding thicker AgCl films (vis a vis the low UV/low ozone conditions where the film thicknesses were lower). However, these thickness measurements are the average of the total coulombic reductions made on each side of the coupon (i.e. the front side of the coupon facing the UV source and the back side of the coupon facing away from the UV source). When the two thicknesses of the AgCl films are plotted for each side of the coupon, there is a visible difference in the values (Figure 52). With the higher thicknesses

Distribution Statement A. Approved for public release.

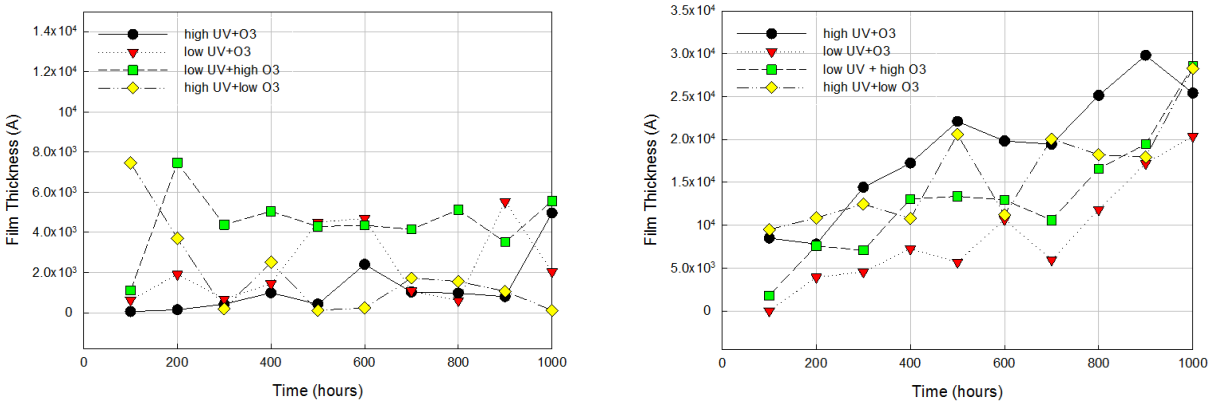

Figure 52. AgCl film thickness on the front (Left) and the back (Right) of pure silver coupons as a function of exposure condition (UV/ozone) over 1000 hours in the modified exposure chamber.

occurring on the backside of the coupons, indicating that it is not necessarily the UV that is contributing to the AgCl film formation, but rather the ozone. The purpose of exposing the pure silver coupons in the field was to investigate what environmental parameters were required for the formation of the AgCl film, since the formation of the films reportedly could not be observed on silver coupons in the B117 chamber. Figure 53 shows the comparison of the formation of AgCl film thickness on pure silver coupons in the modified chamber versus the B117 test chamber. It is clear that the AgCl film formation in the B117 chamber is minimal compared to those exposed under any of the UV/ozone conditions in the modified chamber. When compared to the field exposures (see Table VI), the thickness of the AgCl film on the back of the UV/ozone chamber coupons are equivalent to the thicknesses measured for the entire coupons exposed at Daytona Beach (12-18 months), the West Coast ship and East Coast ship (18 months). If one considers the average thickness of the AgCl film on the UV/ozone exposed coupons after 1000 hours (11,000 – 17,000 angstroms, Figure 50), then the similarities become: Daytona Beach (6-9 months), Pt. Judith (12-24 months), the East Coast and West Coast ships (6-9 months) and Hickam AFB (18-24 months).

Distribution Statement A. Approved for public release.

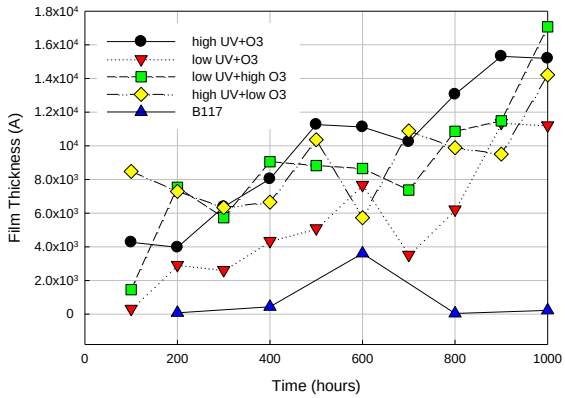

Figure 53. AgCl film thickness measurements on pure silver coupons as a function of exposure condition (UV/ozone) over 1000 hours in the modified exposure chamber and the B117 test chamber.

Comparison of the mass loss of the bare aluminum alloy coupons in the modified chamber to the B117 test chamber is presented in Figure 54 and for the steel alloy in both chambers in Figure 50. It is evident that the role of UV and ozone has a greater effect on the corrosion rate of AA2024-T3 than they do on the corrosion rate of AA7075-T6

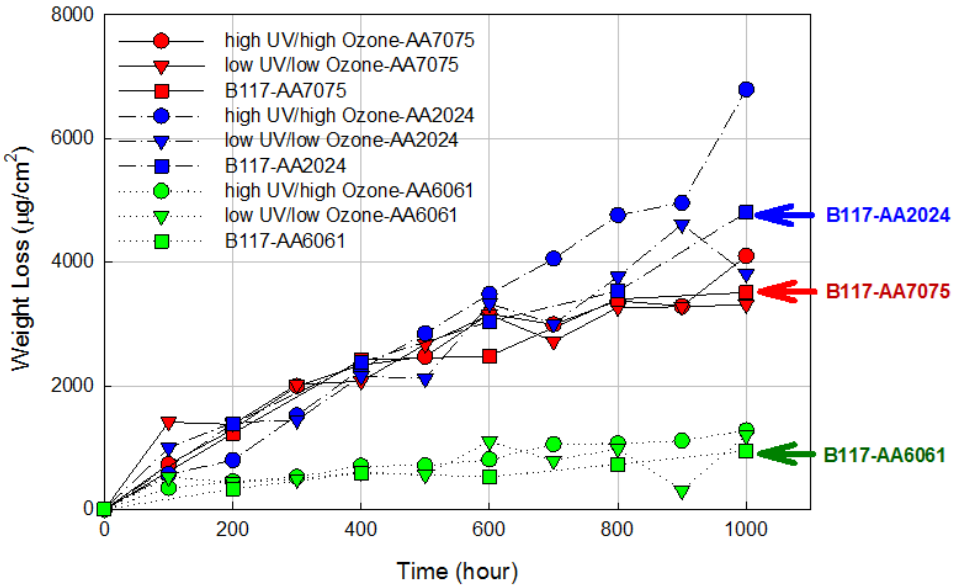

Figure 54. Comparison of mass loss of AA7076-T6, A2024-T3 and AA6061-T6 over 1000 hours exposure in the modified chamber versus the B117 test chamber.

Distribution Statement A. Approved for public release.

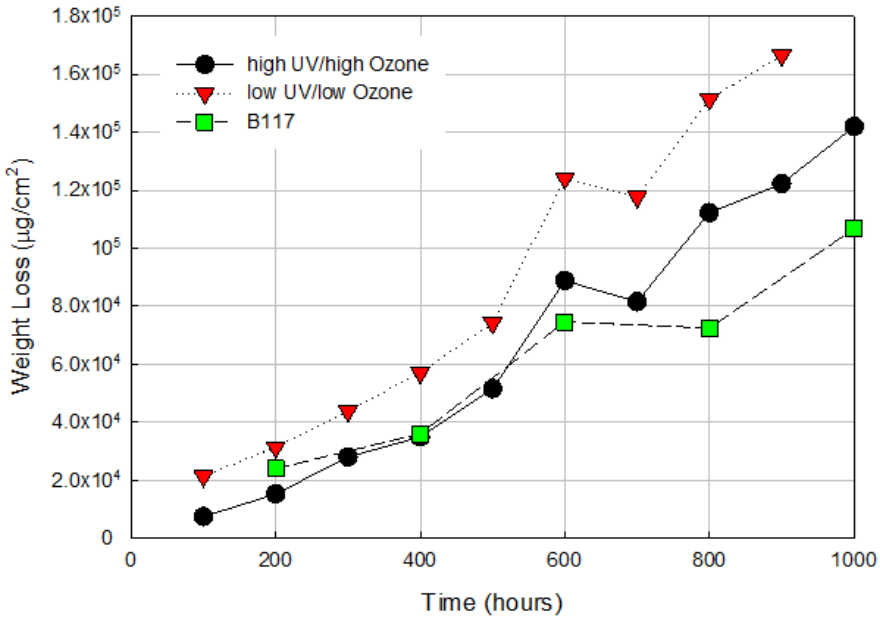

Figure 55. Comparison of mass loss of 1010 steel alloy coupons over 1000 hours exposure in the modified chamber versus the B117 test chamber.

or AA6061-T3, particularly after 600 hours of exposure (Figure 54). This may be related to the high corrosion rate observed for pure copper when exposed to the high UV/high ozone levels (Figure 50), since AA2024-T3 contains the highest amount of copper of the three aluminum alloys (Table VII). The 1010 steel alloy exhibited a similar response, (Figure 55), where either UV/ozone condition resulted in an increased corrosion rate over that observed for the 1010 steel exposed in the B117 test chamber.

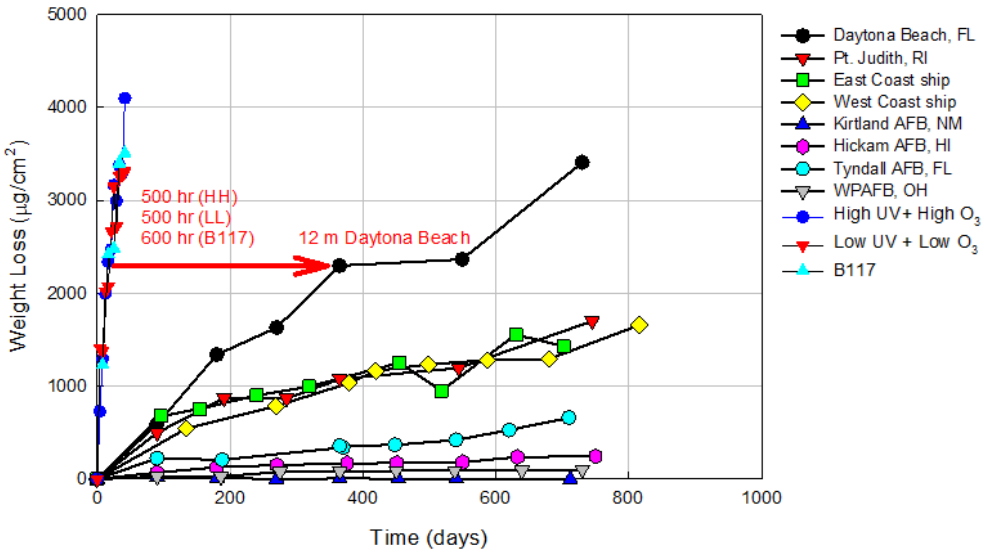

Figure 56. Corrosion rates of AA7075-T6 at the field exposure sites in comparison to the corrosion rates determined for identical coupons exposed in the modified and B117 chambers. The designated comparison is between coupons exhibiting similar mass losses in the modified

Distribution Statement A. Approved for public release.

chamber under both high UV/high ozone (500 hours) and low UV/low ozone conditions (500 hours), B117 chamber test (600 hours) and Daytona Beach (12 months).

A comparison of the corrosion rates of the AA7075-T6 alloy in both chambers to that observed in the field exposures is presented in Figure 56. The data presented in Figure 56 are an example to illustrate what was described previously, which was that the mass loss for a metal coupon at specific time intervals for each exposure condition and field site may be similar, but the surface morphology and elemental composition may differ dramatically. This can be seen in Figure 57, where SEM images and an elemental composition comparison is presented for the designated comparison example in Figure 56 is presented. The 12 month exposure sample of AA7075-T6 exhibits a markedly different surface morphology as compared to the 500 hour exposed samples from the modified chamber as well as the sample from the B117 test chamber. When the elemental composition of the samples are compared, it can be seen that while there is a similarity in terms of relative atomic percent of aluminum between the high UV/high ozone 500 hour exposure condition and the 12 month Daytona Beach exposure, there remains a large variability in any similarity in the remaining elements detected on the coupon surfaces. This phenomenon is repeated for the other bare metal substrates as well. Therefore, these results suggest that while the chamber exposure tests do indeed result in a much more accelerated corrosion rate of the samples as compared to that observed in the field, there remains a lack of similarity in the overall chemical and morphological character of the corroded surfaces. These findings reinforce the notion that the incorporation of UV and ozone into an accelerated test chamber in an attempt at reproducing a valid accelerated corrosion test is far more difficult than estimated at the beginning of this study. It is clear that specific combination of exposure time, UV irradiance level, ozone level and duration of wet/dry cycles can be critical in the reproduction of a corroded metal surface that is similar in mass loss, morphology and chemistry to a field exposure in an accelerated test protocol. A complete set of SEM images of the bare coupons exposed to the modified and B117 chambers are presented in Appendices M – P; EDS analysis of the bare coupons are presented in Appendix Q.

Distribution Statement A. Approved for public release.

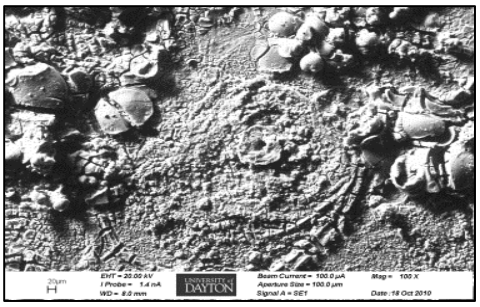

(a)

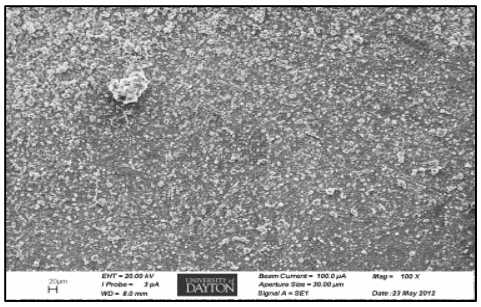

(b)

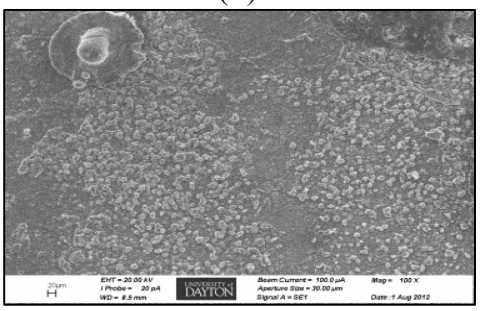

(c)

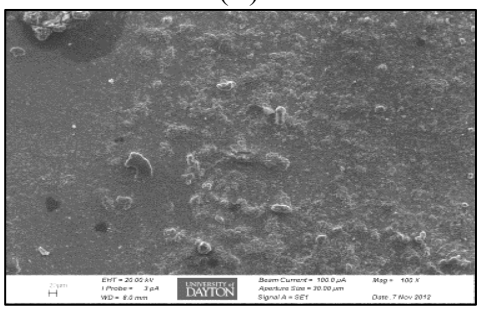

(d)

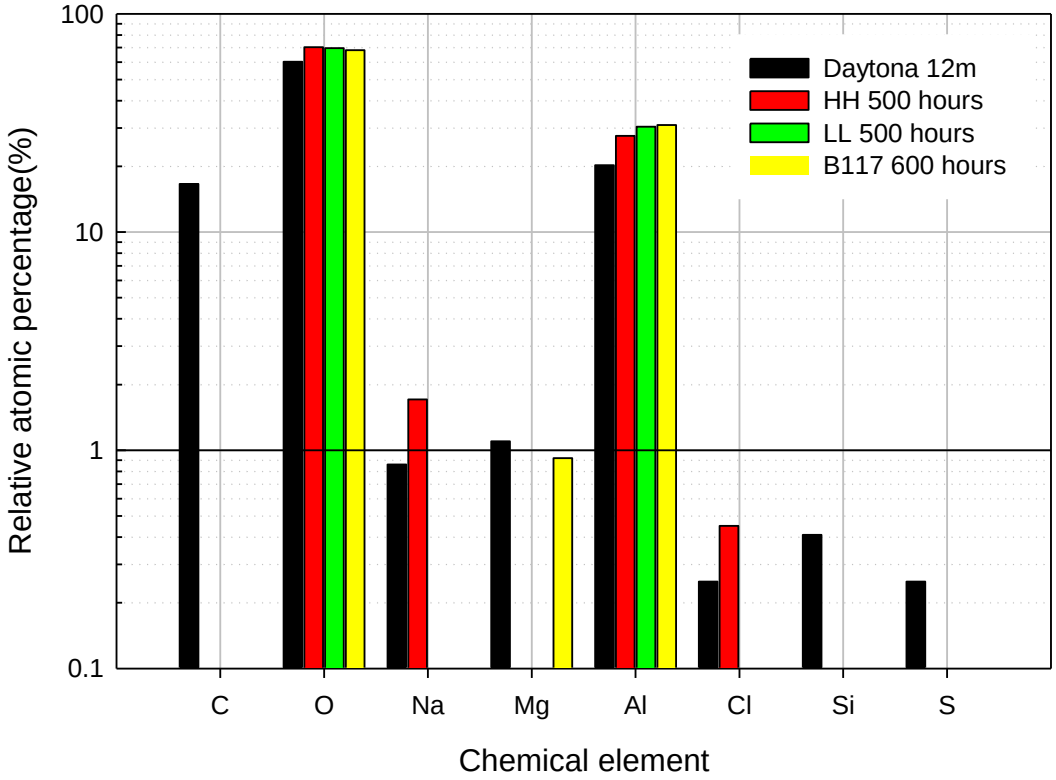

(e)

Figure 1. SEM images of AA7075-T6 samples at (a) 12 months Daytona Beach site, (b) 500 hours high UV/high ozone, (c) 500 hours low UV/low ozone, (d) 600 hours B117, and (e) 18 months and (f) EDS analysis of AA7075-T6 samples.

Figure 57. SEM images of AA7075-T6 coupon surfaces at (a) Daytona Beach, 12 months; (b) high UV/high ozone, 500 hours; (c) low UV/low ozone, 500 hours; B117 test, 600 hours; and (e) EDS analysis of the respective A7075-T6 surfaces.

Distribution Statement A. Approved for public release.

Coated Panels: Three coating systems were exposed in both the modified chamber and the B117 chamber. Table X is a summary review of the coating systems tested. Coating systems H and A are the same systems as deployed in the field, only re-designated with a different alphabet code due to coating processing; coating system H is the full chromate coating system deployed in the field and coating system A is the magnesium rich coating system deployed in the field; coating system J is a replacement for coating system F (SICO 577-630), since it was no longer commercially available for testing when these coated panels were made for the chamber testing. In addition, the rare earth conversion coating system (RECC, coating system J) was under testing and evaluation under another DoD program effort and it was decided to include this coating in the chamber studies. A complete set of images of the coated panels from the B117 and modified chamber exposure tests are presented in Appendix R. A complete comparison of the EDS analysis of the coated panels from the field and the exposure chambers (modified and B117) are presented in Appendix S.

Table X. Summary table of coating systems tested in the modified and B117 exposure chambers.

Coating System	Substrate	Pretreatment	Primer	Topcoat	Notes
H	AA2024 Panel	Alodine 1600	Deft 02-Y-040	Deft 99-GY-001	Full Cr
A	AA2024 Panel	Prekote	ANAC 2100	ANAC Aerodur 5000	NonCr - MRP
C	AA2024 Panel	RECC1041\RECC3031	Deft 02-GN-093	Deft 99-GY-001	RECC

MRP: Magnesium Rich Primer
RECC: Rare Earth Conversion Coat

Coated panels of each coating system in Table X were exposed under high ozone / low UV-A conditions for 1000 hours immediately followed by low ozone / high UV-A conditions for an additional 1000 hours for a total of 2000 hours exposure testing. The coated panels were removed at 400 hour intervals and analyzed and compared with identical coated samples exposed for 1 and 2 years in the field, as well as identical samples exposed for 1000 hours in the B117 test chamber. Table XI is a summary of the resulting rankings of the coating system performance from the chamber exposures. It is important to note that according to the standard, the rankings are assigned to the sample in comparison to the other samples within the same sample set (in this case the B117 and UV/ozone chamber exposures); the numerical rankings assigned to chamber samples should not be compared to numerical rankings of the coated samples retrieved from the field.

Table XI. Summary of rankings of coating performance for the three coating systems exposed in the modified and B117 test exposure chambers. A ranking of 1 = best performance and 3= worst performance.

Coating System	400 Hrs		800 Hrs		1200 Hrs		1600 Hrs		2000 Hrs	
	B117	UV/O_3	B117	UV/O_3	B117	UV/O_3	B117	UV/O_3	B117	UV/O_3
A: Akzo Nobel 2100 Mg Rich/Aerodur 5000 (Non-Cr/Mg Rich Primer)	1	1	1	1	1	1	1	1	1	1
C: RECC1041-RECC3031/02GN093/990GY001	2	2	2	2	3	2	2	2	2	2
H: Deft 02-Y-40/Deft 99-GY-001 (Full Cr system)	2	2	2	1	2	1	2	1	3	1

Distribution Statement A. Approved for public release.

From the visual inspections of these coated samples, it was determined that the full chromate system (coating system H in chamber tests, coating system A in the field exposures) performance in both chamber exposures are worse than the 2 year outdoor exposures; even at the shortest time intervals when the corrosion present in the scribe is compared to the East Coast ship, West Coast ship and Pt. Judith exposure sites, which were determined to be the most aggressive outdoor exposure sites for the full chromate coating system (see Figure 58).

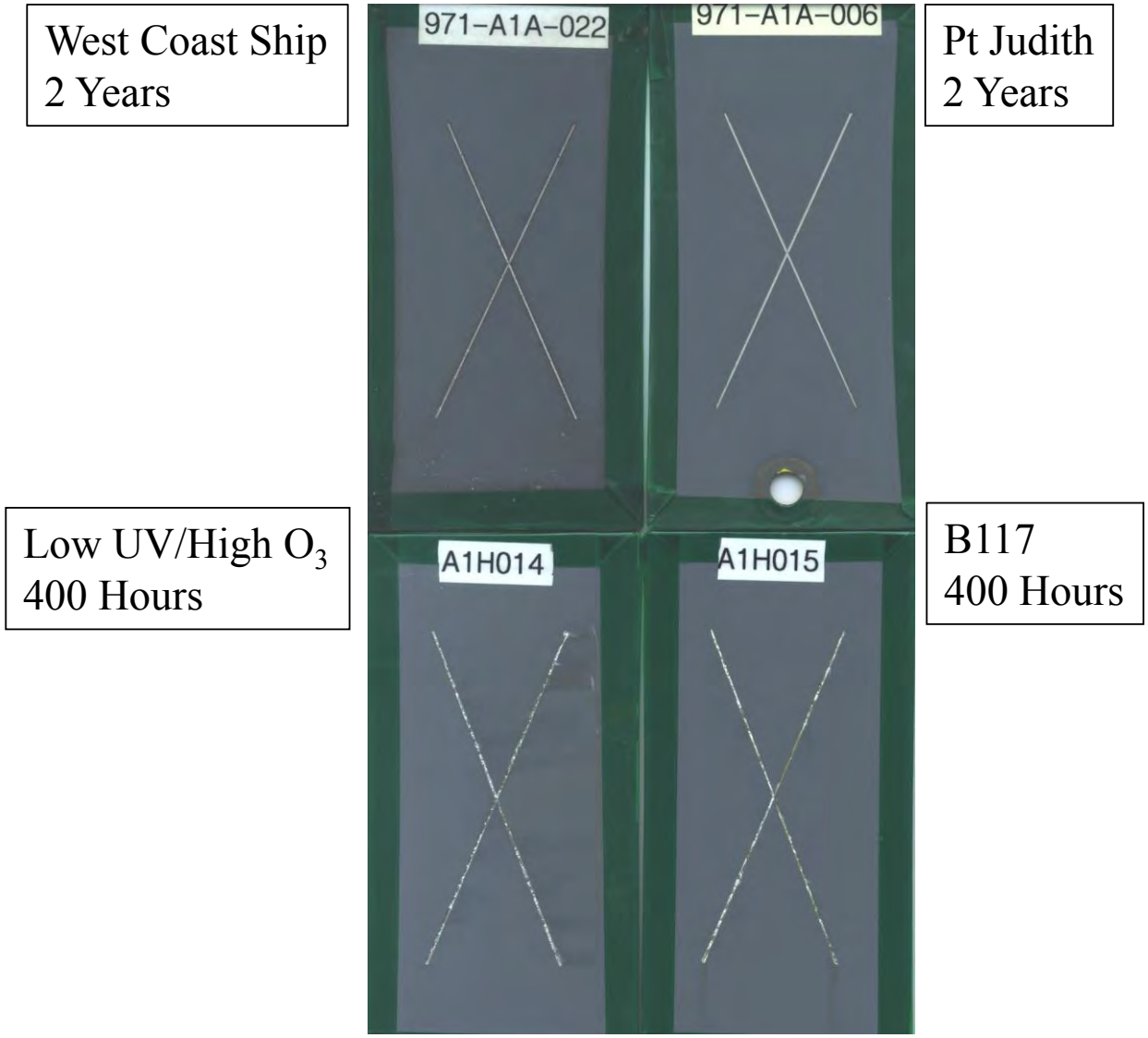

Figure 58. Comparison of 2 year exposures of the full chromate coating system (top) at the West Coast ship and Pt. Judith exposure sites to (bottom) 400 hours exposure of the same coating system in either the modified UV/ozone or B117 chambers.

Distribution Statement A. Approved for public release.

The magnesium rich coating system (coating system A in the chamber tests, coating system G in the field exposures) performed better in the field exposures (see Figure 59) than the chamber exposures. These results are representative of the performance of the full chromate and magnesium-rich coating systems, where their performance was determined to be worse in the chambers than in the field exposures (see Figure 60). In particular, the performance of the Mg-rich and RECC coating systems fared much worse in the UV/ozone chamber than in the B117 test.

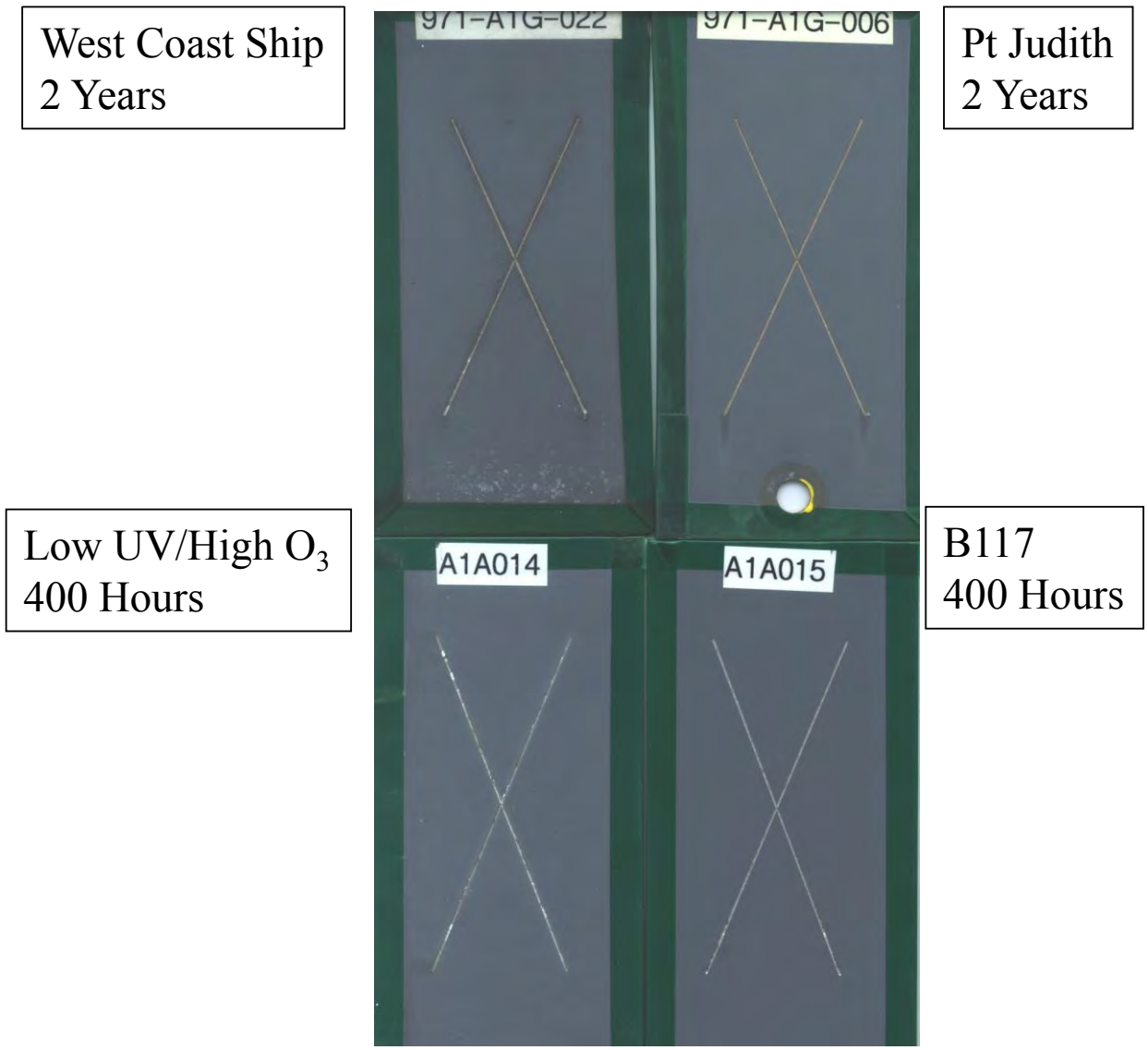

Figure 59. Comparison of 2 year exposures of the magnesium rich coating system (top) at the West Coast ship and Pt. Judith exposure sites to (bottom) 400 hours exposure of the same coating system in either the modified UV/ozone or B117 chambers.

Distribution Statement A. Approved for public release.

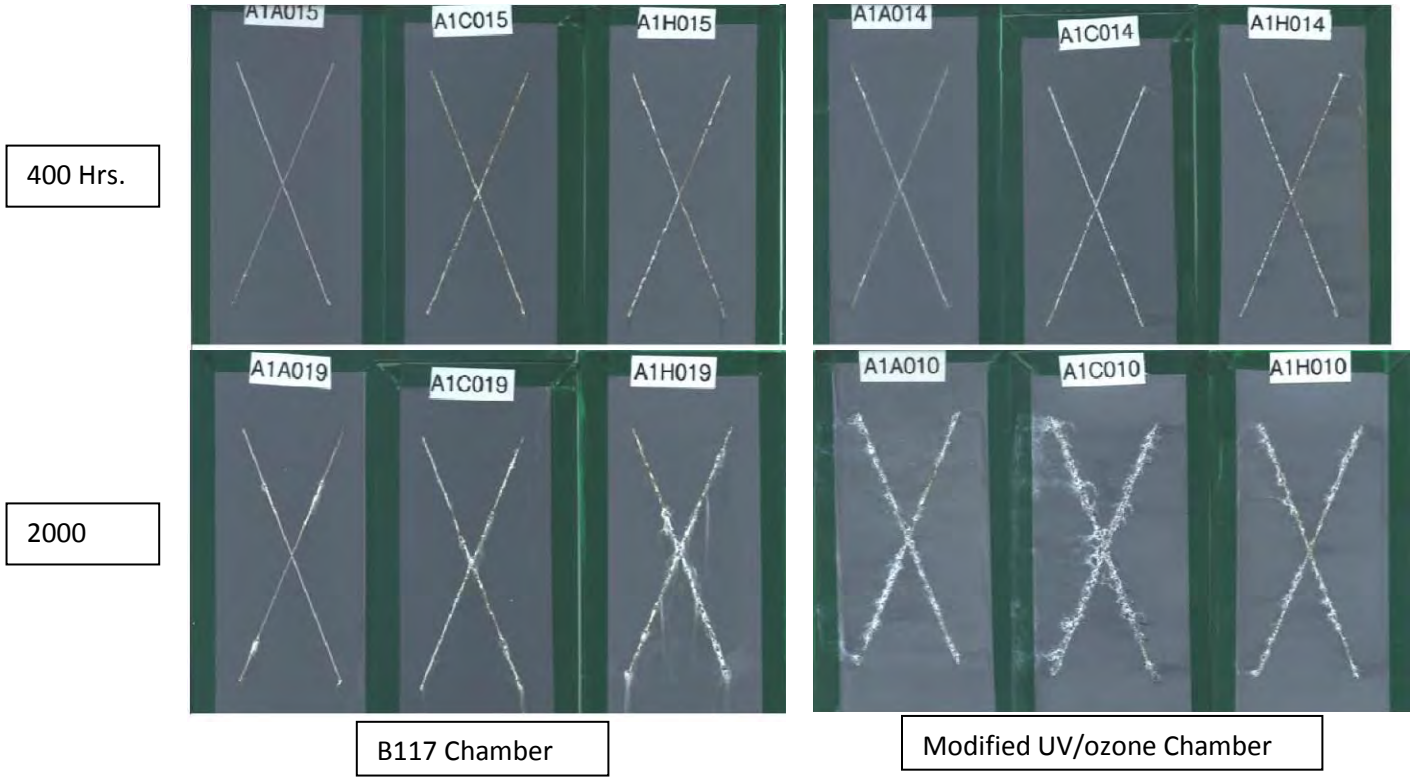

Figure 60. Side-by-side chamber exposure comparison of the three coating systems on AA2024-T3 panels at (top) 400 hours and (bottom) 2000 hours exposure in the modified UV/ozone and B117 chambers, respectively. Panel coating designation code: A1A: magnesium rich coating system; A1C: rare earth conversion coat (RECC) system; A1H: full chromate coating system.

These results suggested that regardless of coating stackup, the coated test panels that were subjected to UV/Ozone in addition to the sodium chloride electrolyte had higher relative percentages of oxidation in the scribe (location 1) over the duration of exposure, when compared to the B117 exposure. It was observed for the coating surfaces analyzed (at location 3) for the fully chromated (Figure 61), Mg rich (Figure 62) and RECC (Figures 63) coating systems that longer exposures in the modified chamber contribute to not only increased oxidation of the scribe but also of the coating as compared to the baseline analyses of the full chromate or Mg rich coatings (Figures 46 and 47, respectively). Furthermore, higher percentages of aluminum, titanium, and especially silicon are noted with time in the modified chamber. These results are significant because the UV/Ozone conditions in the modified chamber are at or lower than the cumulative values observed in the field and, in this instance, are an indication of degradation of the advanced performance coatings in the modified chamber that are normally very resistant to weathering, chalking, and color changes in the field. It also must be noted that the modified and B117 chamber exposures were in constant spray conditions, whereas the field sites experienced intermittent wet and dry exposure cycles. These results suggest, therefore, that the coating resin is becoming more enriched in pigment particles at the coating surface and are associated with coating system degradation over time.

Distribution Statement A. Approved for public release.

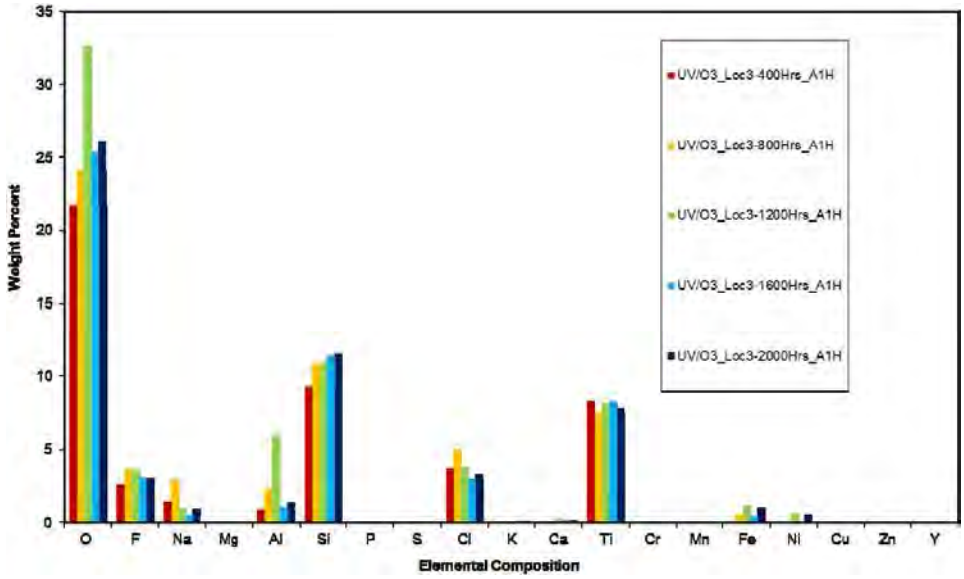

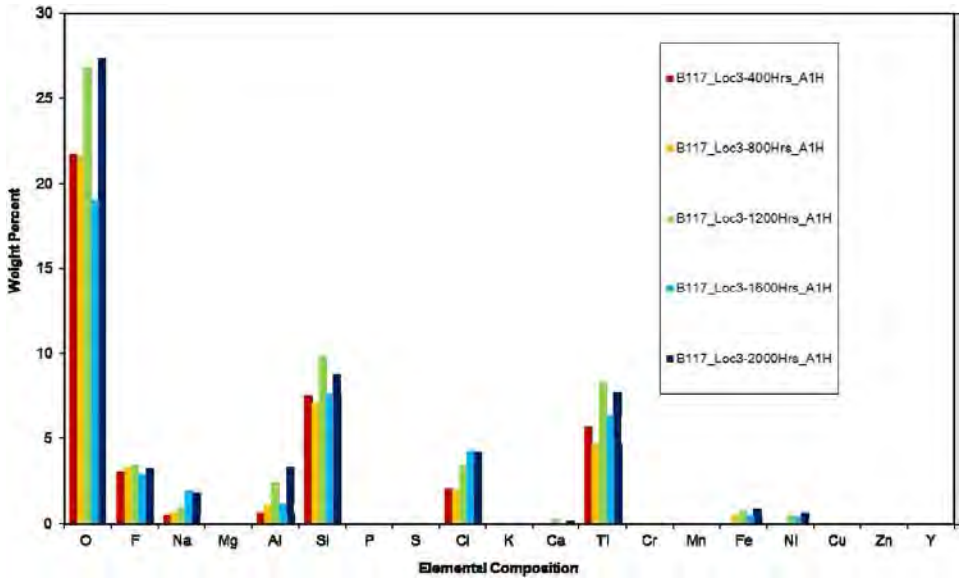

(b) Figure 6: Compositional analysis of fully chromated coated test panels at location 3 (on coating) from (a) UV/O_3 chamber and (b) B117 chamber.

Figure 61. EDS analysis of fully chromated coating system (location 3) exposure panels from (top) modified UV/ozone chamber and (bottom) B117 chamber.

Distribution Statement A. Approved for public release.

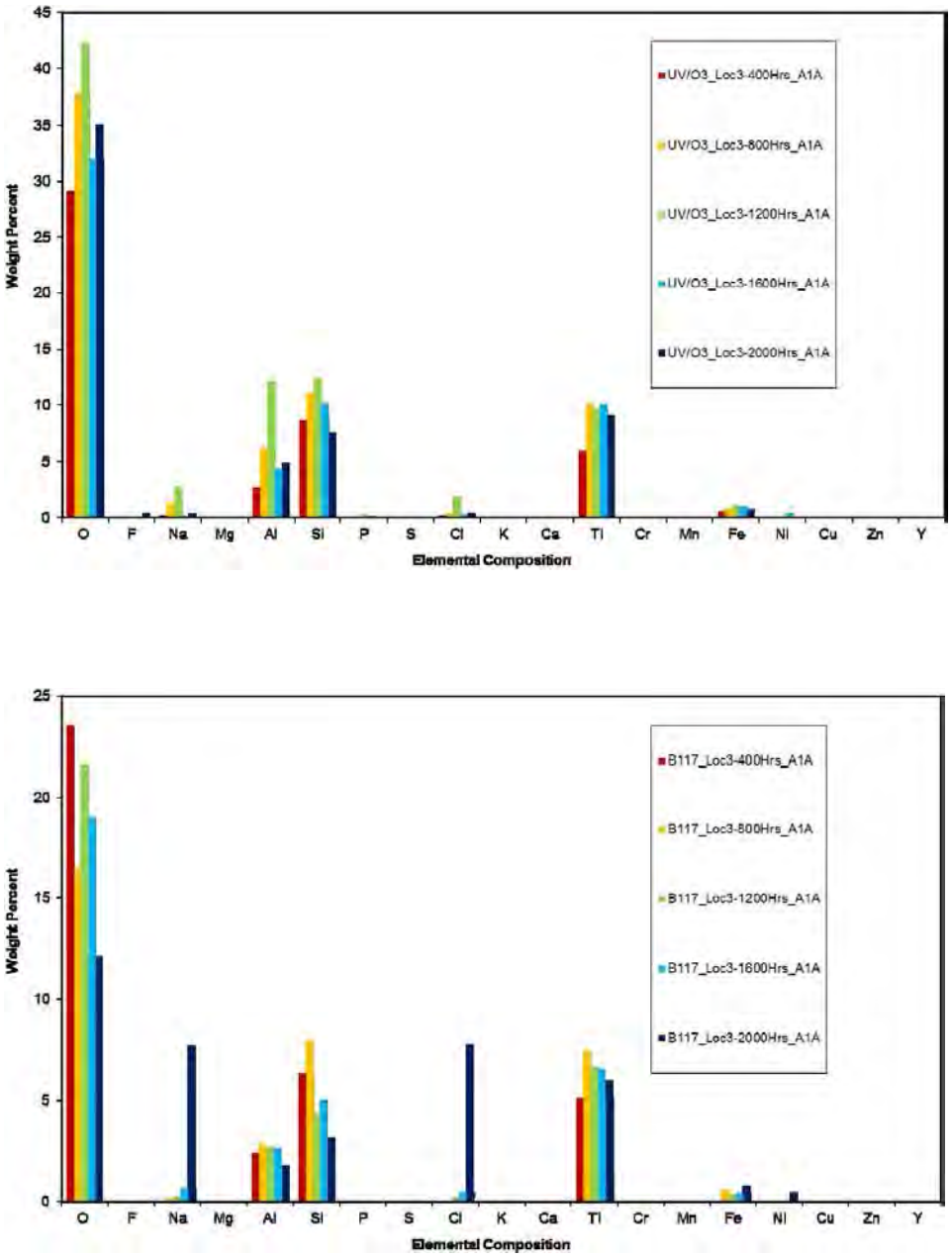

Figure 62. EDS analysis of magnesium rich coating system (location 3) exposure panels from (top) modified UV/ozone chamber and (bottom) B117 chamber.

Distribution Statement A. Approved for public release.

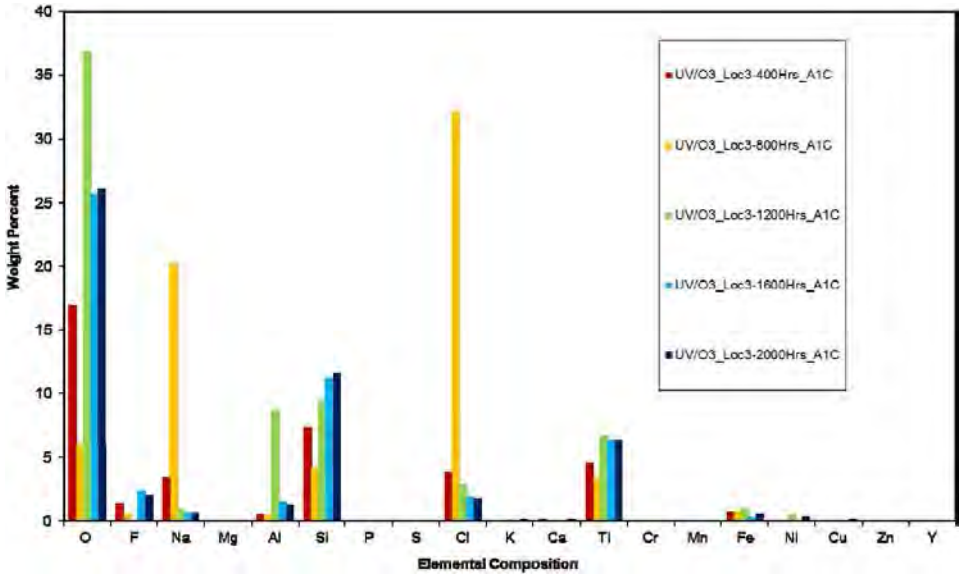

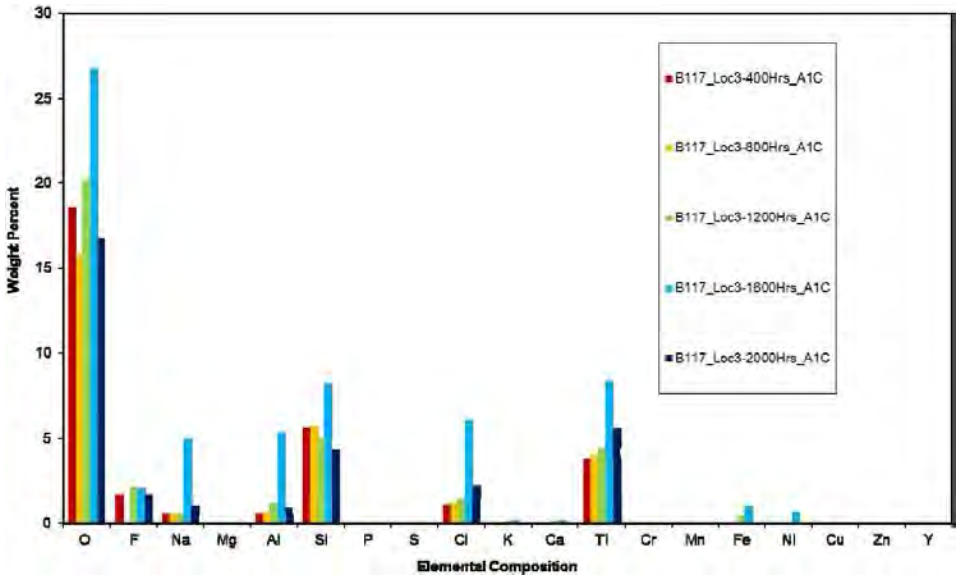

(b)

Figure 63. EDS analysis of rare earth conversion coating system (location 3) exposure panels from (top) modified UV/ozone chamber and (bottom) B117 chamber.

Figure 8: Compositional analysis of RECC coated test panels

FT-IR analysis of Coating Systems Exposed in Chambers and Field Sites: Analysis of the magnesium rich and full chromate coating system samples from the Pt. Judith and the West Coast ship field exposure sites (2 years), the B117 test chamber (2000 hours), modified chamber (2000 hours) and the baseline coating system panels were done by FT-IR ATR on multiple locations for each panel, with the location sites approximately where locations 3 and 4 were used for the SEM-EDS analyses (Figure 45). A summary of the identified peak assignments for the

Distribution Statement A. Approved for public release.

baseline coating systems is presented in Table XII. Plots of the FT-IR attenuated total reflectance for each coating system and overlays for the exposures at the field sites and chambers are presented in Figures 64 – 67. The % reflectance (or transmittance) is the opposite of absorbance for the energy bands.

The topcoats for these coating systems can be composed of urethanes, esters, acrylates, ethers, hydroxyls, aromatics and fluoropolymers. When comparing the spectra for the UV/ozone chamber and field exposure samples to the baseline data for the Aerodur 5000 topcoat in the magnesium rich coating system, it can be seen that a decrease in the % reflectance peaks at 2933 and 2858 indicate breakdown of primary or secondary amines present from polyurea; diminution of the 1728 and 1682 peaks have occurred (C=O stretching vibration), indicating that polyurea and polyurethane groups have degraded. A decrease in peaks 1462 and 1239 indicate reduction of C-H and C-O stretching due to chain scission; this peak can also indicate the possible formation of carbamic acid, which is unstable. The absence of the 1239 peak in the Pt Judith data indicates degradation of urethane due to chain scission, and the decrease in peak 1526, which is indicative of the presence of amides (component of urethane) also suggests the degradation of the urethane component of the topcoat. The change in the FT-IR spectra indicating topcoat degradation on the field and modified chamber exposures is in contrast to the spectra from the samples exposed to the B117 chamber, which looks more like the baseline data: peaks 1728 and 1682 are similar in magnitude for both B117 exposed and the baseline for Aerodur 5000 (carbonyl stretching and amide formation from polyurea); the magnitude of peak 1526 is similar between the B117 exposure and the baseline (for amides, a component of urethane); and peak 1462 is similar in magnitude between the B117 exposure and the baseline for Aerodur 5000 (urethane component, scissor vibration of C-H). Therefore, the FT-IR data indicates that degradation of the topcoat components of the magnesium rich coating system exposed in the modified chamber after 2000 hours was much more like the same coating exposed for 2 years at Pt. Judith and the West Coast ship, whereas the coating exposed to the B117 chamber was much more similar to the baseline sample that had not been exposed.

When considering the IR spectra for the full chromate coating system, there are some slight differences in the spectra, and this presumably be attributed to different formulations between the Aerodur 5000 topcoat (for the Mg rich system) and the Deft 99-GY-001 topcoat: for the baseline spectra the peaks 3618, 3525, 3447, and 1239 are absent, and peak 1728 is present as a shoulder on the adjacent 1682 peak, these being representative of amides and urethane components. In terms of observable differences in the spectra between the exposures and the baseline samples, all major peaks are diminished under the UV/ozone exposure after 2000 hours. In addition, the 2925 and 2855 peaks (primary amines, components of polyurethane) under Pt Judith are diminished with their magnitude between the baseline and 2000 hour UV/ozone exposure. In terms of the B117 exposure, all of the major peaks are larger in magnitude than the baseline or field and UV/ozone chamber exposures except for the 1065 peak, which is indicative of the ester component (C-O stretching) which could indicate the initial breakdown occurring on the samples exposed at Pt. Judith and the West Coast ship. Therefore, the FT-IR data for the full chromate coating system formulation tested in the UV/ozone indicates that it is more aggressive in causing the degradation of the coating system components than the B117 chamber test. This suggests that it may be possible to tailor the chamber exposure conditions to yield coating degradation specific to an exposure site in the field.

Distribution Statement A. Approved for public release.

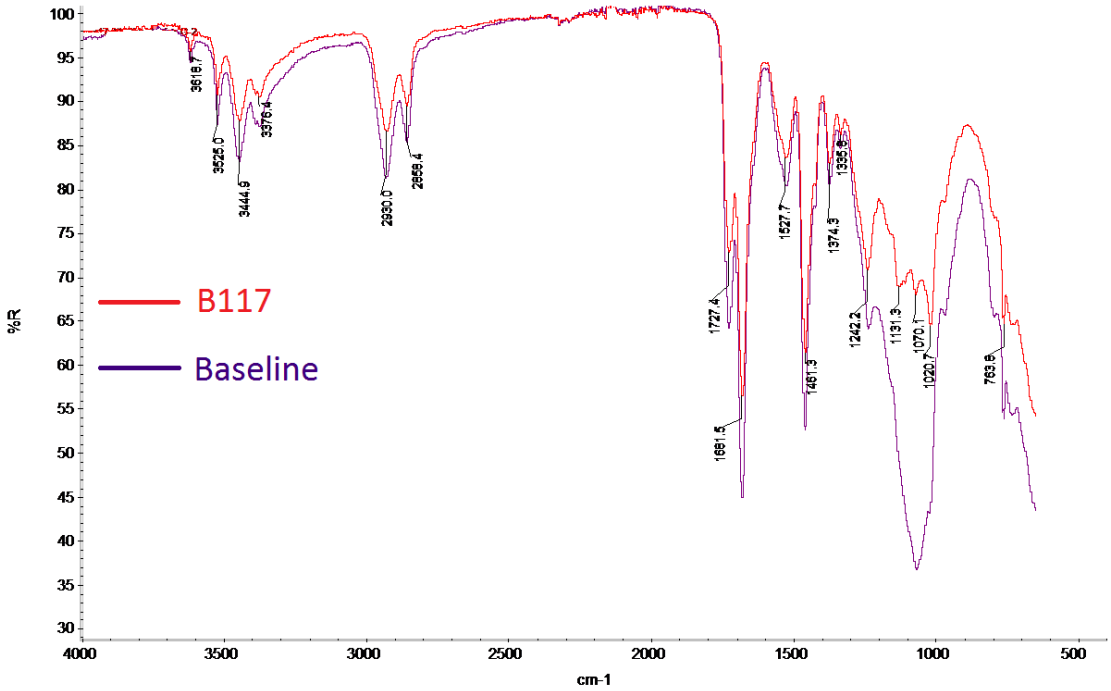

Figure 64. FT-IR ATR % reflectance spectra of the magnesium rich coating system baseline sample and the B117 2000 hour exposure sample. Major absorbance peaks are designated by their wave number.

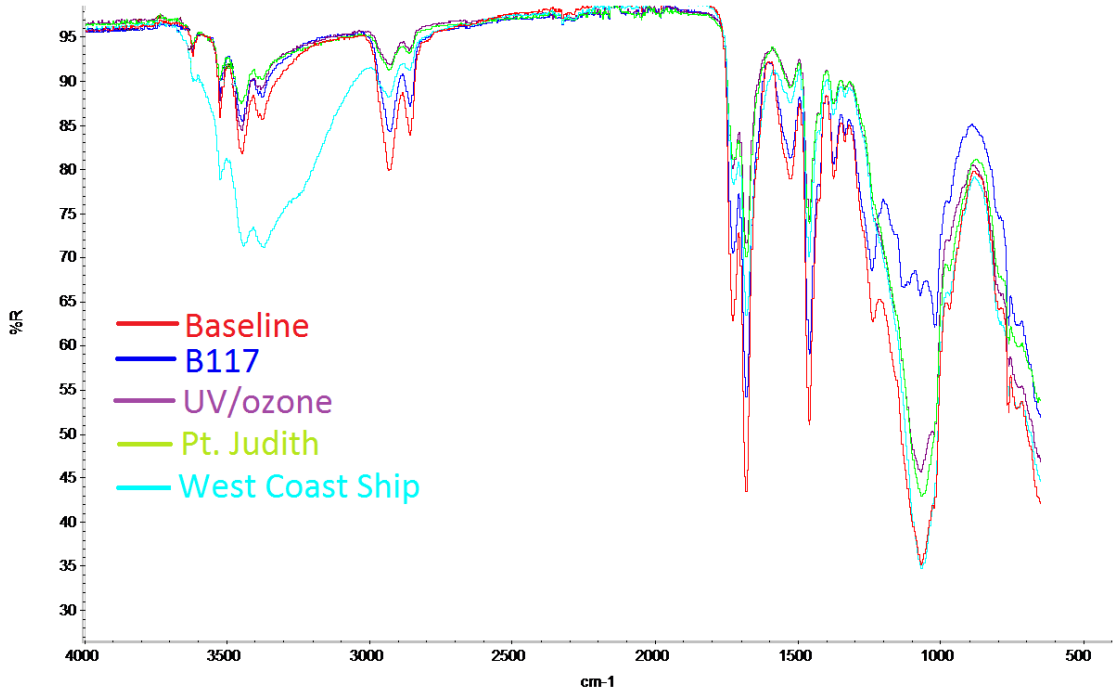

Figure 65. FT-IR ATR % reflectance spectra of the magnesium rich coating system baseline sample and the B117 2000 hour exposure sample, the UV/ozone 2000 hour modified chamber sample, the Pt. Judith and the West Coast ship 2 year exposed sample.

Distribution Statement A. Approved for public release.

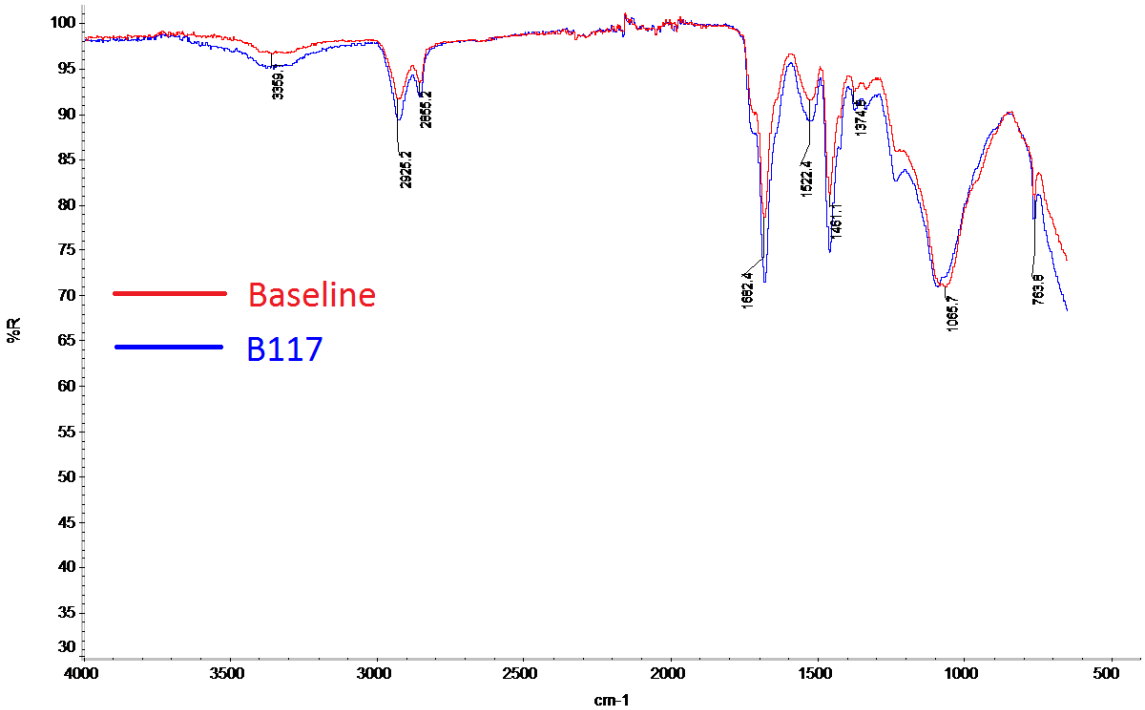

Figure 66. FT-IR ATR % reflectance spectra of the full chromate coating system baseline sample and the B117 2000 hour exposure sample. Major absorbance peaks are designated by their wave number.

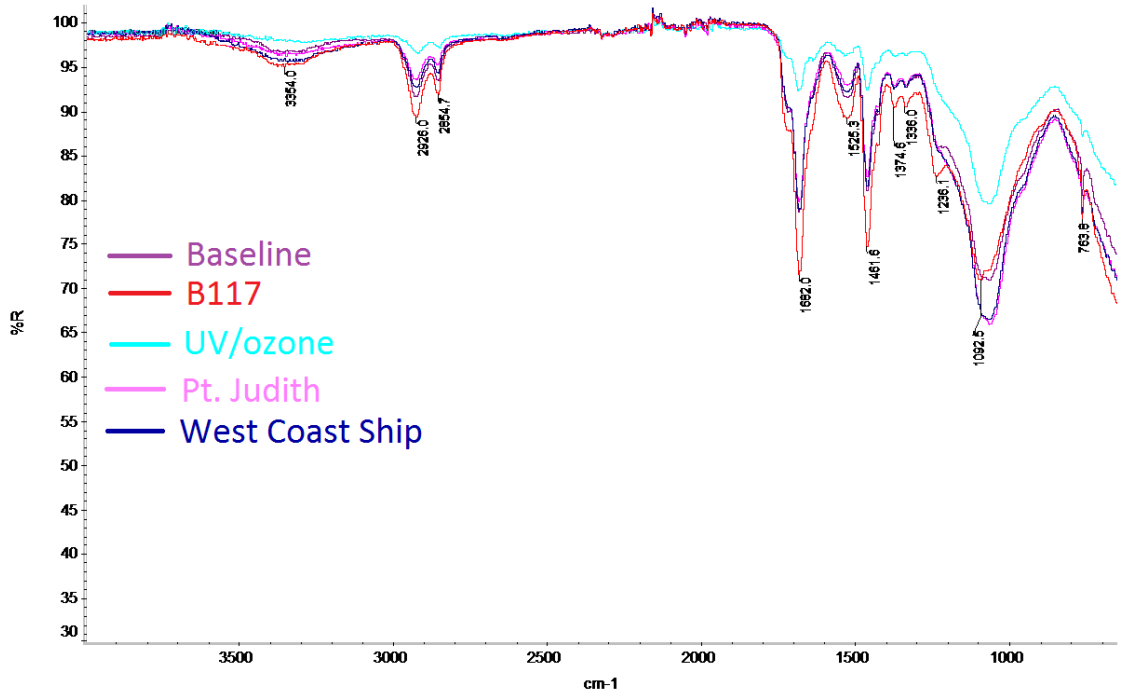

Figure 67. FT-IR ATR % reflectance spectra of the full chromate coating system baseline sample and the B117 2000 hour exposure sample, the UV/ozone 2000 hour modified chamber sample, the Pt. Judith and the West Coast ship 2 year exposed sample.

Distribution Statement A. Approved for public release.

Table XII. Summary of peak assignments for coating systems analyzed from field and chamber exposures.

Coating System							
	Field/Chamber	Peak		Functional Group		Comment	
Mg-Rich	G/A	3618		-OH	free	O-H stretching vibration	
		3525		$CONH_2$	primary amide	assymetric N-H stretching vibration	
		3447		$COONH_2$	urethane	N-H stretching vibration	
		3375		CONH, $COONH_2$	secondary amide, urethane	N-H stretching vibration	
		2933		C-H2		acyclic C-H stretching vibration	
		2858		-OCH3	aliphatic ether	CH3 stretching vibration	
		1728		C=O	carbonyl	stretching	
		1682		R-C=O-N-R2	amides		
		1525		R-C=O-N-R2	amides	N-H deformation and C-N stretching	
		1462		C-H	urethane component	scissor vibration	
		1374		-O-CO-CH3	acetate	C-H symetrical deformation	
		1239		C-O-C, C-O	urethane component	C-O stretching	
		1131		C-O	saturated esters	C-O stretching	
		1070		C-O	esters	C-O stretching	
		763		N-H	primary aliphatic amines	N-H deformations	
Full Cr	A/H			**Functional Group**		**Comment**	
		3618	**absent**	-OH	free		
		3525	**absent**	$CONH_2$	primary amide		
		3447	**absent**	$COONH_2$	urethane		
		3371		CONH, $COONH_2$	amide, urethane	N-H stretching vibration	
		2923		C-H2		acyclic C-H stretching vibration	
		2854		-OCH3	aliphatic ether	CH3 stretching vibration	
		1728	**shoulder**	C=O	carbonyl	stretching	
		1682		R-C=O-N-R2	amides		
		1525		R-C=O-N-R2	amides	N-H deformation and C-N stretching	
		1460		C-H	urethane component	scissor vibration	
		1374		-O-CO-CH3	acetate	C-H symetrical deformation	
		1239	absent	C-O-C, C-O	urethane component		
		1065		C-O	esters	C-O stretching	
		763		N-H	primary aliphatic amines	N-H deformations	

These results, in combination with the EDS data indicate that the coated samples exposed in the modified chamber with the UV and ozone experienced more degradation than those exposed in the B117 chamber, and that different coating formulations will experience different amounts of degradation in the chambers as well.

Distribution Statement A. Approved for public release.

Corrosion Model Calibration and Validation: Figure 68 displays a comparison of mass loss values for AISI 1010 steel that were measured at three calibration sites (Kennedy Space Center, Florida, Rock Island, IL and Fort Drum, NY) to the predicted cumulative mass loss values made using the final proof-of-concept model applied to the calibration data, as described earlier in this report (see discussion on pages 17 -18). Each quarterly data point represents an individual test measurement (x-axis) in relation to its associated prediction (y-axis). The R2 value of 0.9569 indicates a very high degree of fit while the trend line slope of 0.9512 is very close to the optimum value of 1.0. The y-intercept is small in comparison to the maximum value of the data and the individual data points exhibit a low degree of scatter in proximity to the trend line. When taken together, all of these facts indicate that the model accurately predicts corrosion rates for the calibration sites. However, a far better measure of model accuracy is to compare predictions to test measurements at independent validation locations.

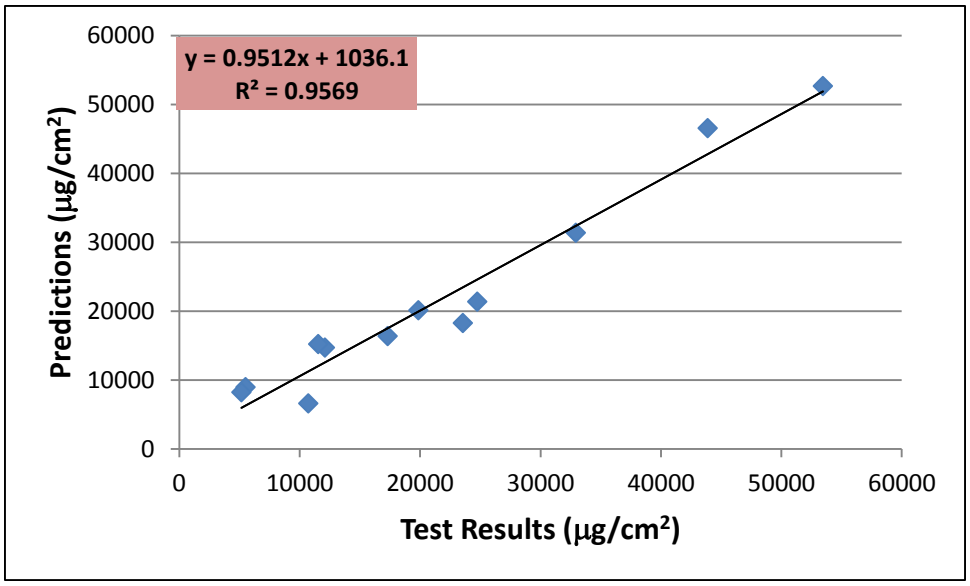

Figure 68. Comparison of Predictions to Test Results (calibration sites)

The hypothesis that formed the basis for the cumulative corrosion damage model described here is that atmospheric corrosion rates of steel vary significantly over short periods of time in response to changes in atmospheric conditions. Furthermore, corrosion rates will fall to zero if the relative humidity level falls to the threshold value of 60%RH (or below) or the temperature falls to the freezing point or below. Such variability in corrosion rates are illustrated by Figure 69, which displays the hourly predictions for a single day of the calibration time period at Kennedy Space Center, Florida.

Distribution Statement A. Approved for public release.

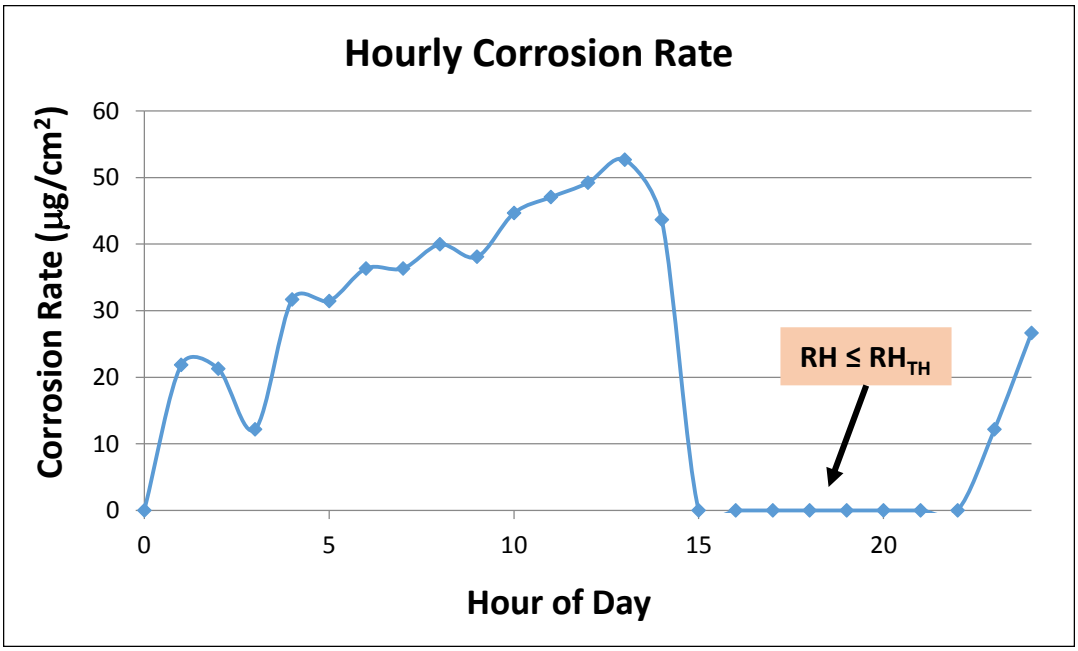

Figure 69. AISI 1010 Steel Hourly Corrosion Rate Predictions for Kennedy Space Center, FL (midnight 12-13-05 to midnight 12-14-05).

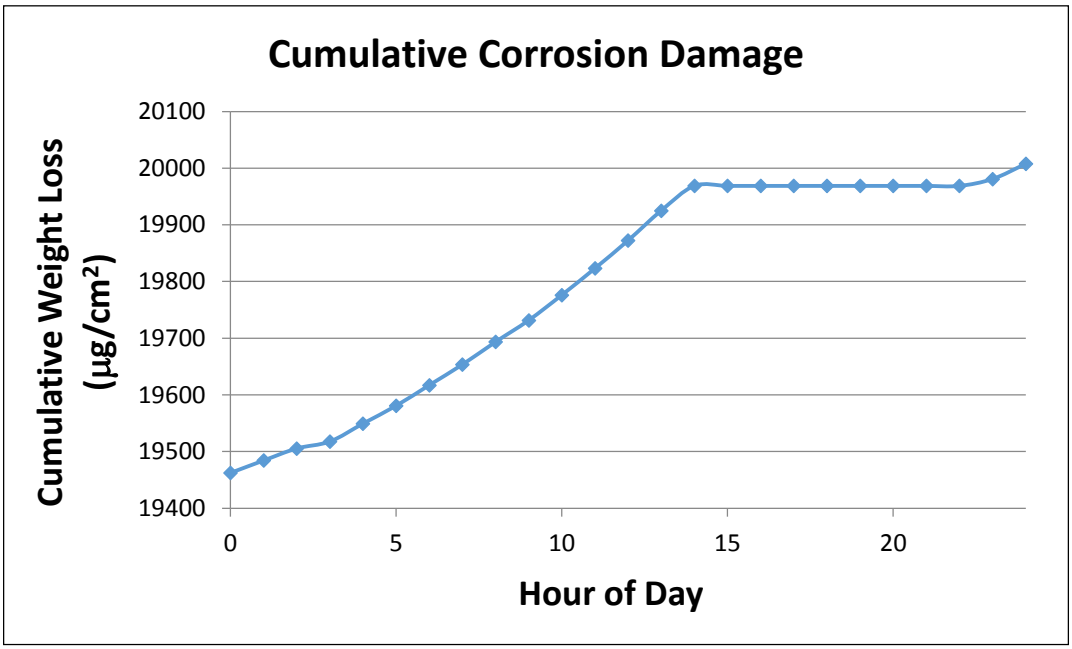

Figure 70. AISI 1010 Steel Cumulative Weight Loss Predictions (midnight 12-13-05 to midnight 12-14-05).

The hourly corrosion rates illustrated by Figure 69 are simply added together in order to calculate cumulative predictions. This process is illustrated by Figure 70, which shows the increase in cumulative weight loss predictions corresponding to the hourly (weight loss) rates shown in Figure 69.

Distribution Statement A. Approved for public release.

Figure 71 illustrates the complete annual cumulative predictions for Kennedy Space Center in comparison to the four quarterly weight loss measurements (test points) used during the calibration process. The arrow shown on the figure corresponds to the approximate time period for the data reported in Figures 69 and 70. As can be seen from this figure, the trend in the predicted cumulative weight loss estimates appears to track closely with the test points used during calibration.

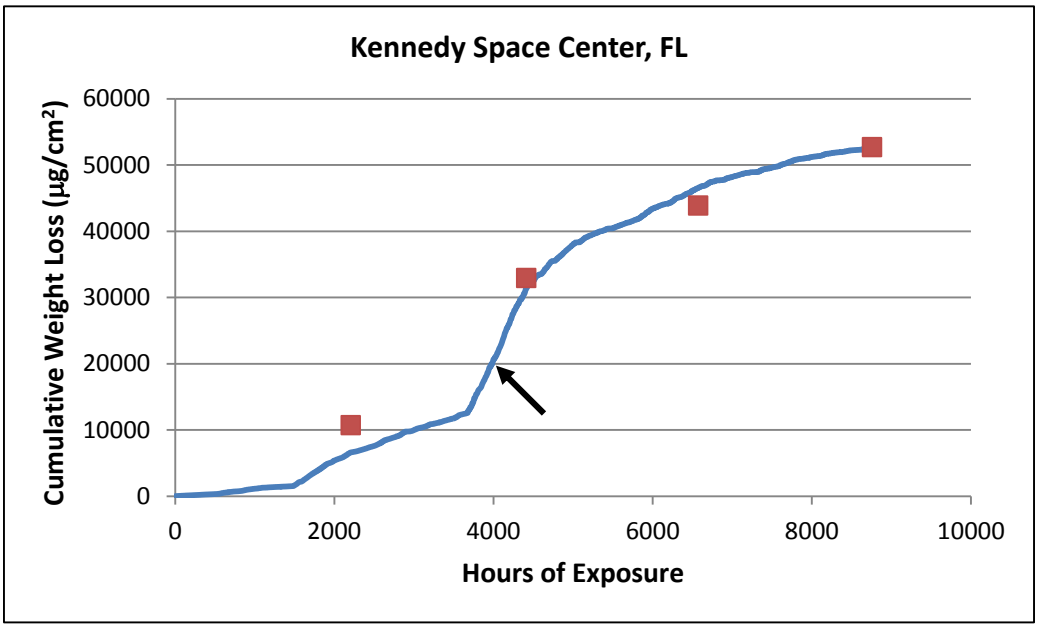

Figure 71. Comparison of AISI 1010 Steel Corrosion Test Points and Associated Predictions (Arrow indicates approximate time period of cumulative predictions illustrated in Figure 12)

Figures 11 and 12 in Appendix A display the annual cumulative predictions for the remaining two calibration sites, which were located at Fort Drum, New York and Rock Island, Illinois. Both of these sites are in cold climate zones, which stand in contrast with the "hot-humid" climate zone at Kennedy Space Center. As seen on these figures, the cumulative predictions for the cold periods of the year for both locations appear to be lower than the corresponding test points used during calibration. One possible reason for this could be due to use of a constant 60% relative humidity threshold (RH_{TH}) rather than a threshold value that varies in response to changing temperature levels. In addition, material thermophysical properties such as the absorptivity and emissivity may play an increased role at low temperatures since they both influence surface temperatures. These two properties are dependent upon surface chemistry/morphology (variable factors due to corrosion product formation), thus it is possible that they could influence higher corrosion rates than expected under low temperature conditions. Additional work may be needed to investigate this issue further.

Table XIII identifies ten different sites initially used to validate candidate models developed under the model development effort described here. As indicated in the table, data for

Distribution Statement A. Approved for public release.

five of these locations was measured under the current SERDP-sponsored program while the remaining data came from past DoD-funded efforts that employed the same test protocols. When developing earlier preliminary models, scatterplots similar to Figure 68 were constructed for the independent validation data pertaining to these sites. It was observed that despite high calibration R^2 values, the resultant validation R^2 values were quite low (~0.28). Visual comparison of the data points with the trend line revealed that data for two SERDP sites, Point Judith, Rhode Island and Daytona Beach, Florida displayed markedly different trends than the others. Both of these sites were located immediately adjacent to coastal surf zones, which are known to experience very high chloride aerosol deposition rates. All candidate models employed chloride deposition data measured no closer than five miles from the coast. As a result, the current modeling approach was not designed to account for locations with very high deposition rates. Thus, Point Judith and Daytona Beach both fall outside of the current calibration parameters and could not be used to validate model accuracy. Another one of the sites shown on the table, Rock Island, IL, was also removed from the validation data set because it became part of the data set used to calibrate the final model. The result was a validation data set pertaining to seven locations with diverse environmental conditions.

Table XIII. Validation Test Sites and Associated Climate Zones

Corrosion Test Site	Climate Zone	Data Source
Kirtland AFB, NM	Mixed Dry	Current SERDP Program
Ft. Hood, TX	Hot – Humid	Past DoD Programs [3]
Tyndall AFB, FL	Hot – Humid	Current SERDP Program
Daytona Beach, FL	Hot – Humid	Current SERDP Program
Ft. Rucker, AL	Hot – Humid	Past DoD Programs [3]
Ft. Campbell, KY	Mixed - Humid	Past DoD Programs [3]
Wright Patterson AFB, OH	Cold	Current SERDP Program
West Jefferson, OH	Cold	Past DoD Programs [3]
Point Judith, RI	Cold	Current SERDP Program
Rock Island Arsenal, IL	Cold	Past DoD Programs [3]

Figure 72 compares quarterly corrosion test results (x-axis) measured at the seven remaining independent sites in comparison to their associated predictions (y-axis). As seen on the figure, the slope of the trend line combined with the R^2 value indicates that the final cumulative corrosion damage model has a high degree of fit to the independent test data measured at multiple locations with diverse environmental conditions. However, the y-intercept value of 2502.7 indicates some inaccuracy and thus represents an opportunity for future efforts to improve model accuracy.

Distribution Statement A. Approved for public release.

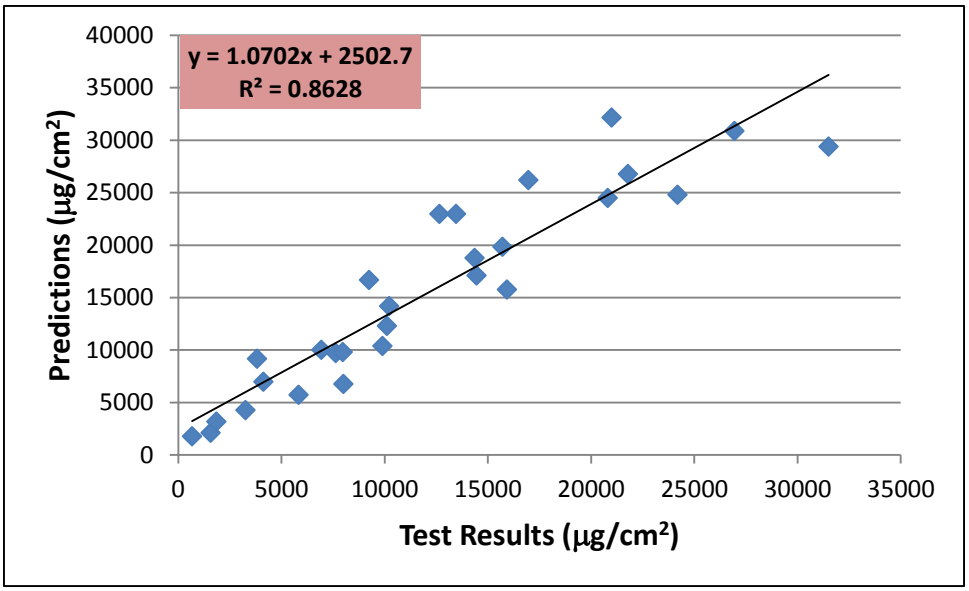

Figure 72. Comparison of Predictions to Test Results (validation sites)

It is obvious that there is more scatter seen on Figure 72 than was seen earlier on Figure 68. There are two likely reasons for this difference. First, the calibration process employed point data, whereby single test measurements were used to represent the corrosion rates (i.e., weight loss per time interval) resulting from the individual coupon exposures at the three calibration locations. Thus, measurement error is not accounted for in these data points. Since the Monte Carlo simulation process employed here is an optimization approach, it results in convergence of the model to the calibration test points with unknown certainty. As a result, the subsequent model will have a lesser degree of fit to independent data than would otherwise be possible had the measurement error been reduced. Calibrating a new model whereby the data used in the process represents the statistical averages of multiple test measurements would reduce the uncertainty and thus provide a more accurate model for all conditions, including those at the validation sites.

The second factor responsible for the increased scatter of the data points seen on Figure 72 has to do with the proxy approach used when calibrating the model and later using it to make predictions. Improved accuracy will result when the environmental characterization data used during the calibration process is measured directly at the associated corrosion test sites. The proxy environmental characterization sites for the corrosion test site at Rock Island, Illinois were quite close but this was not the case for the other two calibration locations. The most accurate model will result when the calibration process employs corrosion test measurements based upon statistical averages of multiple specimens exposed to the same conditions (as discussed previously) combined with environmental characterization data measured directly at the test sites.

Figures 13-19 in Appendix A display the cumulative predictions made by applying independent environmental data for seven validation sites to the final model developed under this effort. Seen on each of these plots are the associated cumulative quarterly weight loss measurements. The validation sites used during this process were located in numerous climate

Distribution Statement A. Approved for public release.

zones. In addition, some of these locations were located near coastal areas where chloride deposition rates were high while others were far inland. In addition, some sites were located in or adjacent to metropolitan areas (significant anthropogenic pollution levels) while others were in more rural areas. The combination of these factors helped ensure that the final model was subjected to data measured under diverse environmental conditions. Specific comments concerning the individual plots are found in the appendix.

Conclusions: As described here, an entirely new approach based upon cumulative damage has been developed to predict atmospheric corrosion rates. The resultant model, which is analogous to random variability fatigue models, shows a high degree of fit to not only the calibration data upon which it is based, but also to data for seven other independent locations with diverse environmental conditions. No past modeling effort found in the literature conducted such independent validation.

Based upon the high R^2 values for both calibration and independent validation data, it is likely that the current model is the most accurate one ever formulated. However, continued refinement is needed to further improve accuracy, reduce the y-intercept value, and enable the model to be applied to high chloride deposition areas adjacent to coastal surf zones. In addition, to be effective for engineering purposes, the methodology needs to be extended to other materials in addition to AISI 1010 steel. If such actions are undertaken, the resultant capabilities would enable the design of new systems and structures specifically constructed to predictably withstand environmental attack in the anticipated operational environments. In addition, such capability could also enable improved sustainment practices such as the prioritization of system/structure maintenance based upon actual environmental exposure.

V. CONCLUSIONS AND IMPLICATIONS FOR FUTURE RESEARCH/IMPLEMENTATION

The project's overall objective was to develop a comprehensive test protocol to accurately predict all aspects of the performance lifetime of DoD coatings. The resultant test protocol was to be independent of substrate composition and accurately rank the performance of any coating system equivalent to the results obtained by long duration outdoor/field exposure. The test protocol would either be specific to a particular service environment or would be dynamically tunable to match the particular service environment in which the coating would be intended to be used. The test protocol would also provide accurate results for particular material configurations, such as fasteners, lap joints, etc. which can create concentration cells and galvanic couples. The test method would allow a reasonable prediction of performance lifetime based upon a relatively short timeframe accelerated test. It was realized early on in the project that the overall objective was a much larger challenge than was originally anticipated. However, several milestones and accomplishments were made under this effort that set the stage for further development and better understanding of how metal substrates corrode and are affected by different weather parameters, all of which are critical in attaining the overall objective of developing a comprehensive accelerated test protocol for coating systems. These accomplishments and milestones are listed and elaborated on in the following discussion, with specific achievements in italics for emphasis.

Distribution Statement A. Approved for public release.

1. **Systematic and Comprehensive Evaluation of Field Exposed Bare Metal and Coated Substrates**

The complete and systematic evaluation of the surface chemistry and surface morphology of bare and coated samples from six different geographic land-based locations and two ocean going vessels has been performed. For the bare metal samples, the nominal elemental composition of the corroded surfaces indicates that differences were observed based upon location, and correlated with the amount of weight loss that occurred. There were elements determined to be present that were of environmental origin, and it is not well known at this time what role they may play in the corrosion behavior of the metal coupons themselves.

2. **Measurement and Correlation of Environmental Data at Land Based Field Exposure Sites with Environmental Protection Agency (EPA) Monitoring Sites**

It was established that there was good agreement between the environmental data as measured at available nearby EPA sites and the weather monitoring systems deployed at field exposure sites, indicating that the reliability of the data measured by the deployed weather monitoring systems had high quality. *The cumulative frequencies of the four weathering parameters (UV, ozone, temperature and RH) measured were determined for the exposure sites.*

3. **Correlation of Ultraviolet Radiation and Ozone Levels in the Field to Corrosion Behavior of Bare and Coated Exposure Samples**

No clear correlation seems to be present between increased corrosion behavior (high mass loss) of the aluminum alloy or steel coupons and locations where there were higher ozone levels (eg. the East Coast ship and Pt. Judith exposure sites). In fact, these locations resulted in intermediate levels of mass loss, being lower than the Daytona Beach exposure site, which had a lower ozone level relative to the other sites. A similar lack of correlation of high mass loss with high UV and ozone levels is evident for the samples analyzed. *However, consideration should be given to the effect of the combination of temperature and RH with the relative levels of UV and ozone. This is precisely what has been done in the corrosion model development that is described in #5 below.*

For the coated and lap joint samples, the most aggressive field exposure sites were determined to be Pt. Judith and the West Coast Ship locations. This was the case, even though these two sites had markedly different average annual values for UV and ozone levels, but very similar temperature and %relative humidity average values. *These results suggest that it may not be the annual average value that is important, but rather the cumulative amount of time that a coated sample may be exposed to a certain environmental parameter or combination of parameters. See #5 below.*

4. **Modification of a Salt Fog Exposure Chamber to Include UV Radiation and Ozone to Accelerate Corrosion of Bare and Coated Metal Substrates**

A standard salt fog chamber was successfully modified to incorporate UV-A radiation with ozone gas to reproducibly stable levels. The chamber conditions used for this study were divided into 4 settings, to determine what effect, if any, the synergistic combination of UV and ozone in a salt spray environment would have on the corrosion rate of bare and coated metal

Distribution Statement A. Approved for public release.

substrates. It was determined that "high" levels of ozone (800 ppb) in combination with a UV-A irradiance level of .86 W/m^2 resulted in a significant increase in the corrosion rate (i.e. mass loss) of the three aluminum alloys and pure copper, whereas it was determined that UV irradiance does not play as significant a role in the formation of AgCl films on pure silver as does the level of ozone. Elevated levels of UV and ozone actually result in a lower corrosion rate for 1010 steel than the low UV/low ozone levels. It was shown that of the three aluminum alloys, AA2024-T3 exhibited the greatest corrosion rate when subjected to the high UV/high ozone conditions. *This apparent sensitivity of AA2024-T3 to elevated UV/ozone levels may be correlated to the observed increase in corrosion rate that the high UV/high ozone condition had on pure copper, since AA2024-T3 alloy has the highest weight percent of copper in its composition of the three aluminum alloys.*

For the coated samples, it was found that even short exposures to "high" UV and ozone levels resulted in an accelerated corrosion phenomenon in the scribe and that was more severe than similar exposure time in the B117 test chamber, or after 2 years of exposure at the most aggressive sites in the field. Degradation of the coating system topcoat was also evident in the FT-IR analysis performed on two coatings exposed in the field as well as in the modified UV/ozone and B117 chambers. Degradation of the components of the high performance polyurethane coatings exposed in the UV/ozone chamber were more pronounced than when exposed in the B117 chamber; the degradation of the Mg-rich coating system in the UV/ozone chamber was more like the degradation seen on the same coating system exposed at Pt. Judith and the West Coast ship after 2 years. For the full chromate coating system, the degradation of the coating in the B117 chamber was more like that of the samples from Pt. Judith and the West Coast ship than the UV/ozone chamber. *These differences indicate that depending upon the coating formulation, it is possible to tailor the chamber conditions to yield coating component degradation to replicate field exposures.*

For the pure silver coupons, it was apparent that accelerated formation of AgCl films was possible, with the film formation rate greater in the UV/ozone chamber than in the B117 chamber over time. Correlation of the AgCl film thickness with hours of exposure time in the UV/ozone chamber to similar thicknesses in the field exposures was achieved, *indicating that in principle, the UV/ozone chamber was possible of replicating the parameter required for the formation of the AgCl film thicknesses seen in the field at various exposure sites.*

5. Development of a Synergistic Corrosion Model Utilizing a Cumulative Damage Approach

An entirely new approach based upon cumulative damage has been developed to predict atmospheric corrosion rates. The resultant model, which is analogous to random variability fatigue models, shows a high degree of fit to not only the calibration data upon which it is based, but also to data for seven independent locations with diverse environmental conditions. *Based upon the high R^2 values for both calibration and independent validation data, it is likely that the current model is the most accurate one ever formulated. Further development and calibration/validation utilizing the modified UV/ozone chamber will allow further refinement of the model to potentially increase its R^2 correlation and its application as a predictive tool.*

Distribution Statement A. Approved for public release.

6. Development of a Dynamic Multivariate Accelerated Corrosion Test Protocol

Based upon the results of this study, it was determined that the modified UV/ozone chamber is capable of yielding differences in corrosion rates (i.e. mass loss/unit time) for different metal alloys, and coating degradation results which are different from the standard B117 tests, all at an accelerated rate. *Therefore a protocol outlining the UV and ozone level requirements and sample preparation and analysis procedures has been generated and is presented as a separate document.*

7. Benefits and Implications for Future Research/Technology Transition

This project and other similar efforts have laid the groundwork for research program investments in multiple DoD laboratories (e.g. AFRL, NAVAIR) that are developing and implementing new accelerated test methodologies for management of weapon systems. DoD laboratory activities in accelerated test methodology and other technology development are now coordinated via the science and technology working integrated product team (S&T WIPT) which meet 3 times a year as part of the DoD Corrosion Forum which are sponsored by the Office of Secretary of Defense (OSD) Office of Corrosion Policy and Oversight (CPO). As an example, AFRL is developing a next-generation accelerated corrosion chamber, via a small business innovative research (SBIR) project, and developing test articles that are more representative of aircraft structural components. *The next-generation test chamber will expand the capabilities of the prototype chamber used in this current study and will have additional functionalities such as: mixed gas capability which can mimic atmospheric conditions found in the service environments; improved cyclic temperature and humidity control; and cyclic mechanical loading in addition to UV and ozone conditions. The goal of these coordinated projects is to develop tests that simulate real world environments that will result in failure modes similar to those occurring in service.*

Distribution Statement A. Approved for public release.

Literature Cited

[1] S. Oesch and M. Faller, *Corrosion Science,* vol. 39, pp. 1505-1530, 1997.

[2] N. Tomashov, Theory of Corrosion and Protection of Metals, New York, NY: MacMillan, 1966.

[3] W. Vernon, *Trans. Faraday Society,* vol. 31, pp. 1668-1700, 1935.

[4] A. Corvo and F. Mendoza, *Corrosion Science,* vol. 42, pp. 1123-1147, 2000.

[5] J. Seinfeld, Atmospheric Chemistry and Physics of Air Pollution, New York, NY: J. Wiley and Sons, 1986.

[6] P. Roberge, R. Klassen and P. Haberecht, *Materials and Design,* vol. 23, pp. 321-330, 2002.

[7] R. Bucheit, M. Cunningham, H. Jensen, M. Kendig and M. Martinez, *Corrosion,* vol. 54, pp. 61-72, 1998.

[8] Z. Chen, D. Liang, G. Ma, G. Frankel, H. Allen and R. Kelly, *Corrosion Eng. Sci. and Tech.,* vol. 45, pp. 2169-2180, 2010.

[9] ASTM B117-11, "Standard Practice for Operating Salt Spray (Fog) Apparatus," ASTM International, West Conshohocken, PA, 2009.

[10] Y. Wan, E. Macha and R. Kelly, *Corrosion ,* vol. 68, pp. 1-10, 2012.

[11] D. Liang, H. Allen, G. Frankel, Z. Chen, R. Kelly and M. Martinez, *J. Electrochem. Soc. Vol 157:,* vol. 157, no. 4, pp. C146-C156., 2010.

[12] F. Deflorian, S. Rossi, L. Fedrizzi and C. Zanella, *Progress in Organic Coatings,* vol. 59, pp. 244-250., 2007.

[13] W. Abbott, "A Decade of Corrosion Monitoring in the World's Military Operating Environments: A Summary of Results.," DoD CorrDefense, Columbus, OH, 2008.

[14] D. Liang, H. Allen, G. Frankel, Z. Chen, R. Kelly, Y. Wu and B. Wyslouzil, *J. Electrochem. Soc.,* vol. 157, pp. C146-C156., 2010.

[15] D. Odnevall and C. Leygraf, "The Atmospheric Corrosion of Copper - A Multilanalytical Approach," in *13th International Corrosion Congress*, Melbourne, Australia, 1996.

Distribution Statement A. Approved for public release.

[16] ASTM G1, "Standard Practice for Preparing, Cleaning and Evaluating Corrosion Test Specimens," ASTM International, West Conshohocken, PA, 2011.

[17] ASTM B825, "Standard Test Method for Coulometric Reduction of Surface Films on Metallic Test Samples," ASTM International, West Conshohocken, PA, 2008.

[18] D. Hansen, E. McCafferty, C. Lins and J. Fitzpatrick, *Applied Surface Science,* vol. 84, pp. 85-90, 1995.

[19] D. Rose, "A Cumulative Damage Approach to Modeling Atmospheric Corrosion of Steel." Ph.D. Dissertation, Dayton: University of Dayton, 2014.

[20] NIST/SEMATECH, "e-Handbook of Statistical Methods," National Institute of Standards and Technology, [Online]. Available: http://www.itl.nist.gov/div898/handbook.

[21] W. Abbott, "A Decade of Corrosion Monitoring in the World's Military Operating Environments: A Summary of Results.", Columbus, OH: Battelle Memorial Institute, 2008.

[22] "EPA Air Quality System (AQS) Databaase," [Online]. Available: http://www.epa.gov/ttn/airs/airsaqs/detaildata/downloadaqsdata.htm.

[23] "Natioanl Atmospheric Deposition Program database," [Online]. Available: http://nadp.sws.uiuc.edu/sites/ntnmap.asp.

[24] I. Odnevall and C. Leygraf, *Journal of The Electrochemical Society,* vol. 142, no. 11, pp. 3682-3689., 1995.

[25] L. Nunez, E. Reguera, F. Corzo, E. Gonzalez and C. Vazquez, *Corrosion Science,* vol. 47, pp. 461-484., 2005.

[26] J. Beckner and P. Mozley, "Origin and Spatial Distribution of Early Vadose and Phreatic Clacite Cements in the Zia Formation, Albuquerque Basin, New Mexico, USA.:," in *Carbonate Cementation in Sandstones*, Blackwell Publishing Ltd., 1998, pp. 27-51.

Distribution Statement A. Approved for public release.

Appendix A

Weather Data

Distribution Statement A. Approved for public release.

FIGURES

Page

Figure A- 1. Yearly temperature pattern at Kirtland AFB exposure site. 4

Figure A- 2. Yearly relative humidity pattern at Kirtland AFB exposure site. 5

Figure A- 3. Yearly UV pattern at Kirtland AFB exposure site. 6

Figure A- 4. Yearly UV pattern at Prewitt, NM near Kirtland AFB exposure site. 7

Figure A- 5. Yearly Ozone pattern at Kirtland AFB exposure site. 8

Figure A- 6. Yearly Ozone pattern at local EPA site (Albuquerque, NM) near Kirtland AFB exposure site.. ...9

Figure A- 7. Yearly temperature pattern at Tyndall AFB exposure site. 10

Figure A- 8. Yearly relative humidity pattern at Tyndall AFB exposure site. 11

Figure A- 9. Yearly UV pattern at Tyndall AFB exposure site. 12

Figure A- 10. Yearly Ozone pattern at Tyndall AFB exposure site. 13

Figure A- 11. Yearly Ozone pattern at local EPA site (Panama City, FL) near Tyndall AFB exposure site. 14

Figure A- 12. Yearly temperature pattern at Daytona Beach exposure site. 15

Figure A- 13. Yearly relative humidity pattern at Daytona Beach exposure site. 16

Figure A- 14. Yearly Ozone pattern at local EPA site near Daytona Beach exposure site.. 17

Figure A- 15. Yearly temperature pattern at Pt. Judith exposure site. 18

Figure A- 16. Yearly relative humidity pattern at Pt. Judith exposure site. 19

Figure A- 17. Yearly UV pattern at Pt. Judith exposure site. 20

Figure A- 18 Yearly Ozone pattern at Pt. Judith exposure site. 21

Figure A- 19. Yearly Ozone pattern at local EPA site (Narragansett, RI) near Pt. Judith exposure site. 22

Figure A- 20. Yearly temperature pattern at Wright-Patterson AFB exposure site. 23

Figure A- 21. Yearly relative humidity pattern at Wright-Patterson AFB exposure site. 24

Figure A- 22. Yearly UV pattern at Wright-Patterson AFB exposure site. 25

Figure A- 23. Yearly Ozone pattern at Wright-Patterson AFB exposure site. 26

Figure A- 24. Yearly Ozone pattern at local EPA site (Xenia, OH) near Wright-Patterson AFB exposure site. 27

Figure A - 25. Yearly temperature pattern at East Coast Ship site. 28

Figure A- 26. Yearly relative humidity pattern at East Coast Ship site. 29

Distribution Statement A. Approved for Public Release.

FIGURES (Continued)

Page

Figure A- 27. Yearly UV pattern at East Coast Ship site. 30

Figure A- 28. Yearly Ozone pattern at East Coast Ship site.....31

Figure A- 29. Yearly Ozone pattern at local EPA site near East Coast Ship site.....32

Figure A- 30. Yearly temperature pattern at West Coast Ship site. 33

Figure A- 31. Yearly relative humidity pattern at West Coast Ship site. 34

Figure A- 32. Yearly UV pattern at West Coast Ship site. 35

Figure A- 33. Yearly Ozone pattern at West Coast Ship site.....36

Figure A- 34. Yearly Ozone pattern at local EPA site near West Coast Ship site.....37

Distribution Statement A. Approved for Public Release.

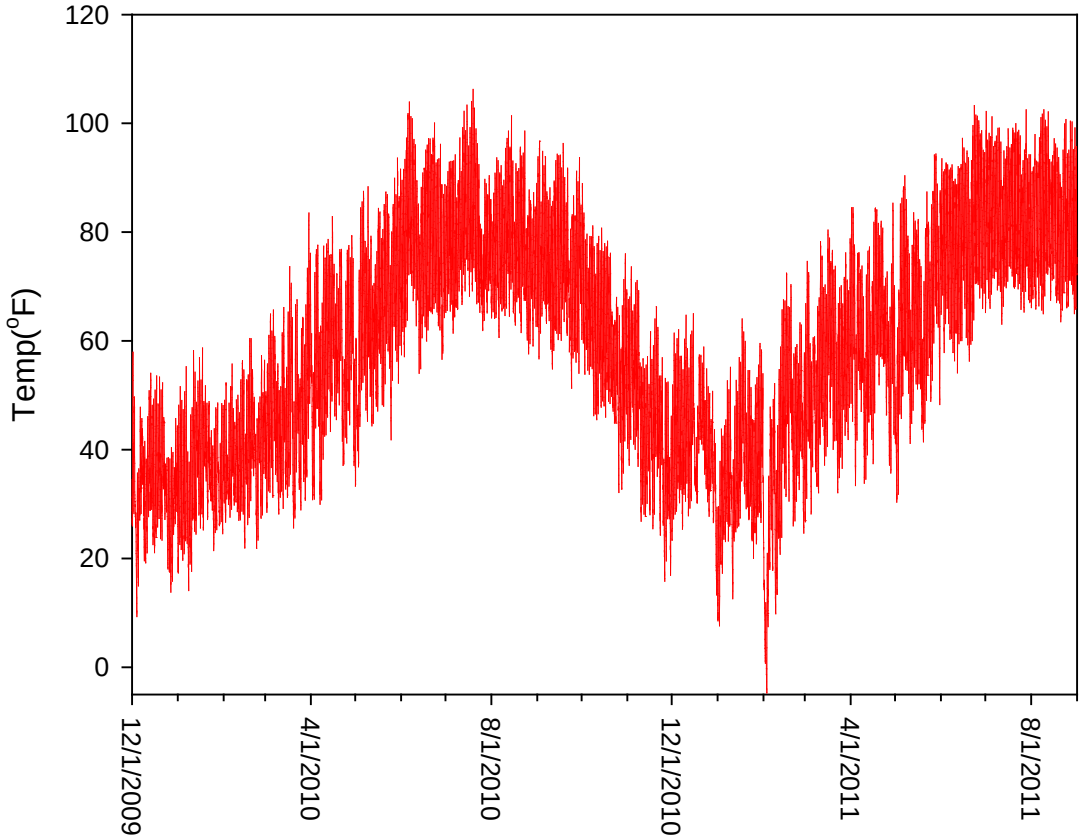

Figure A- 1. Yearly temperature pattern at Kirtland AFB exposure site.

Distribution Statement A. Approved for Public Release.

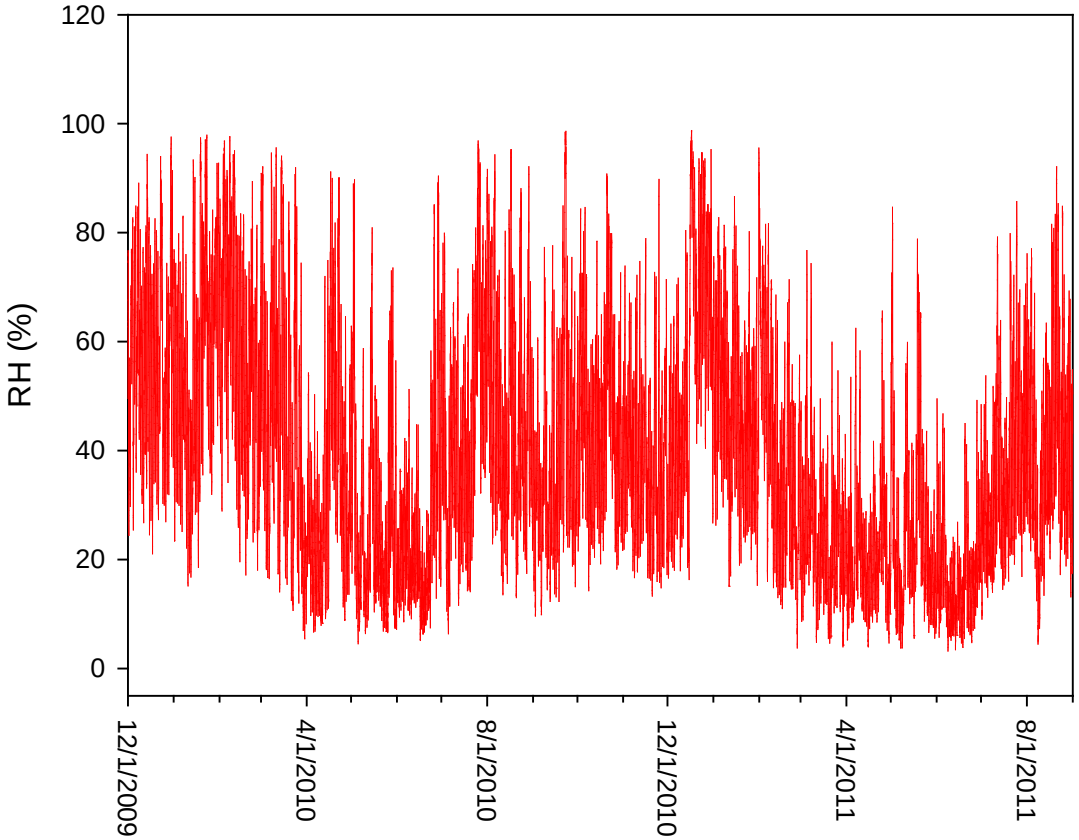

Figure A- 2. Yearly relative humidity pattern at Kirtland AFB exposure site.

Distribution Statement A. Approved for Public Release.

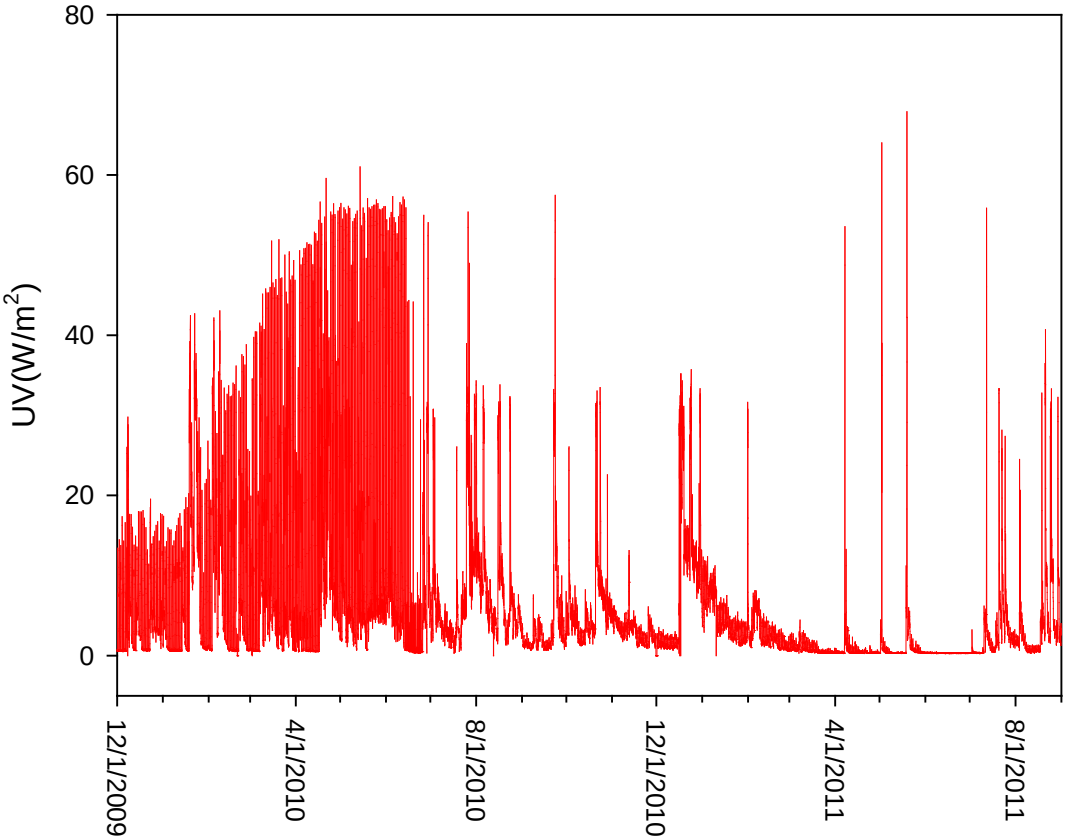

Figure A- 3. Yearly UV pattern at Kirtland AFB exposure site.

Distribution Statement A. Approved for Public Release.

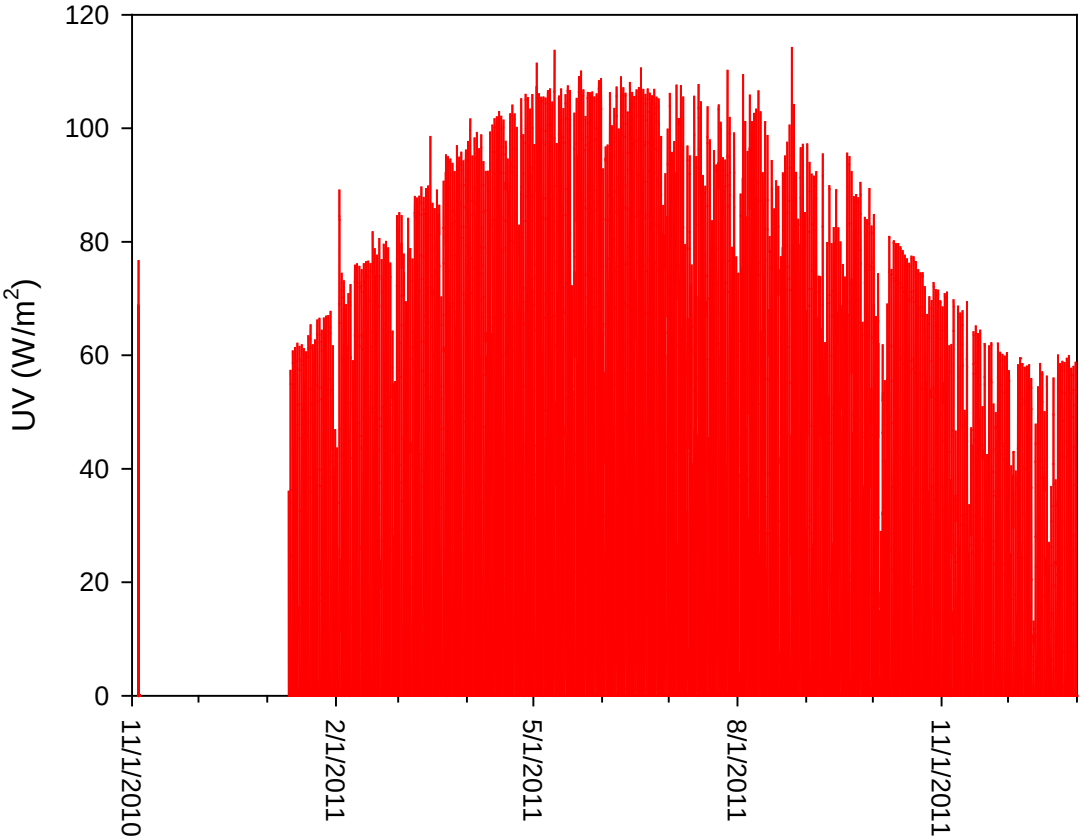

Figure A- 4. Yearly UV pattern at Prewitt, NM near Kirtland AFB exposure site.

Distribution Statement A. Approved for Public Release.

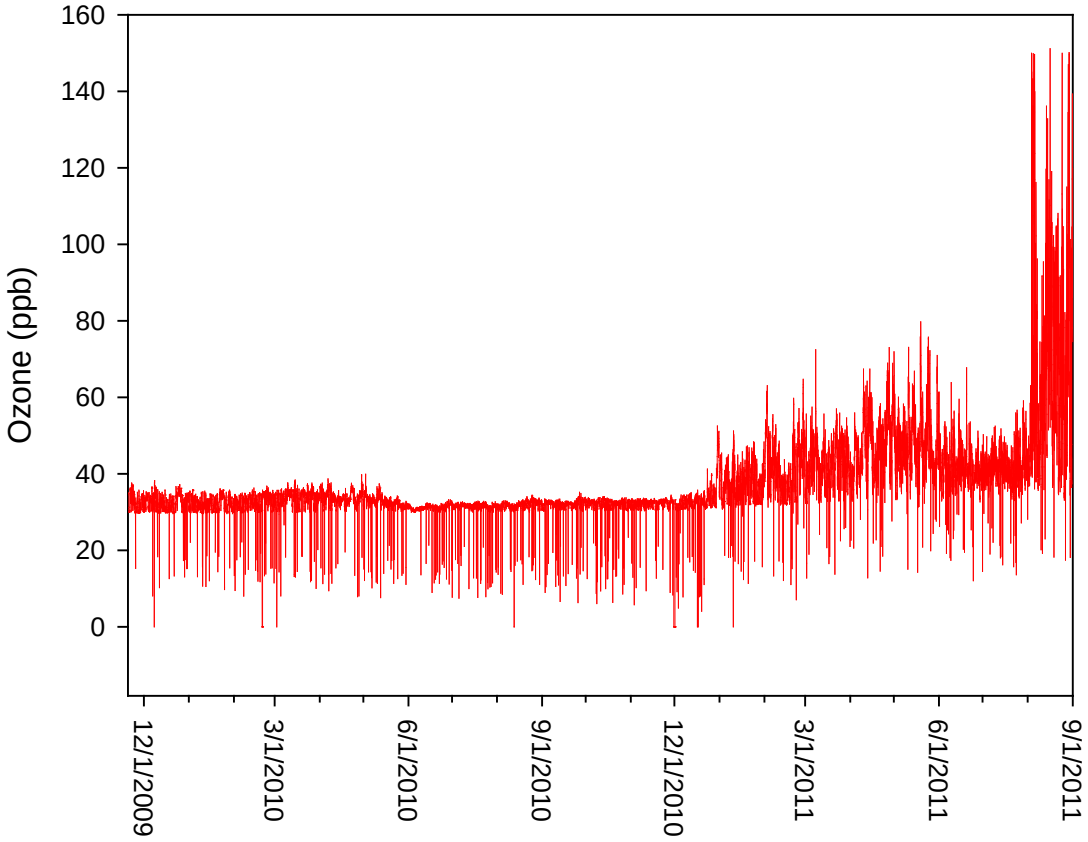

Figure A- 5. Yearly Ozone pattern at Kirtland AFB exposure site.

Distribution Statement A. Approved for Public Release.

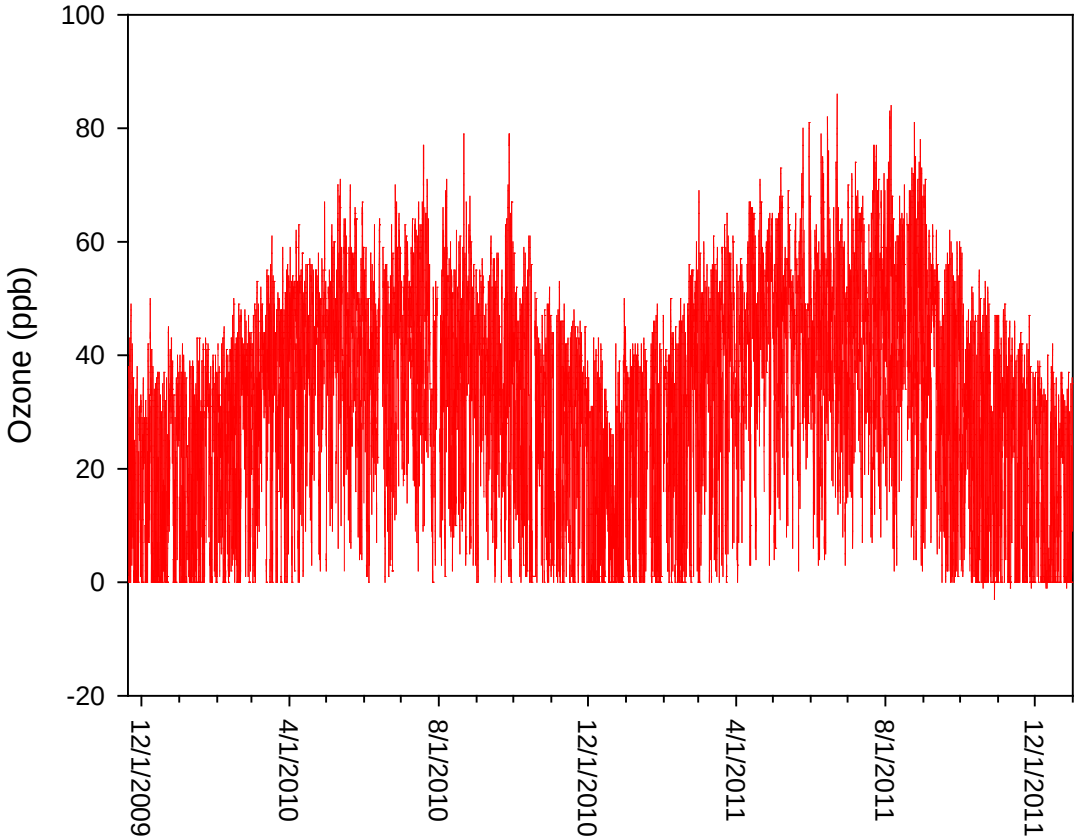

Figure A- 6. Yearly Ozone pattern at local EPA site (Albuquerque, NM) near Kirtland AFB exposure site.

Distribution Statement A. Approved for Public Release.

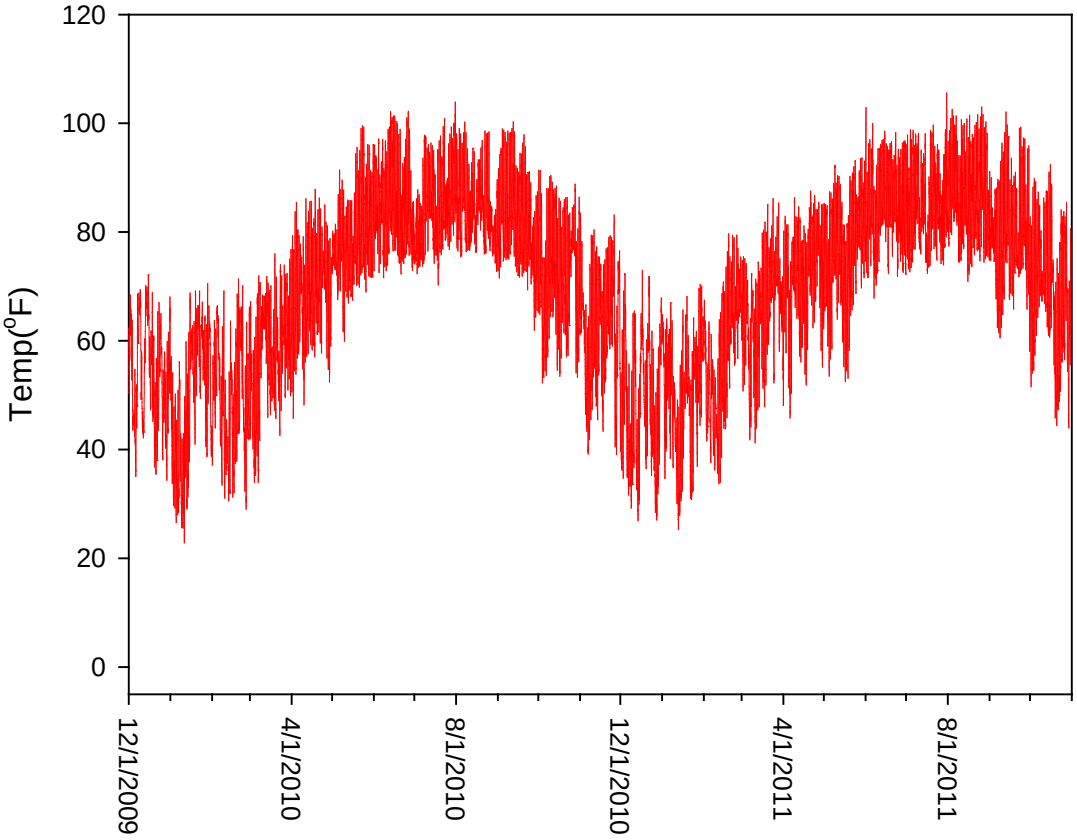

Figure A- 7. Yearly temperature pattern at Tyndall AFB exposure site.

Distribution Statement A. Approved for Public Release.

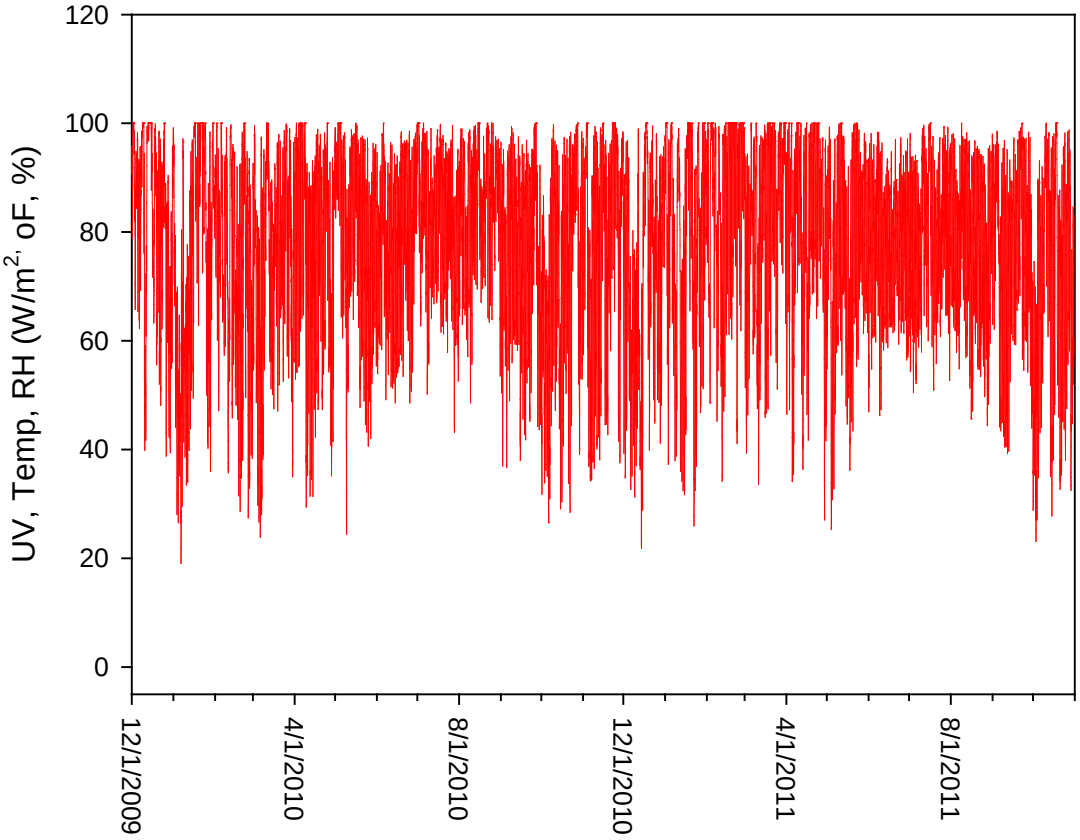

Figure A- 8. Yearly relative humidity pattern at Tyndall AFB exposure site.

Distribution Statement A. Approved for Public Release.

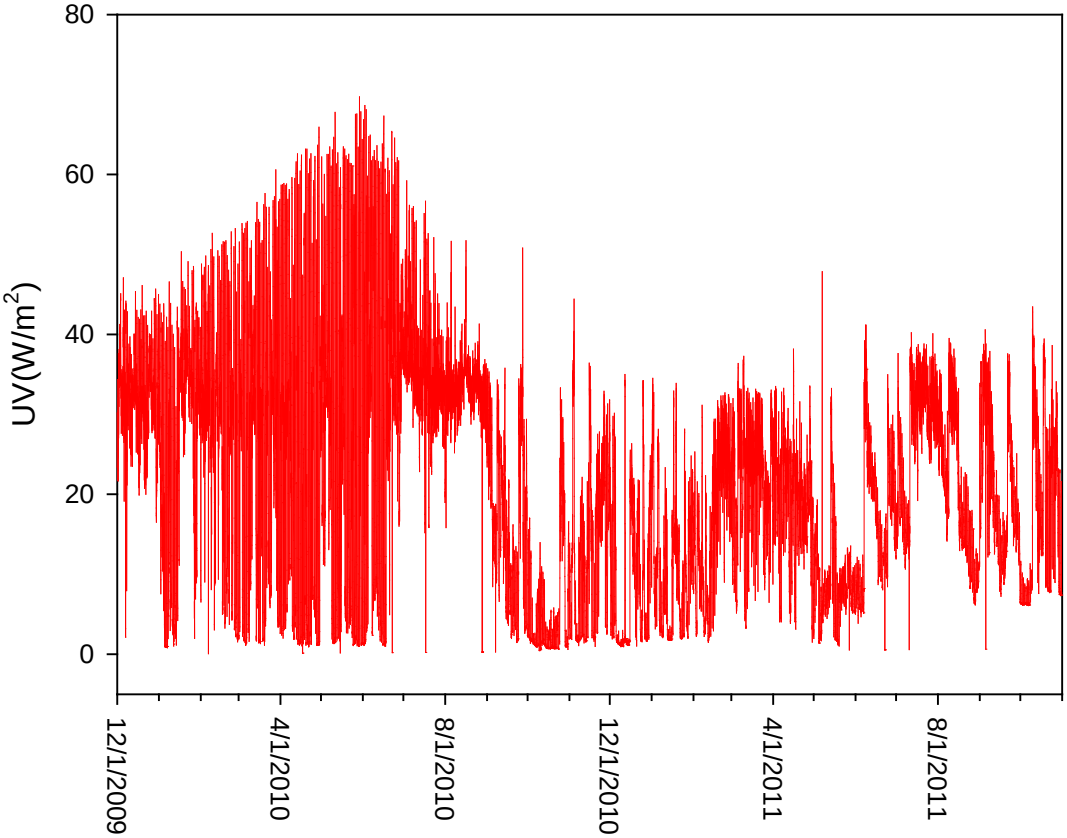

Figure A- 9. Yearly UV pattern at Tyndall AFB exposure site.

Distribution Statement A. Approved for Public Release.

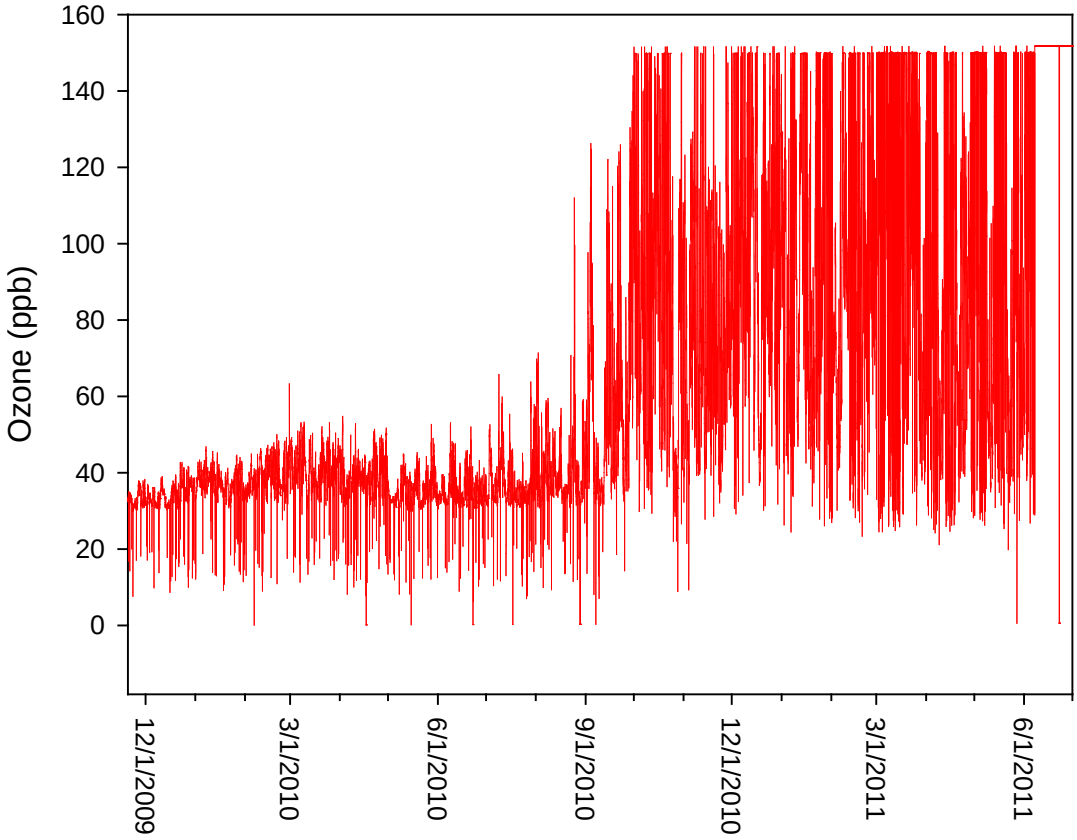

Figure A- 10. Yearly Ozone pattern at Tyndall AFB exposure site.

Distribution Statement A. Approved for Public Release.

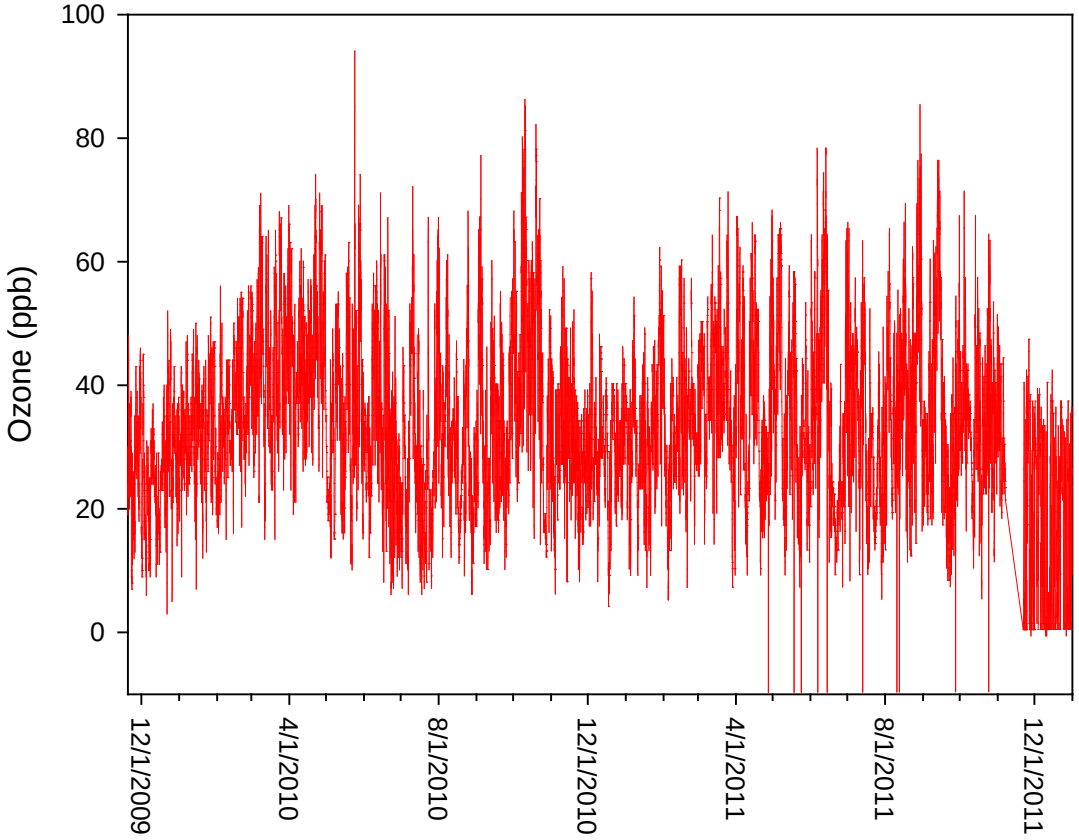

Figure A- 11. Yearly Ozone pattern at local EPA site (Panama City, FL) near Tyndall AFB exposure site.

Distribution Statement A. Approved for Public Release.

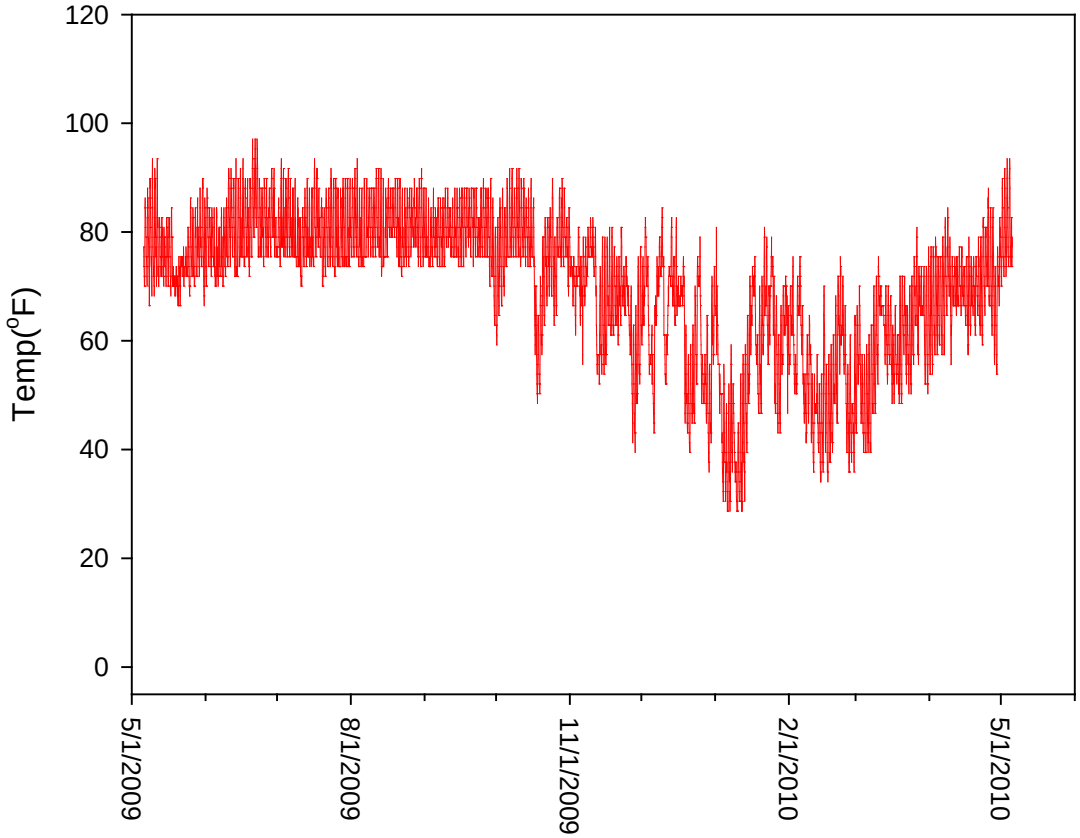

Figure A- 12. Yearly temperature pattern at Daytona Beach exposure site.

Distribution Statement A. Approved for Public Release.

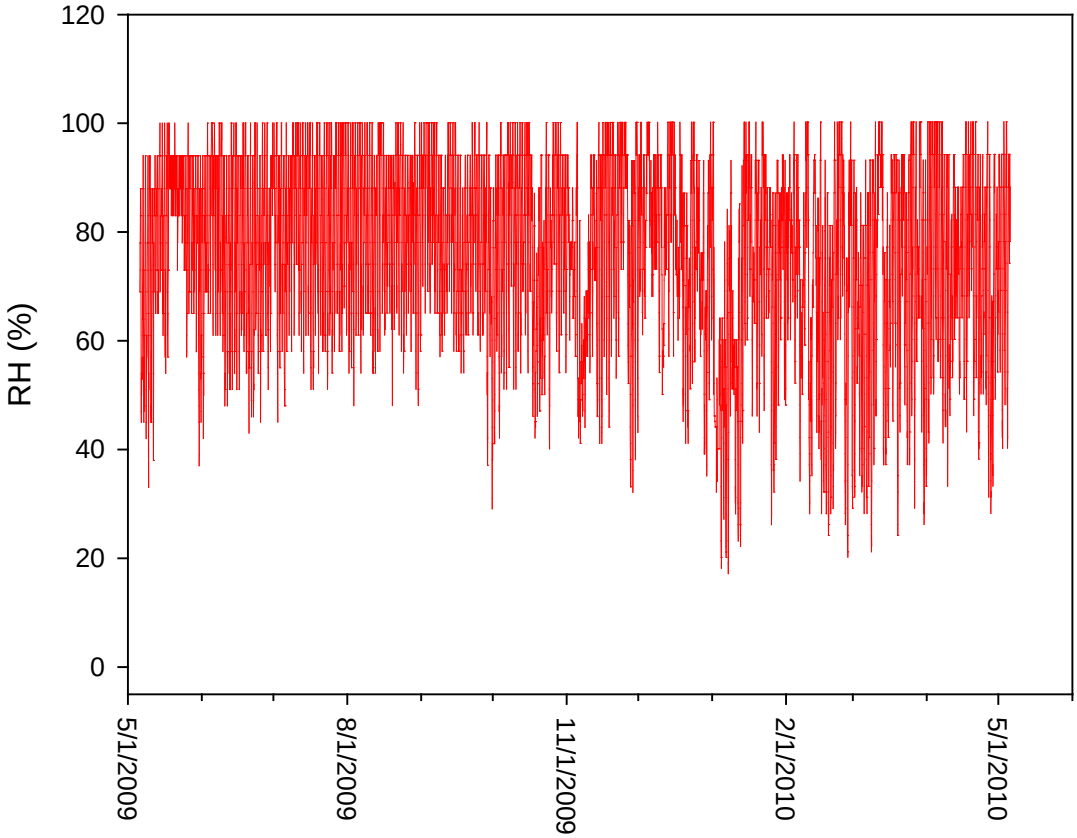

Figure A- 13. Yearly relative humidity pattern at Daytona Beach exposure site.

Distribution Statement A. Approved for Public Release.

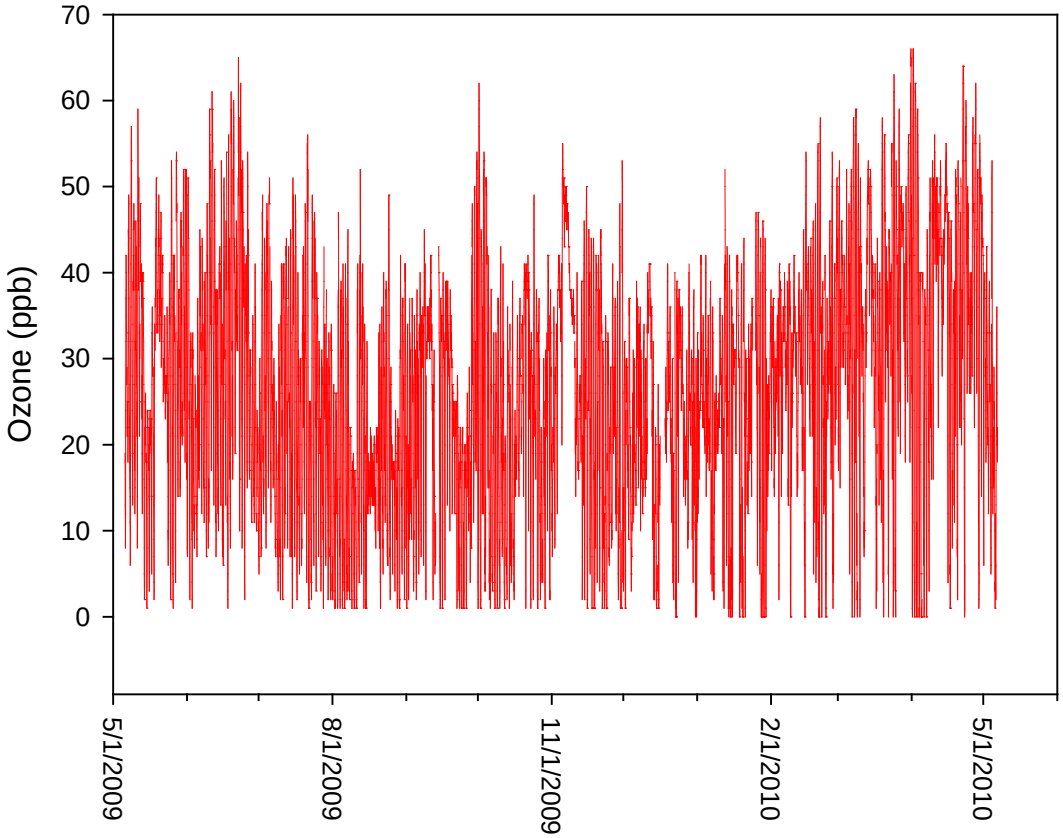

Figure A- 14. Yearly Ozone pattern at local EPA site near Daytona Beach exposure site.

Distribution Statement A. Approved for Public Release.

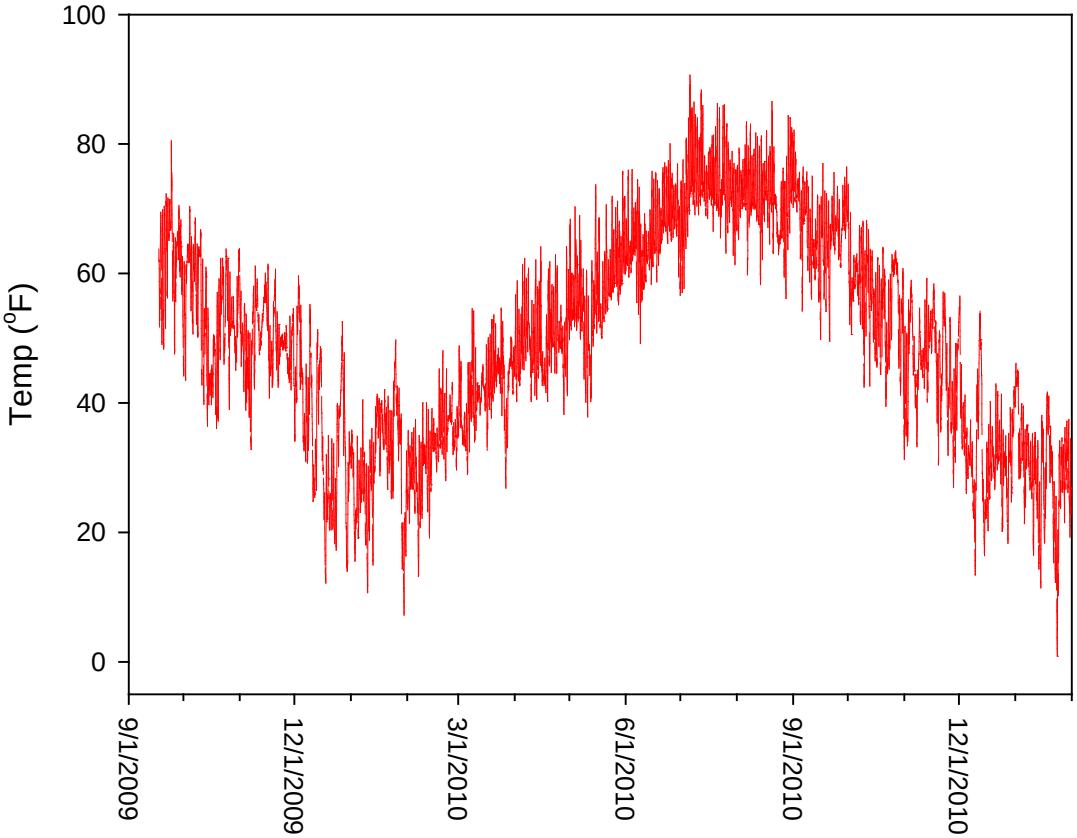

Figure A- 15. Yearly temperature pattern at Pt. Judith exposure site.

Distribution Statement A. Approved for Public Release.

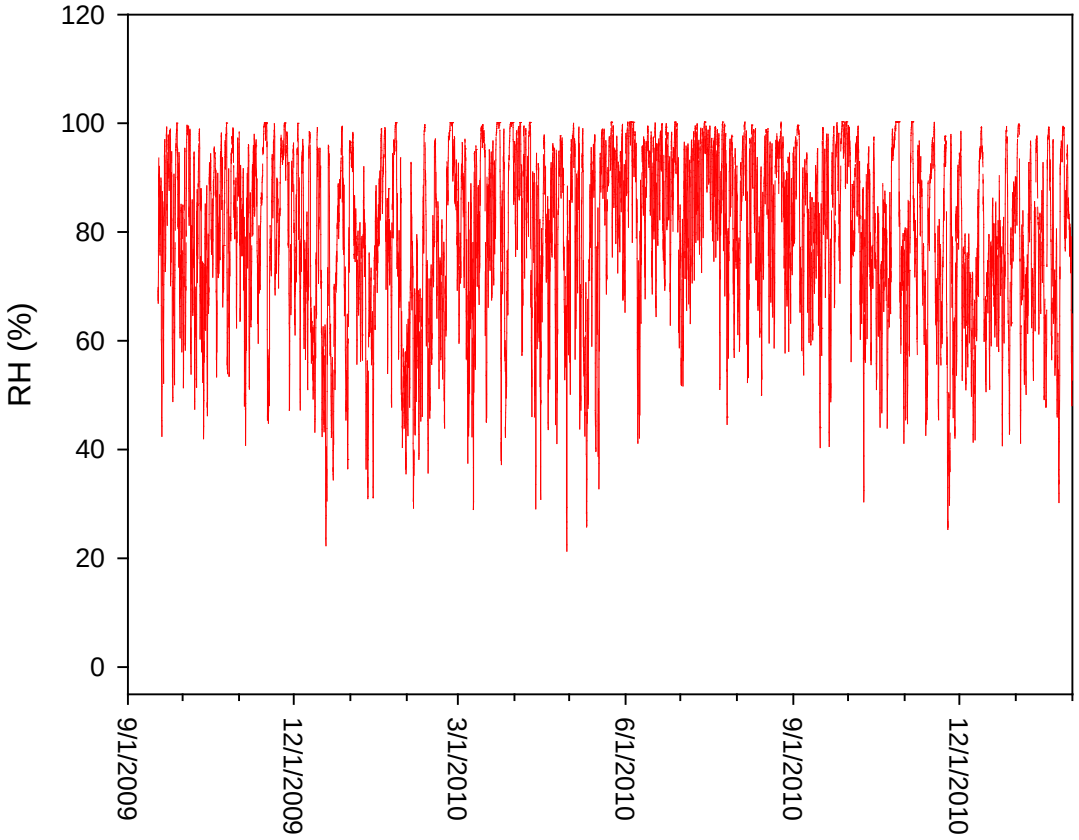

Figure A- 16. Yearly relative humidity pattern at Pt. Judith exposure site.

Distribution Statement A. Approved for Public Release.

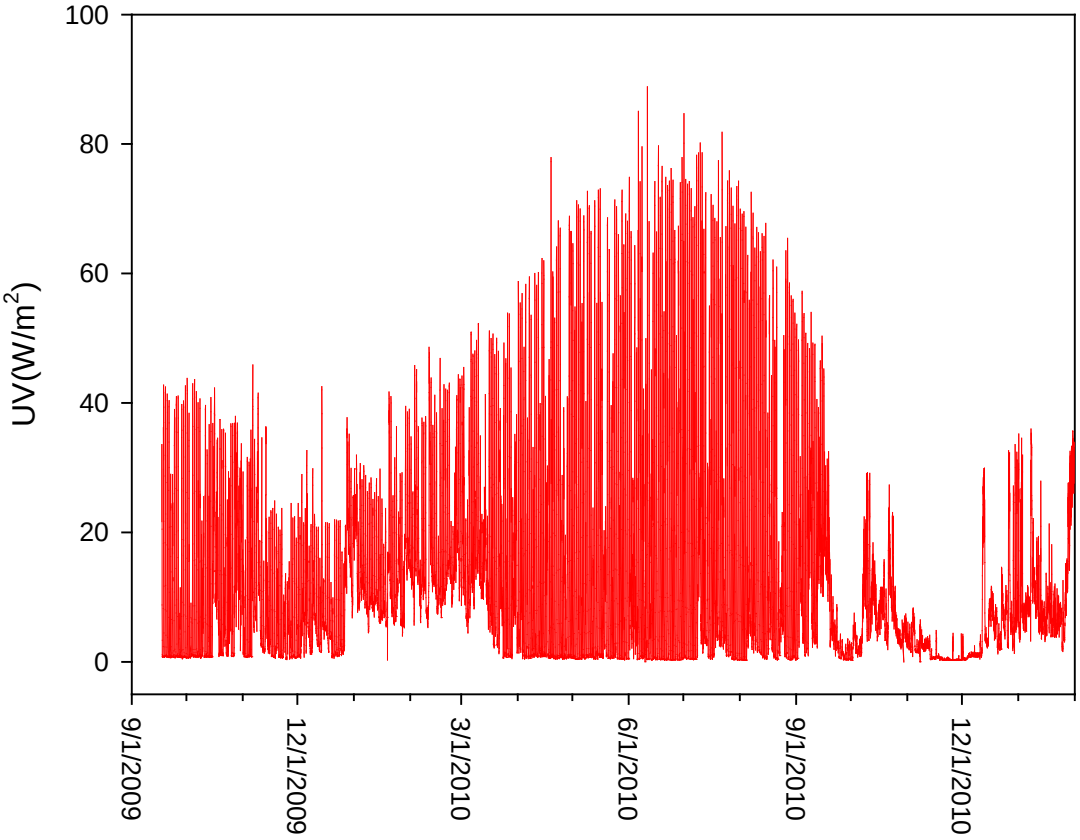

Figure A- 17. Yearly UV pattern at Pt. Judith exposure site.

Distribution Statement A. Approved for Public Release.

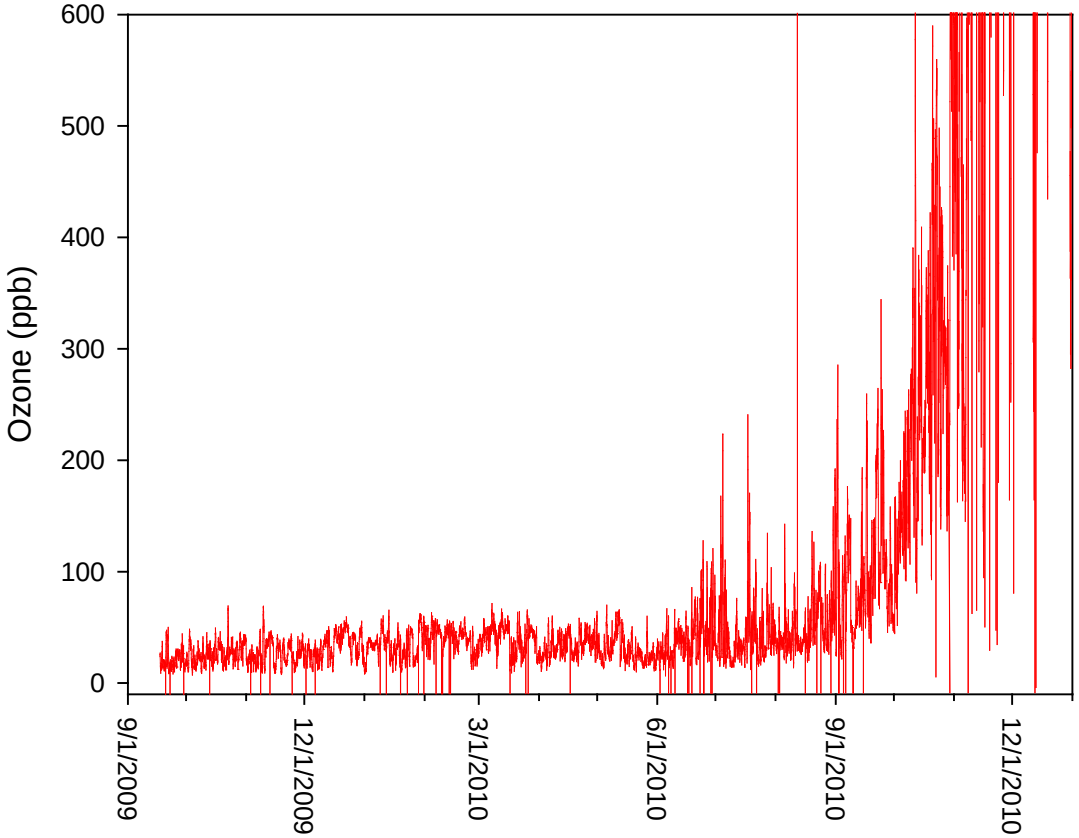

Figure A- 18 Yearly Ozone pattern at Pt. Judith exposure site.

Distribution Statement A. Approved for Public Release.

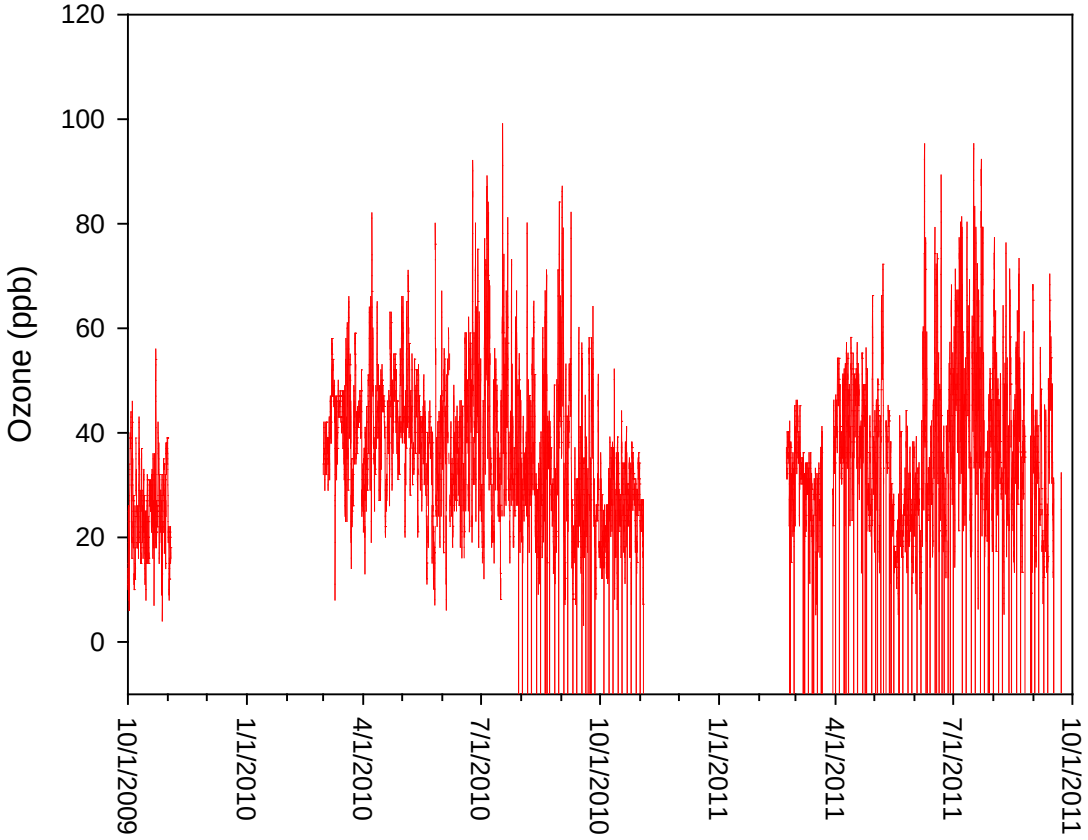

Figure A- 19. Yearly Ozone pattern at local EPA site (Narragansett, RI) near Pt. Judith exposure site.

Distribution Statement A. Approved for Public Release.

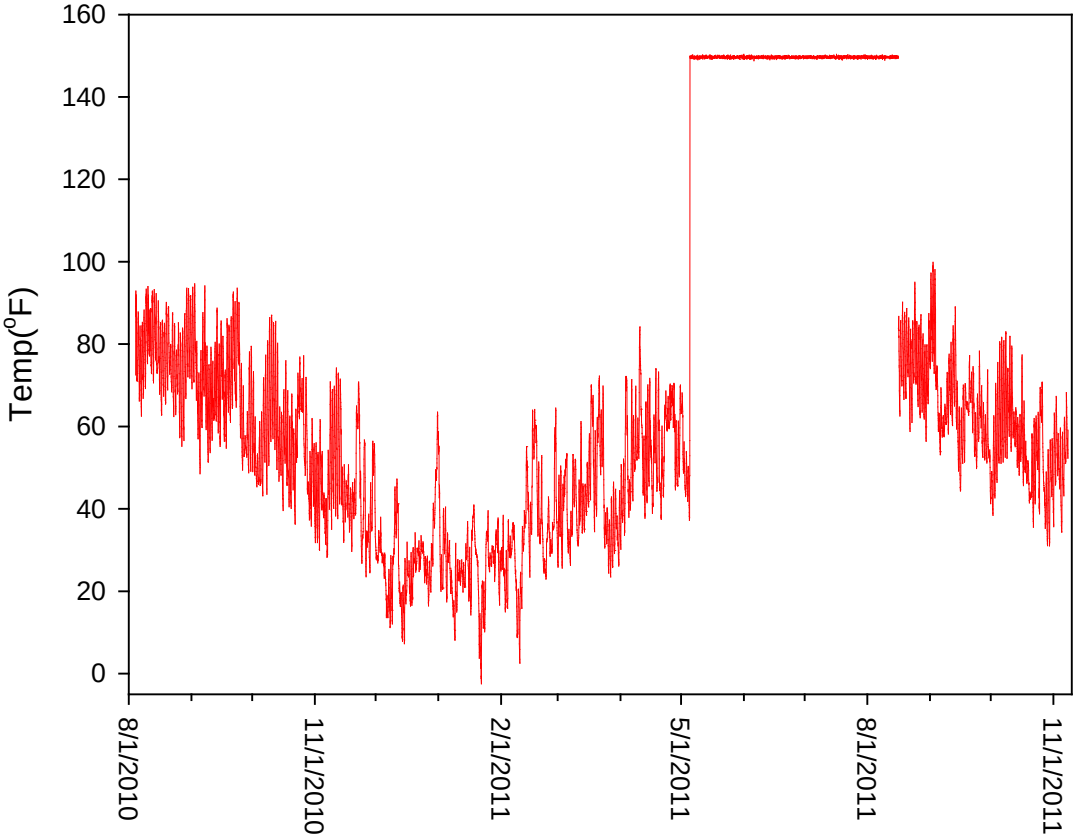

Figure A- 20. Yearly temperature pattern at Wright-Patterson AFB exposure site.

Distribution Statement A. Approved for Public Release.

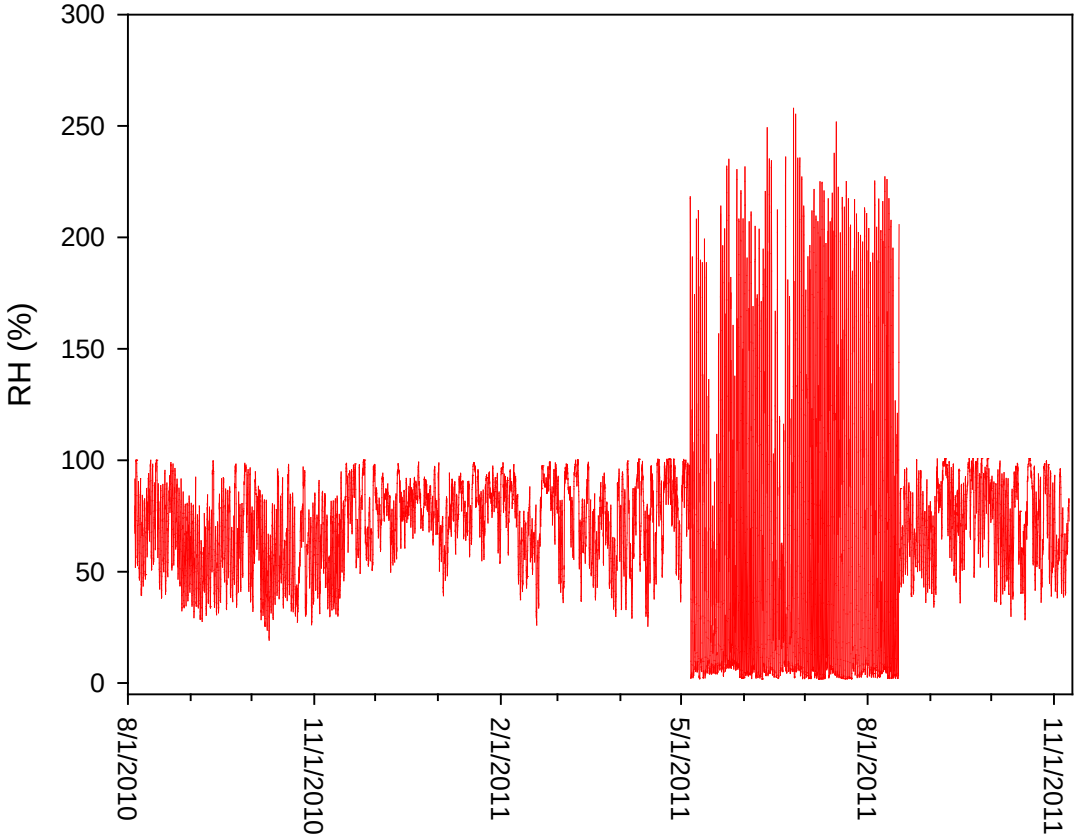

Figure A- 21. Yearly relative humidity pattern at Wright-Patterson AFB exposure site.

Distribution Statement A. Approved for Public Release.

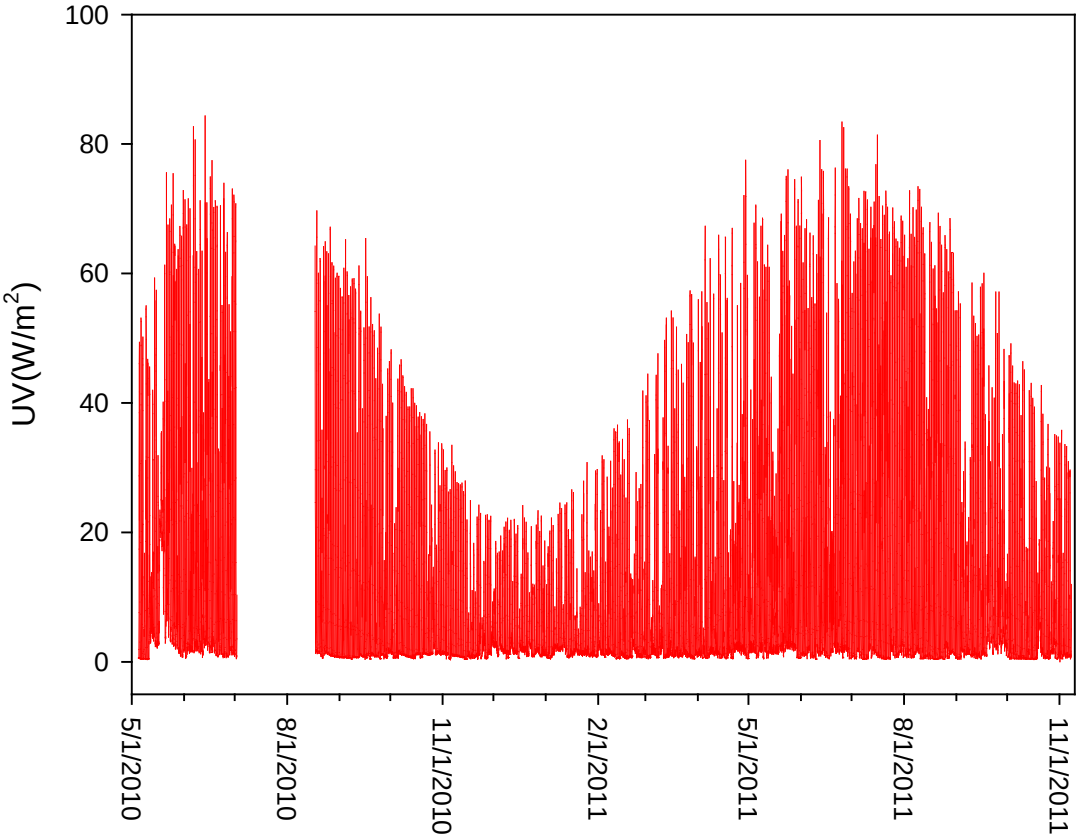

Figure A- 22. Yearly UV pattern at Wright-Patterson AFB exposure site.

Distribution Statement A. Approved for Public Release.

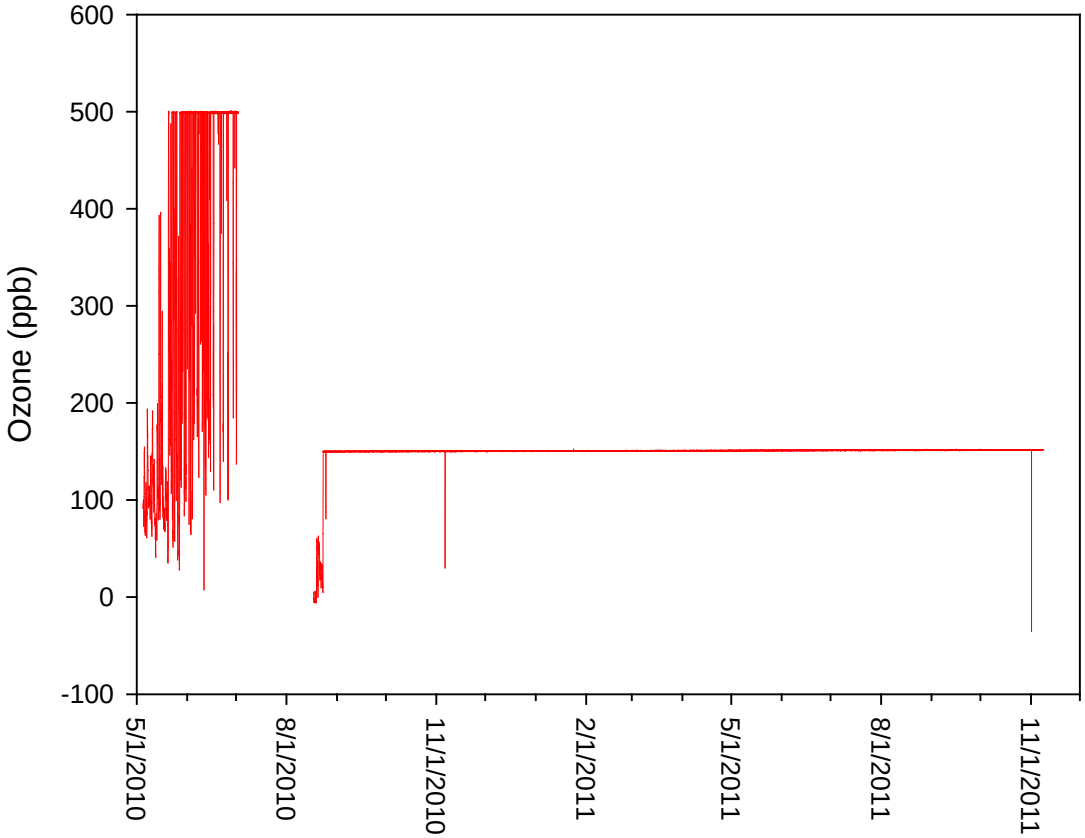

Figure A- 23. Yearly Ozone pattern at Wright-Patterson AFB exposure site.

Distribution Statement A. Approved for Public Release.

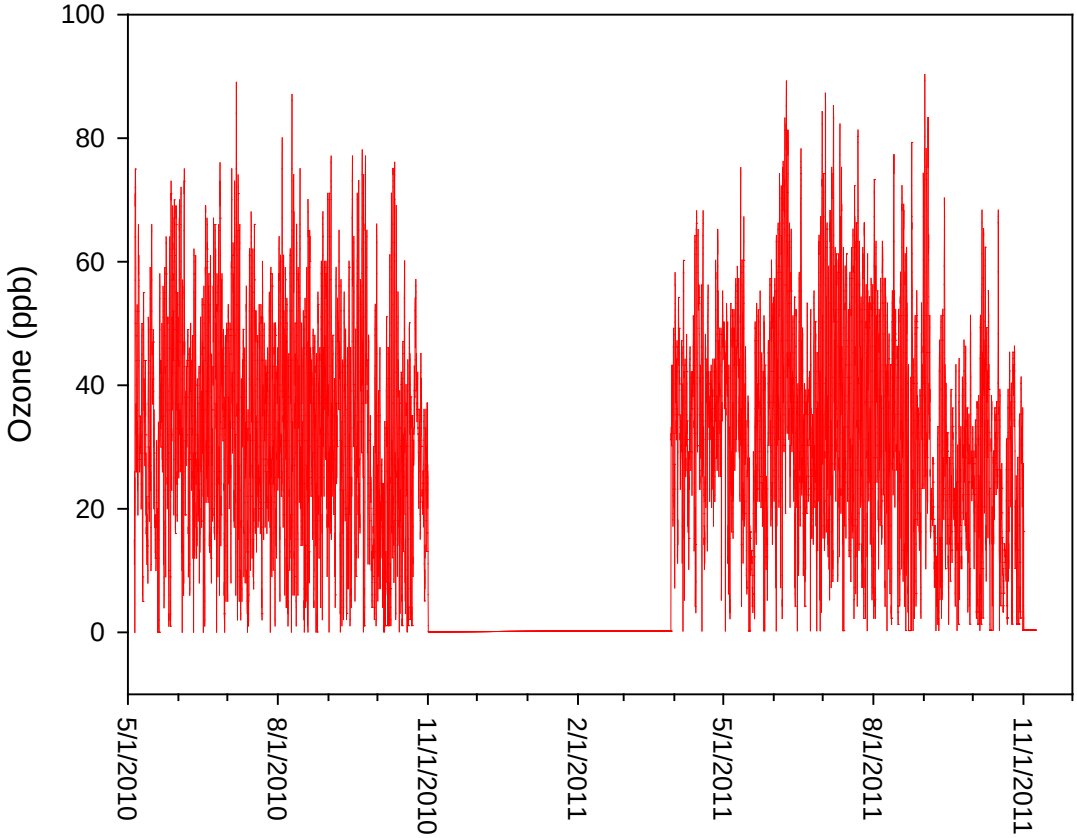

Figure A- 24. Yearly Ozone pattern at local EPA site (Xenia, OH) near Wright-Patterson AFB exposure site.

Distribution Statement A. Approved for Public Release.

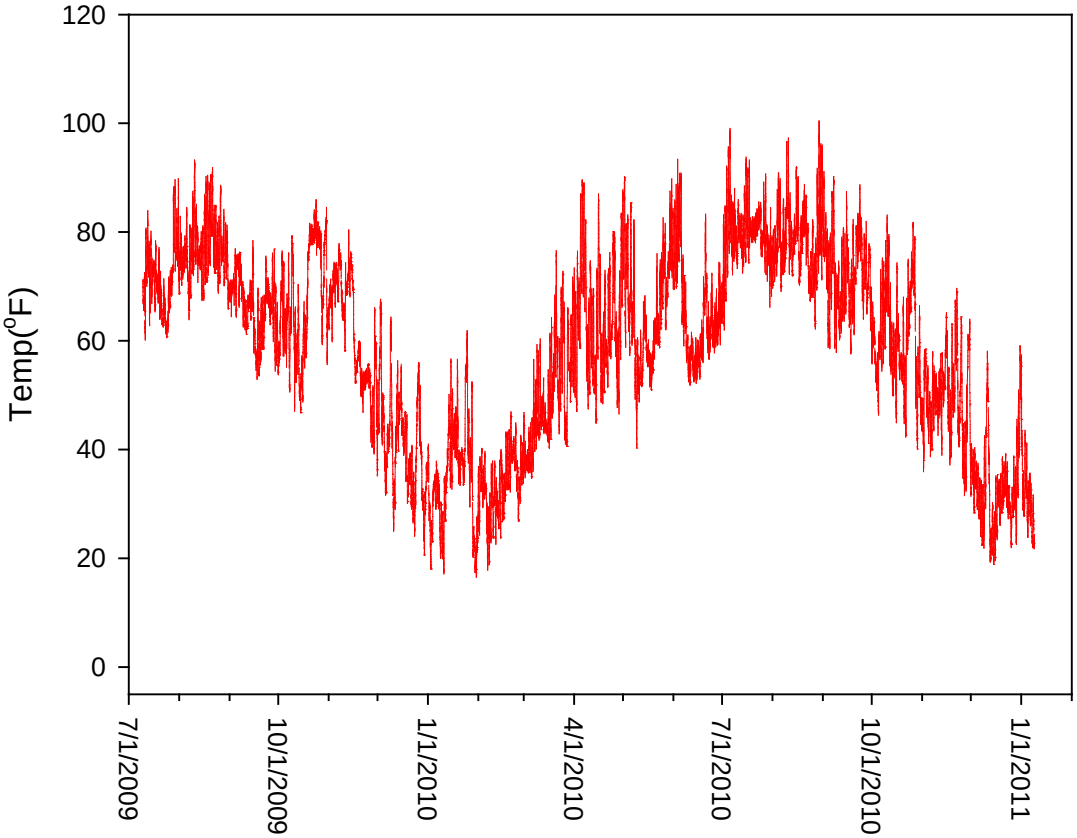

Figure A- 25. Yearly temperature pattern at East Coast Ship site.

Distribution Statement A. Approved for Public Release.

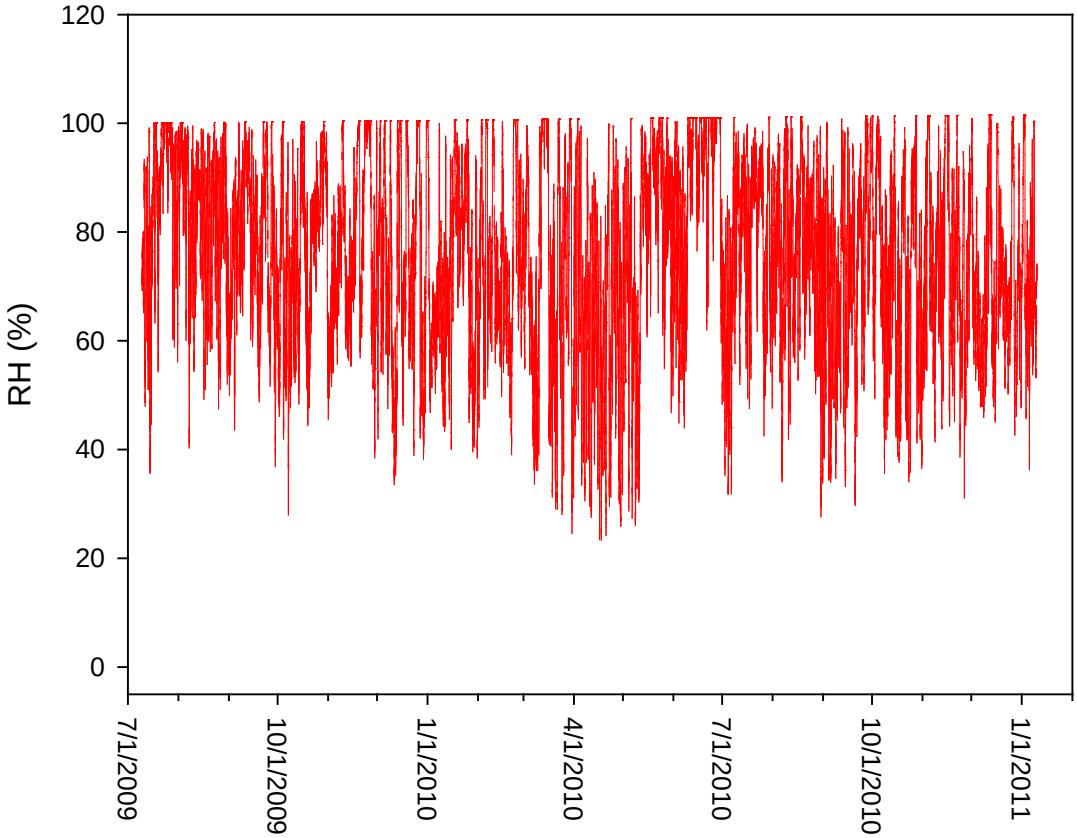

Figure A- 26. Yearly relative humidity pattern at East Coast Ship site.

Distribution Statement A. Approved for Public Release.

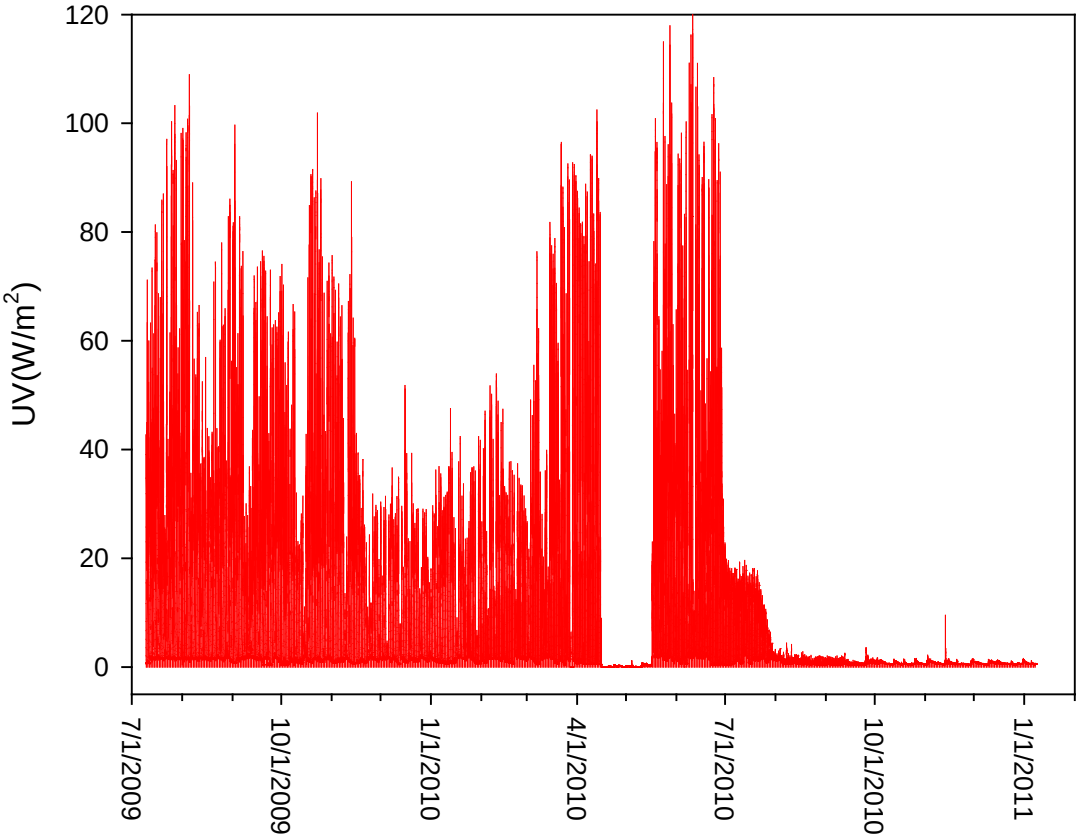

Figure A- 27. Yearly UV pattern at East Coast Ship site.

Distribution Statement A. Approved for Public Release.

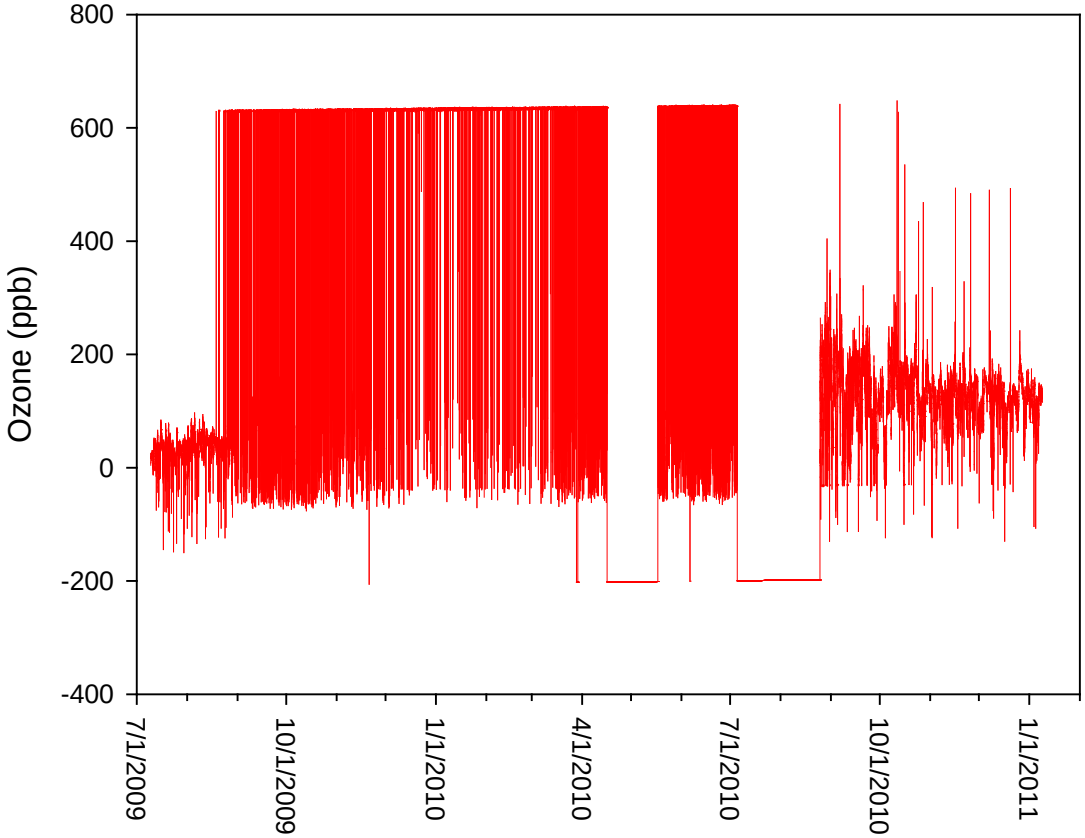

Figure A- 28. Yearly Ozone pattern at East Coast Ship site.

Distribution Statement A. Approved for Public Release.

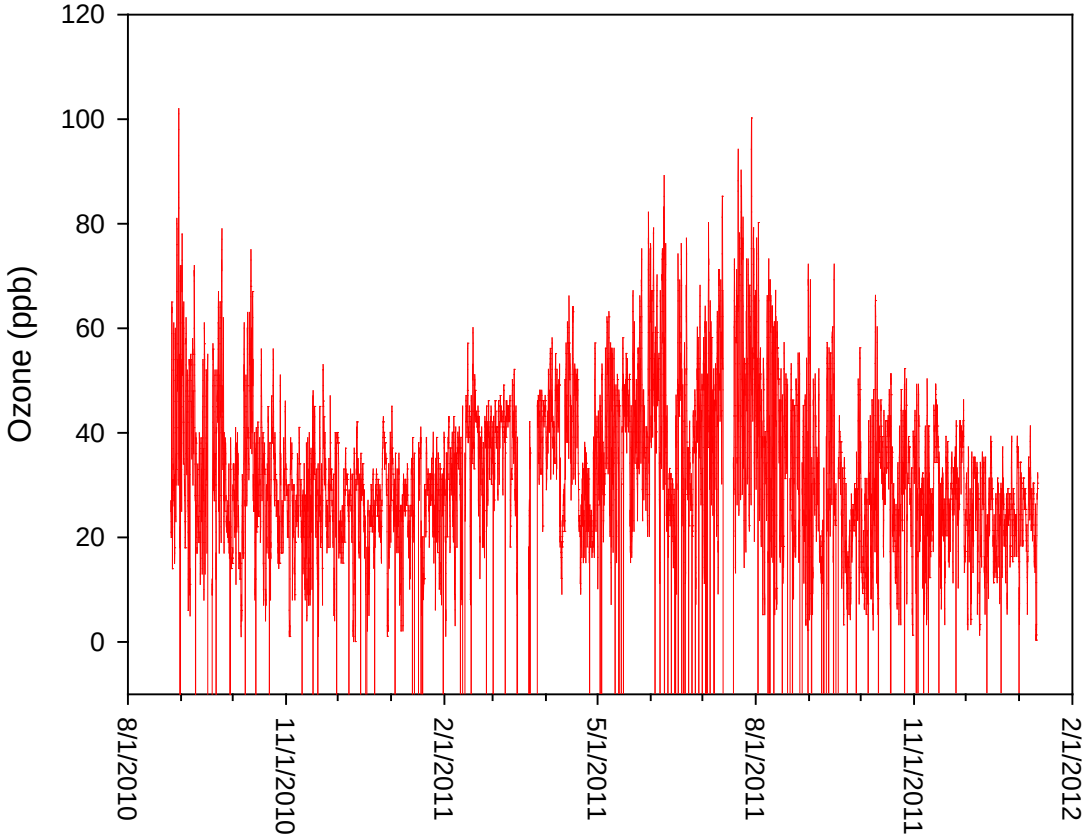

Figure A- 29. Yearly Ozone pattern at local EPA site near East Coast Ship site.

Distribution Statement A. Approved for Public Release.

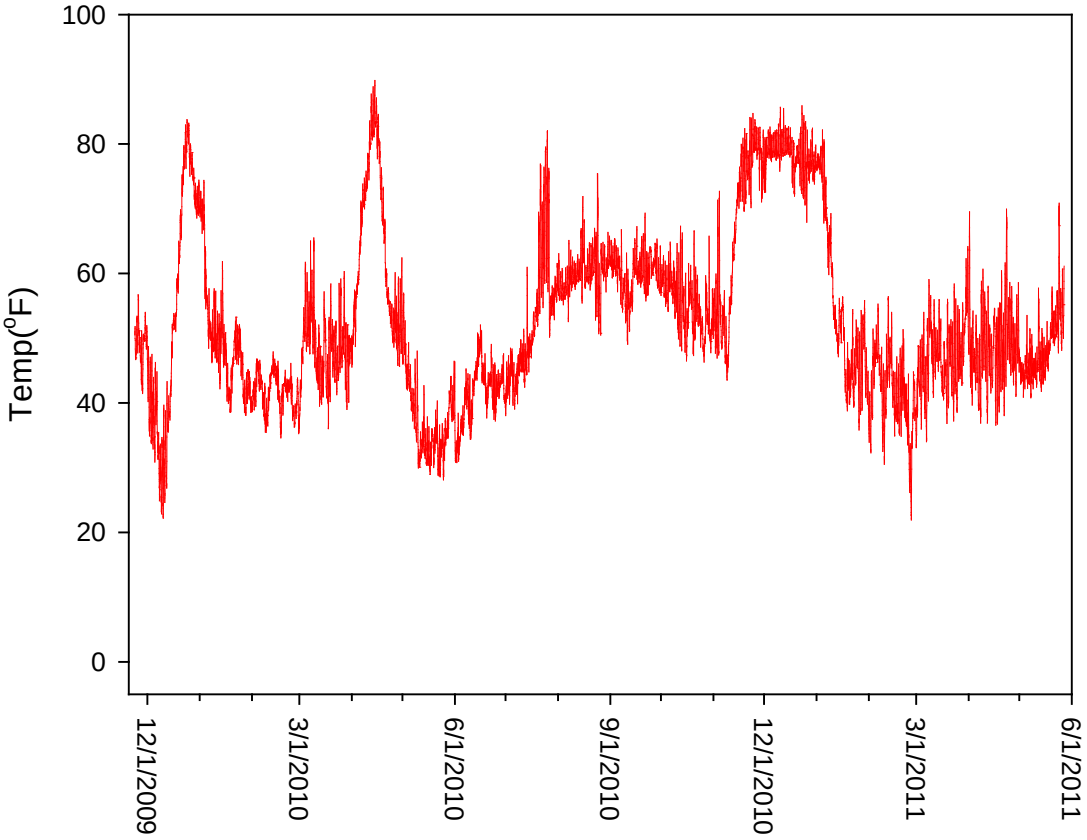

Figure A- 30. Yearly temperature pattern at West Coast Ship site.

Distribution Statement A. Approved for Public Release.

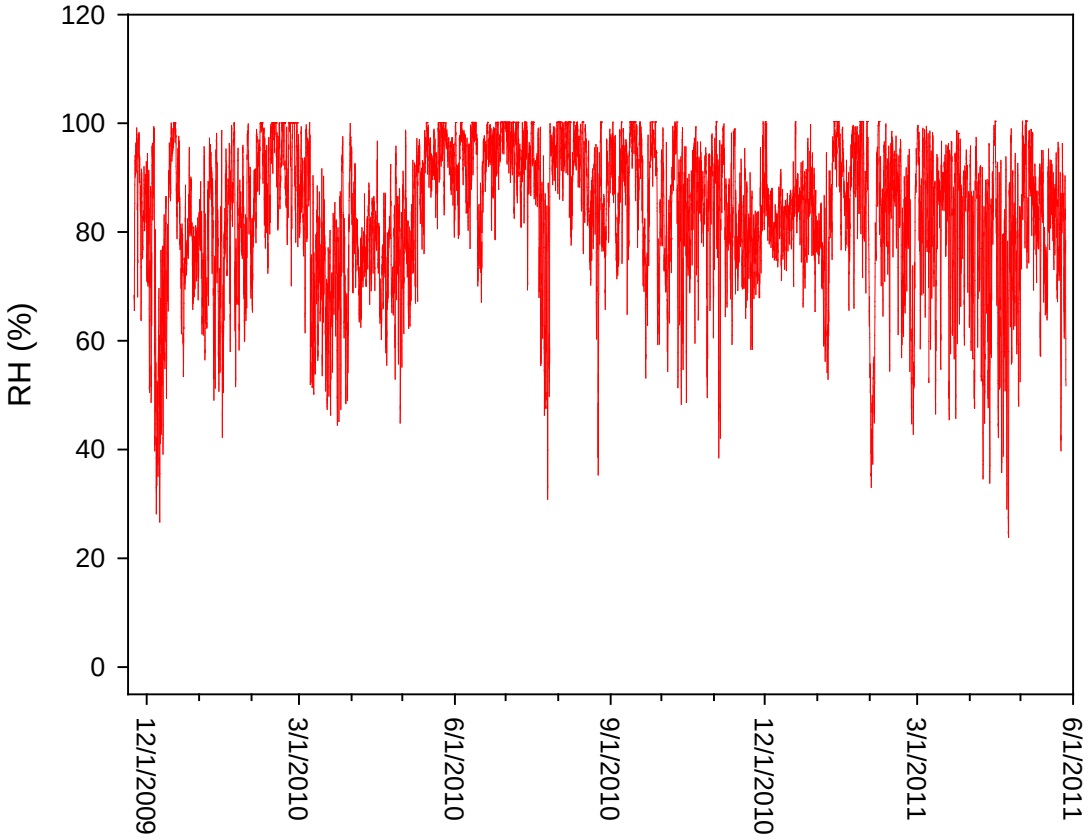

Figure A- 31. Yearly relative humidity pattern at West Coast Ship site.

Distribution Statement A. Approved for Public Release.

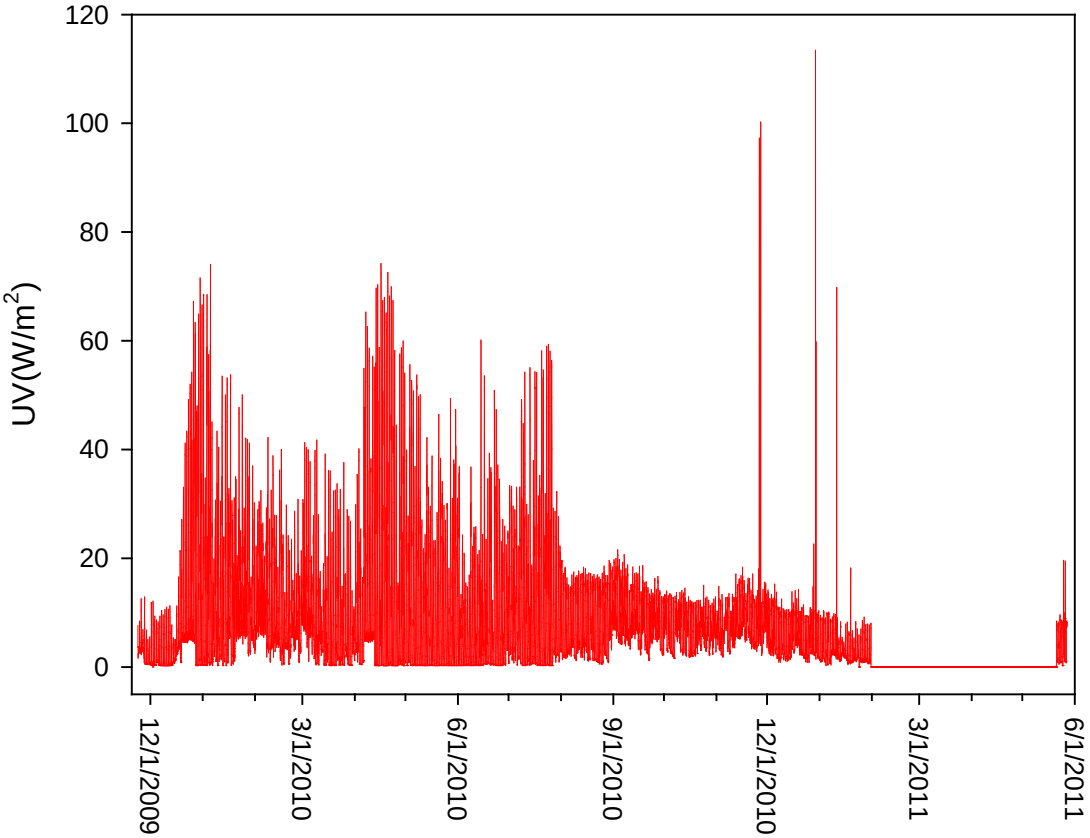

Figure A- 32. Yearly UV pattern at West Coast Ship site.

Distribution Statement A. Approved for Public Release.

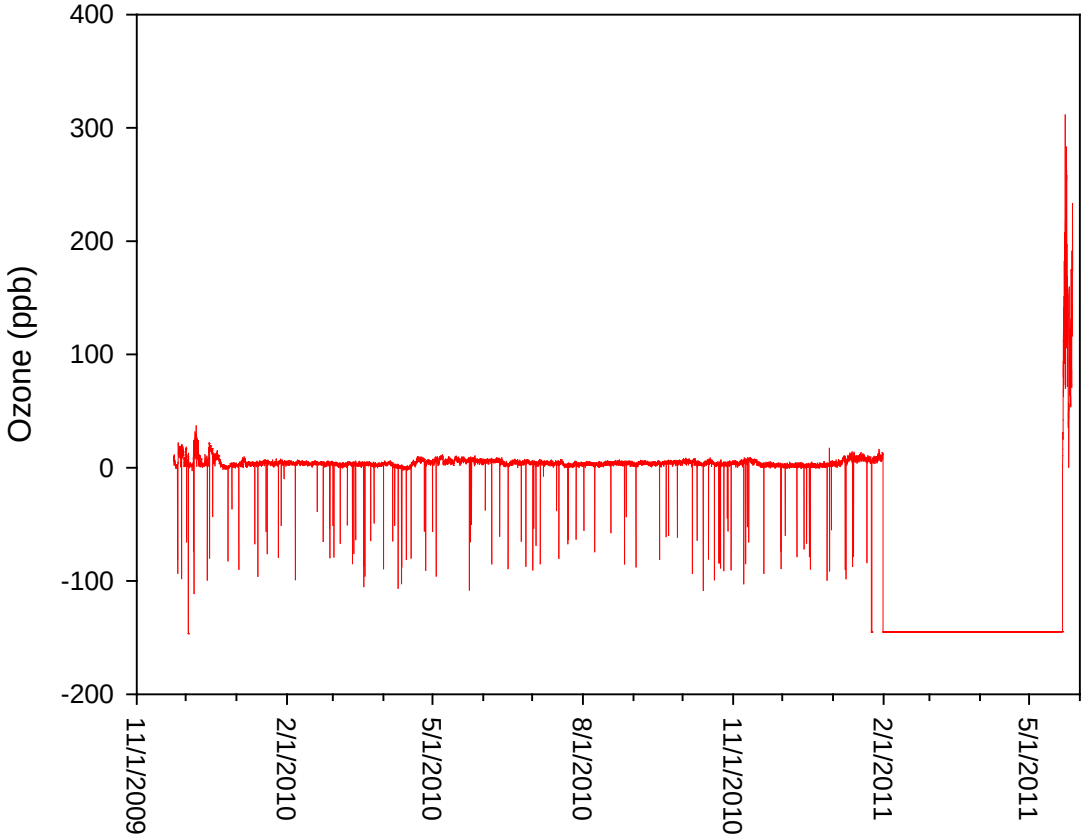

Figure A- 33. Yearly Ozone pattern at West Coast Ship site.

Distribution Statement A. Approved for Public Release.

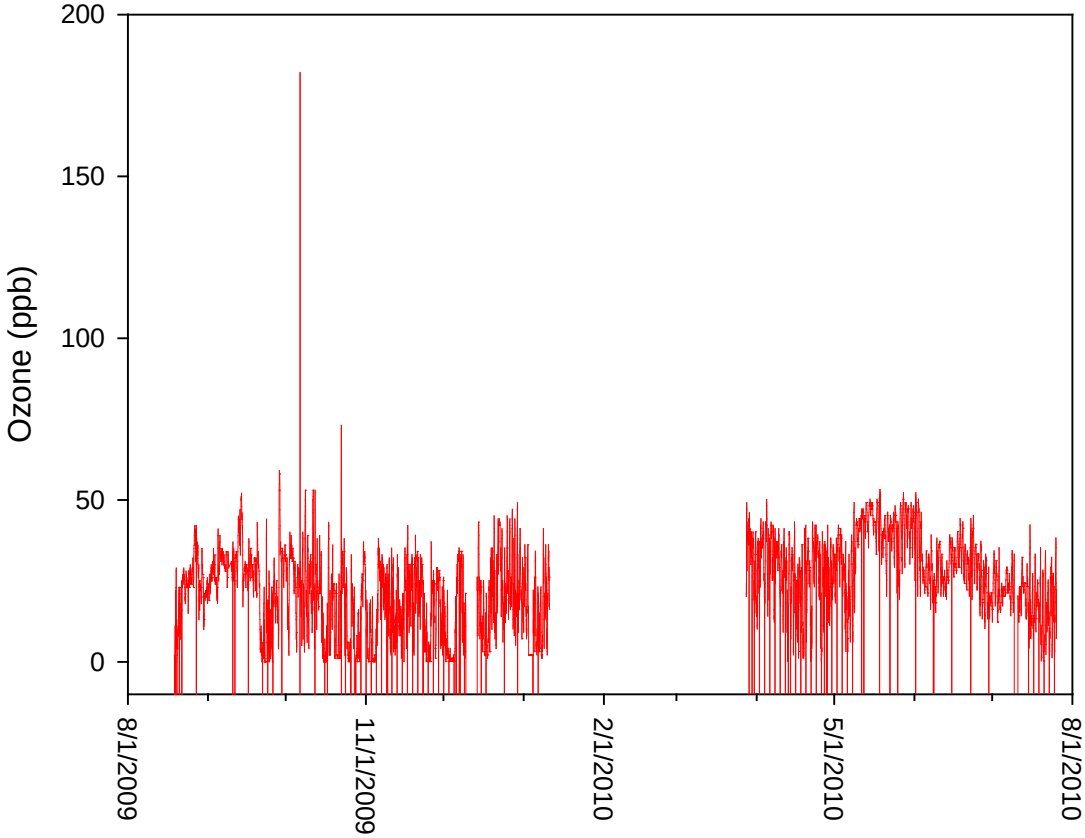

Figure A- 34. Yearly Ozone pattern at local EPA site near West Coast Ship site.

Distribution Statement A. Approved for Public Release.

Appendix B

Scanning Electron Microscopy Images

(Dayton Beach, FL)

Distribution Statement A. Approved for Public Release.

FIGURES

Page

Figure B-1. SEM images of pure silver sample retrieved on 24 months exposure from Daytona Beach site. (a) 100X magnification (b) 250X magnification, (c) 500X magnification, and (d) 2500X magnification. 5

Figure B-2.SEM images of pure silver sample retrieved on 18 months exposure from Daytona Beach site. (a) 100X magnification (b) 250X magnification, (c) 500X magnification, and (d) 2500X magnification. 6

Figure B-3. SEM images of pure silver sample retrieved on 12 months exposure from Daytona Beach site. (a) 100X magnification (b) 250X magnification, (c) 500X magnification, and (d) 2500X magnification. 7

Figure B-4. SEM images of pure silver sample retrieved on 9 months exposure from Daytona Beach site. (a) 100X magnification (b) 250X magnification, (c) 500X magnification, and (d) 1000X magnification. 8

Figure B-5. SEM images of pure silver sample retrieved on 6 months exposure from Daytona Beach site. (a) 250X magnification (b) 500X magnification, (c) 1000X magnification, and (d) 2000X magnification. 9

Figure B-6. SEM images of pure silver sample retrieved on 3 months exposure from Daytona Beach site. (a) 250X magnification (b) 1000X magnification, and (c) 5000X magnification. 10

Figure B-7. SEM images of aluminum alloy 7075 sample retrieved on 24 months exposure from Daytona Beach site. (a) 100X magnification (b) 250X magnification, (c) 500X magnification, and (d) 2500X magnification. .. 11

Figure B-8. SEM images of aluminum alloy 7075 sample retrieved on 18 months exposure from Daytona Beach site. (a) 100X magnification (b) 250X magnification, (c) 500X magnification, and (d) 2500X magnification. .. 12

Figure B-9. SEM images of aluminum alloy 7075 sample retrieved on 12 months exposure from Daytona Beach site. (a) 100X magnification (b) 250X magnification, (c) 500X magnification, and (d) 2500X magnification. .. 13

Figure B-10. SEM images of aluminum alloy 7075 sample retrieved on 9 months exposure from Daytona Beach site. (a) 100X magnification (b) 250X magnification, (c) 500X magnification, and (d) 500X magnification..... 14

Figure B-11. SEM images of aluminum alloy 7075 sample retrieved on 6 months exposure from Daytona Beach site. (a) 100X magnification (b) 250X magnification, (c) 500X magnification, and (d) 2500X magnification. .. 15

Figure B-12. SEM images of aluminum alloy 7075 sample retrieved on 3 months exposure from Daytona Beach site. (a) 50X magnification (b) 50X magnification, (c) 50X magnification, and (d) 300X magnification. 16

Figure B-13. SEM images of aluminum alloy 6061 sample retrieved on 24 months exposure from Daytona Beach site. (a) 100X magnification (b) 250X magnification, (c) 500X magnification, and (d) 2500X magnification. 17

Distribution Statement A. Approved for Public Release.

Figure B-14. SEM images of aluminum alloy 6061 sample retrieved on 18 months exposure from Daytona Beach site. (a) 100X magnification (b) 250X magnification, (c) 500X magnification, and (d) 2500X magnification 18

Figure B-15. SEM images of aluminum alloy 6061 sample retrieved on 12 months exposure from Daytona Beach site. (a) 100X magnification (b) 250X magnification, (c) 500X magnification, and (d) 2500X magnification. 19

Figure B-16. SEM images of aluminum alloy 6061 sample retrieved on 9 months exposure from Daytona Beach site. (a) 100X magnification (b) 250X magnification, (c) 500X magnification, and (d) 1000X magnification. .. 20

Figure B-17. SEM images of aluminum alloy 6061 sample retrieved on 6 months exposure from Daytona Beach site. (a) 100X magnification (b) 250X magnification, (c) 500X magnification, and (d) 1000X magnification. .. 21

Figure B-18. SEM images of aluminum alloy 6061 sample retrieved on 3 months exposure from Daytona Beach site. (a) 30X magnification (b) 50X magnification, (c) 100X magnification, and (d) 300X magnification. 22

Figure B-19. SEM images of aluminum alloy 2024 sample retrieved on 24 months exposure from Daytona Beach site. (a) 100X magnification (b) 250X magnification, (c) 500X magnification, and (d) 2500X magnification. 23

Figure B-20. SEM images of aluminum alloy 2024 sample retrieved on 18 months exposure from Daytona Beach site. (a) 100X magnification (b) 250X magnification, (c) 500X magnification, and (d) 1000X magnification. 24

Figure B-21. SEM images of aluminum alloy 2024 sample retrieved on 12 months exposure from Daytona Beach site. (a) 100X magnification (b) 250X magnification, (c) 500X magnification, and (d) 2500X magnification. 25

Figure B-22. SEM images of aluminum alloy 2024 sample retrieved on 9 months exposure from Daytona Beach site. (a) 100X magnification (b) 250X magnification, (c) 500X magnification, and (d) 1000X magnification. .. 26

Figure B-23. SEM images of aluminum alloy 2024 sample retrieved on 6 months exposure from Daytona Beach site. (a) 100X magnification (b) 250X magnification, (c) 500X magnification, and (d) 1000X magnification. .. 27

Figure B-24. SEM images of aluminum alloy 2024 sample retrieved on 3 months exposure from Daytona Beach site. (a) 100X magnification. 28

Figure B-25. SEM images of pure copper sample retrieved on 24 months exposure from Daytona Beach site. (a) 100X magnification (b) 250X magnification, (c) 500X magnification, and (d) 2000X magnification. 29

Figure B-26. SEM images of pure copper sample retrieved on 18 months exposure from Daytona Beach site. (a) 100X magnification (b) 250X magnification, (c) 500X magnification, and (d) 2000X magnification. 30

Figure B-27. SEM images of pure copper sample retrieved on 12 months exposure from Daytona Beach site. (a) 100X magnification (b) 250X magnification, (c) 500X magnification, and (d) 2000X magnification. 31

Distribution Statement A. Approved for Public Release.

Figure B-28. SEM images of pure copper sample retrieved on 9 months exposure from Daytona Beach site. (a) 100X magnification (b) 250X magnification, (c) 500X magnification, and (d) 1000X magnification. 32

Figure B-29. SEM images of pure copper sample retrieved on 6 months exposure from Daytona Beach site. (a) 100X magnification (b) 250X magnification, (c) 500X magnification, and (d) 5000X magnification. 33

Figure B-30. SEM images of pure copper sample retrieved on 3 months exposure from Daytona Beach site. (a) 100X magnification (b) 150X magnification, (c) 250X magnification, and (d) 800X magnification. 34

Figure B-31. SEM images of 1010 steel sample retrieved on 24 months exposure from Daytona Beach site. (a) 100X magnification (b) 250X magnification, (c) 500X magnification, and (d) 2000X magnification. 35

Figure B-32. SEM images of 1010 steel sample retrieved on 18 months exposure from Daytona Beach site. (a) 100X magnification (b) 250X magnification, (c) 500X magnification, and (d) 2000X magnification. 36

Figure B-33. SEM images of 1010 steel sample retrieved on 12 months exposure from Daytona Beach site. (a) 100X magnification (b) 250X magnification, (c) 500X magnification, and (d) 2000X magnification. 37

Figure B-34. SEM images of 1010 steel sample retrieved on 9 months exposure from Daytona Beach site. (a) 100X magnification (b) 250X magnification, (c) 500X magnification, and (d) 1000X magnification. 38

Figure B-35. SEM images of 1010 steel sample retrieved on 6 months exposure from Daytona Beach site. (a) 100X magnification (b) 500X magnification, (c) 5000X magnification, and (d) 5000X magnification. 39

Figure B-36. SEM images of 1010 steel sample retrieved on 3 months exposure from Daytona Beach site. (a) 50X magnification (b) 100X magnification, (c) 250X magnification, and (d) 500X magnification. 40

Distribution Statement A. Approved for Public Release.

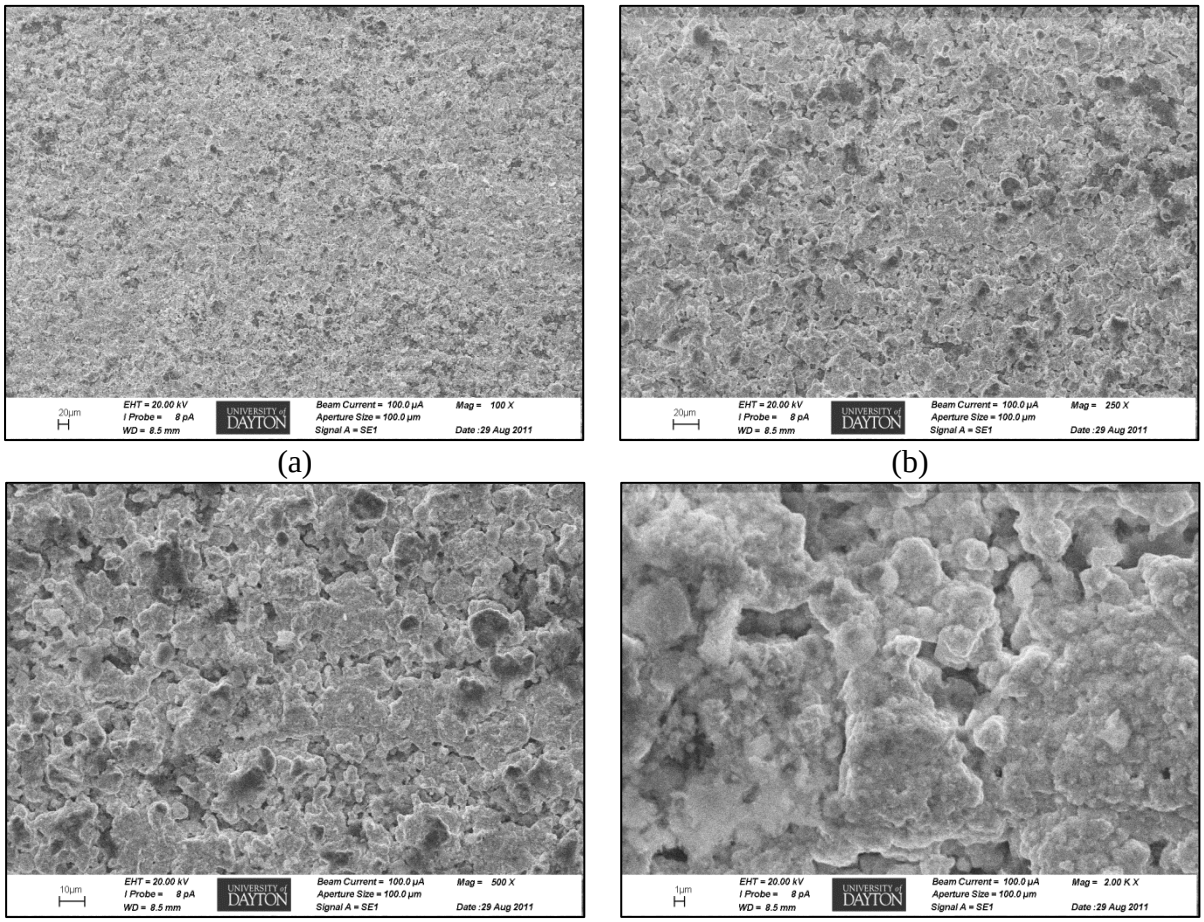

Figure B-1. SEM images of pure silver sample retrieved on 24 months exposure from Daytona Beach site. (a) 100X magnification (b) 250X magnification, (c) 500X magnification, and (d) 2500X magnification.

Distribution Statement A. Approved for Public Release.

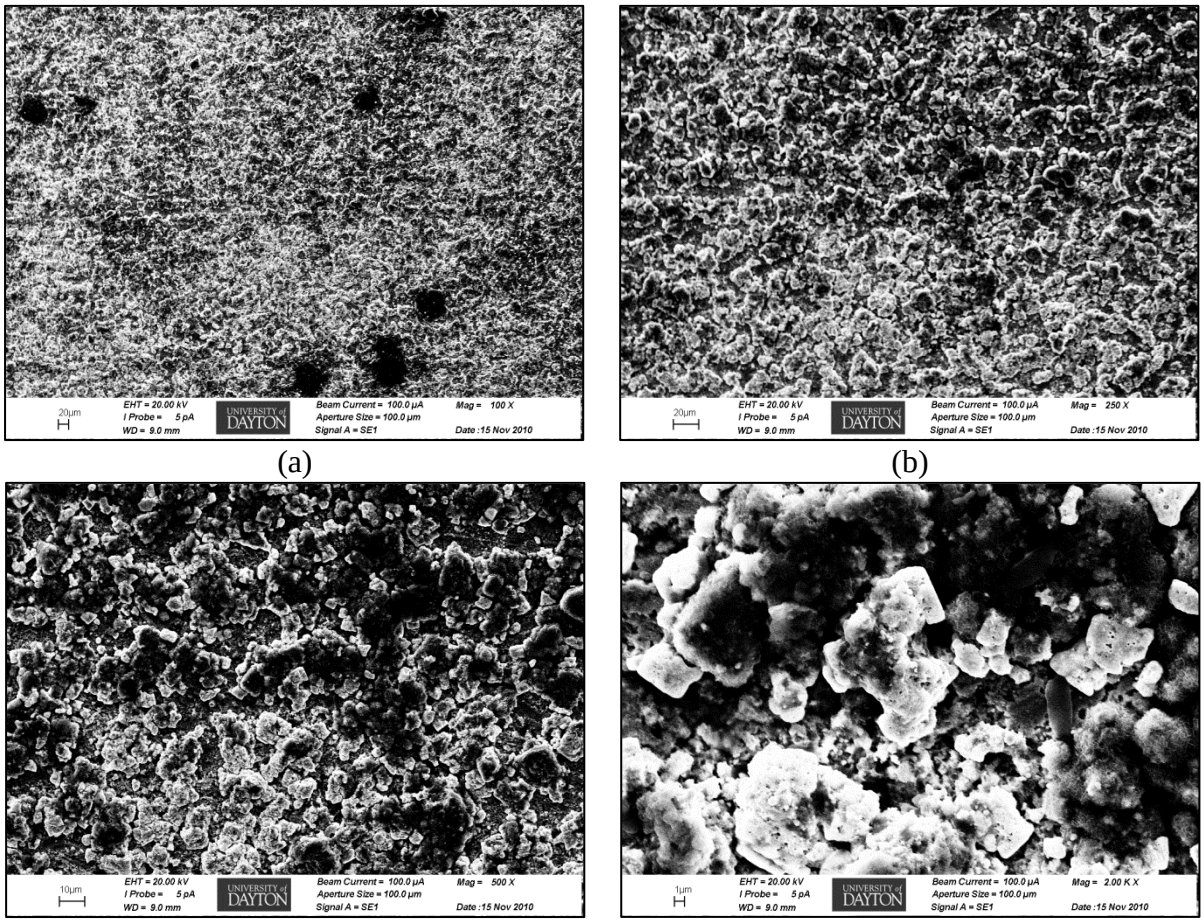

Figure B-2. SEM images of pure silver sample retrieved on 18 months exposure from Daytona Beach site. (a) 100X magnification (b) 250X magnification, (c) 500X magnification, and (d) 2500X magnification.

Distribution Statement A. Approved for Public Release.

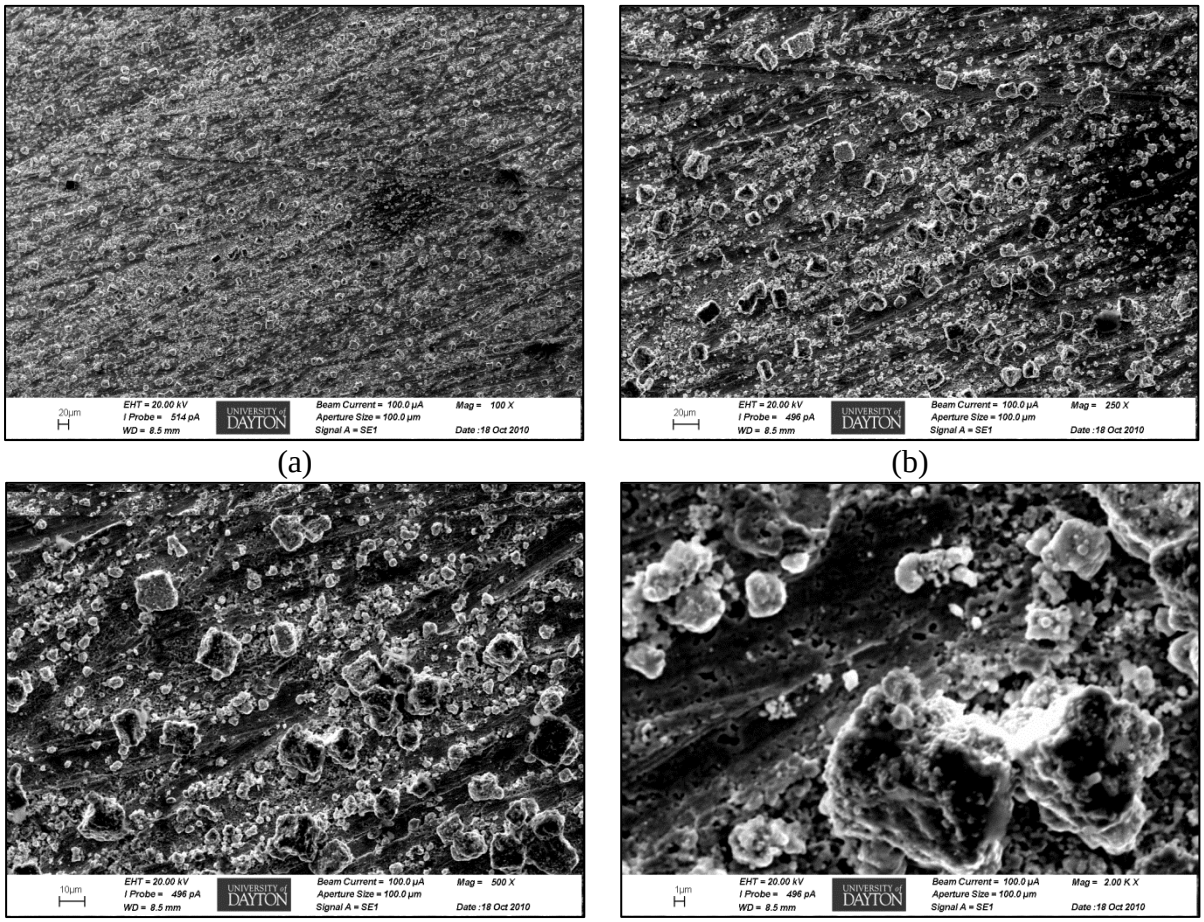

Figure B-3. SEM images of pure silver sample retrieved on 12 months exposure from Daytona Beach site. (a) 100X magnification (b) 250X magnification, (c) 500X magnification, and (d) 2500X magnification.

Distribution Statement A. Approved for Public Release.

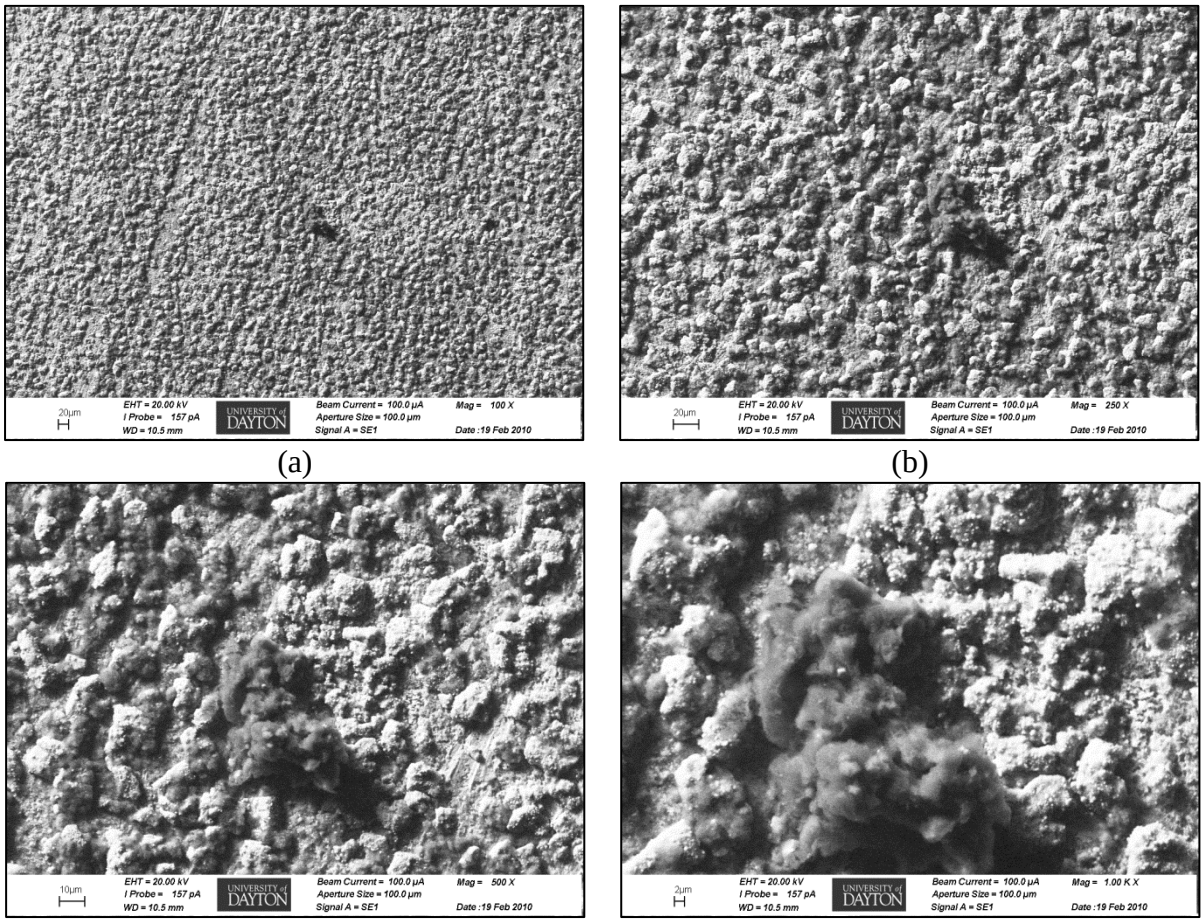

Figure B-4. SEM images of pure silver sample retrieved on 9 months exposure from Daytona Beach site. (a) 100X magnification (b) 250X magnification, (c) 500X magnification, and (d) 1000X magnification.

Distribution Statement A. Approved for Public Release.

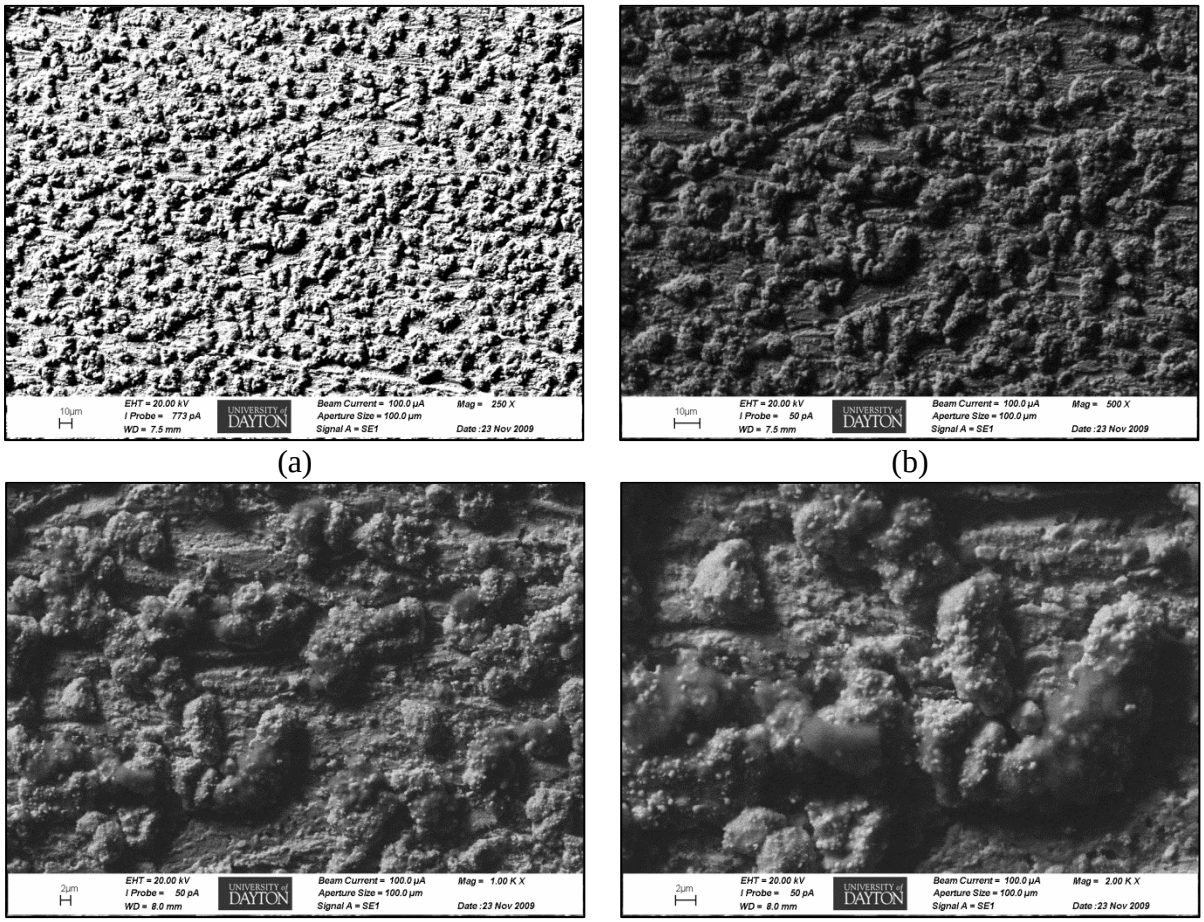

Figure B-5. SEM images of pure silver sample retrieved on 6 months exposure from Daytona Beach site. (a) 250X magnification (b) 500X magnification, (c) 1000X magnification, and (d) 2000X magnification.

Distribution Statement A. Approved for Public Release.

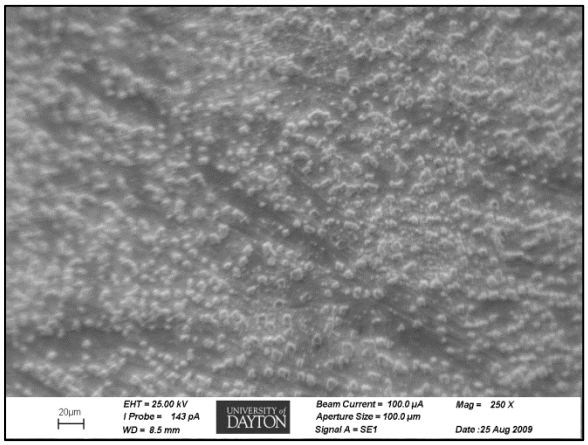

(a)

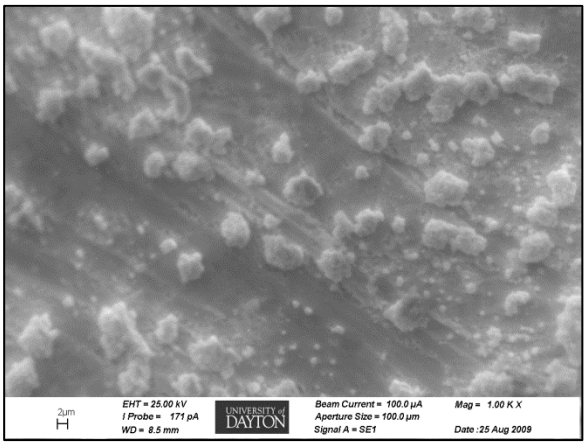

(b)

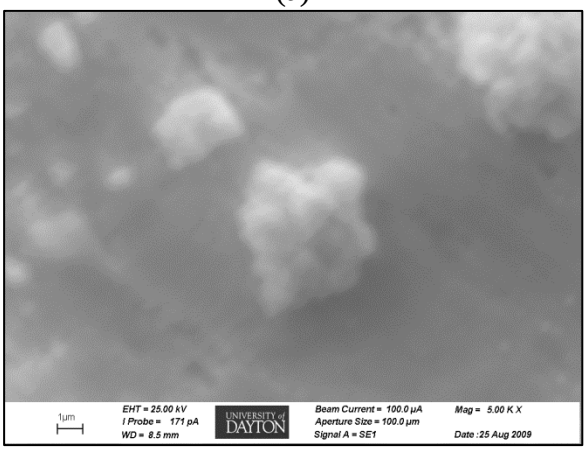

(c)

Figure B-6. SEM images of pure silver sample retrieved on 3 months exposure from Daytona Beach site. (a) 250X magnification (b) 1000X magnification, and (c) 5000X magnification.

Distribution Statement A. Approved for Public Release.

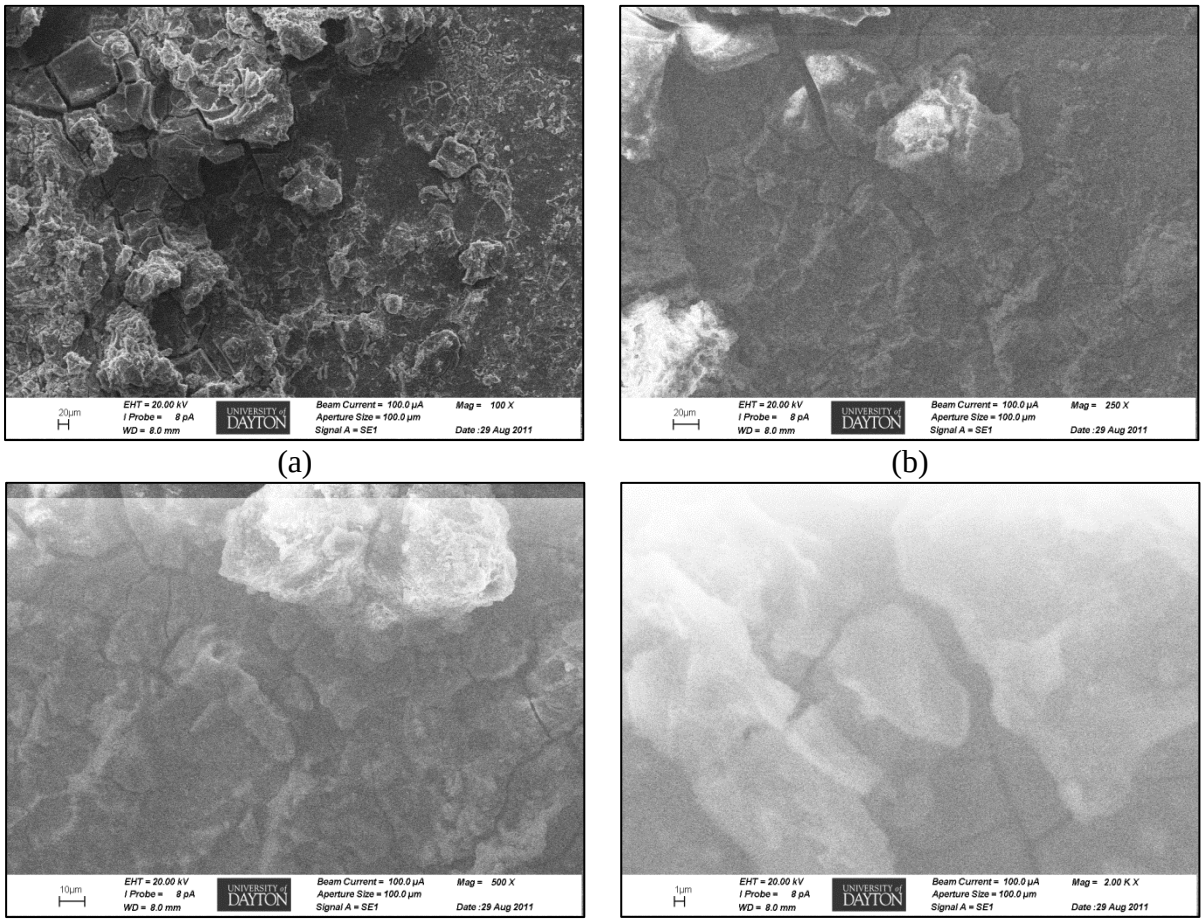

Figure B-7. SEM images of aluminum alloy 7075 sample retrieved on 24 months exposure from Daytona Beach site. (a) 100X magnification (b) 250X magnification, (c) 500X magnification, and (d) 2500X magnification.

Distribution Statement A. Approved for Public Release.

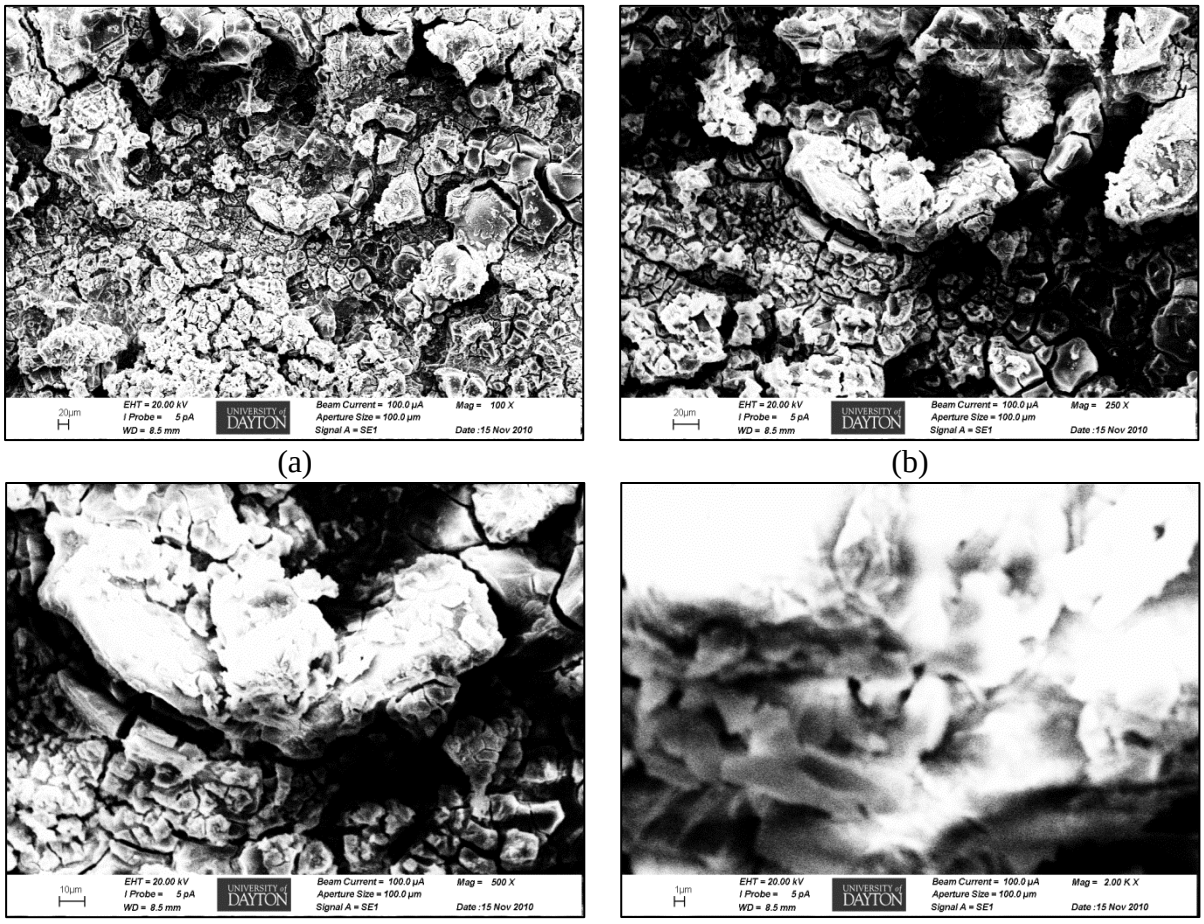

Figure B-8. SEM images of aluminum alloy 7075 sample retrieved on 18 months exposure from Daytona Beach site. (a) 100X magnification (b) 250X magnification, (c) 500X magnification, and (d) 2500X magnification.

Distribution Statement A. Approved for Public Release.

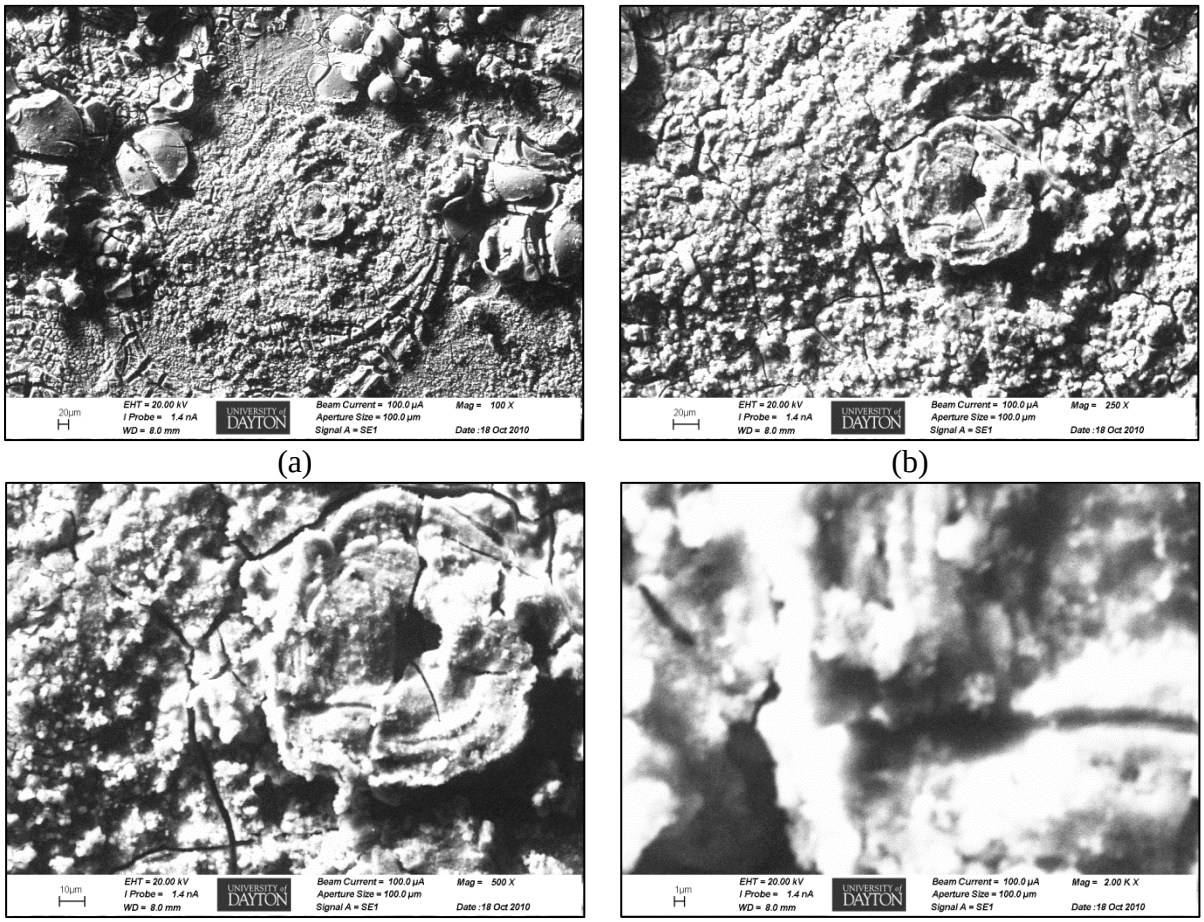

Figure B-9. SEM images of aluminum alloy 7075 sample retrieved on 12 months exposure from Daytona Beach site. (a) 100X magnification (b) 250X magnification, (c) 500X magnification, and (d) 2500X magnification.

Distribution Statement A. Approved for Public Release.

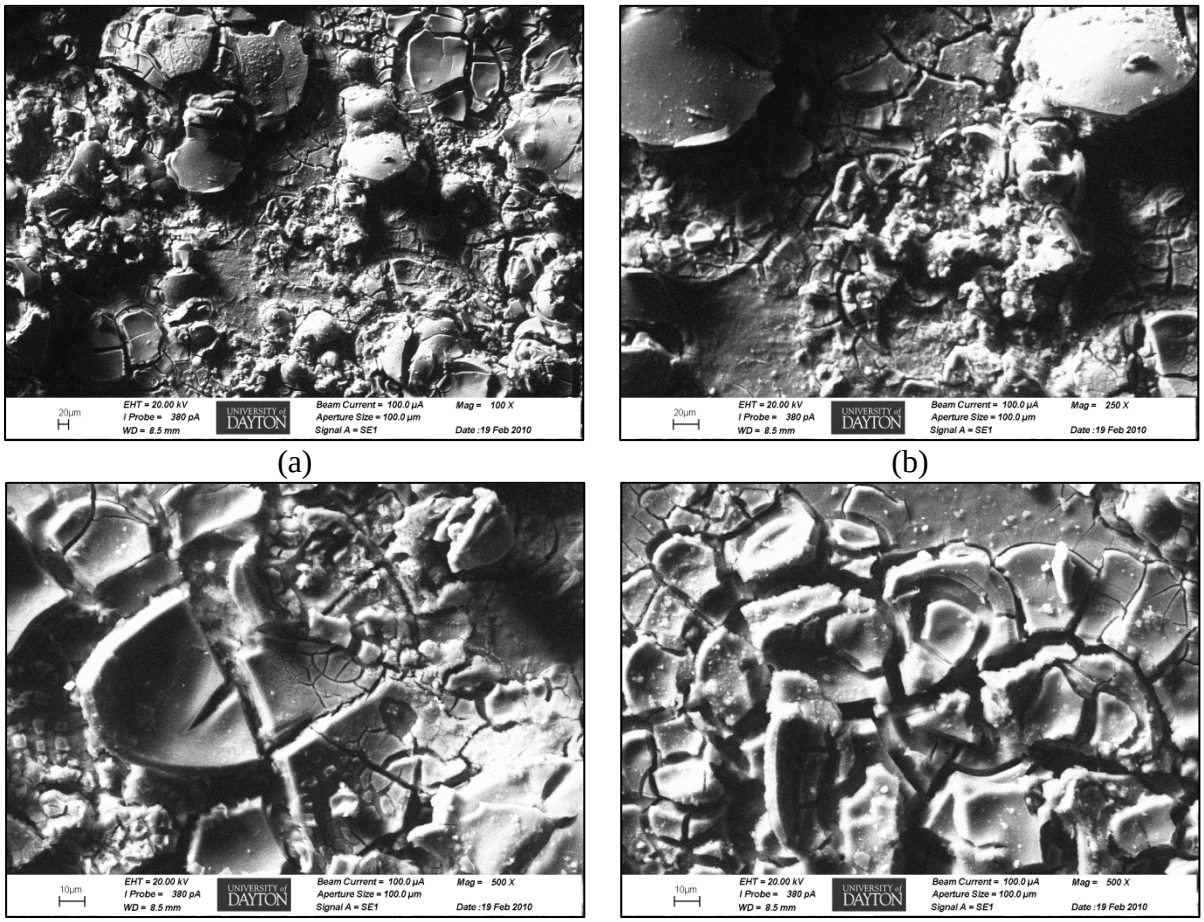

Figure B-10. SEM images of aluminum alloy 7075 sample retrieved on 9 months exposure from Daytona Beach site. (a) 100X magnification (b) 250X magnification, (c) 500X magnification, and (d) 500X magnification.

Distribution Statement A. Approved for Public Release.

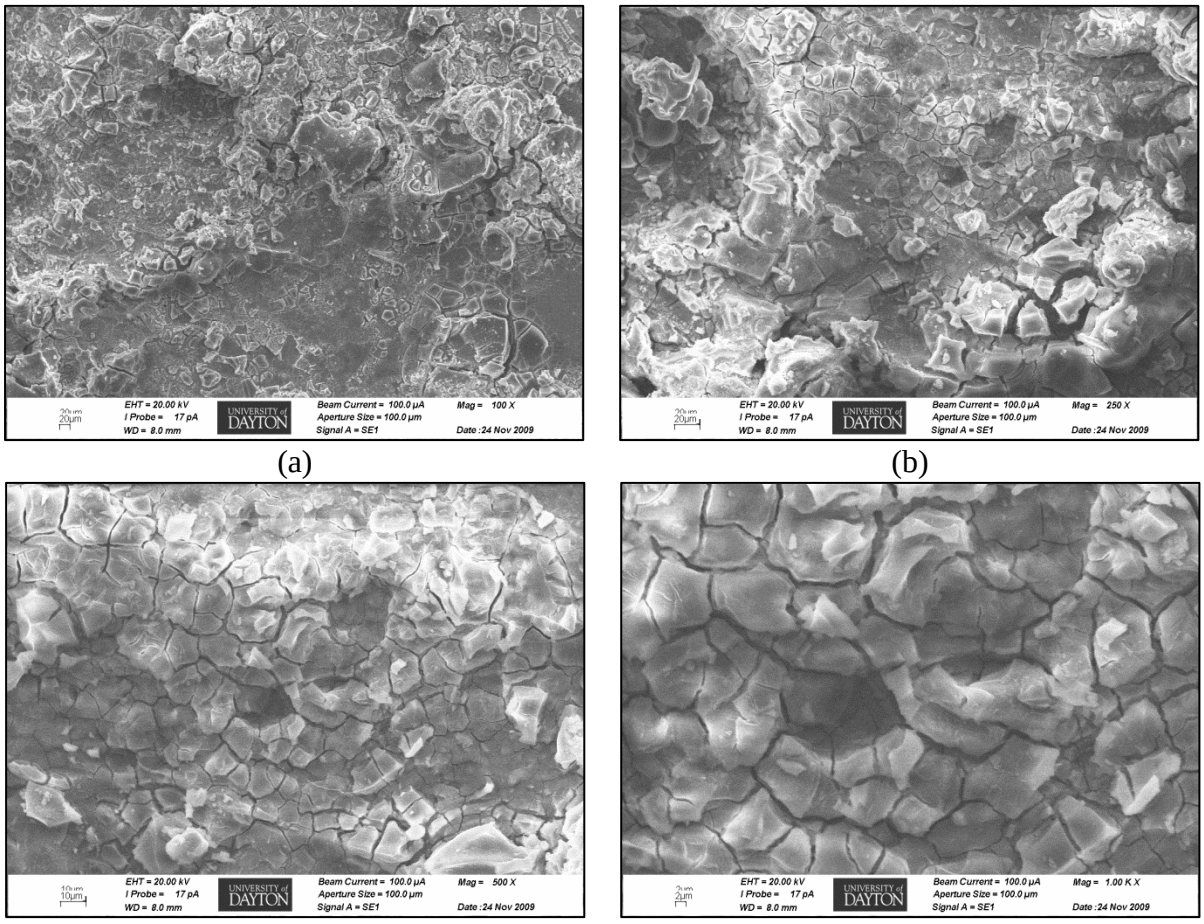

Figure B-11. SEM images of aluminum alloy 7075 sample retrieved on 6 months exposure from Daytona Beach site. (a) 100X magnification (b) 250X magnification, (c) 500X magnification, and (d) 2500X magnification.

.

Distribution Statement A. Approved for Public Release.

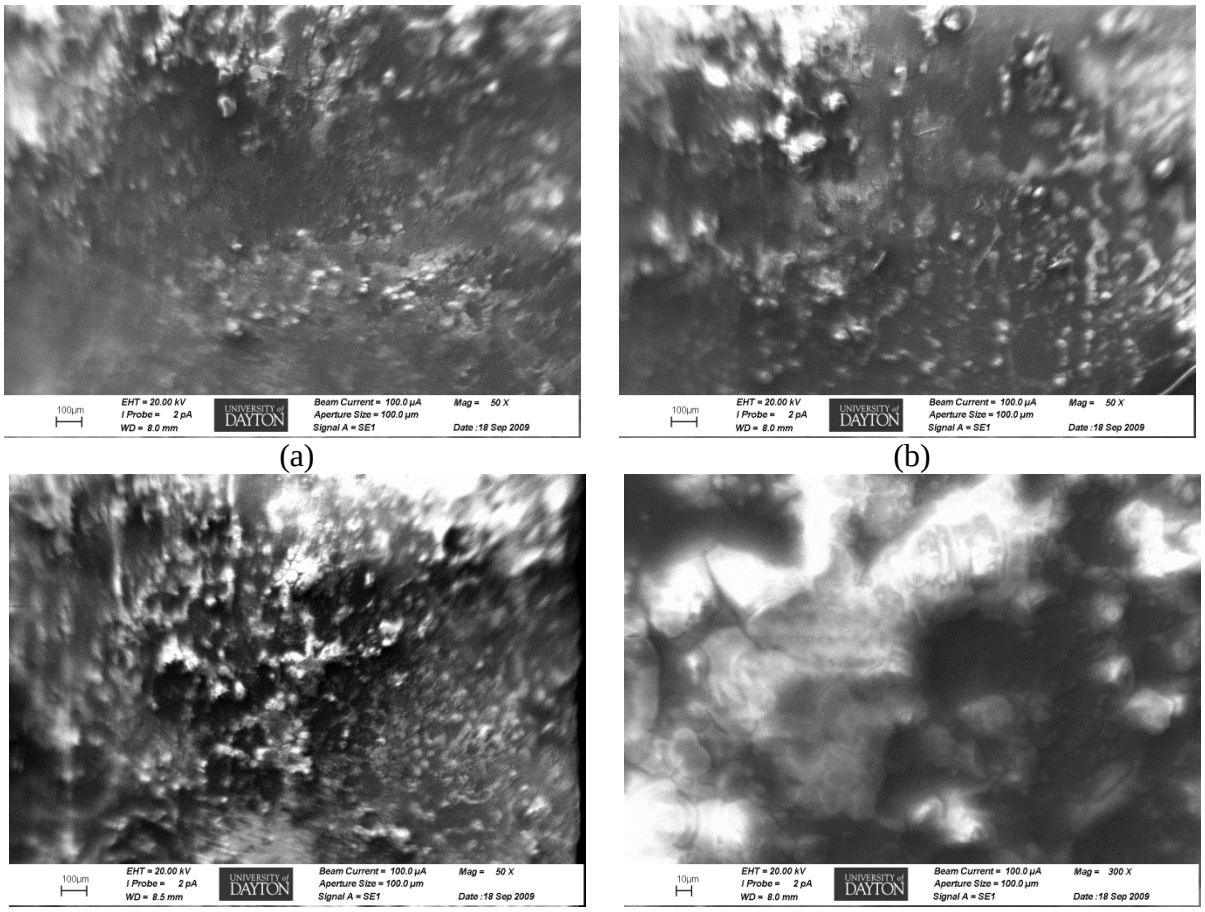

Figure B-12. SEM images of aluminum alloy 7075 sample retrieved on 3 months exposure from Daytona Beach site. (a) 50X magnification (b) 50X magnification, (c) 50X magnification, and (d) 300X magnification.

.

Distribution Statement A. Approved for Public Release.

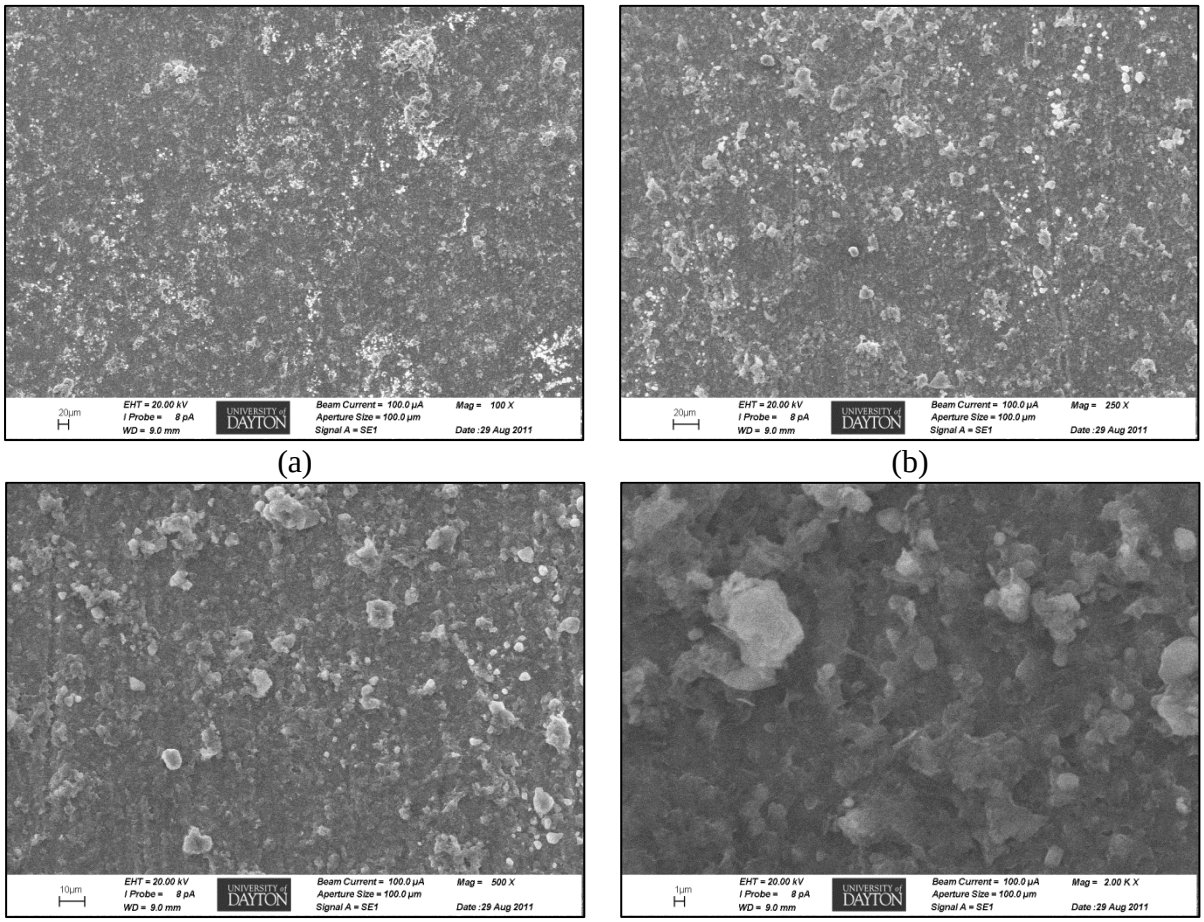

Figure B-13. SEM images of aluminum alloy 6061 sample retrieved on 24 months exposure from Daytona Beach site. (a) 100X magnification (b) 250X magnification, (c) 500X magnification, and (d) 2500X magnification.

Distribution Statement A. Approved for Public Release.

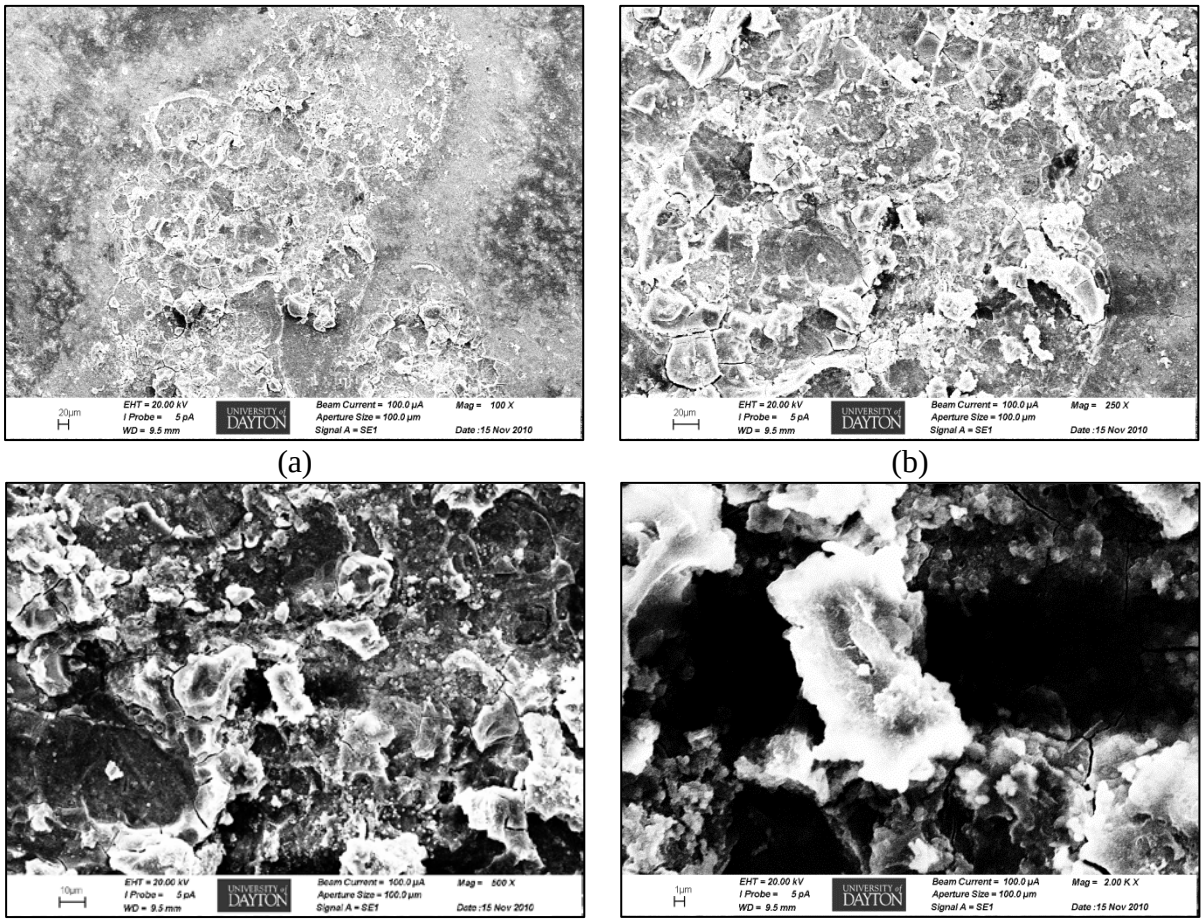

(a) (b)

(c) (d)

Figure B-14. SEM images of aluminum alloy 6061 sample retrieved on 18 months exposure from Daytona Beach site. (a) 100X magnification (b) 250X magnification, (c) 500X magnification, and (d) 2500X magnification

.

Distribution Statement A. Approved for Public Release.

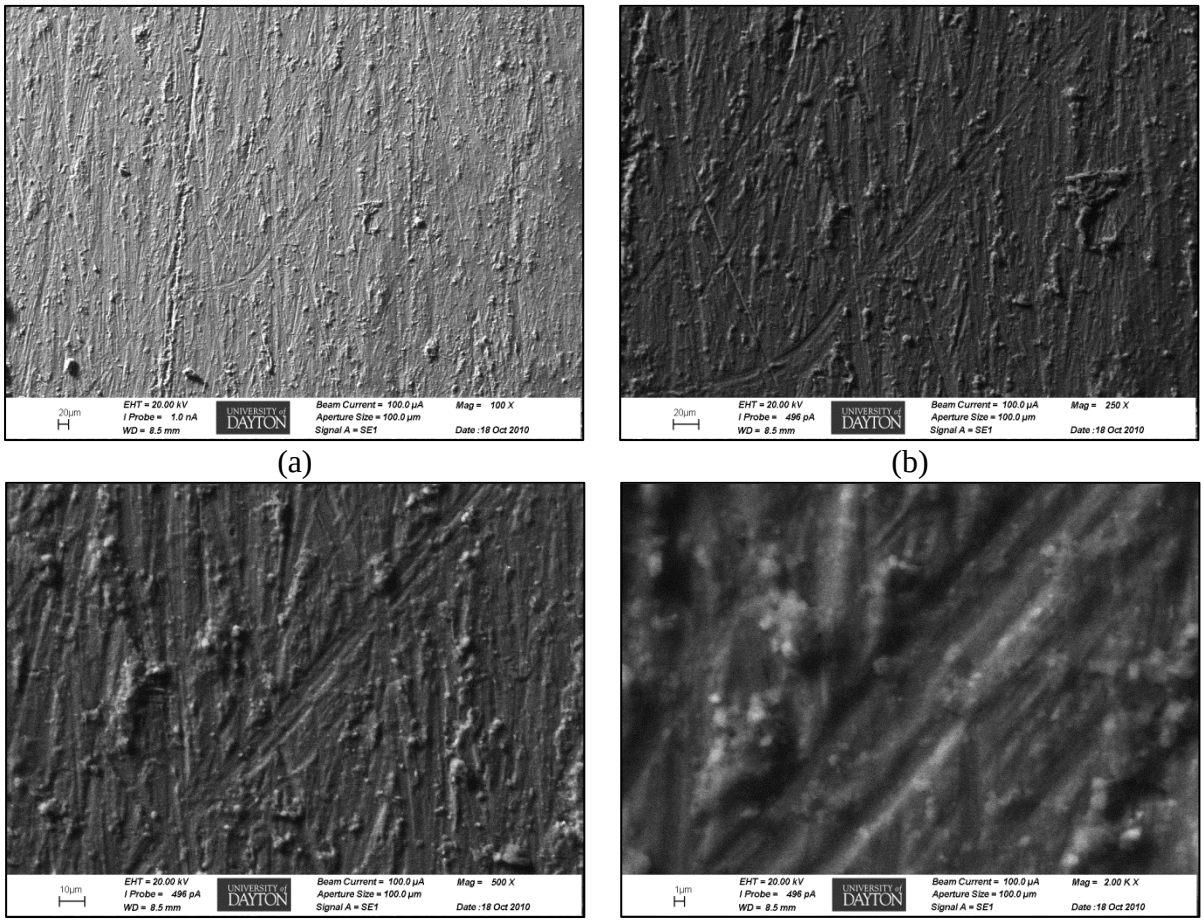

Figure B-15. SEM images of aluminum alloy 6061 sample retrieved on 12 months exposure from Daytona Beach site. (a) 100X magnification (b) 250X magnification, (c) 500X magnification, and (d) 2500X magnification.

Distribution Statement A. Approved for Public Release.

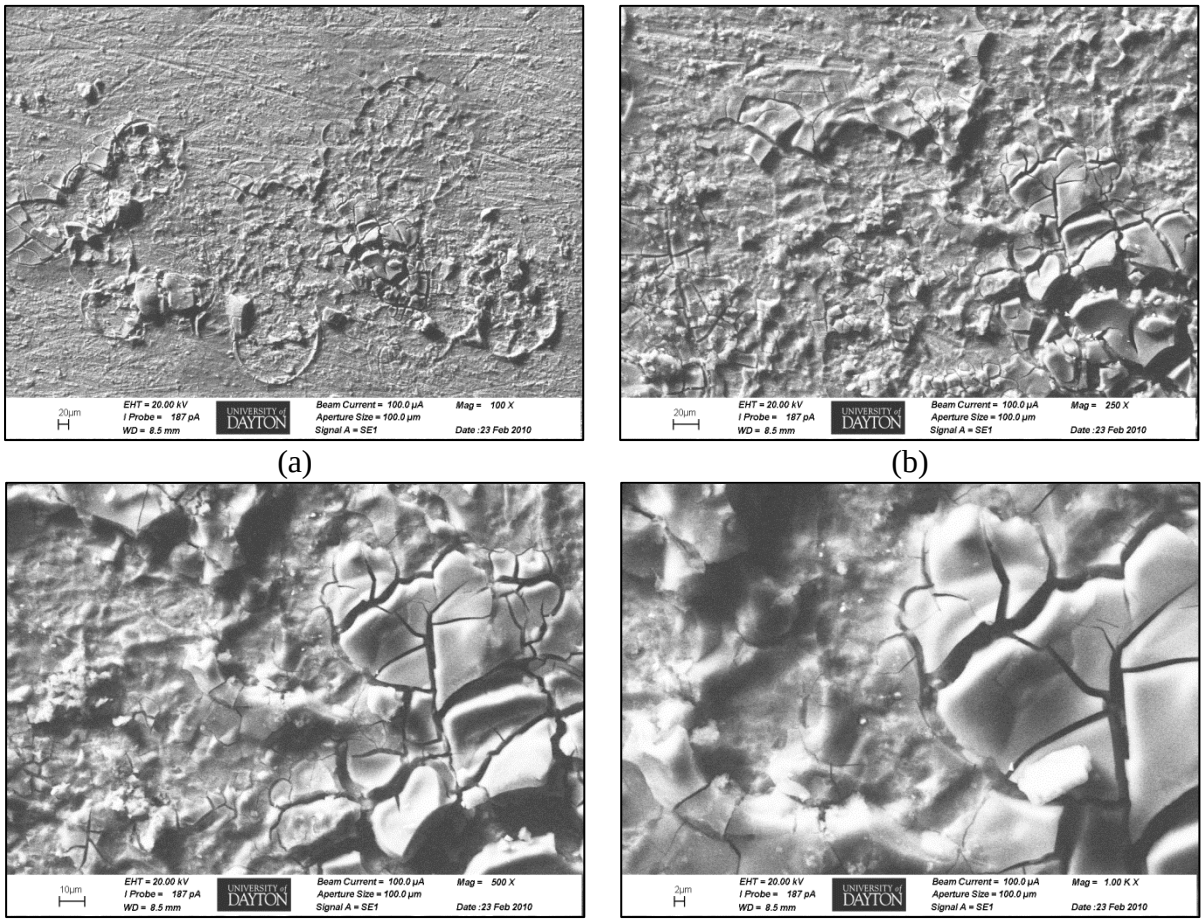

Figure B-16. SEM images of aluminum alloy 6061 sample retrieved on 9 months exposure from Daytona Beach site. (a) 100X magnification (b) 250X magnification, (c) 500X magnification, and (d) 1000X magnification.

Distribution Statement A. Approved for Public Release.

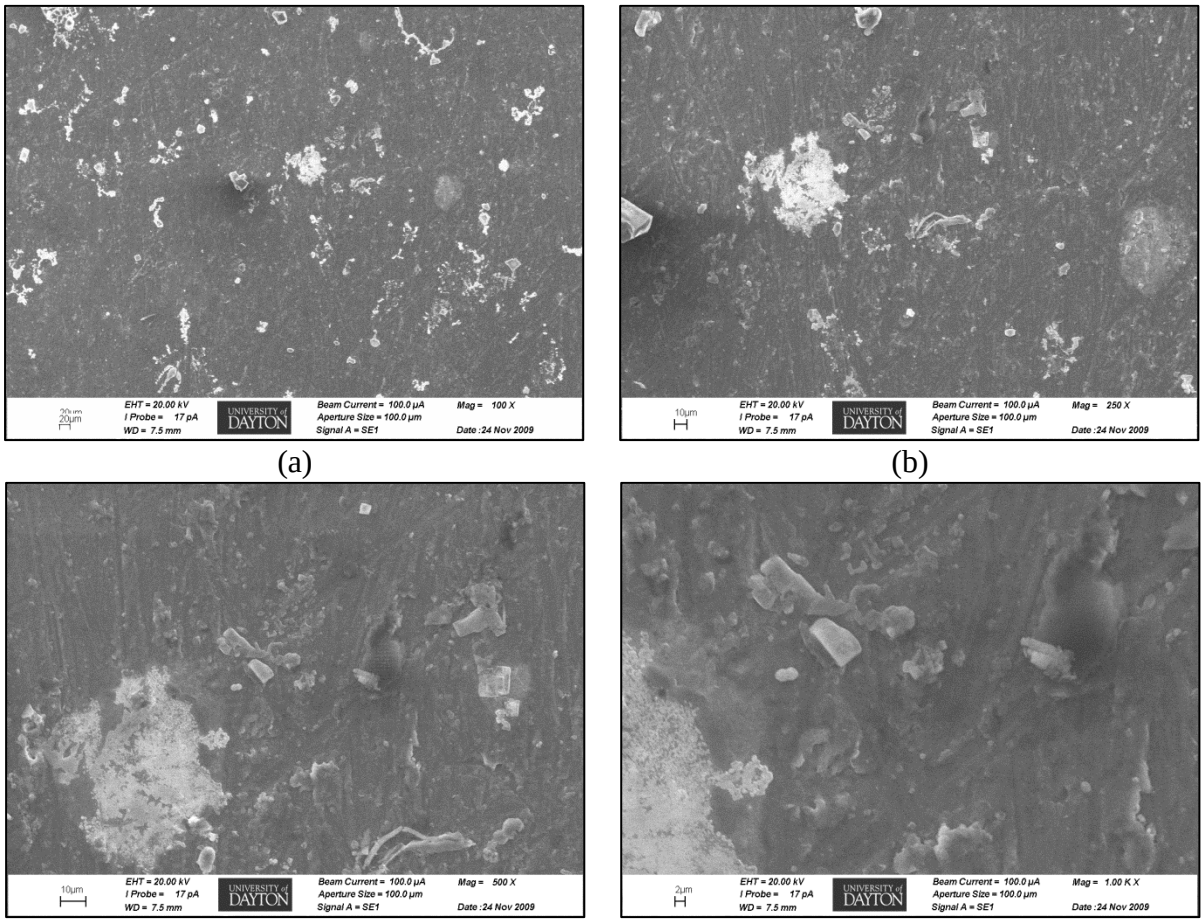

(a) (b)

(c) (d)

Figure B-17. SEM images of aluminum alloy 6061 sample retrieved on 6 months exposure from Daytona Beach site. (a) 100X magnification (b) 250X magnification, (c) 500X magnification, and (d) 1000X magnification.

.

Distribution Statement A. Approved for Public Release.

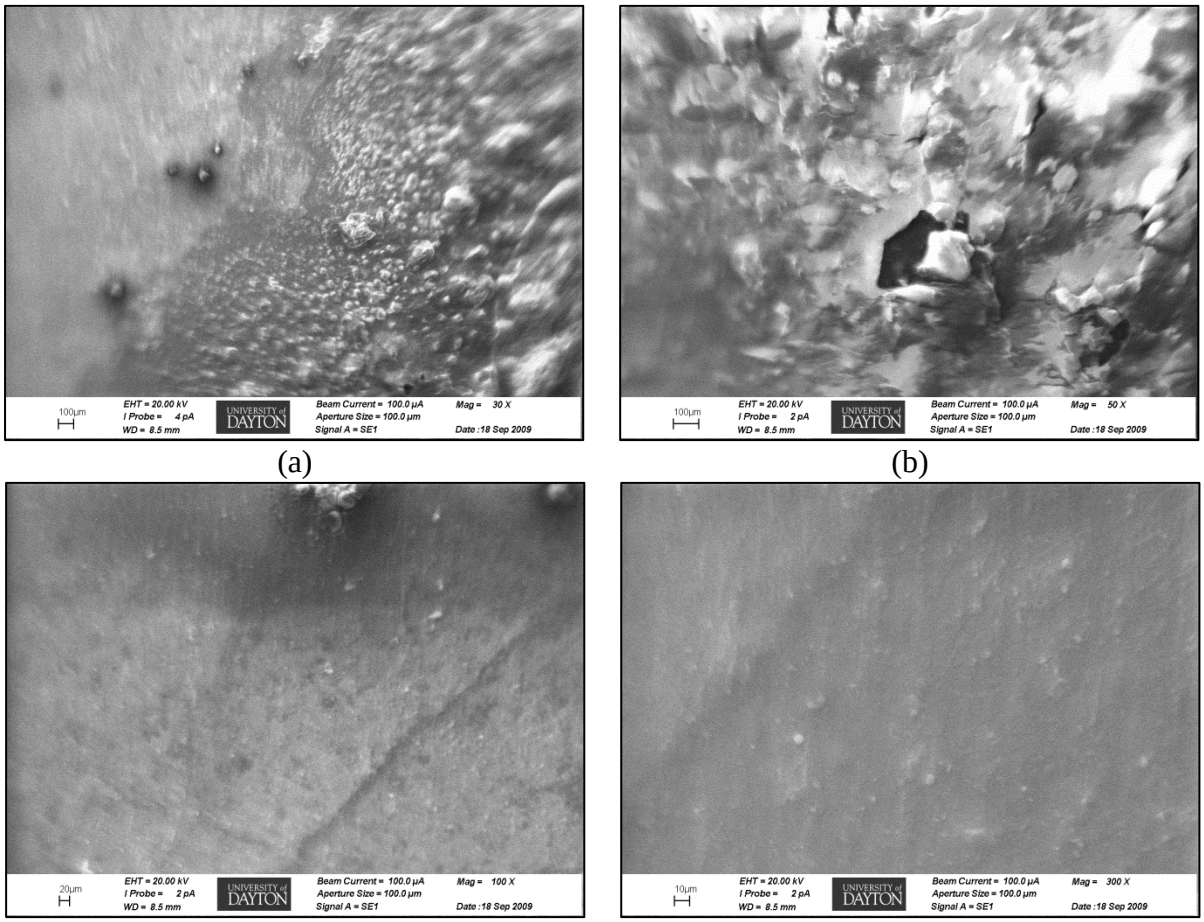

Figure B-18. SEM images of aluminum alloy 6061 sample retrieved on 3 months exposure from Daytona Beach site. (a) 30X magnification (b) 50X magnification, (c) 100X magnification, and (d) 300X magnification.

Distribution Statement A. Approved for Public Release.

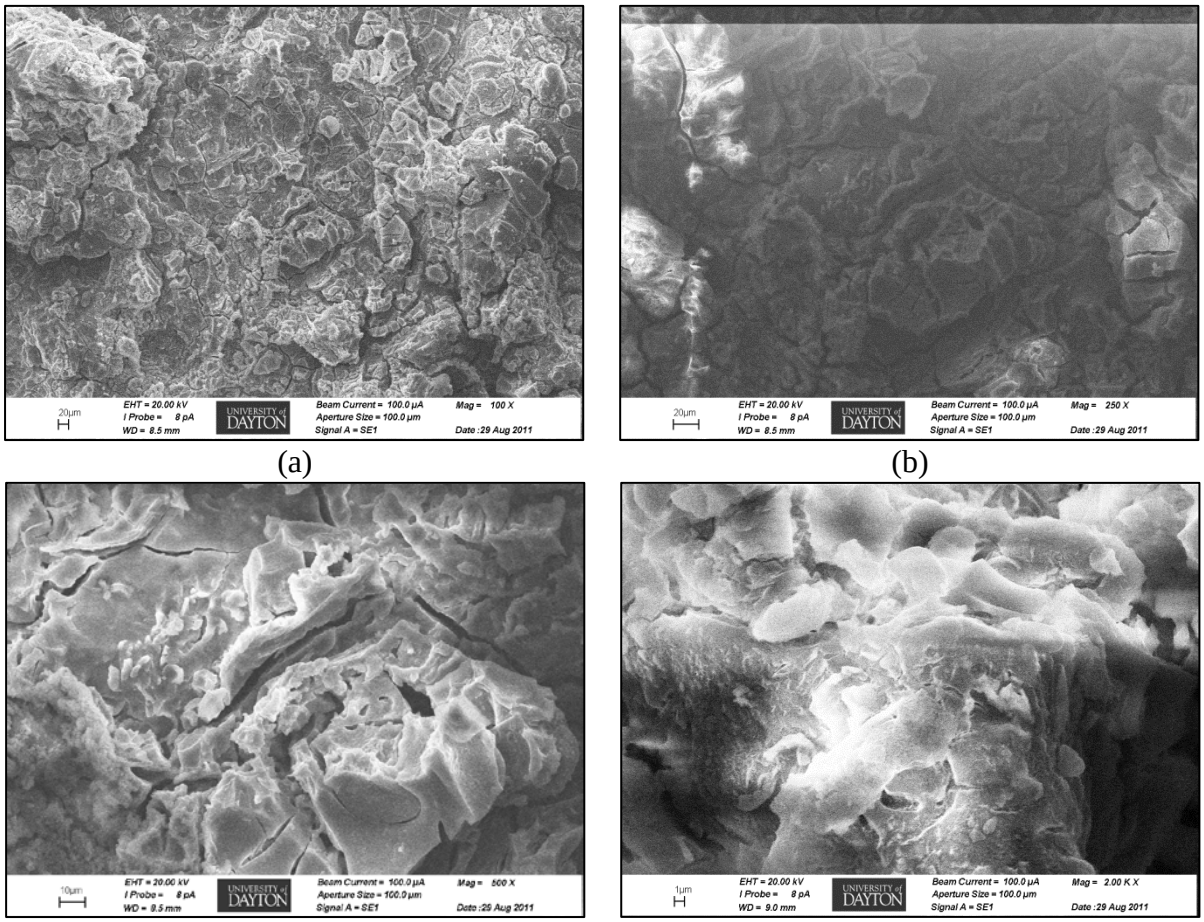

Figure B-19. SEM images of aluminum alloy 2024 sample retrieved on 24 months exposure from Daytona Beach site. (a) 100X magnification (b) 250X magnification, (c) 500X magnification, and (d) 2500X magnification.

Distribution Statement A. Approved for Public Release.

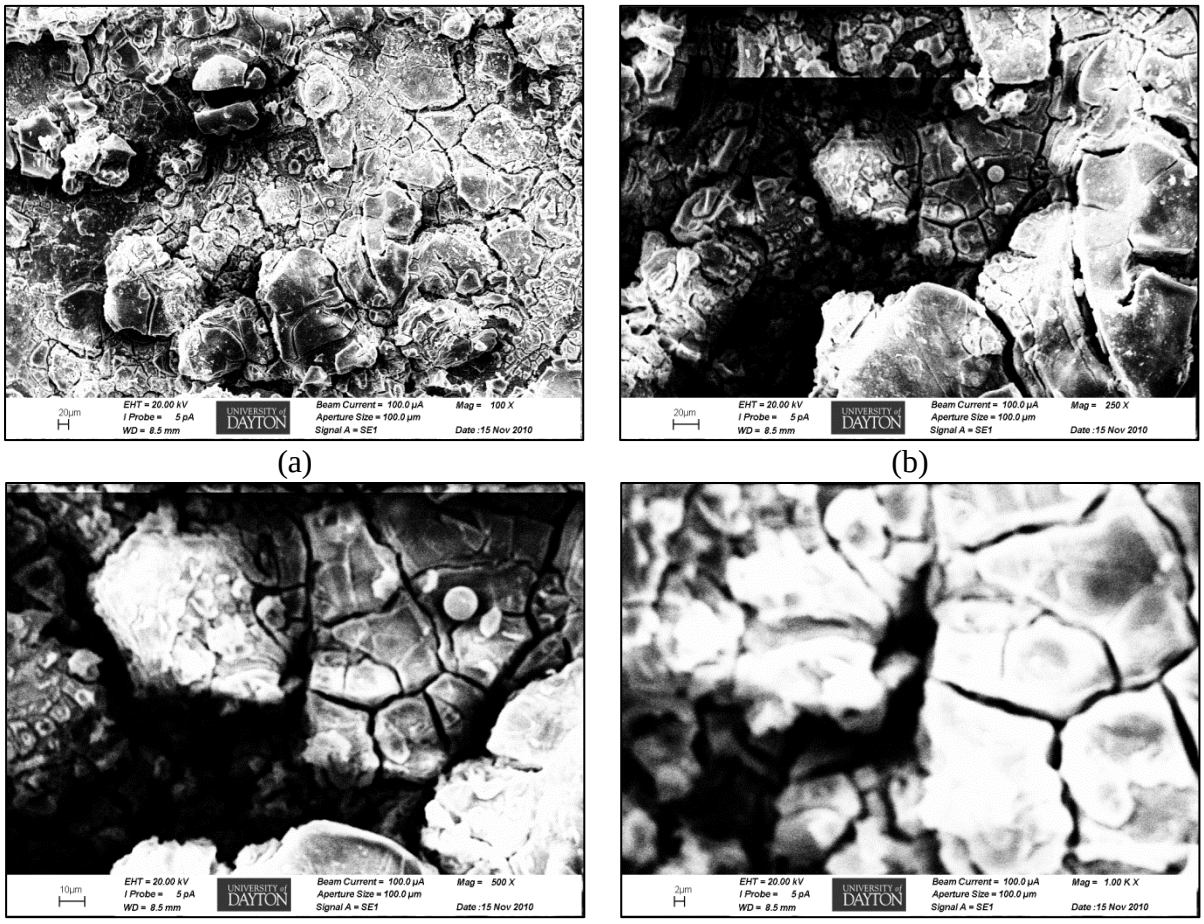

(a) (b)

(c) (d)

Figure B-20. SEM images of aluminum alloy 2024 sample retrieved on 18 months exposure from Daytona Beach site. (a) 100X magnification (b) 250X magnification, (c) 500X magnification, and (d) 1000X magnification.

Distribution Statement A. Approved for Public Release.

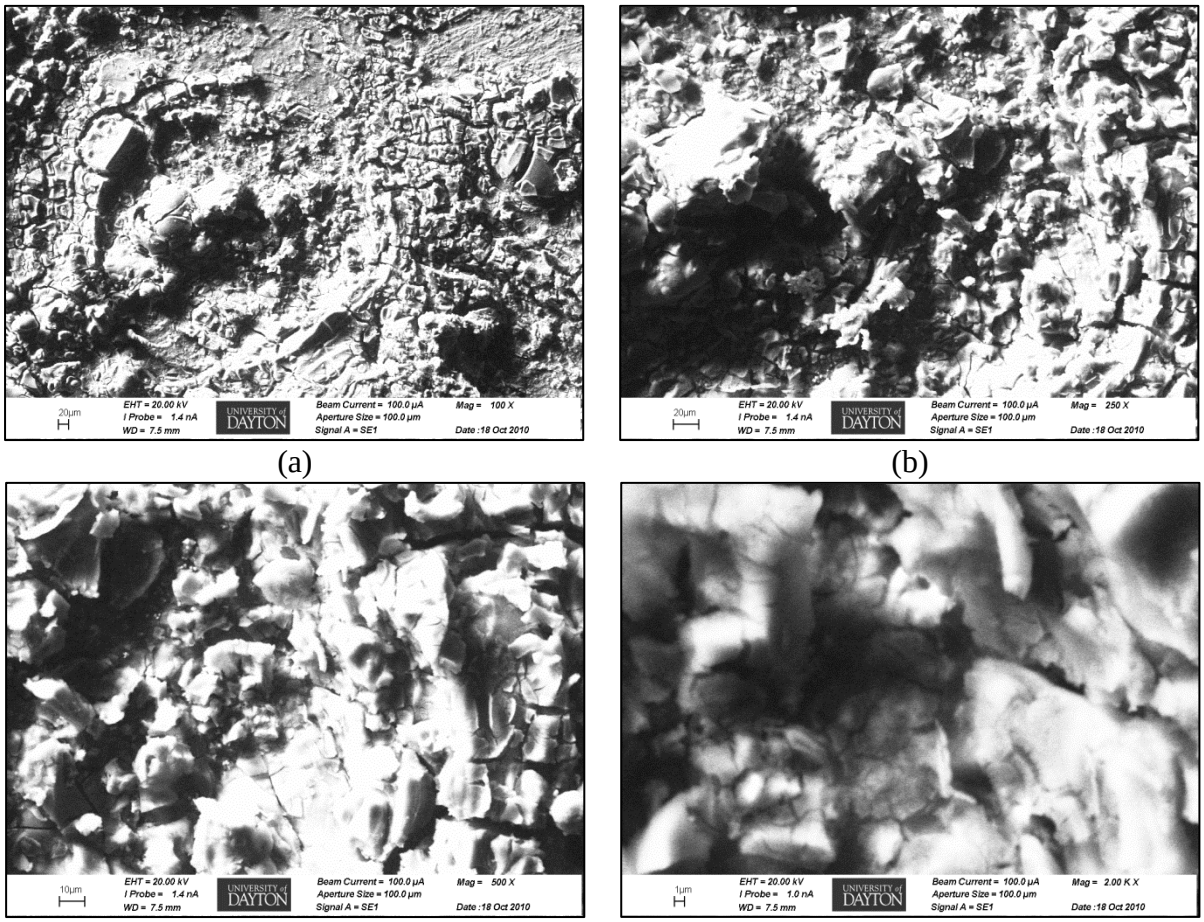

Figure B-21. SEM images of aluminum alloy 2024 sample retrieved on 12 months exposure from Daytona Beach site. (a) 100X magnification (b) 250X magnification, (c) 500X magnification, and (d) 2500X magnification.

Distribution Statement A. Approved for Public Release.

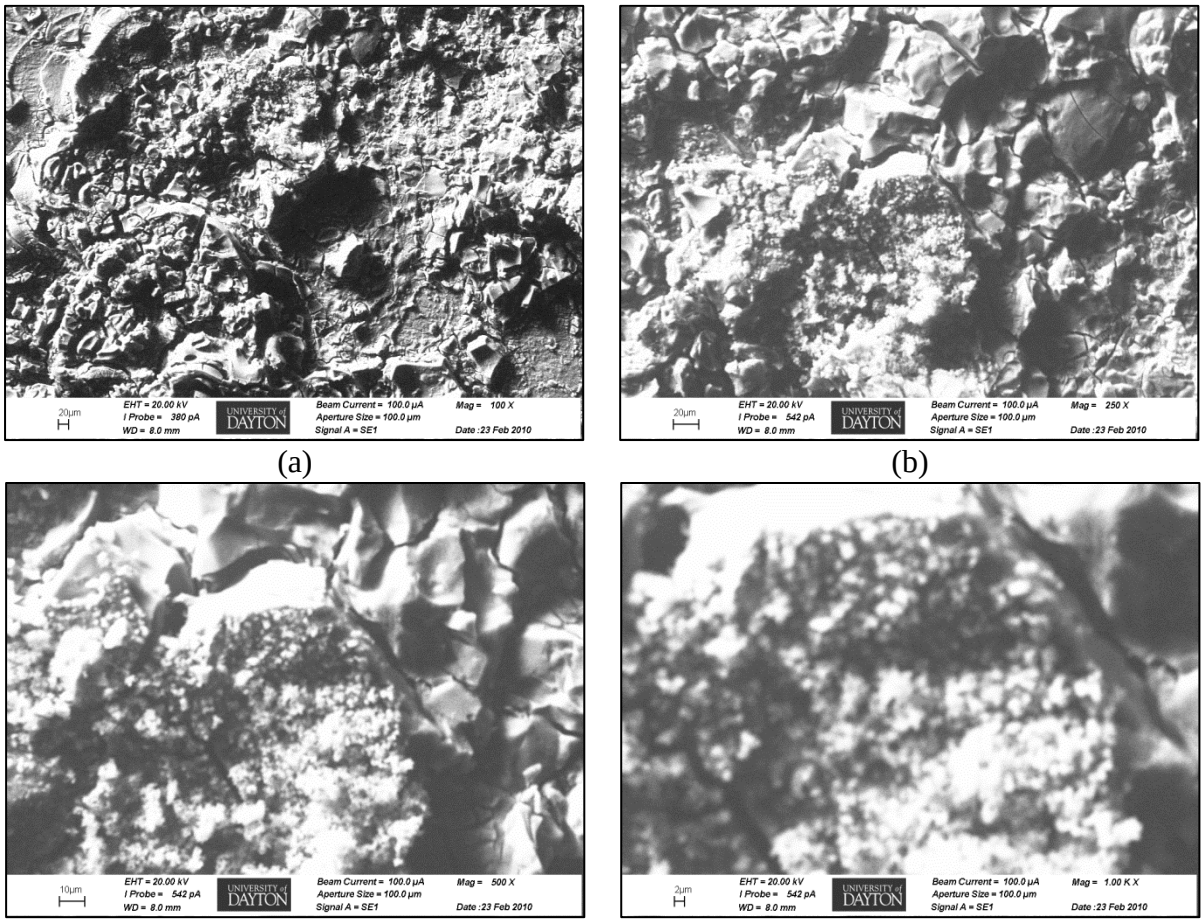

Figure B-22. SEM images of aluminum alloy 2024 sample retrieved on 9 months exposure from Daytona Beach site. (a) 100X magnification (b) 250X magnification, (c) 500X magnification, and (d) 1000X magnification.

Distribution Statement A. Approved for Public Release.

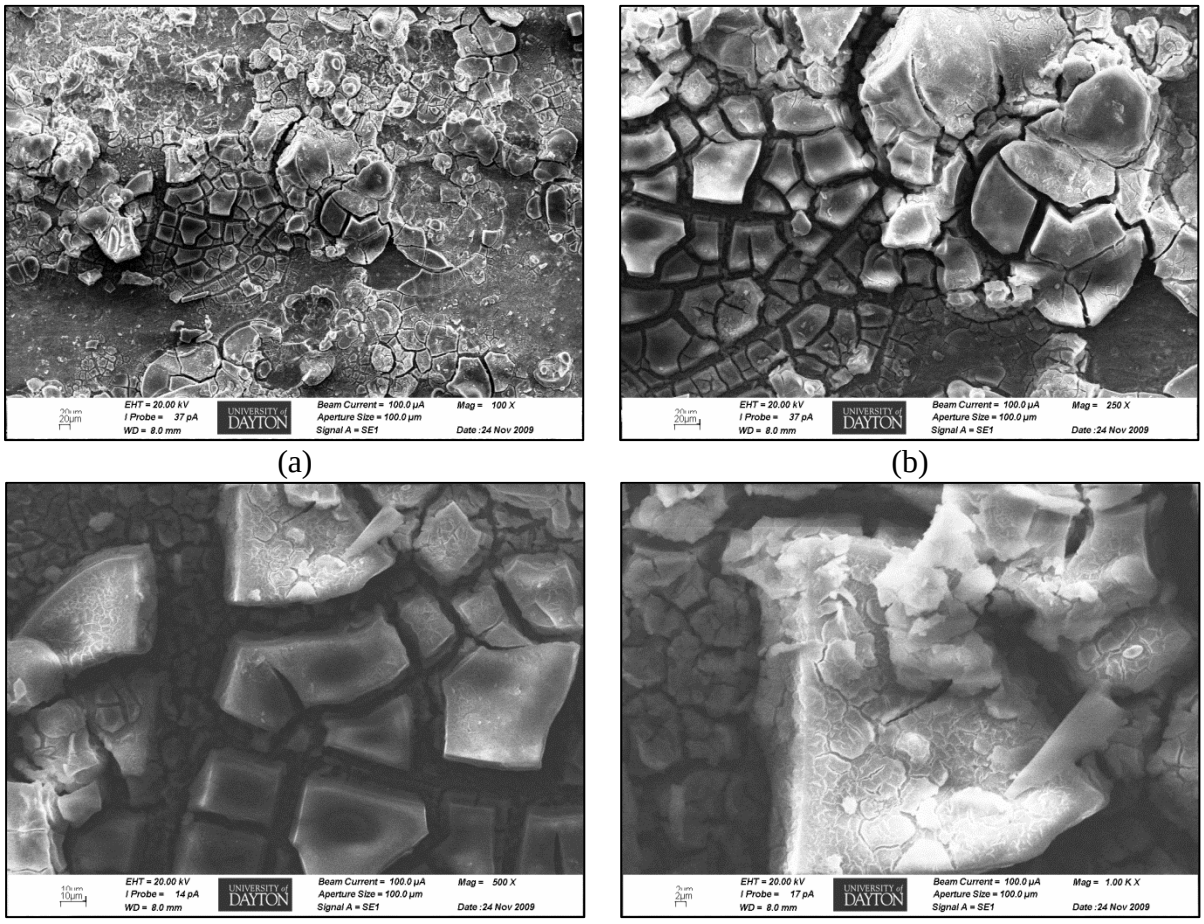

Figure B-23. SEM images of aluminum alloy 2024 sample retrieved on 6 months exposure from Daytona Beach site. (a) 100X magnification (b) 250X magnification, (c) 500X magnification, and (d) 1000X magnification.

Distribution Statement A. Approved for Public Release.

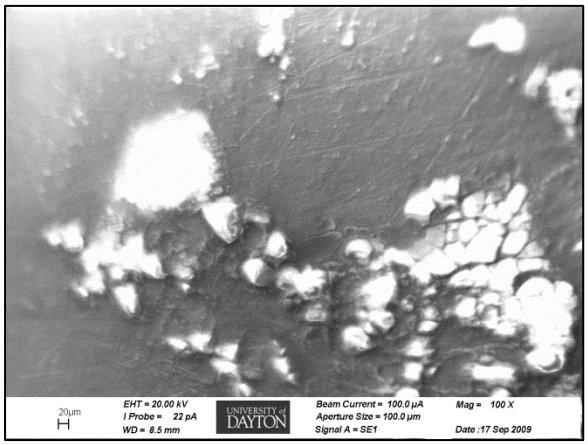

(a)

Figure B-24. SEM images of aluminum alloy 2024 sample retrieved on 3 months exposure from Daytona Beach site. (a) 100X magnification.

Distribution Statement A. Approved for Public Release.

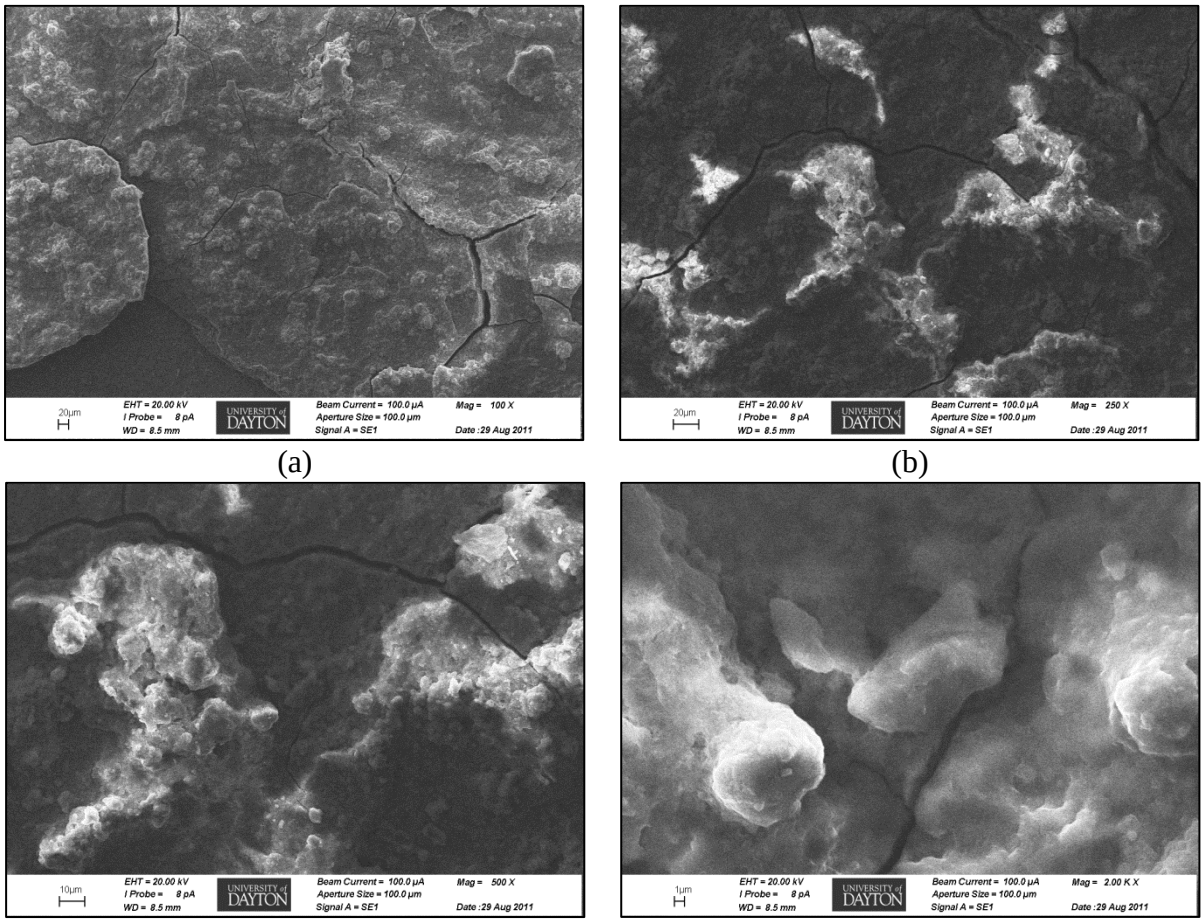

Figure B-25. SEM images of pure copper sample retrieved on 24 months exposure from Daytona Beach site. (a) 100X magnification (b) 250X magnification, (c) 500X magnification, and (d) 2000X magnification.

Distribution Statement A. Approved for Public Release.

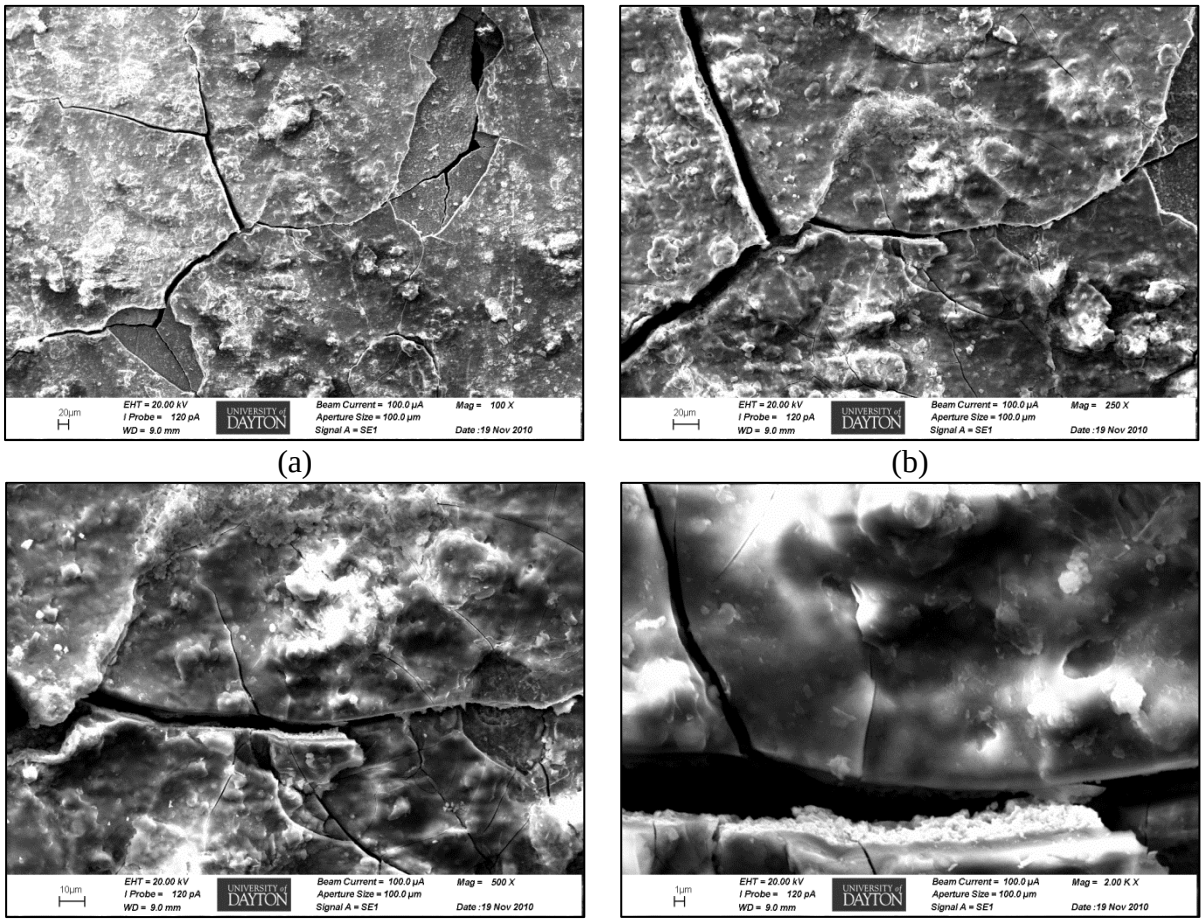

Figure B-26. SEM images of pure copper sample retrieved on 18 months exposure from Daytona Beach site. (a) 100X magnification (b) 250X magnification, (c) 500X magnification, and (d) 2000X magnification.

Distribution Statement A. Approved for Public Release.

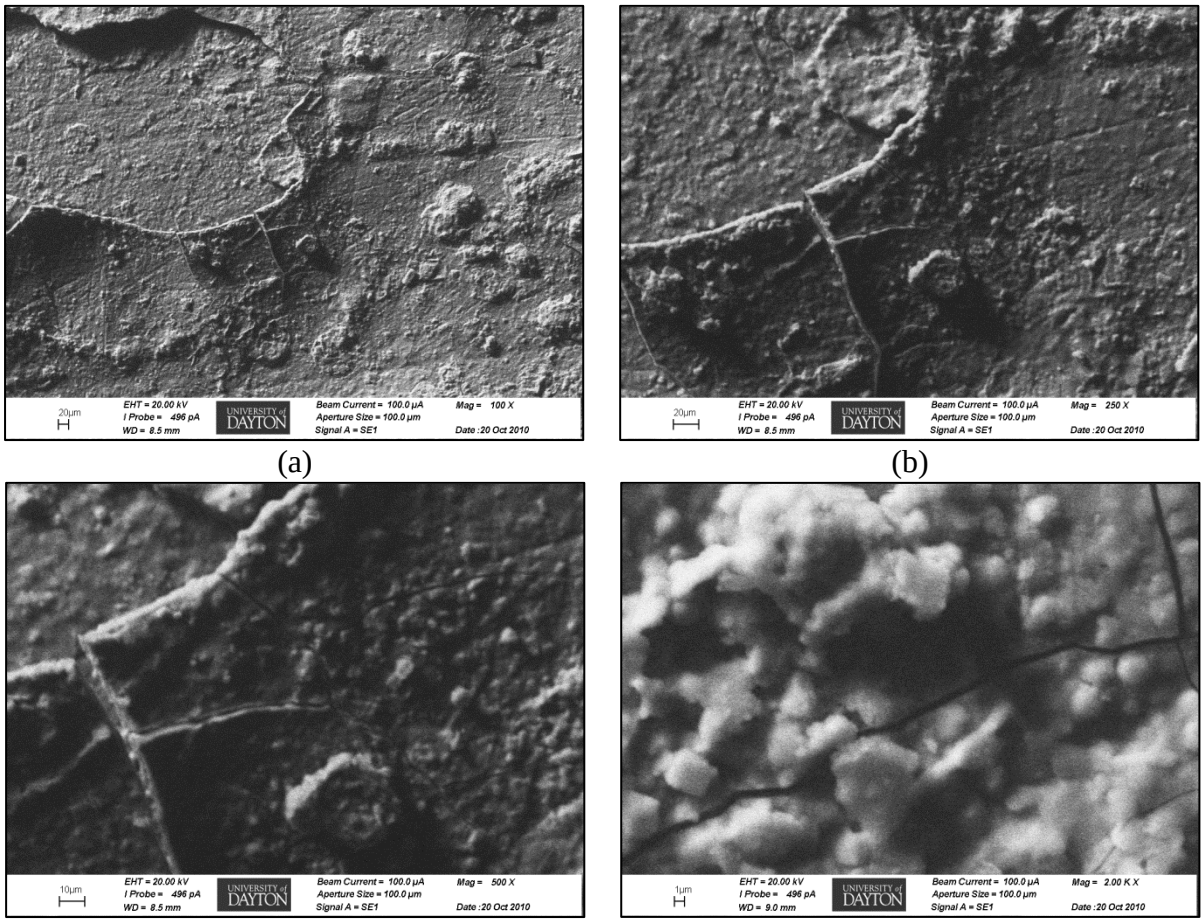

Figure B-27. SEM images of pure copper sample retrieved on 12 months exposure from Daytona Beach site. (a) 100X magnification (b) 250X magnification, (c) 500X magnification, and (d) 2000X magnification.

Distribution Statement A. Approved for Public Release.

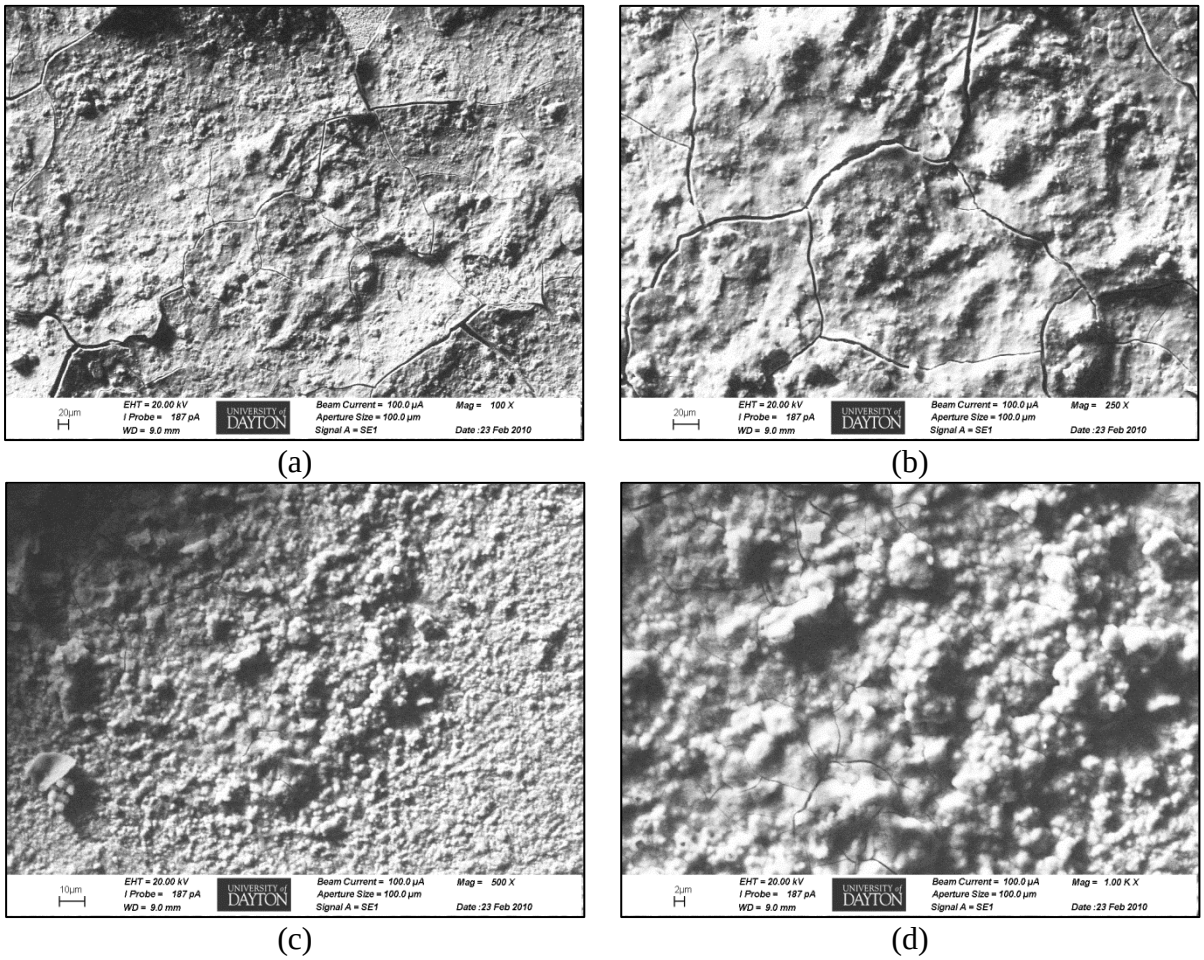

Figure B-28. SEM images of pure copper sample retrieved on 9 months exposure from Daytona Beach site. (a) 100X magnification (b) 250X magnification, (c) 500X magnification, and (d) 1000X magnification.

Distribution Statement A. Approved for Public Release.

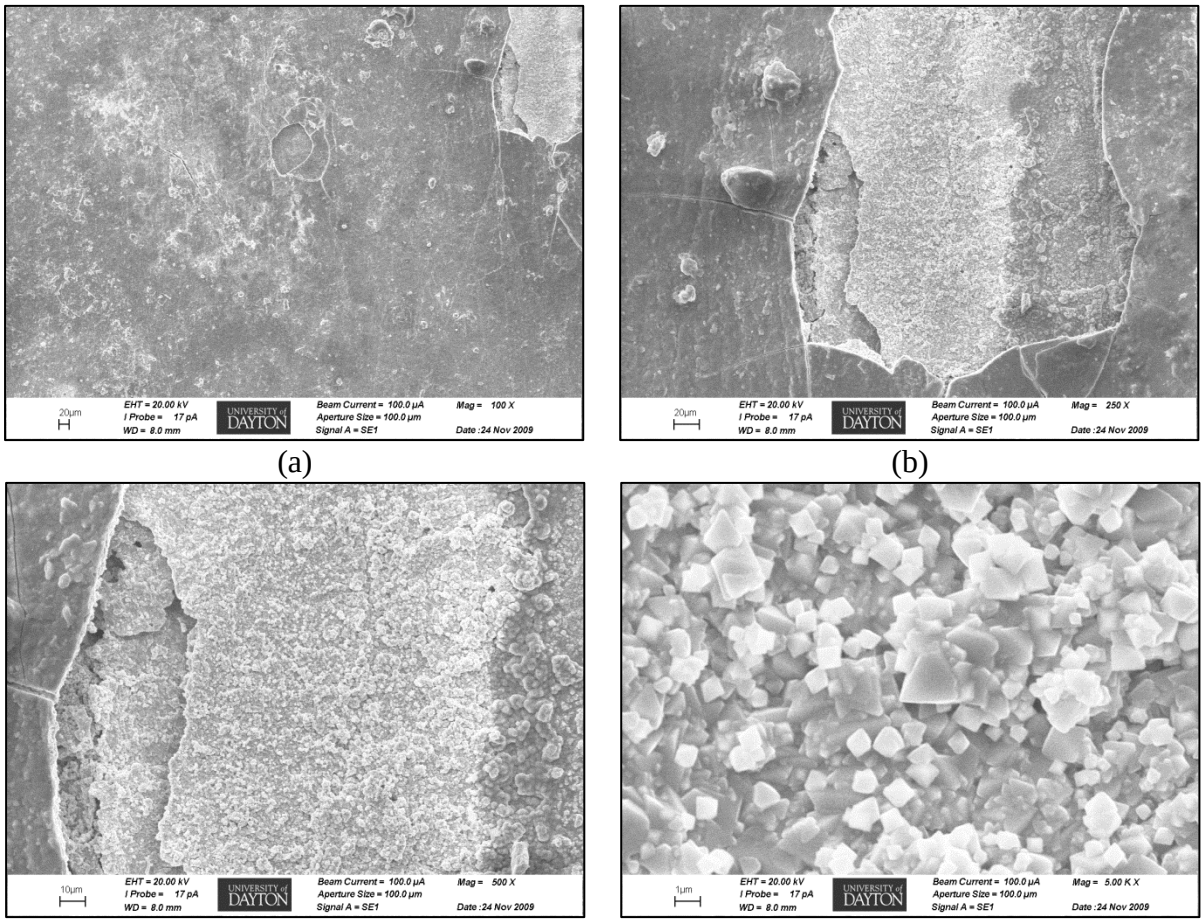

Figure B-29. SEM images of pure copper sample retrieved on 6 months exposure from Daytona Beach site. (a) 100X magnification (b) 250X magnification, (c) 500X magnification, and (d) 5000X magnification.

Distribution Statement A. Approved for Public Release.

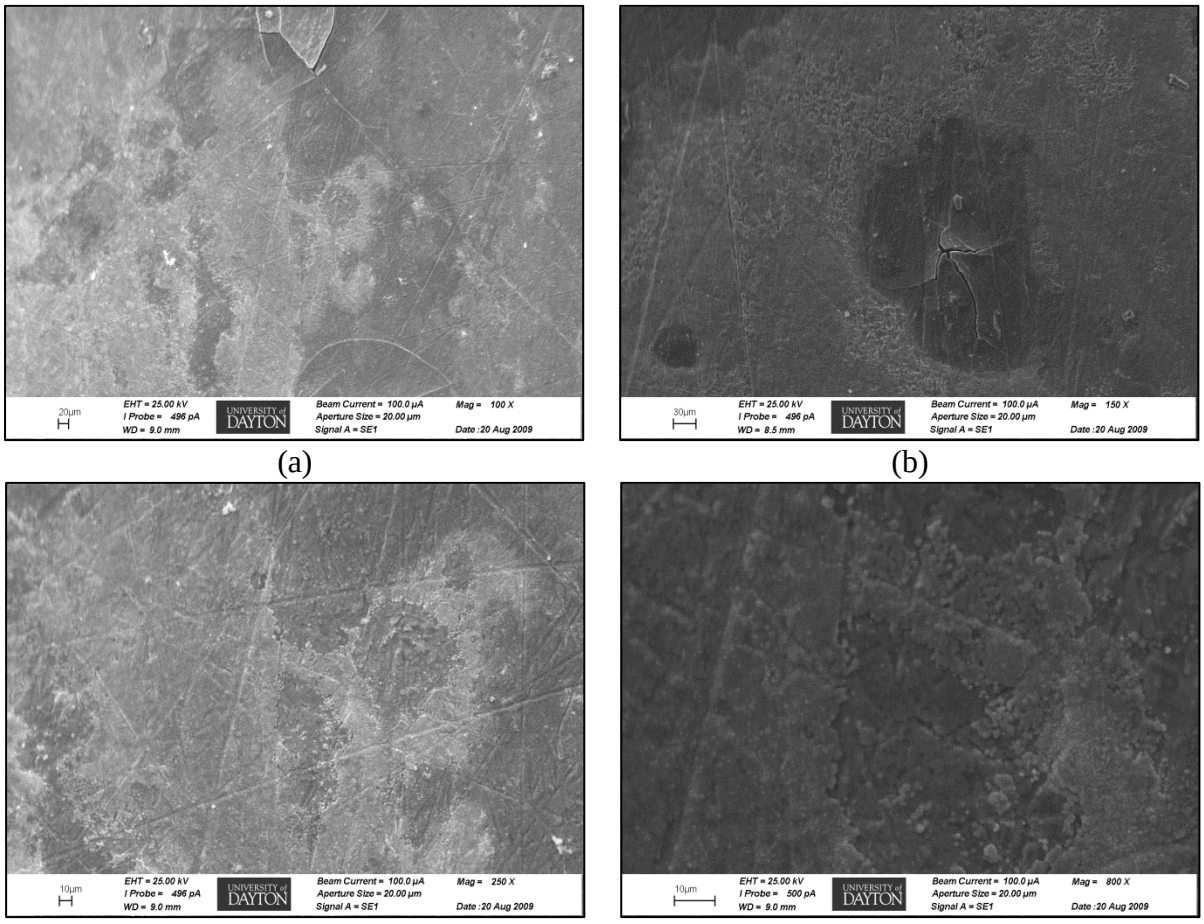

(a) (b)

(c) (d)

Figure B-30. SEM images of pure copper sample retrieved on 3 months exposure from Daytona Beach site. (a) 100X magnification (b) 150X magnification, (c) 250X magnification, and (d) 800X magnification.

Distribution Statement A. Approved for Public Release.

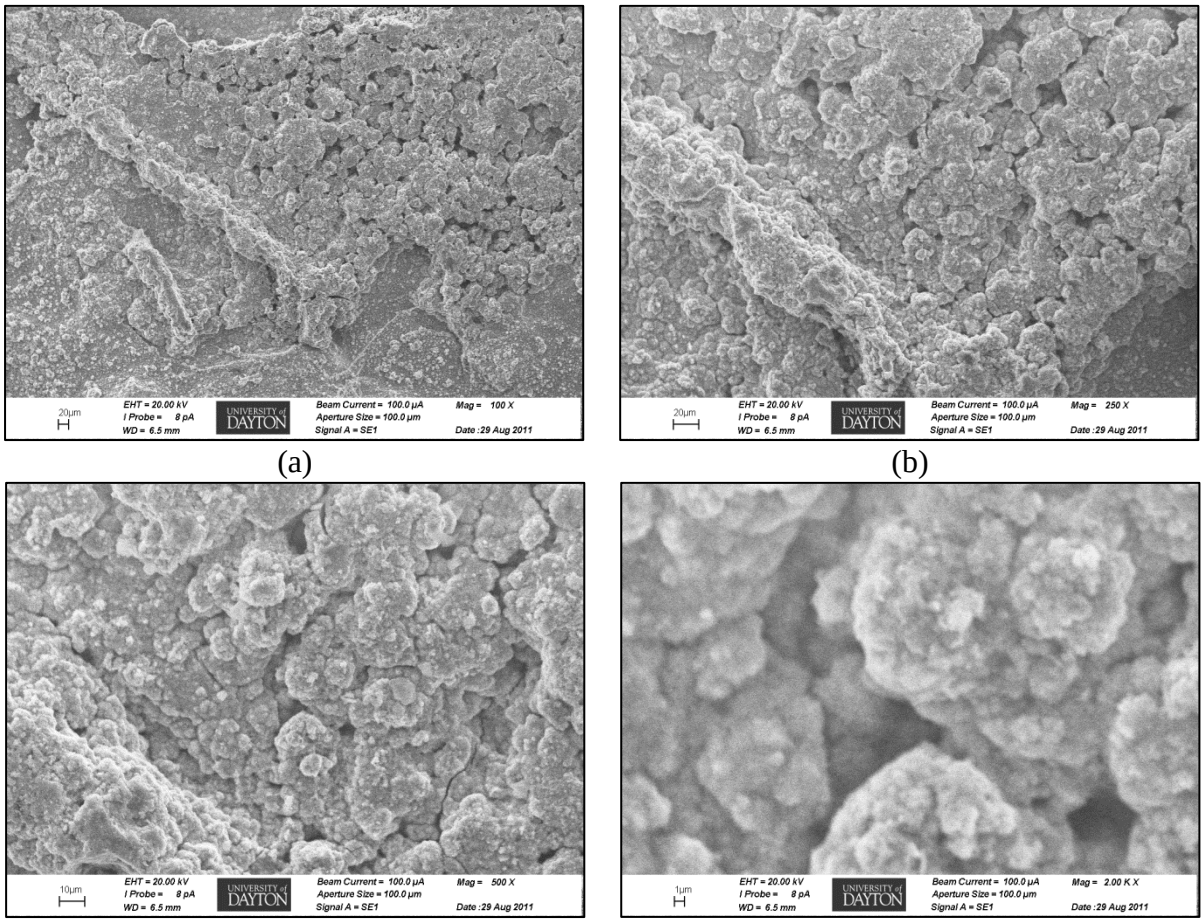

Figure B-31. SEM images of 1010 steel sample retrieved on 24 months exposure from Daytona Beach site. (a) 100X magnification (b) 250X magnification, (c) 500X magnification, and (d) 2000X magnification.

Distribution Statement A. Approved for Public Release.

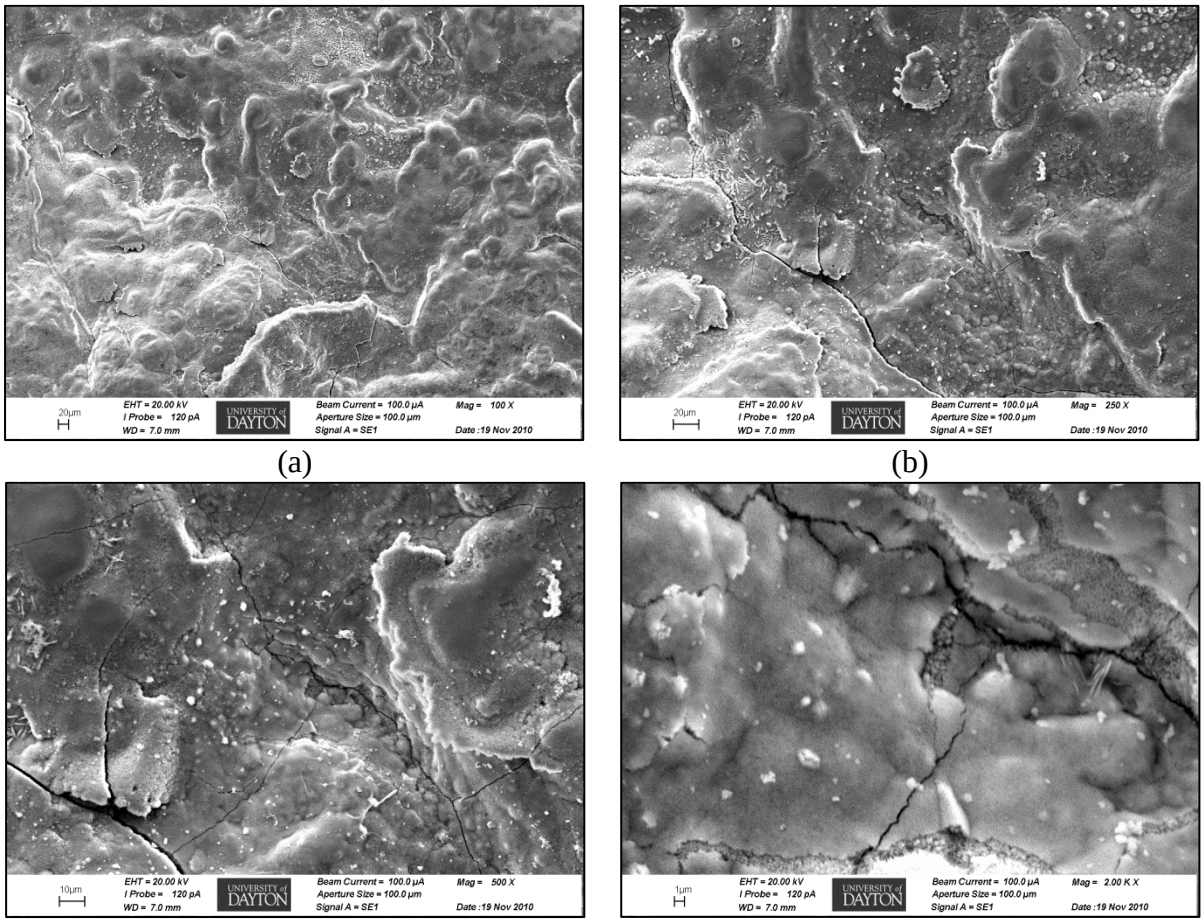

Figure B-32. SEM images of 1010 steel sample retrieved on 18 months exposure from Daytona Beach site. (a) 100X magnification (b) 250X magnification, (c) 500X magnification, and (d) 2000X magnification.

Distribution Statement A. Approved for Public Release.

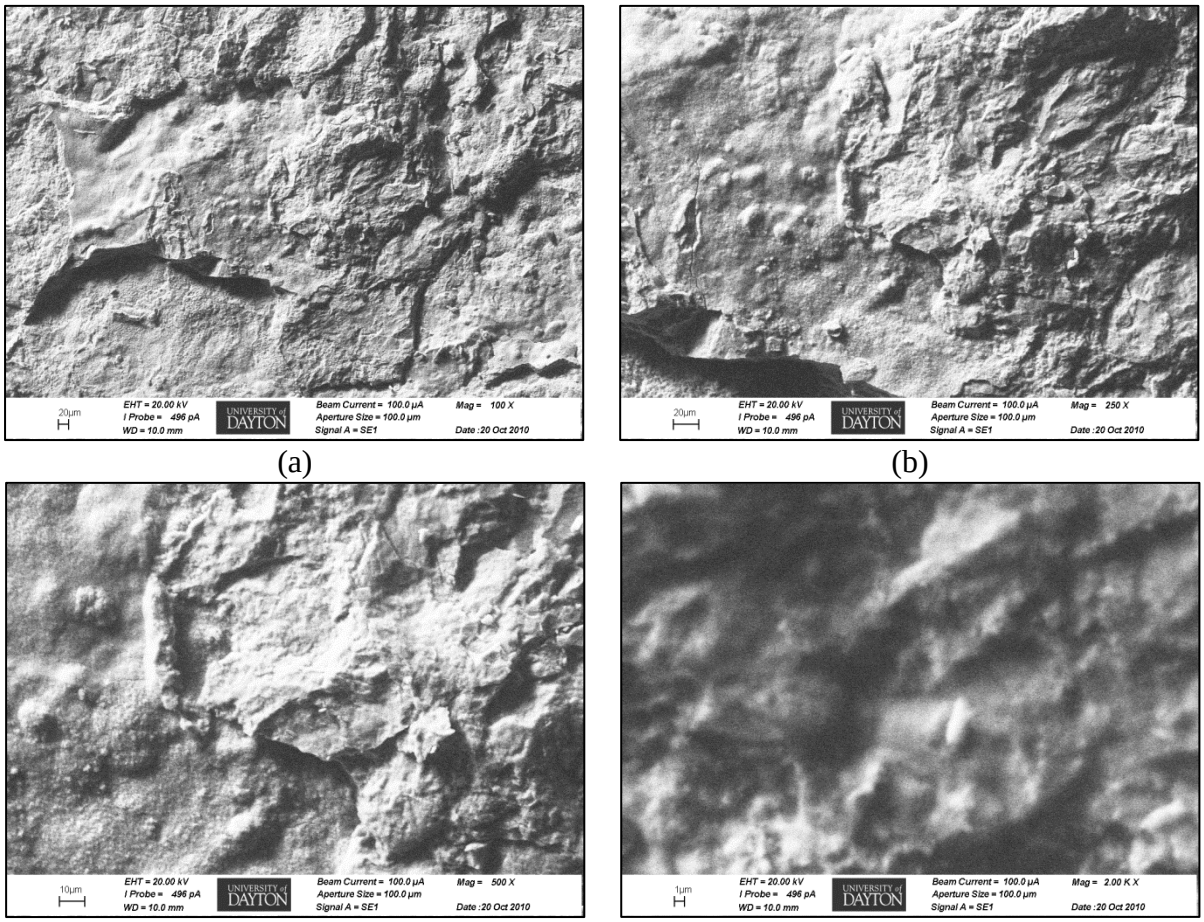

Figure B-33. SEM images of 1010 steel sample retrieved on 12 months exposure from Daytona Beach site. (a) 100X magnification (b) 250X magnification, (c) 500X magnification, and (d) 2000X magnification.

Distribution Statement A. Approved for Public Release.

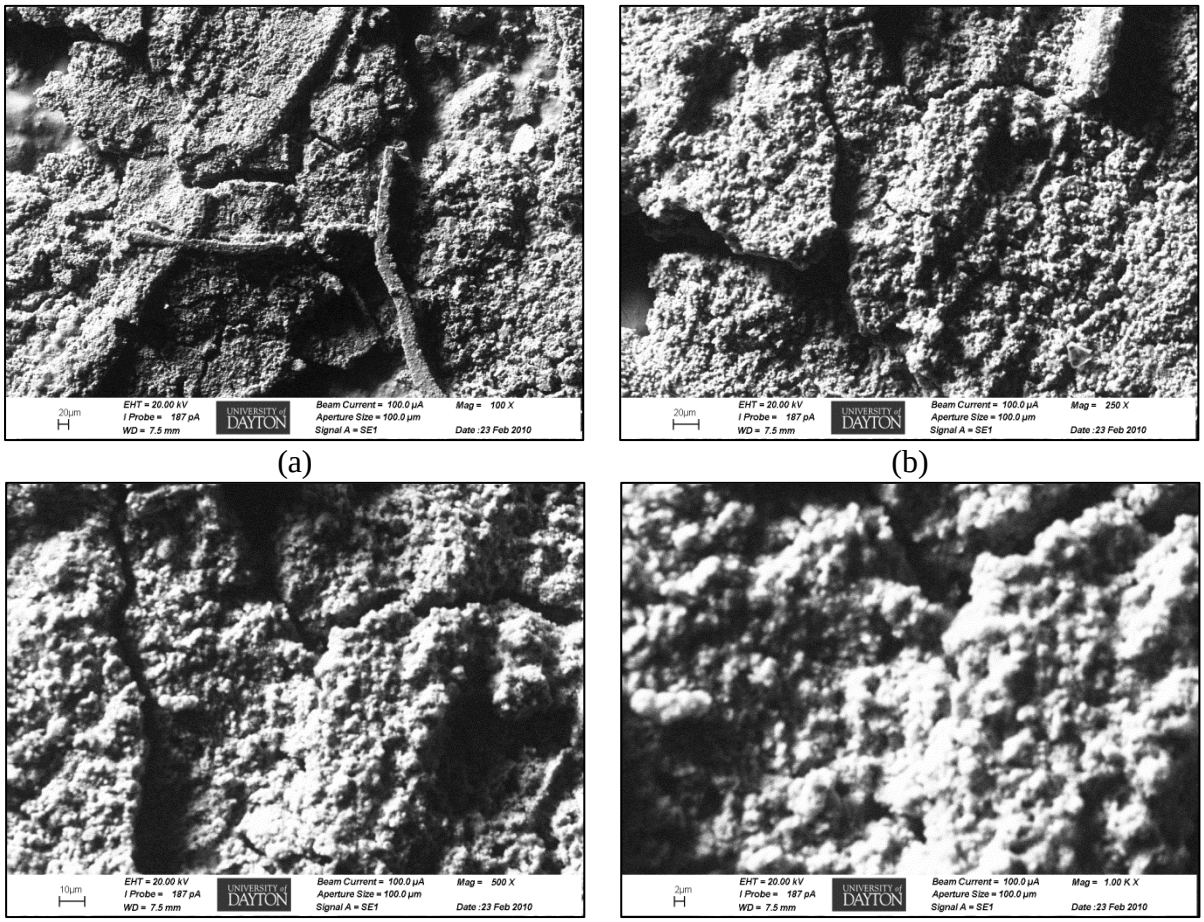

Figure B-34. SEM images of 1010 steel sample retrieved on 9 months exposure from Daytona Beach site. (a) 100X magnification (b) 250X magnification, (c) 500X magnification, and (d) 1000X magnification.

Distribution Statement A. Approved for Public Release.

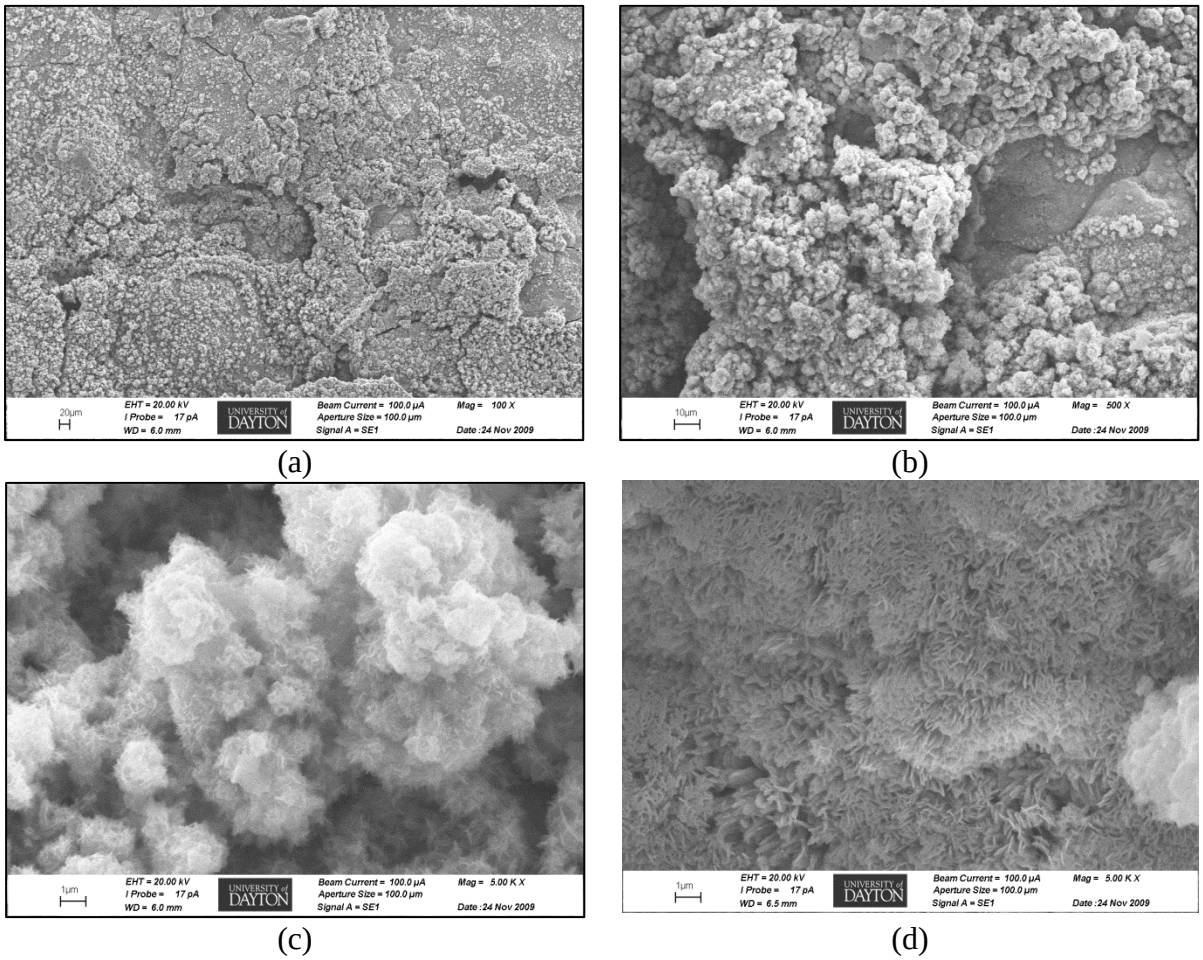

(a) (b)

(c) (d)

Figure B-35. SEM images of 1010 steel sample retrieved on 6 months exposure from Daytona Beach site. (a) 100X magnification (b) 500X magnification, (c) 5000X magnification, and (d) 5000X magnification.

Distribution Statement A. Approved for Public Release.

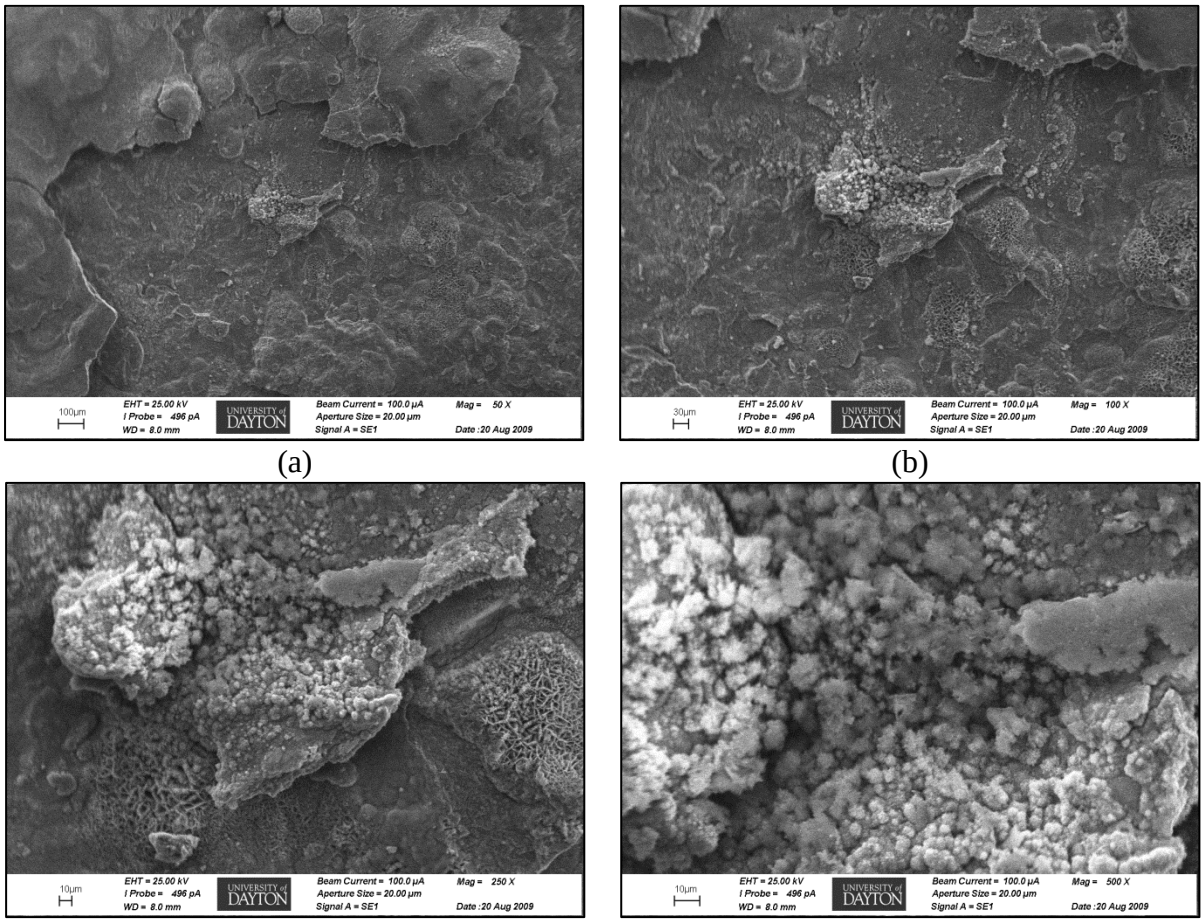

(a) (b)

(c) (d)

Figure B-36. SEM images of 1010 steel sample retrieved on 3 months exposure from Daytona Beach site. (a) 50X magnification (b) 100X magnification, (c) 250X magnification, and (d) 500X magnification.

Distribution Statement A. Approved for Public Release.

Appendix C

Scanning Electron Microscopy Images

(Pt. Judith, RI)

Distribution Statement A. Approved for Public Release.

FIGURES

Page

Figure C-1. SEM images of pure silver sample retrieved on 24 months exposure from Pt. Judith site. (a) 100X magnification (b) 250X magnification, (c) 500X magnification, and (d) 2000X magnification..... 5

Figure C-2.SEM images of pure silver sample retrieved on 18 months exposure from Pt. Judith site. (a) 100X magnification (b) 250X magnification, (c) 500X magnification, and (d) 2000X magnification..... 6

Figure C-3. SEM images of pure silver sample retrieved on 12 months exposure from Pt. Judith site. (a) 100X magnification (b) 250X magnification, (c) 500X magnification, and (d) 2000X magnification..... 7

Figure C-4. SEM images of pure silver sample retrieved on 9 months exposure from Pt. Judith site. (a) 100X magnification (b) 250X magnification, (c) 500X magnification, and (d) 1000X magnification..... 8

Figure C-5. SEM images of pure silver sample retrieved on 6 months exposure from Pt. Judith site. (a) 100X magnification (b) 250X magnification, (c) 500X magnification, and (d) 1000X magnification..... 9

Figure C-6. SEM images of pure silver sample retrieved on 3 months exposure from Pt. Judith site. (a) 50X magnification (b) 500X magnification, and (c) 2000X magnification..... 10

Figure C-7. SEM images of aluminum alloy 7075 sample retrieved on 24 months exposure from Pt. Judith site. (a) 100X magnification (b) 250X magnification, (c) 500X magnification, and (d) 2000X magnification..... 11

Figure C-8. SEM images of aluminum alloy 7075 sample retrieved on 18 months exposure from Pt. Judith site. (a) 100X magnification (b) 250X magnification, (c) 500X magnification, and (d) 2000X magnification..... 12

Figure C-9. SEM images of aluminum alloy 7075 sample retrieved on 12 months exposure from Pt. Judith site. (a) 100X magnification (b) 250X magnification, (c) 500X magnification, and (d) 2000X magnification..... 13

Figure C-10. SEM images of aluminum alloy 7075 sample retrieved on 9 months exposure from Pt. Judith site. (a) 100X magnification (b) 250X magnification, (c) 500X magnification, and (d) 1000X magnification..... 14

Figure C-11. SEM images of aluminum alloy 7075 sample retrieved on 6 months exposure from Pt. Judith site. (a) 100X magnification (b) 250X magnification, (c) 500X magnification, and (d) 1000X magnification..... 15

Figure C-12. SEM images of aluminum alloy 7075 sample retrieved on 3 months exposure from Pt. Judith site. (a) 50X magnification and (b) 500X magnification 16

Figure C-13. SEM images of aluminum alloy 6061 sample retrieved on 24 months exposure from Pt. Judith site. (a) 100X magnification (b) 250X magnification, (c) 500X magnification, and (d) 2000X magnification..... 17

Figure C-14. SEM images of aluminum alloy 6061 sample retrieved on 18 months exposure from Pt. Judith site. (a) 100X magnification (b) 250X magnification, (c) 500X magnification, and (d) 2000X magnification..... 18

Distribution Statement A. Approved for Public Release.

Figure C-15. SEM images of aluminum alloy 6061 sample retrieved on 12 months exposure from Pt. Judith site. (a) 100X magnification (b) 250X magnification, (c) 500X magnification, and (d) 2000X magnification. 19

Figure C-16. SEM images of aluminum alloy 6061 sample retrieved on 9 months exposure from Pt. Judith site. (a) 100X magnification (b) 250X magnification, (c) 500X magnification, and (d) 1000X magnification. 20

Figure C-17. SEM images of aluminum alloy 6061 sample retrieved on 6 months exposure from Pt. Judith site. (a) 100X magnification (b) 250X magnification, (c) 500X magnification, and (d) 1000X magnification. 21

Figure C-18. SEM images of aluminum alloy 6061 sample retrieved on 3 months exposure from Pt. Judith site. (a) 26X magnification (b) 100X magnification, (c) 500X magnification, and (d) 2000X magnification. 22

Figure C-19. SEM images of aluminum alloy 2024 sample retrieved on 24 months exposure from Pt. Judith site. (a) 100X magnification (b) 250X magnification, (c) 500X magnification, and (d) 2000X magnification. 23

Figure C-20. SEM images of aluminum alloy 2024 sample retrieved on 18 months exposure from Pt. Judith site. (a) 100X magnification (b) 250X magnification, (c) 500X magnification, and (d) 2000X magnification. 24

Figure C-21. SEM images of aluminum alloy 2024 sample retrieved on 12 months exposure from Pt. Judith site. (a) 100X magnification (b) 250X magnification, (c) 500X magnification, and (d) 2000X magnification. 25

Figure C-22. SEM images of aluminum alloy 2024 sample retrieved on 9 months exposure from Pt. Judith site. (a) 100X magnification (b) 250X magnification, (c) 500X magnification, and (d) 1000X magnification. 26

Figure C-23. SEM images of aluminum alloy 2024 sample retrieved on 6 months exposure from Pt. Judith site. (a) 100X magnification (b) 250X magnification, (c) 500X magnification, and (d) 1000X magnification. 27

Figure C-24. SEM images of aluminum alloy 2024 sample retrieved on 3 months exposure from Pt. Judith site. (a) 50X magnification (b) 100X magnification, (c) 500X magnification, and (d) 1500X magnification. 28

Figure C-25. SEM images of pure copper sample retrieved on 24 months exposure from Pt. Judith site. (a) 100X magnification (b) 250X magnification, (c) 500X magnification, and (d) 2000X magnification..... 29

Figure C-26. SEM images of pure copper sample retrieved on 18 months exposure from Pt. Judith site. (a) 100X magnification (b) 250X magnification, (c) 500X magnification, and (d) 2000X magnification..... 30

Figure C-27. SEM images of pure copper sample retrieved on 12 months exposure from Pt. Judith site. (a) 100X magnification (b) 250X magnification, (c) 500X magnification, and (d) 2000X magnification..... 31

Figure C-28. SEM images of pure copper sample retrieved on 9 months exposure from Pt. Judith site. (a) 100X magnification (b) 250X magnification, (c) 500X magnification, and (d) 1000X magnification..... 32

Figure C-29. SEM images of pure copper sample retrieved on 6 months exposure from Pt. Judith site. (a) 100X magnification (b) 250X magnification, (c) 500X magnification, and (d) 5000X magnification..... 33

Distribution Statement A. Approved for Public Release.

Figure C-30. SEM images of pure copper sample retrieved on 3 months exposure from Pt. Judith site. (a) 50X magnification (b) 500X magnification, and (c) 2000X magnification..... 34

Figure C-31. SEM images of 1010 steel sample retrieved on 24 months exposure from Pt. Judith site. (a) 100X magnification (b) 250X magnification, (c) 500X magnification, and (d) 2000X magnification..... 35

Figure C-32. SEM images of 1010 steel sample retrieved on 18 months exposure from Pt. Judith site. (a) 100X magnification (b) 250X magnification, (c) 500X magnification, and (d) 2000X magnification..... 36

Figure C-33. SEM images of 1010 steel sample retrieved on 12 months exposure from Pt. Judith site. (a) 100X magnification (b) 250X magnification, (c) 500X magnification, and (d) 2000X magnification..... 37

Figure C-34. SEM images of 1010 steel sample retrieved on 9 months exposure from Pt. Judith site. (a) 100X magnification (b) 250X magnification, (c) 500X magnification, and (d) 1000X magnification..... 38

Figure C-35. SEM images of 1010 steel sample retrieved on 6 months exposure from Pt. Judith site. (a) 100X magnification (b) 250X magnification, (c) 500X magnification, and (d) 1000X magnification..... 39

Figure C-36. SEM images of 1010 steel sample retrieved on 3 months exposure from Pt. Judith site. (a)100X magnification (b) 500X magnification, and (d) 2000X magnification. 40

Distribution Statement A. Approved for Public Release.

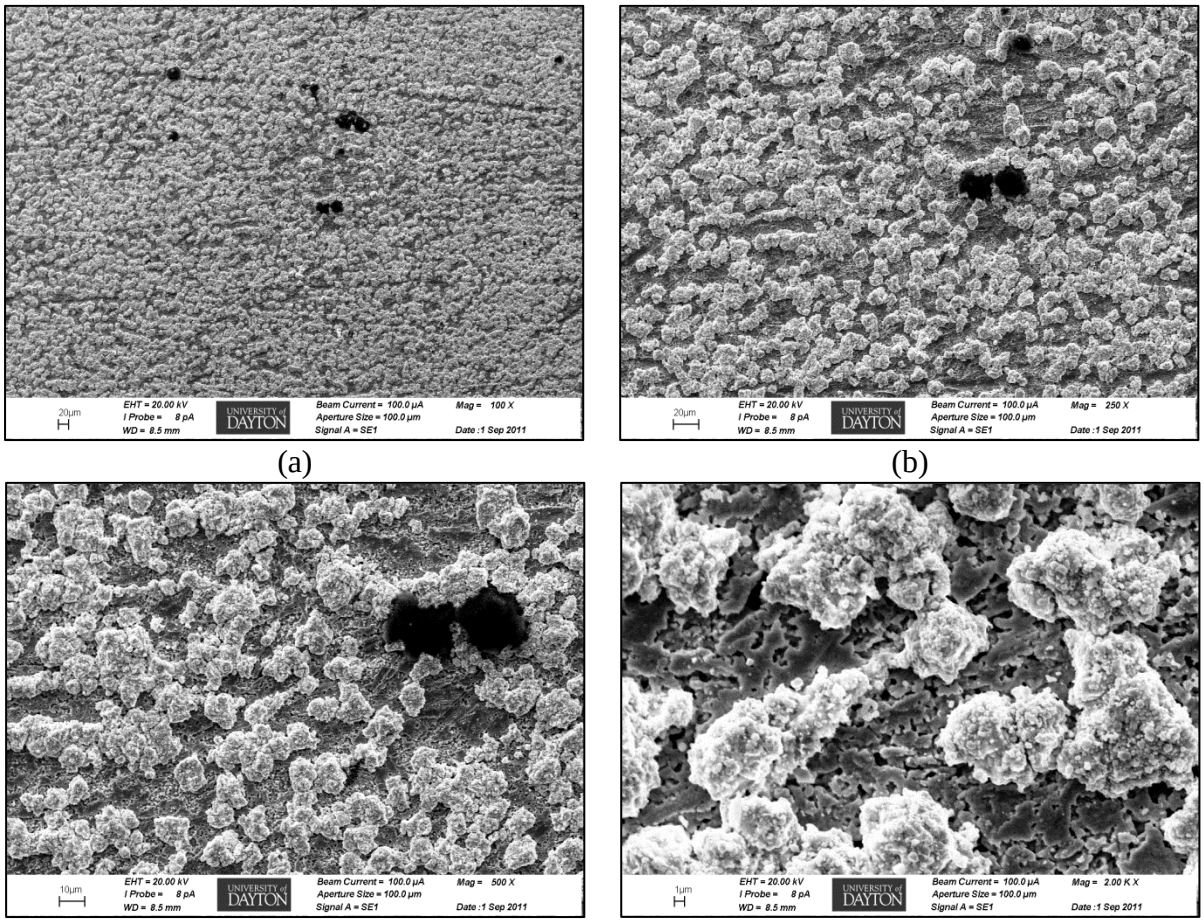

Figure C-1. SEM images of pure silver sample retrieved on 24 months exposure from Pt. Judith site. (a) 100X magnification (b) 250X magnification, (c) 500X magnification, and (d) 2000X magnification.

Distribution Statement A. Approved for Public Release.

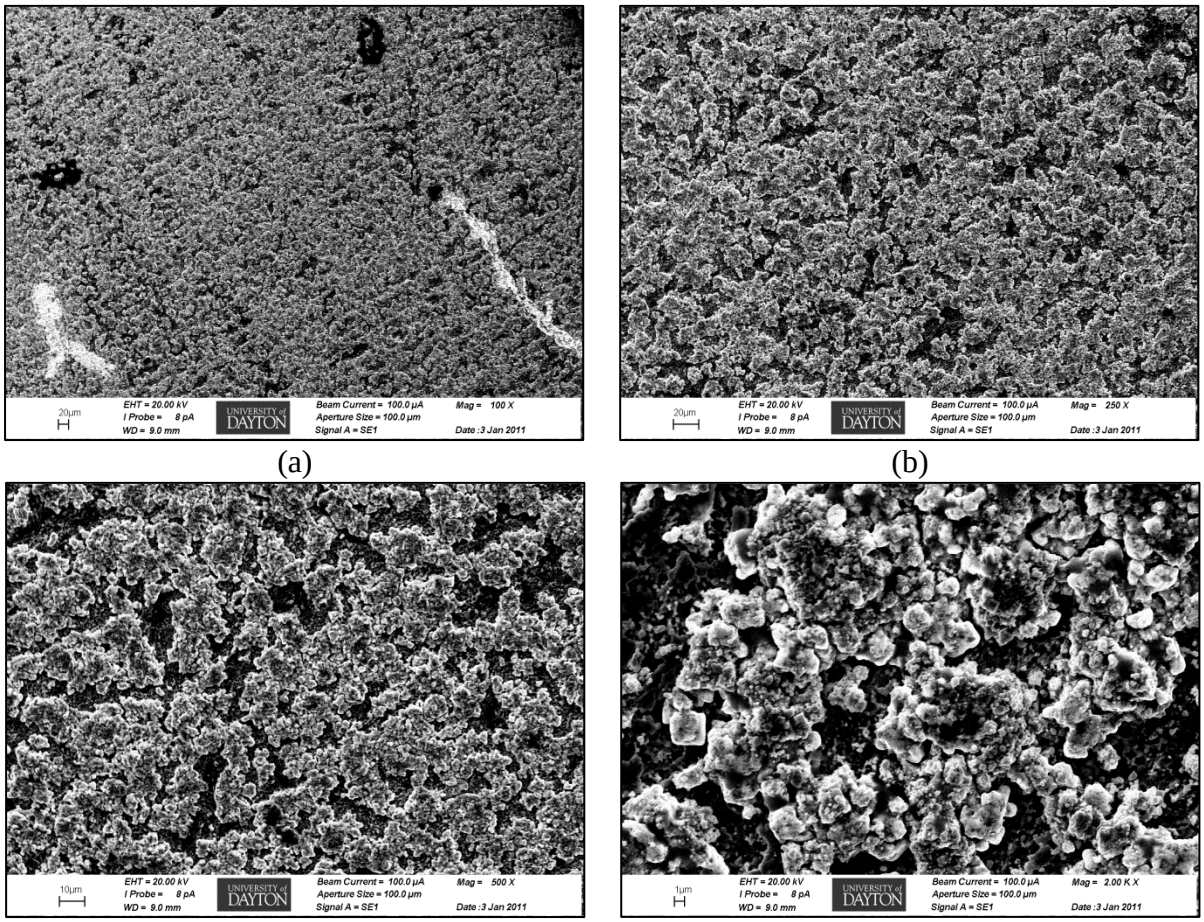

Figure C-2. SEM images of pure silver sample retrieved on 18 months exposure from Pt. Judith site. (a) 100X magnification (b) 250X magnification, (c) 500X magnification, and (d) 2000X magnification.

Distribution Statement A. Approved for Public Release.

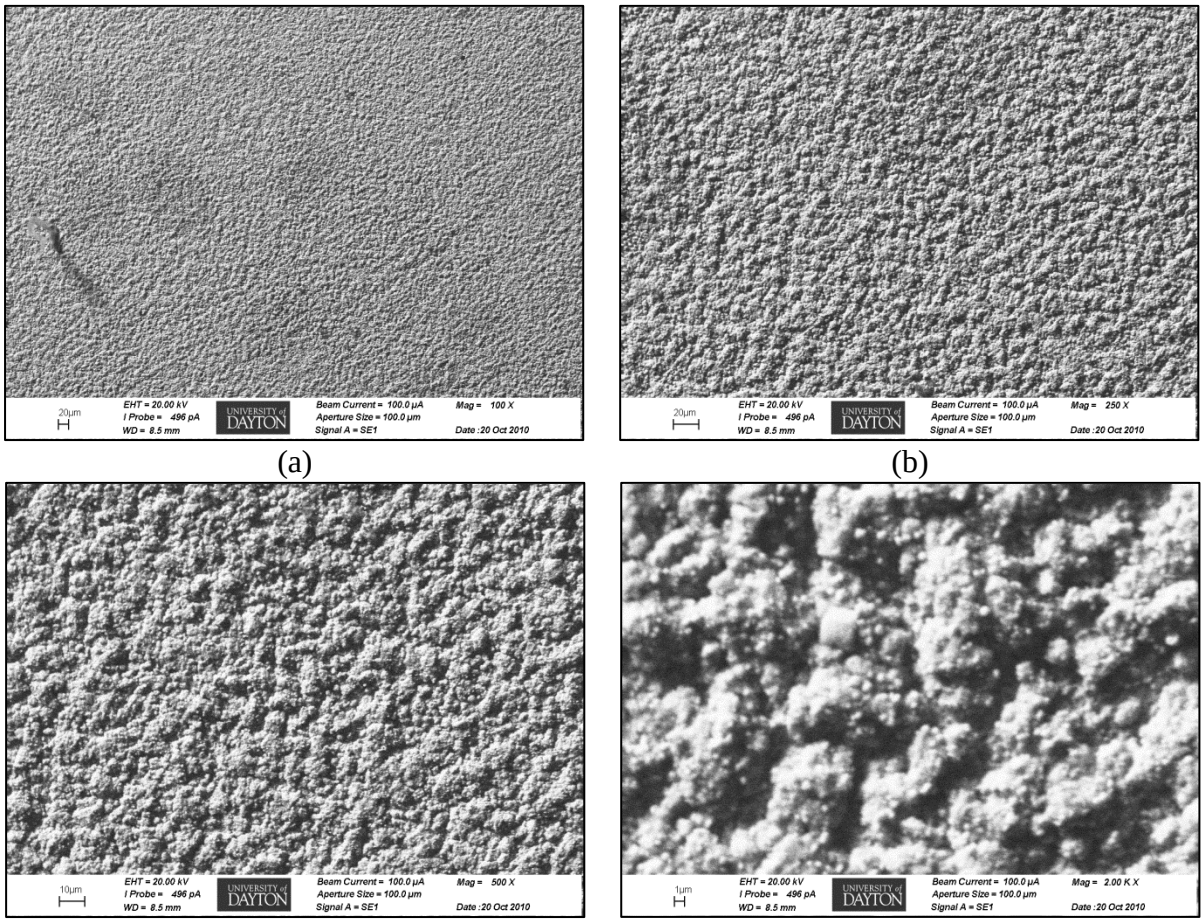

Figure C-3. SEM images of pure silver sample retrieved on 12 months exposure from Pt. Judith site. (a) 100X magnification (b) 250X magnification, (c) 500X magnification, and (d) 2000X magnification.

Distribution Statement A. Approved for Public Release.

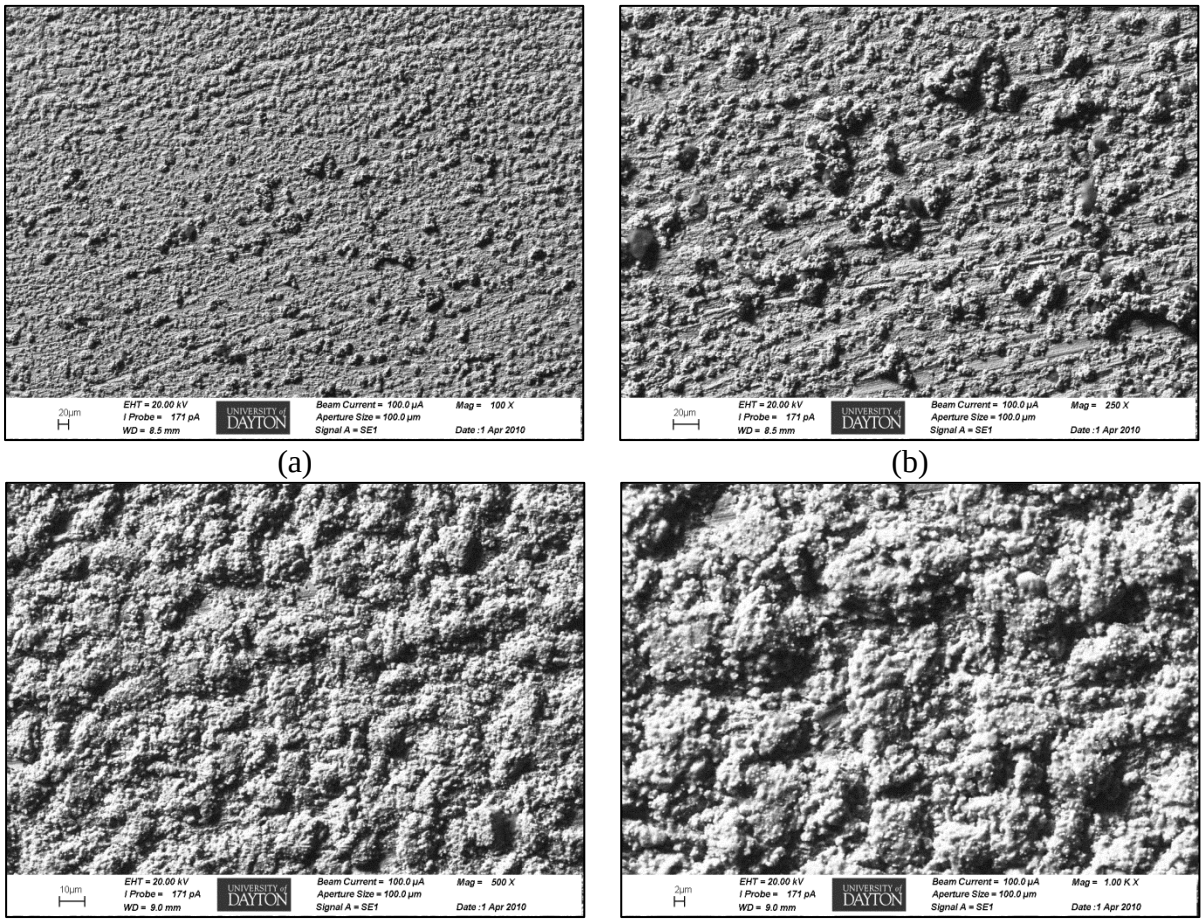

Figure C-4. SEM images of pure silver sample retrieved on 9 months exposure from Pt. Judith site. (a) 100X magnification (b) 250X magnification, (c) 500X magnification, and (d) 1000X magnification.

Distribution Statement A. Approved for Public Release.

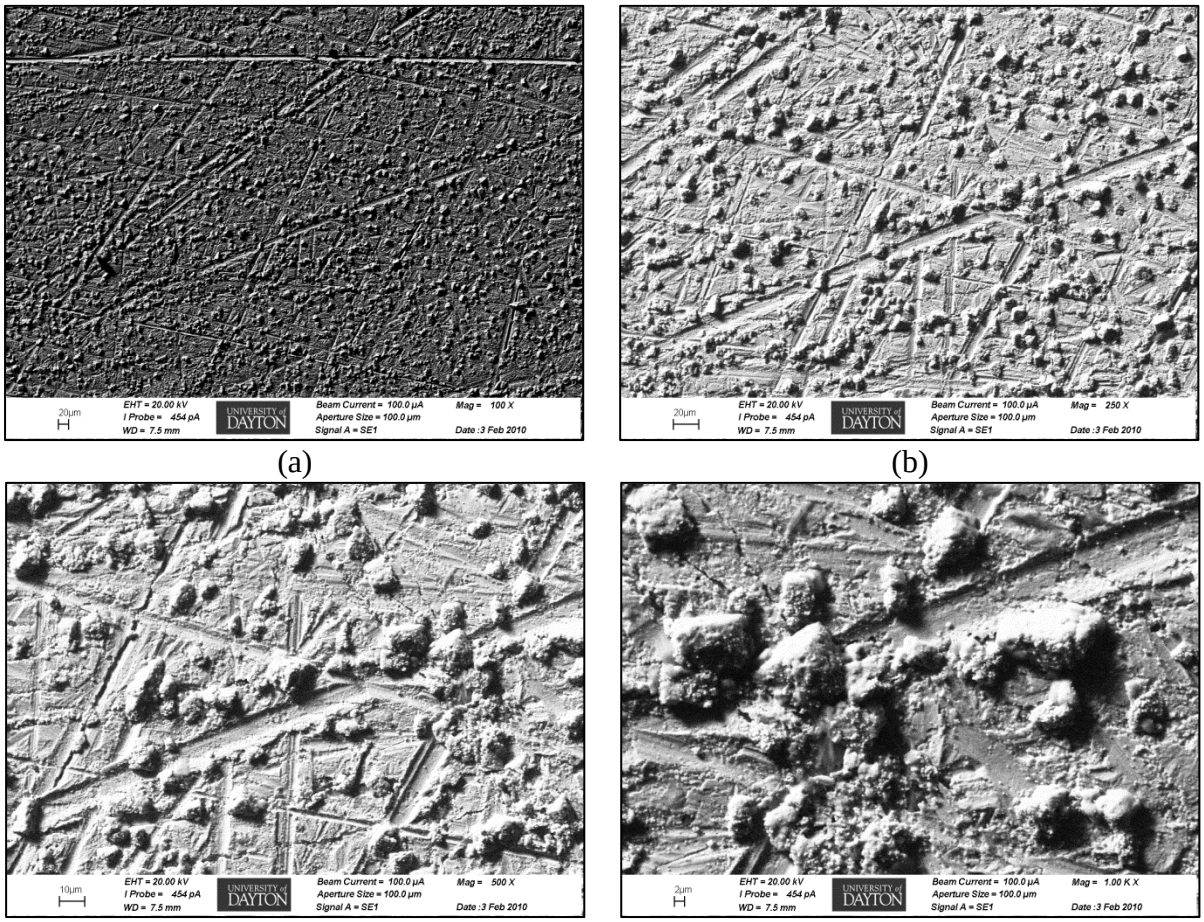

Figure C-5. SEM images of pure silver sample retrieved on 6 months exposure from Pt. Judith site. (a) 100X magnification (b) 250X magnification, (c) 500X magnification, and (d) 1000X magnification.

Distribution Statement A. Approved for Public Release.

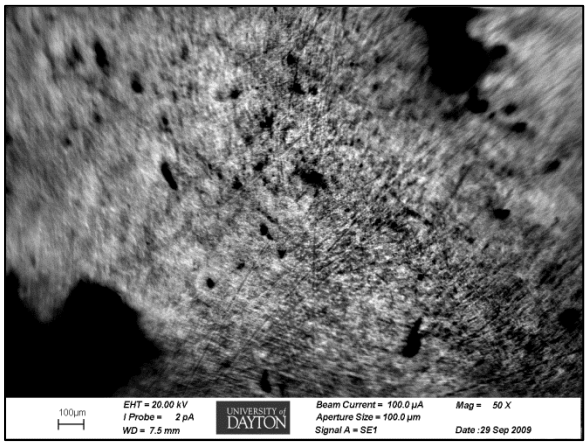

(a)

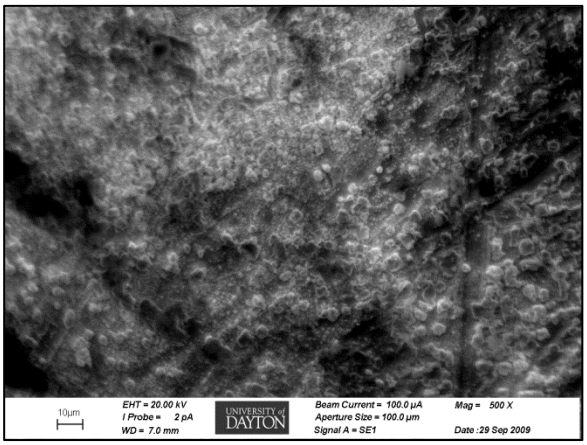

(b)

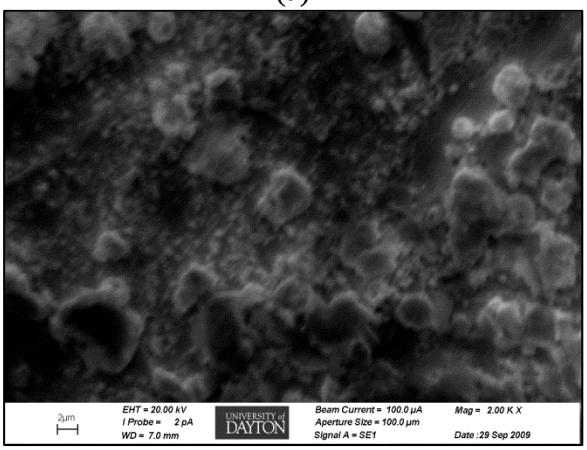

(c)

Figure C-6. SEM images of pure silver sample retrieved on 3 months exposure from Pt. Judith site. (a) 50X magnification (b) 500X magnification, and (c) 2000X magnification.

Distribution Statement A. Approved for Public Release.

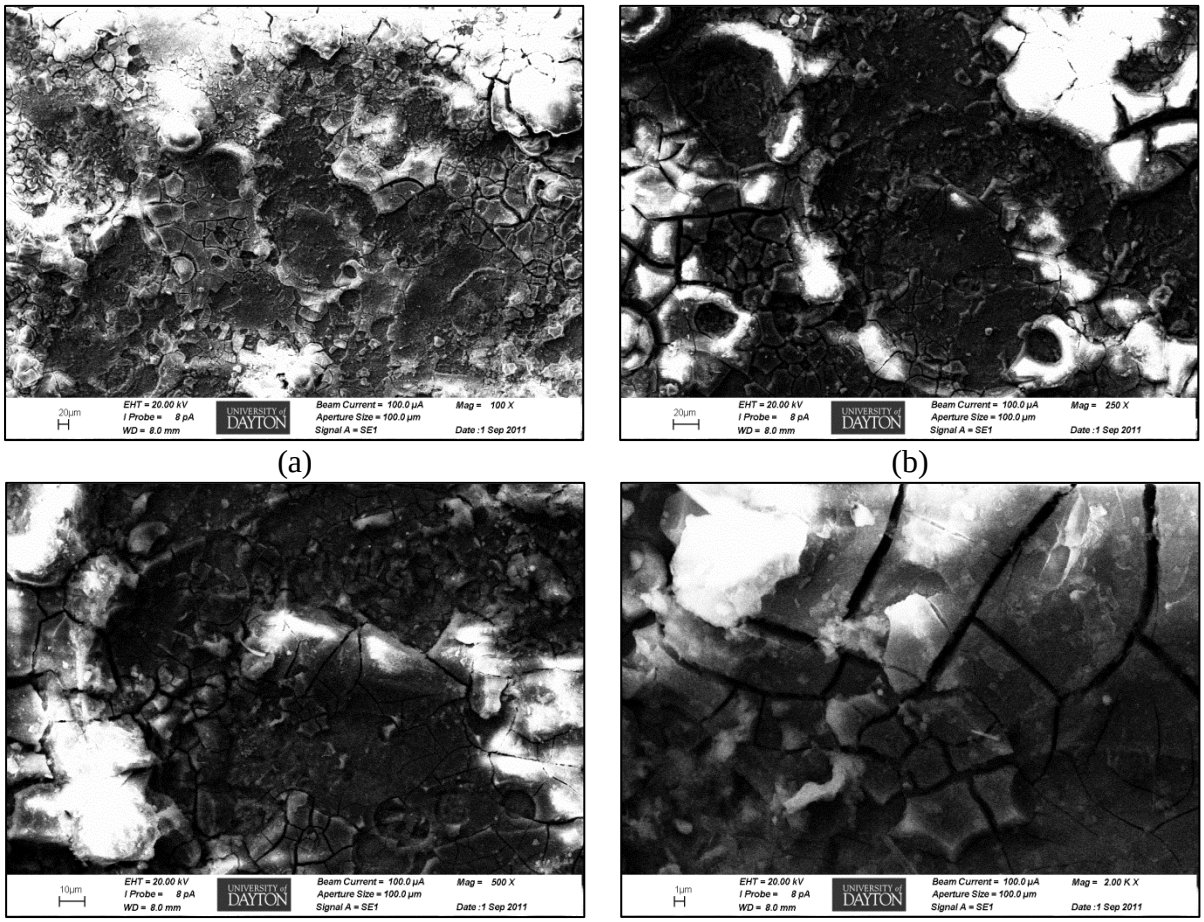

Figure C-7. SEM images of aluminum alloy 7075 sample retrieved on 24 months exposure from Pt. Judith site. (a) 100X magnification (b) 250X magnification, (c) 500X magnification, and (d) 2000X magnification.

Distribution Statement A. Approved for Public Release.

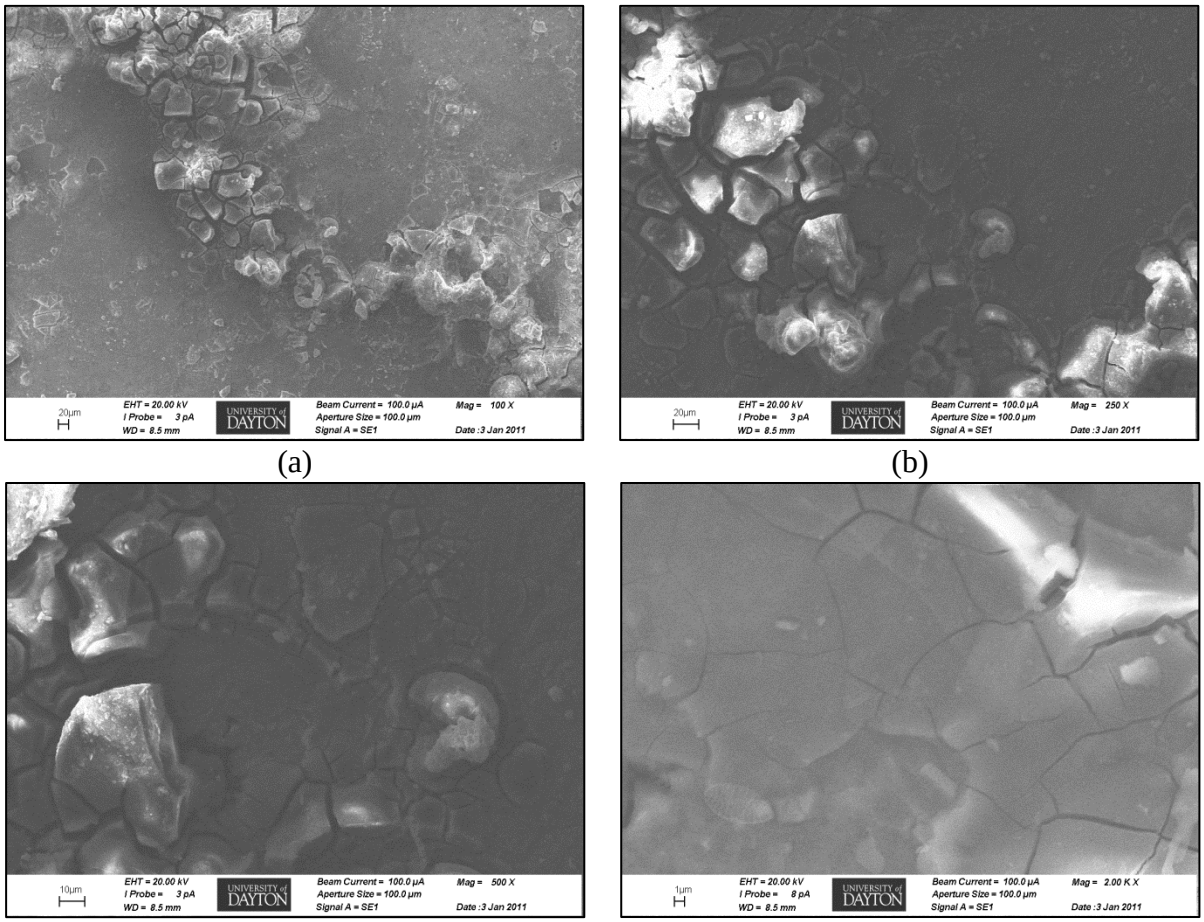

Figure C-8. SEM images of aluminum alloy 7075 sample retrieved on 18 months exposure from Pt. Judith site. (a) 100X magnification (b) 250X magnification, (c) 500X magnification, and (d) 2000X magnification.

Distribution Statement A. Approved for Public Release.

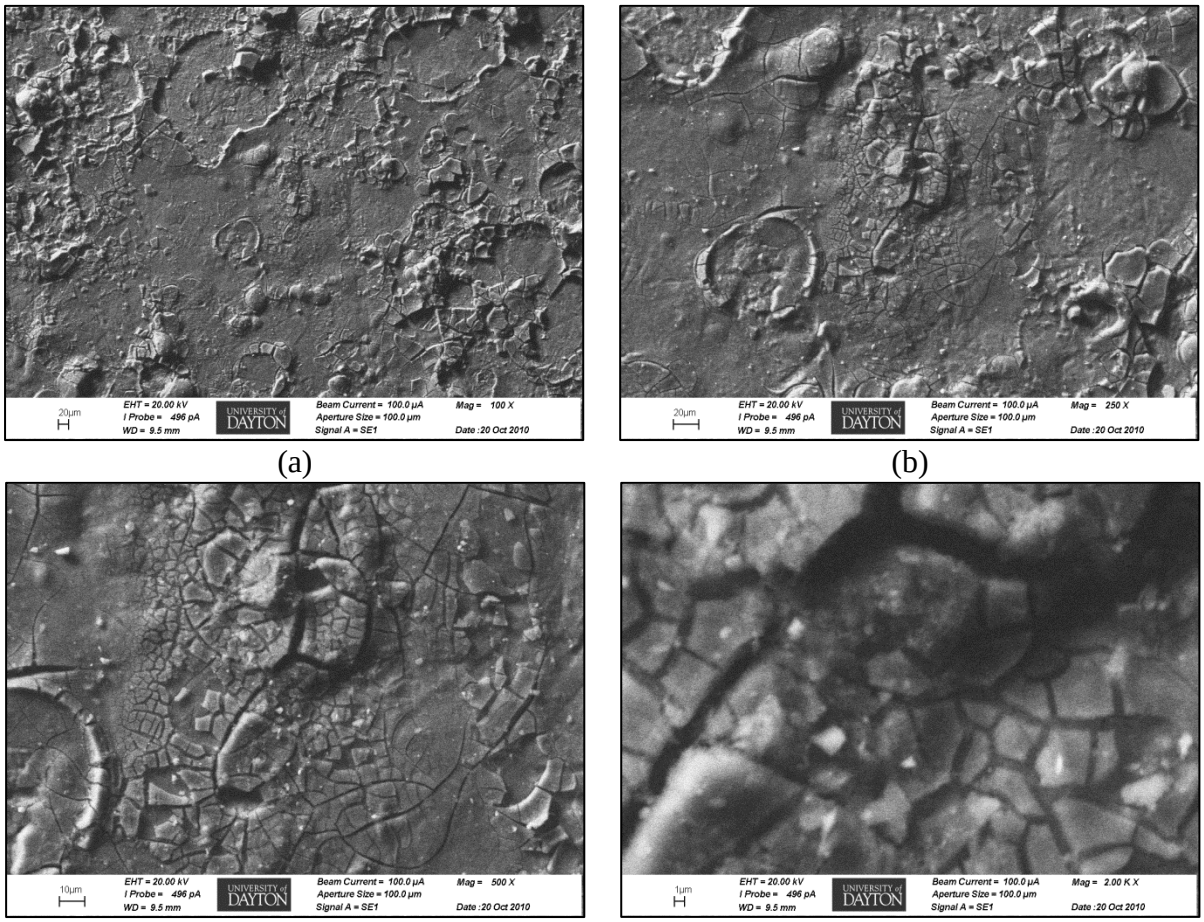

Figure C-9. SEM images of aluminum alloy 7075 sample retrieved on 12 months exposure from Pt. Judith site. (a) 100X magnification (b) 250X magnification, (c) 500X magnification, and (d) 2000X magnification.

Distribution Statement A. Approved for Public Release.

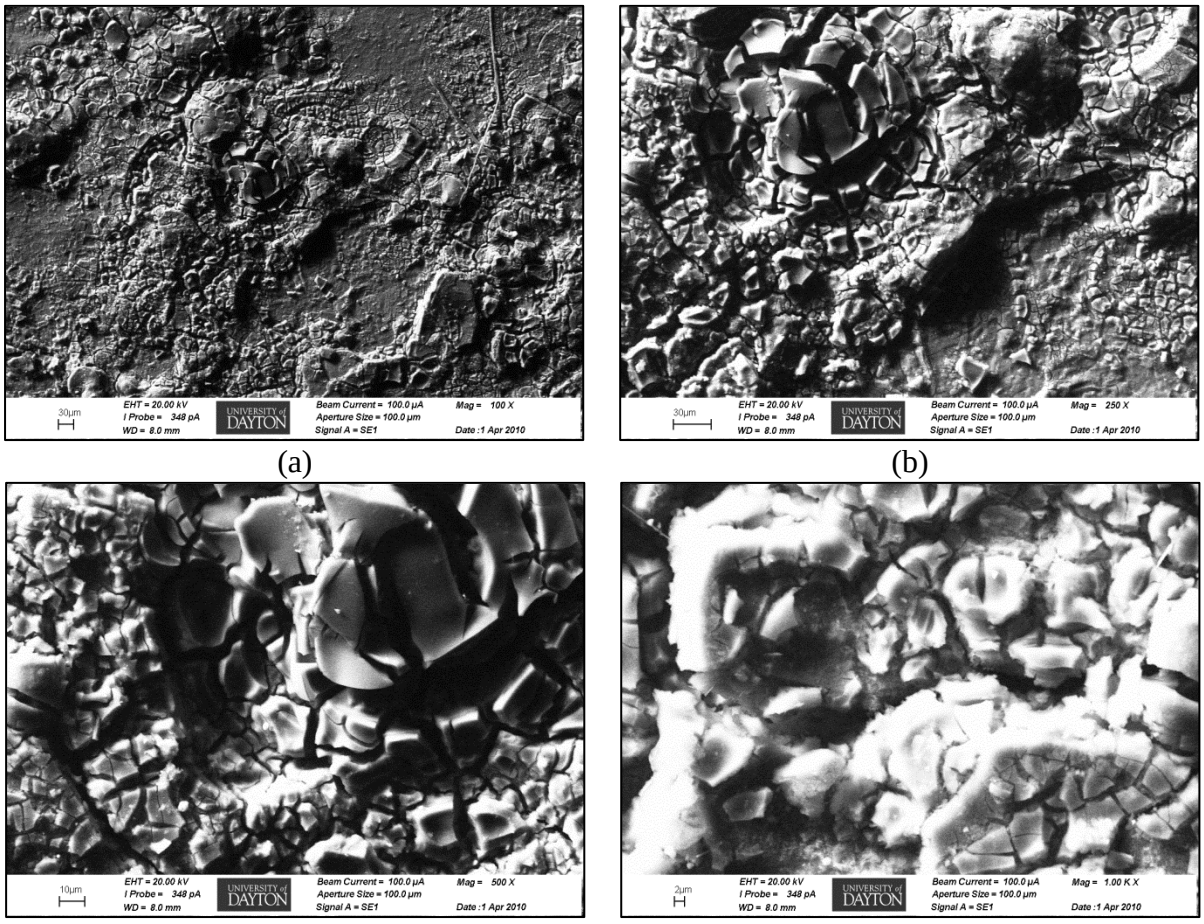

Figure C-10. SEM images of aluminum alloy 7075 sample retrieved on 9 months exposure from Pt. Judith site. (a) 100X magnification (b) 250X magnification, (c) 500X magnification, and (d) 1000X magnification.

Distribution Statement A. Approved for Public Release.

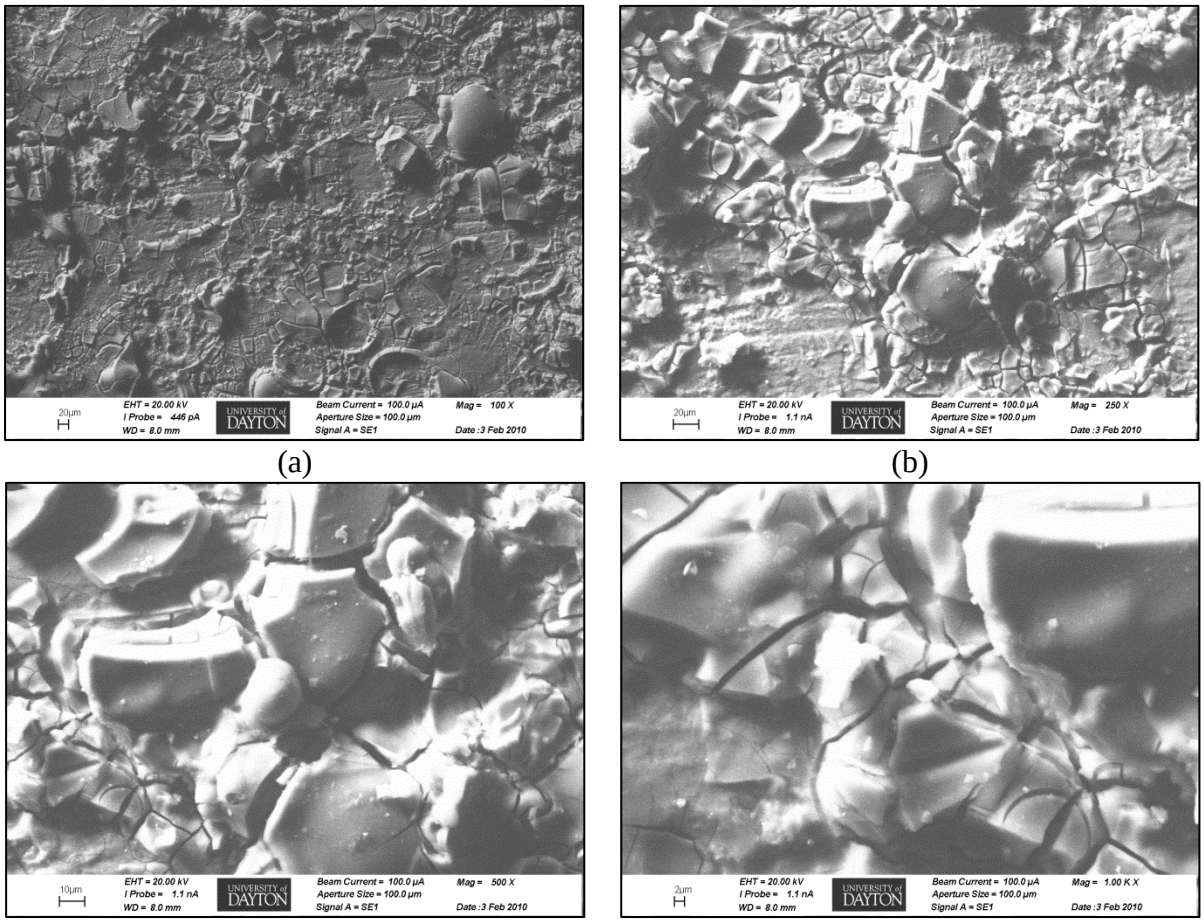

Figure C-11. SEM images of aluminum alloy 7075 sample retrieved on 6 months exposure from Pt. Judith site. (a) 100X magnification (b) 250X magnification, (c) 500X magnification, and (d) 1000X magnification.

.

Distribution Statement A. Approved for Public Release.

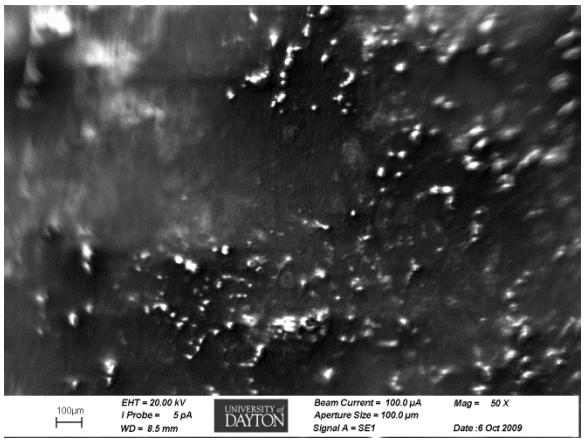

(a)

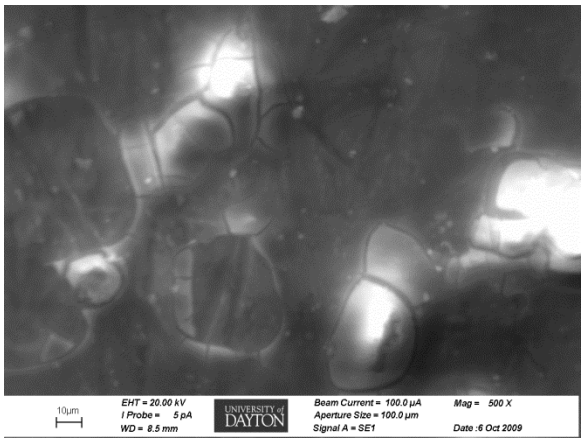

(b)

Figure C-12. SEM images of aluminum alloy 7075 sample retrieved on 3 months exposure from Pt. Judith site. (a) 50X magnification and (b) 500X magnification

.

Distribution Statement A. Approved for Public Release.

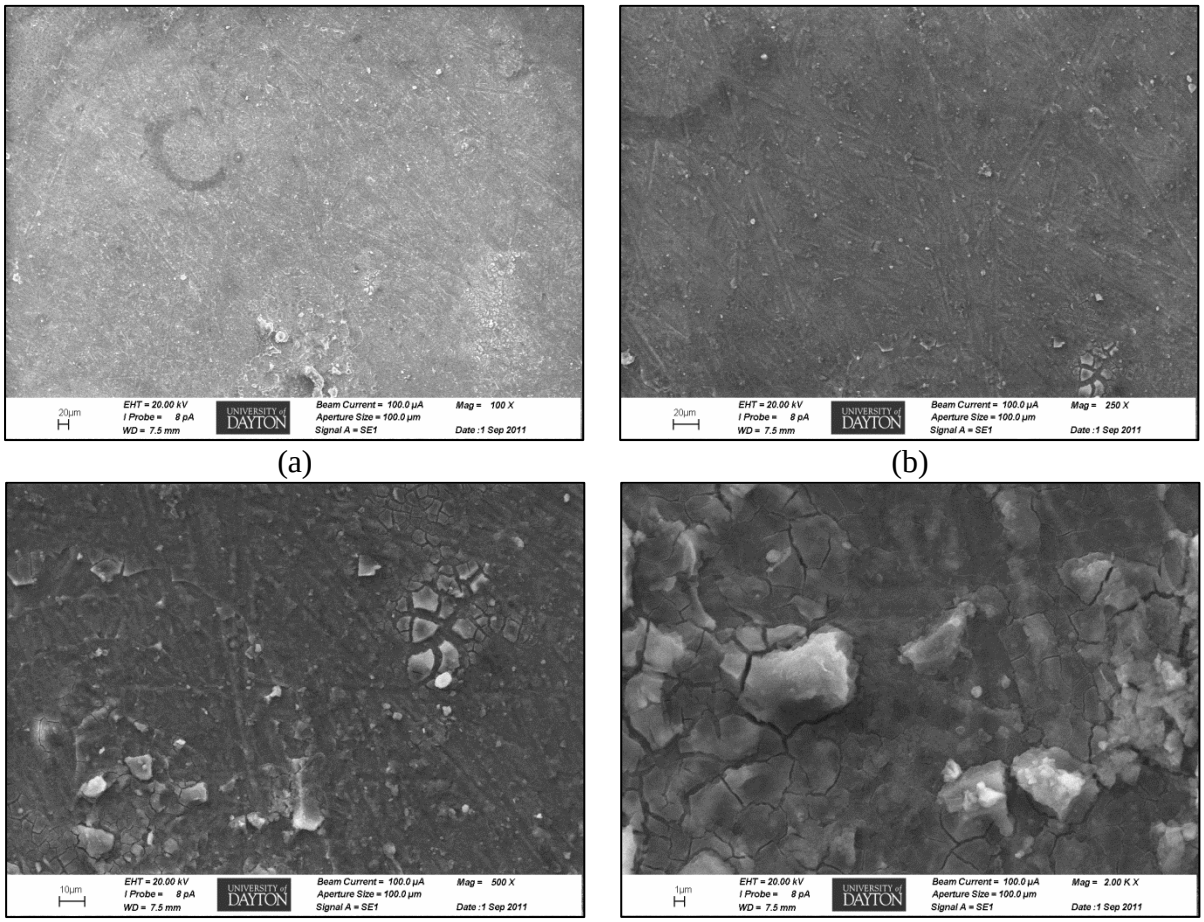

(a) (b)

(c) (d)

Figure C-13. SEM images of aluminum alloy 6061 sample retrieved on 24 months exposure from Pt. Judith site. (a) 100X magnification (b) 250X magnification, (c) 500X magnification, and (d) 2000X magnification.

Distribution Statement A. Approved for Public Release.

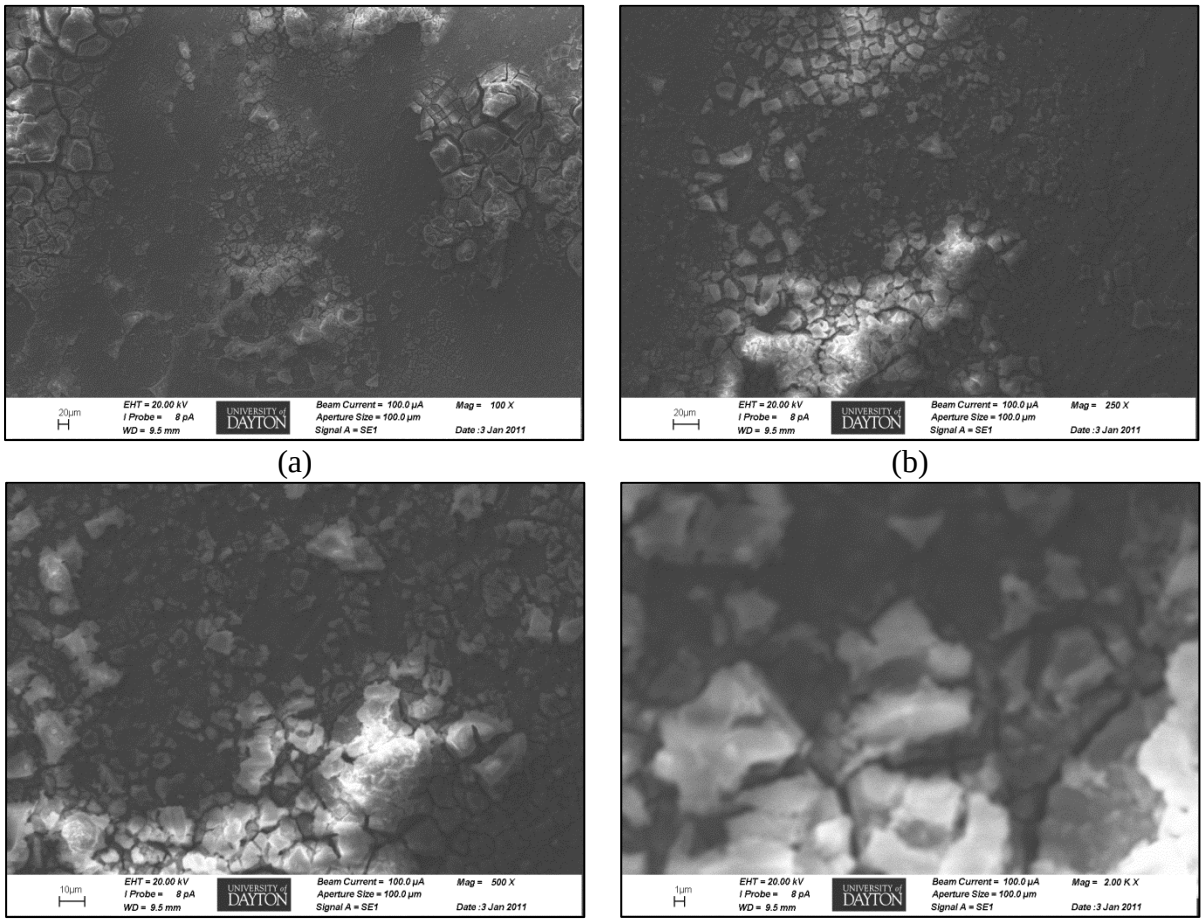

Figure C-14. SEM images of aluminum alloy 6061 sample retrieved on 18 months exposure from Pt. Judith site. (a) 100X magnification (b) 250X magnification, (c) 500X magnification, and (d) 2000X magnification

.

Distribution Statement A. Approved for Public Release.

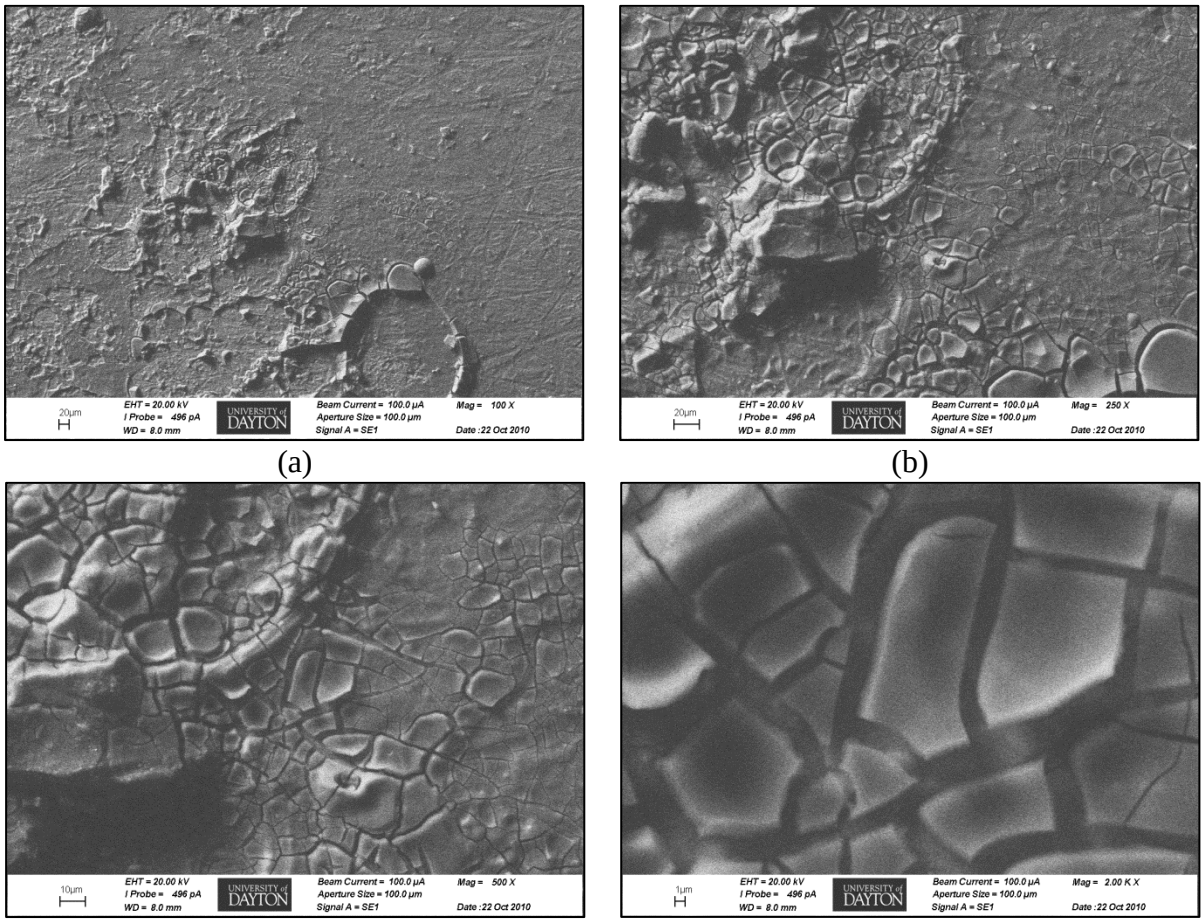

Figure C-15. SEM images of aluminum alloy 6061 sample retrieved on 12 months exposure from Pt. Judith site. (a) 100X magnification (b) 250X magnification, (c) 500X magnification, and (d) 2000X magnification.

Distribution Statement A. Approved for Public Release.

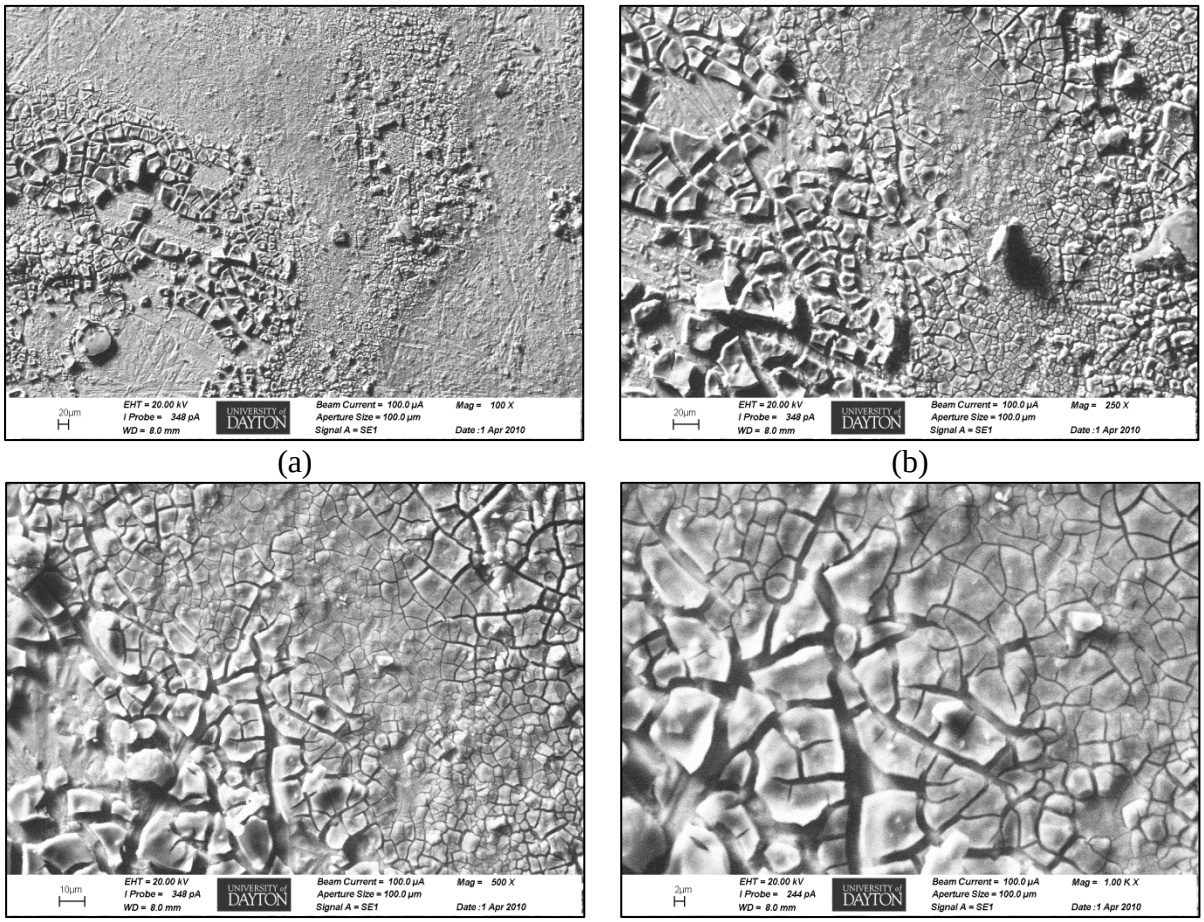

Figure C-16. SEM images of aluminum alloy 6061 sample retrieved on 9 months exposure from Pt. Judith site. (a) 100X magnification (b) 250X magnification, (c) 500X magnification, and (d) 1000X magnification.

Distribution Statement A. Approved for Public Release.

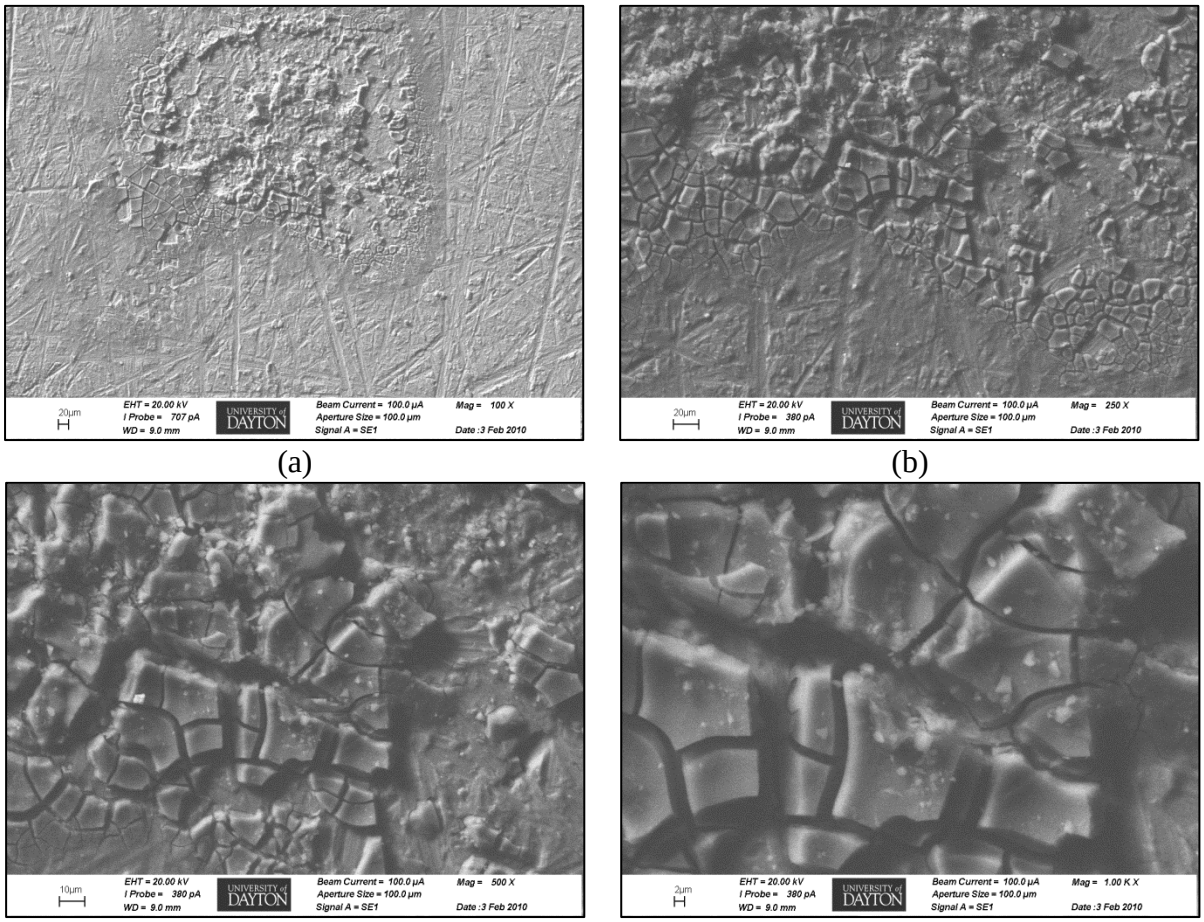

(a) (b)

(c) (d)

Figure C-17. SEM images of aluminum alloy 6061 sample retrieved on 6 months exposure from Pt. Judith site. (a) 100X magnification (b) 250X magnification, (c) 500X magnification, and (d) 1000X magnification.

.

Distribution Statement A. Approved for Public Release.

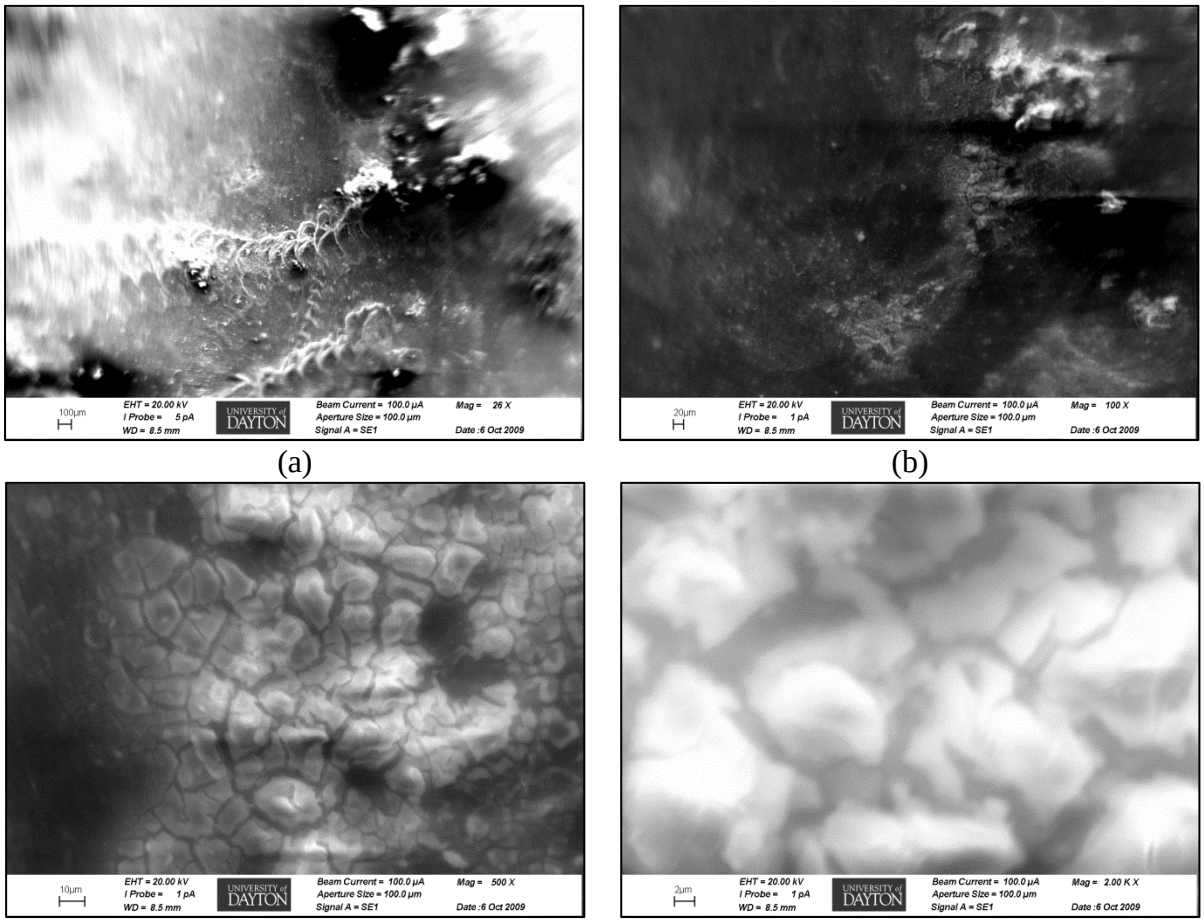

Figure C-18. SEM images of aluminum alloy 6061 sample retrieved on 3 months exposure from Pt. Judith site. (a) 26X magnification (b) 100X magnification, (c) 500X magnification, and (d) 2000X magnification.

Distribution Statement A. Approved for Public Release.

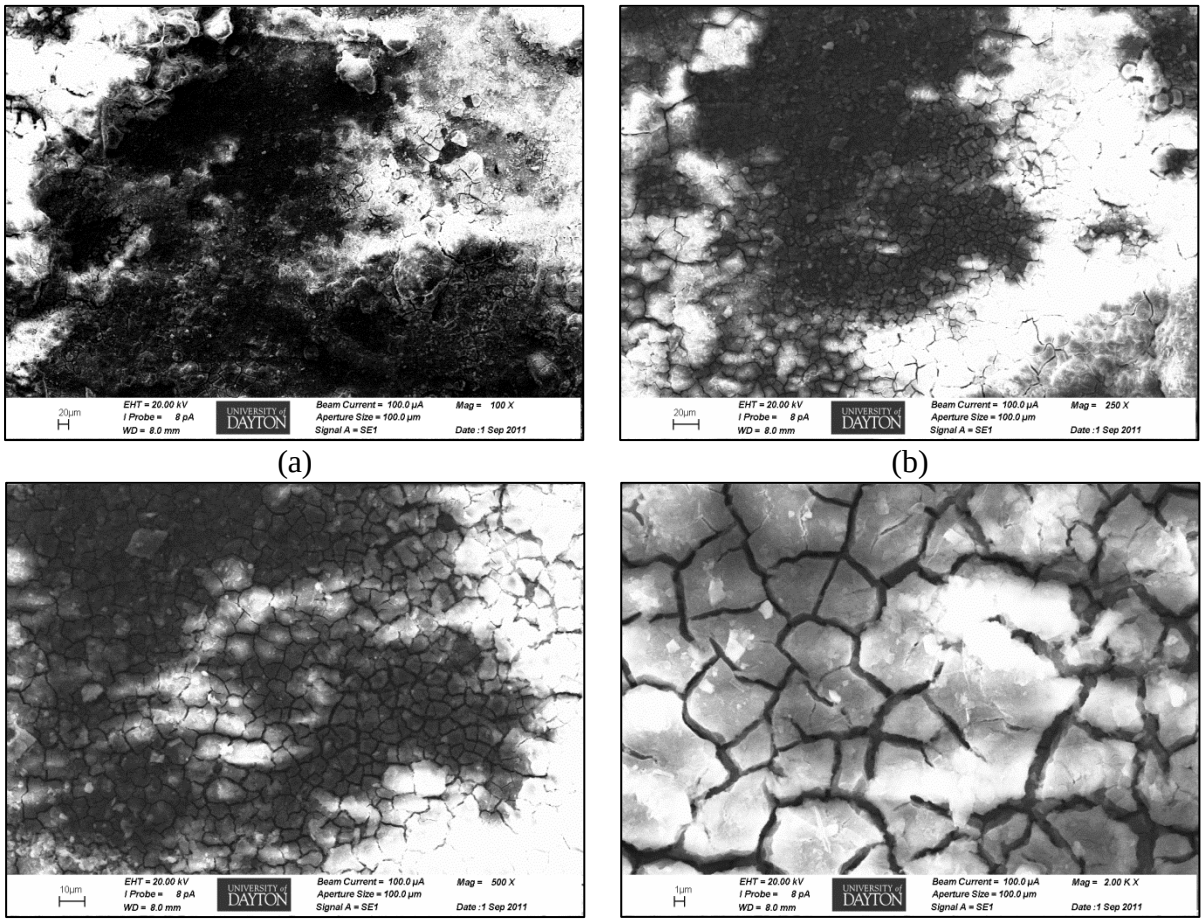

(a) (b)

(c) (d)

Figure C-19. SEM images of aluminum alloy 2024 sample retrieved on 24 months exposure from Pt. Judith site. (a) 100X magnification (b) 250X magnification, (c) 500X magnification, and (d) 2000X magnification.

Distribution Statement A. Approved for Public Release.

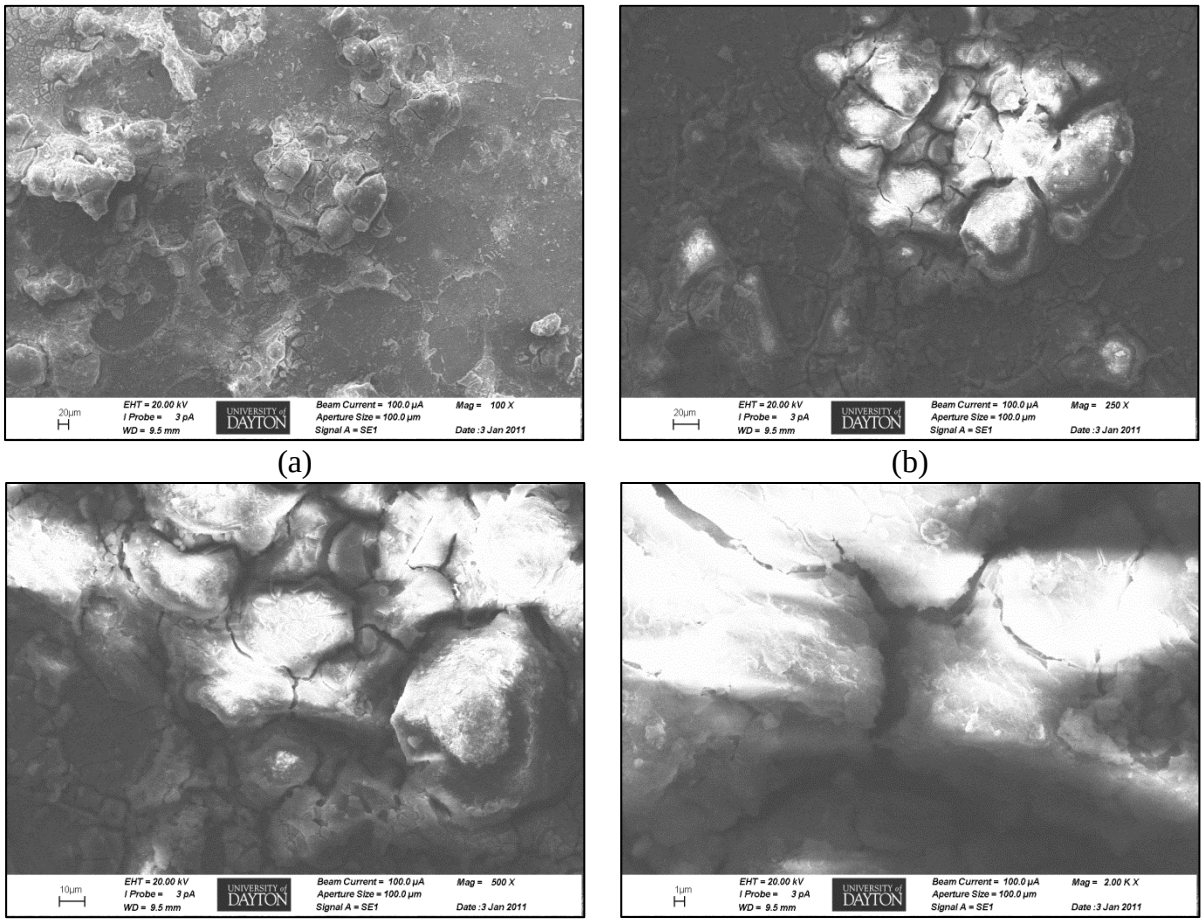

Figure C-20. SEM images of aluminum alloy 2024 sample retrieved on 18 months exposure from Pt. Judith site. (a) 100X magnification (b) 250X magnification, (c) 500X magnification, and (d) 2000X magnification.

Distribution Statement A. Approved for Public Release.

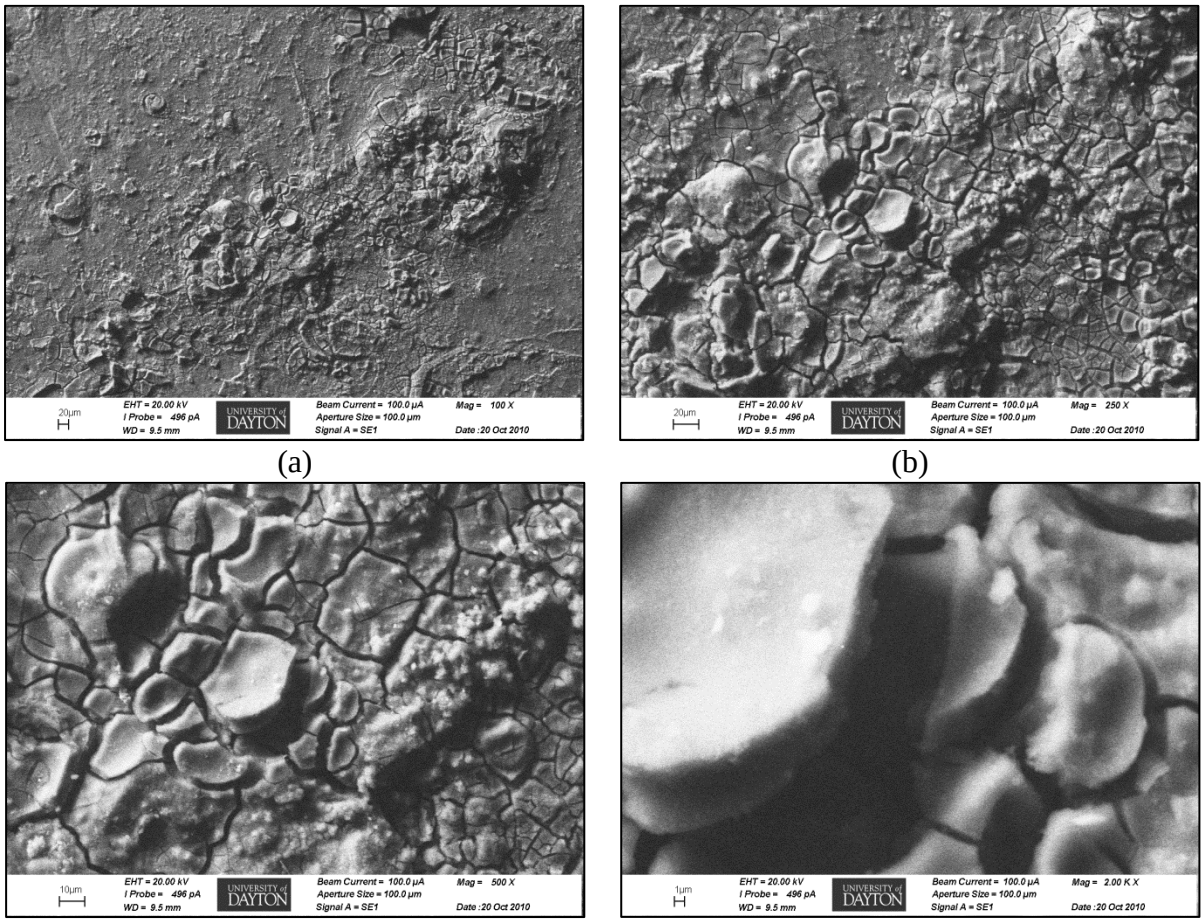

(a) (b)

(c) (d)

Figure C-21. SEM images of aluminum alloy 2024 sample retrieved on 12 months exposure from Pt. Judith site. (a) 100X magnification (b) 250X magnification, (c) 500X magnification, and (d) 2000X magnification.

Distribution Statement A. Approved for Public Release.

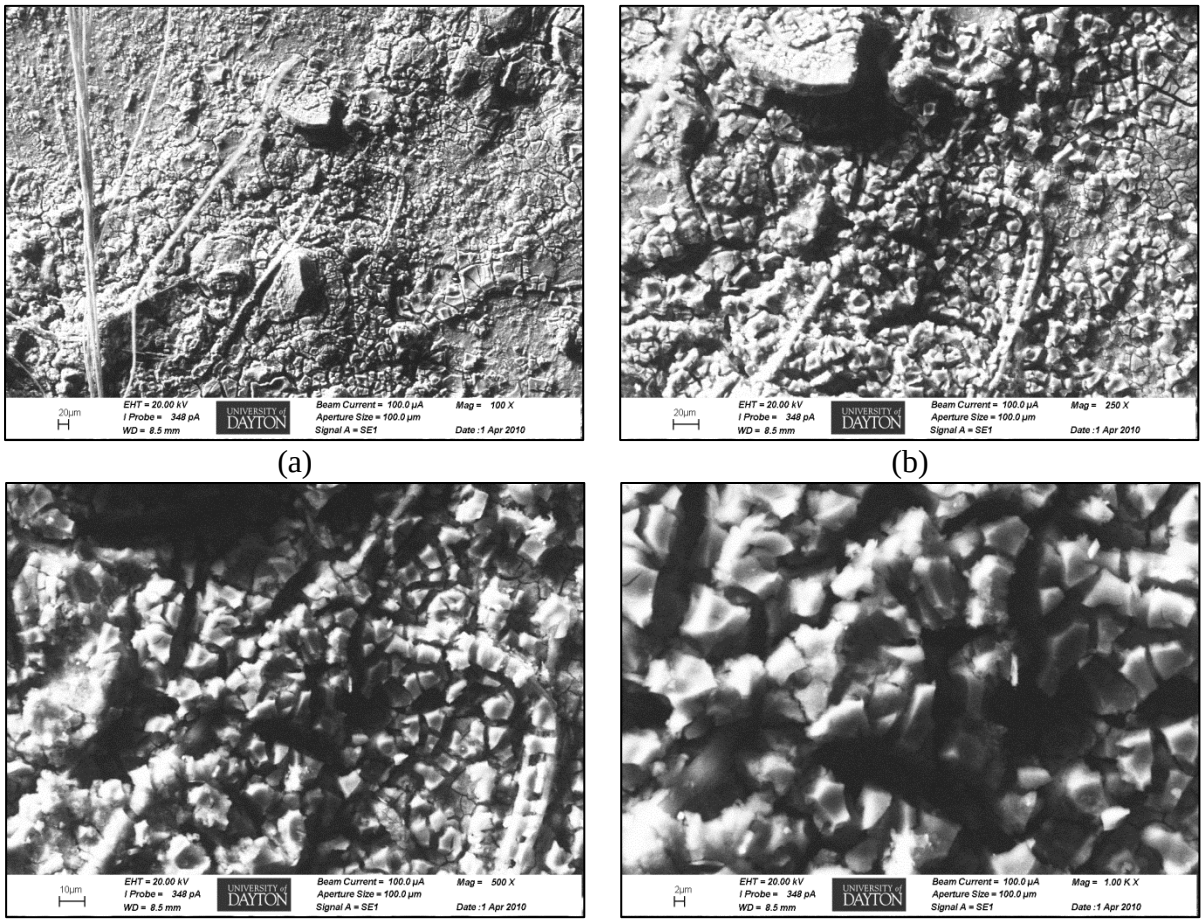

Figure C-22. SEM images of aluminum alloy 2024 sample retrieved on 9 months exposure from Pt. Judith site. (a) 100X magnification (b) 250X magnification, (c) 500X magnification, and (d) 1000X magnification.

Distribution Statement A. Approved for Public Release.

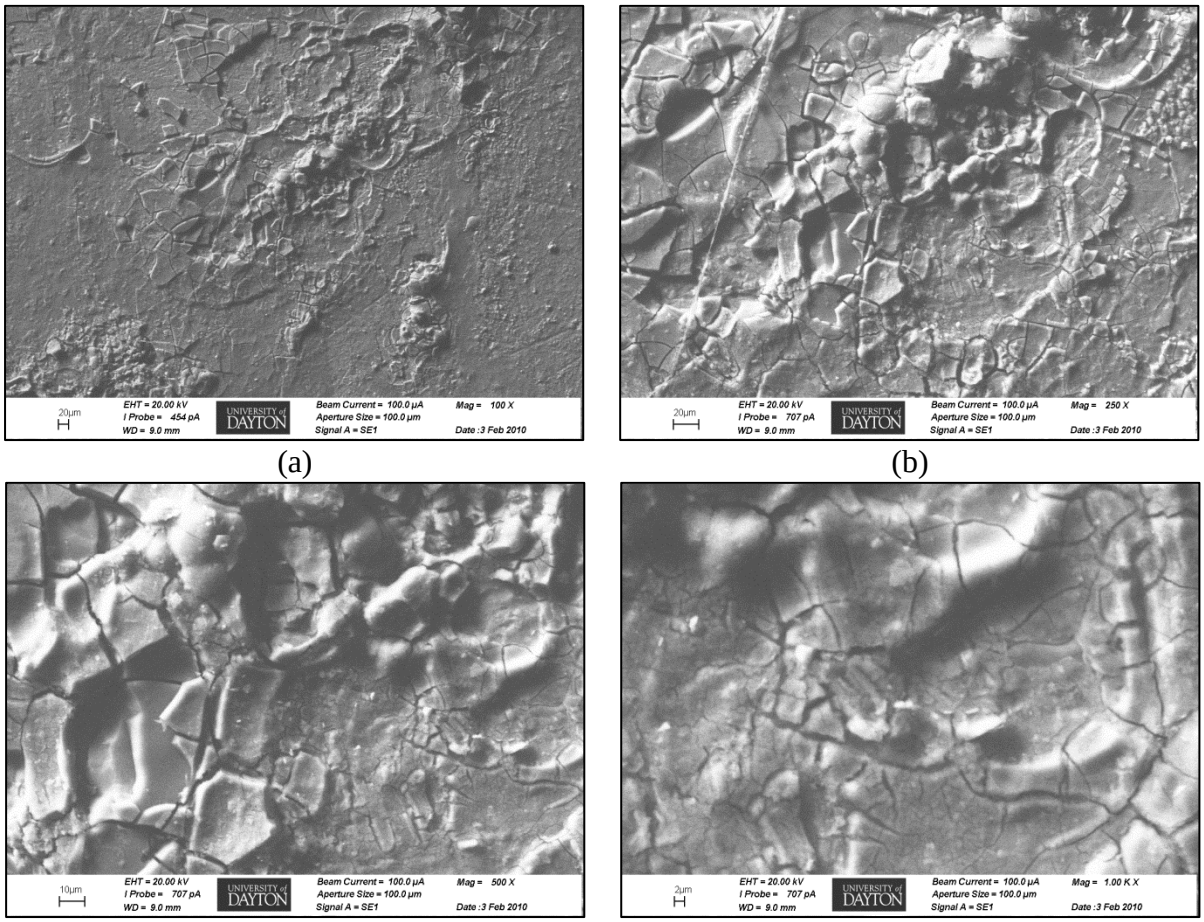

Figure C-23. SEM images of aluminum alloy 2024 sample retrieved on 6 months exposure from Pt. Judith site. (a) 100X magnification (b) 250X magnification, (c) 500X magnification, and (d) 1000X magnification.

Distribution Statement A. Approved for Public Release.

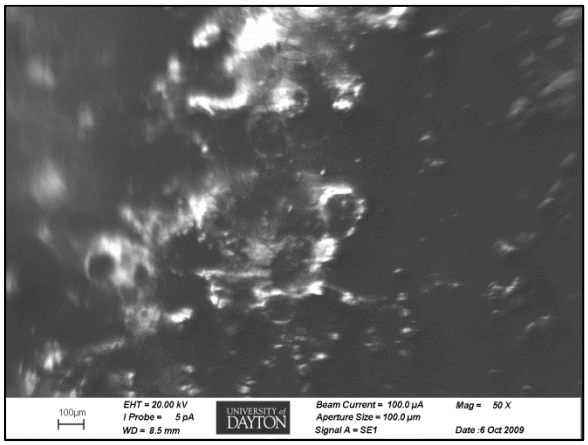

(a)

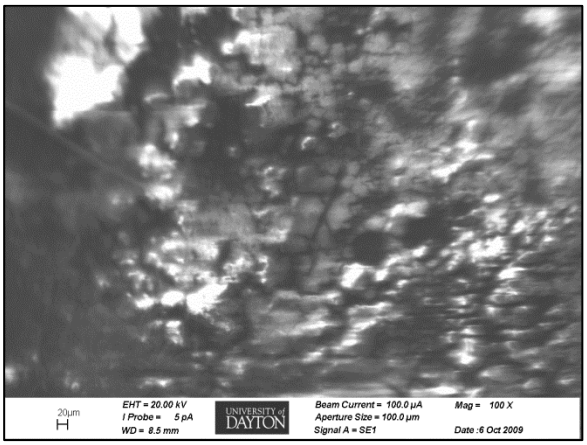

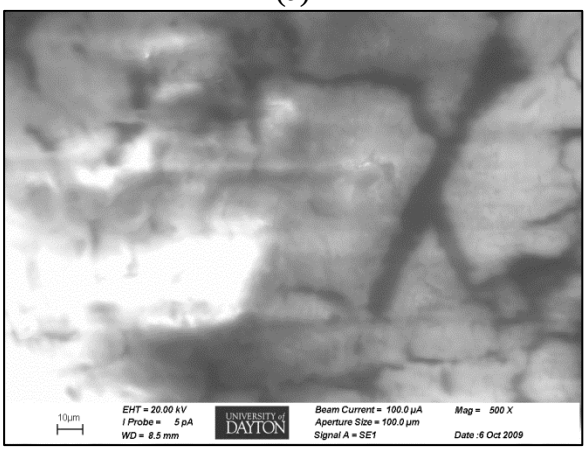

(c)

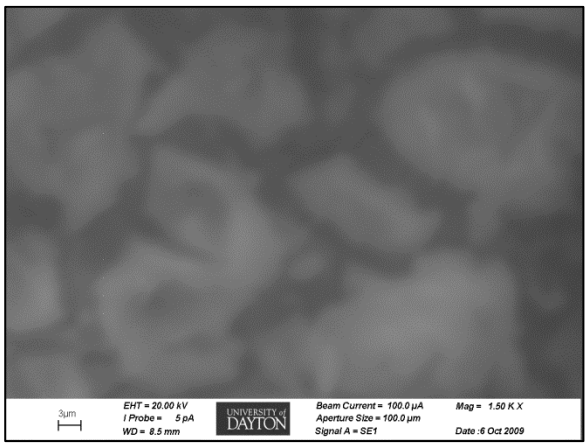

(d)

Figure C-24. SEM images of aluminum alloy 2024 sample retrieved on 3 months exposure from Pt. Judith site. (a) 50X magnification (b) 100X magnification, (c) 500X magnification, and (d) 1500X magnification.

Distribution Statement A. Approved for Public Release.

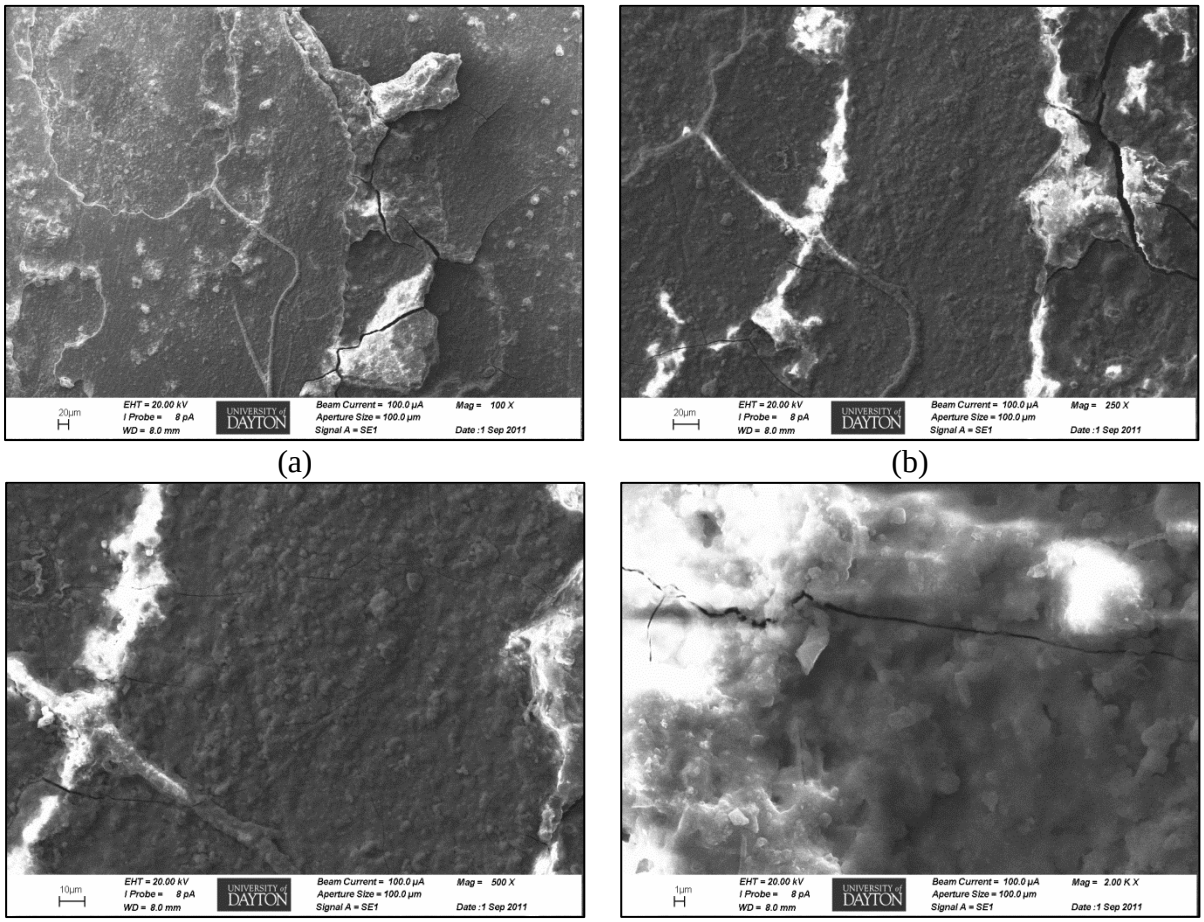

(a) (b)

(c) (d)

Figure C-25. SEM images of pure copper sample retrieved on 24 months exposure from Pt. Judith site. (a) 100X magnification (b) 250X magnification, (c) 500X magnification, and (d) 2000X magnification.

Distribution Statement A. Approved for Public Release.

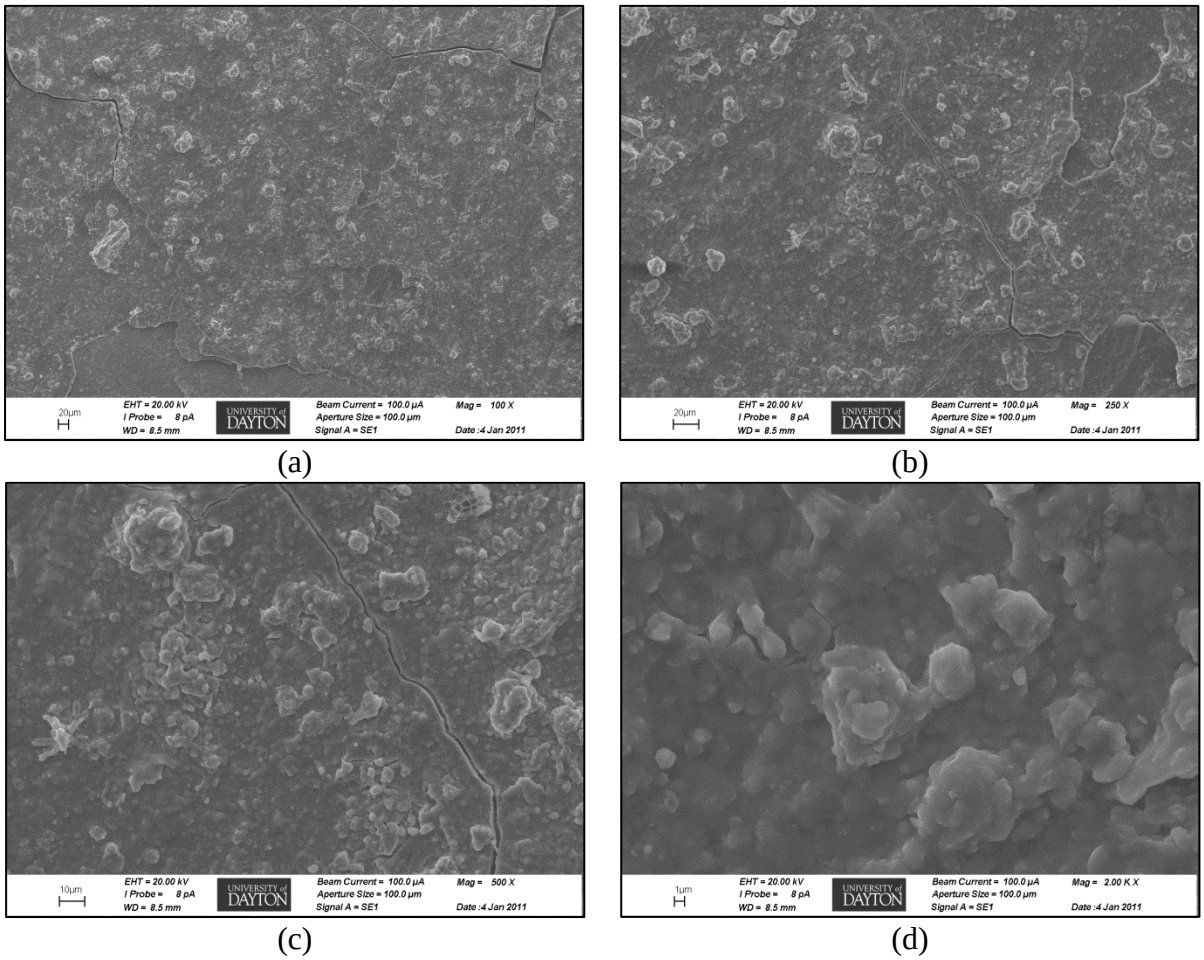

Figure C-26. SEM images of pure copper sample retrieved on 18 months exposure from Pt. Judith site. (a) 100X magnification (b) 250X magnification, (c) 500X magnification, and (d) 2000X magnification.

Distribution Statement A. Approved for Public Release.

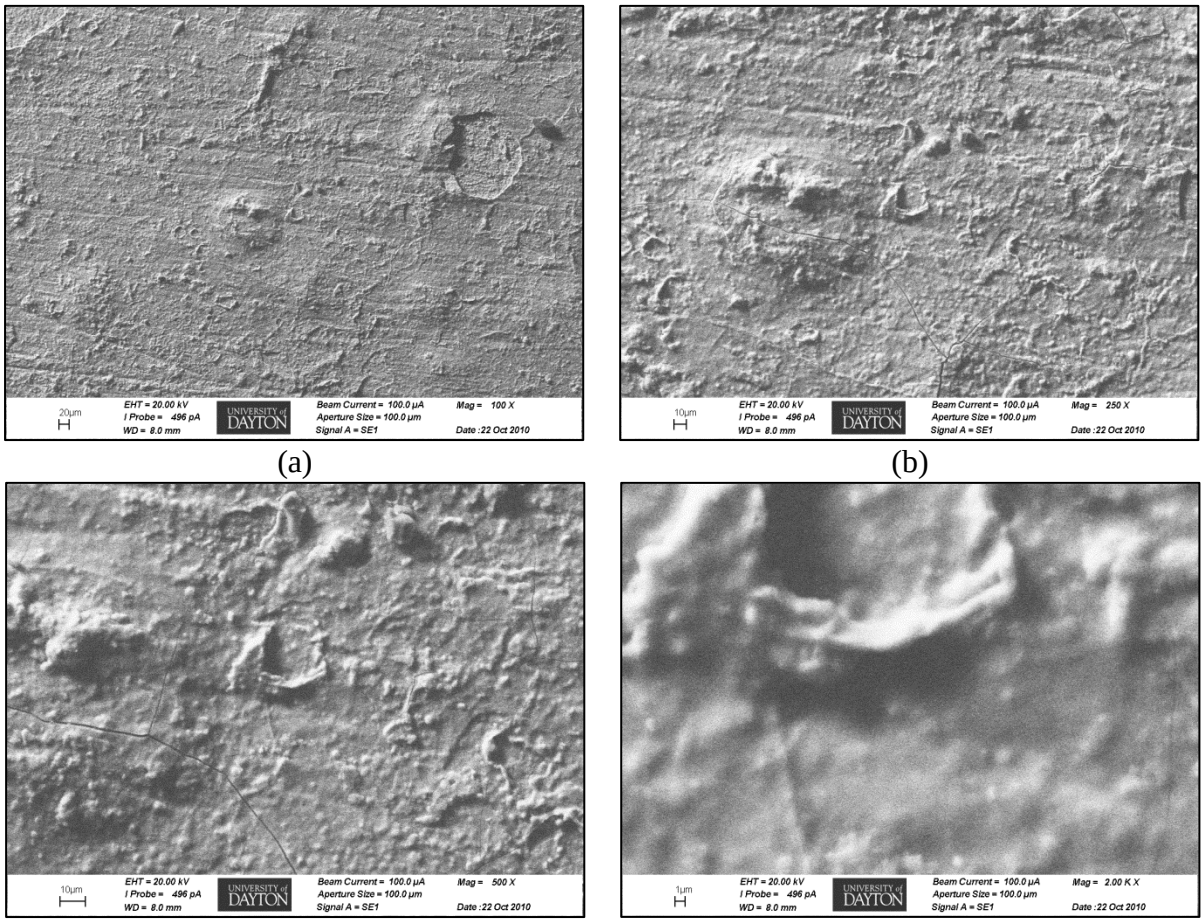

Figure C-27. SEM images of pure copper sample retrieved on 12 months exposure from Pt. Judith site. (a) 100X magnification (b) 250X magnification, (c) 500X magnification, and (d) 2000X magnification.

Distribution Statement A. Approved for Public Release.

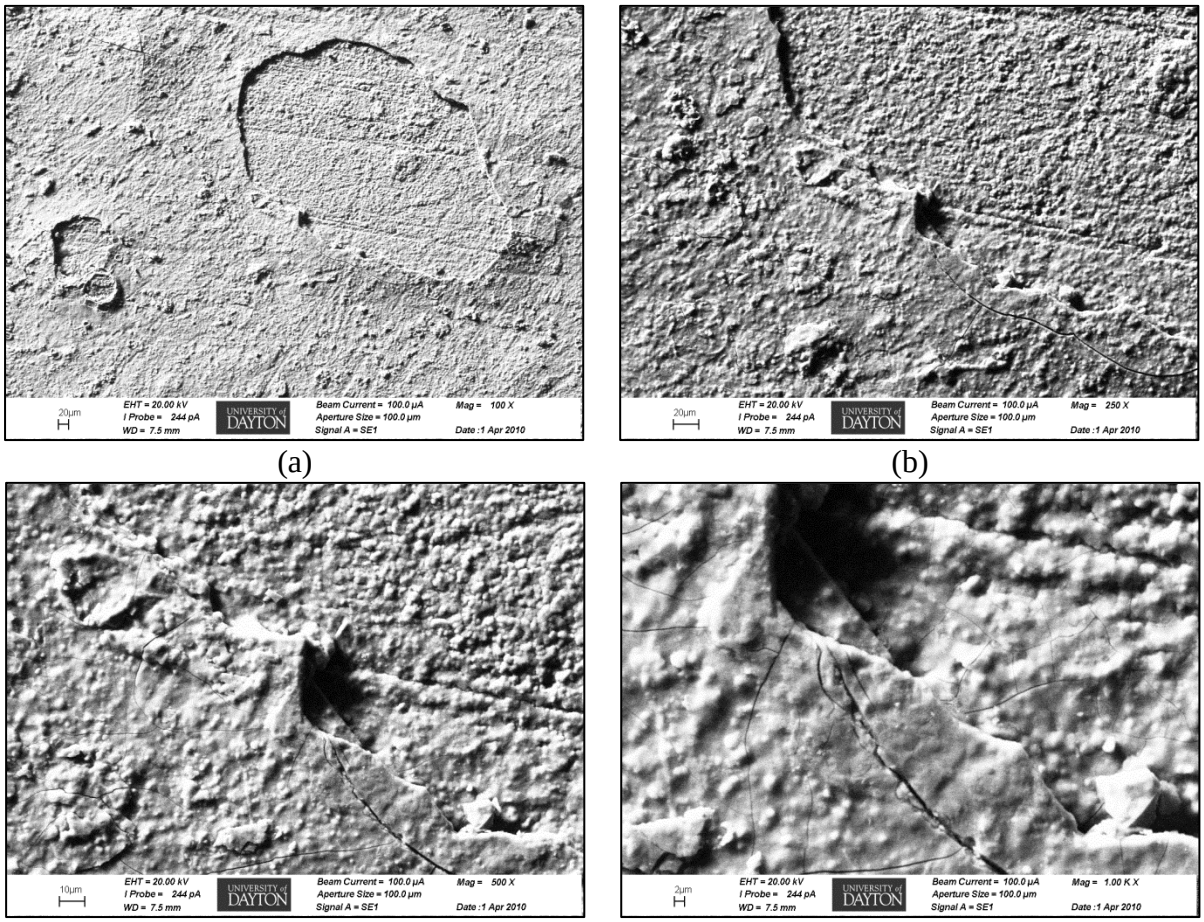

Figure C-28. SEM images of pure copper sample retrieved on 9 months exposure from Pt. Judith site. (a) 100X magnification (b) 250X magnification, (c) 500X magnification, and (d) 1000X magnification.

Distribution Statement A. Approved for Public Release.

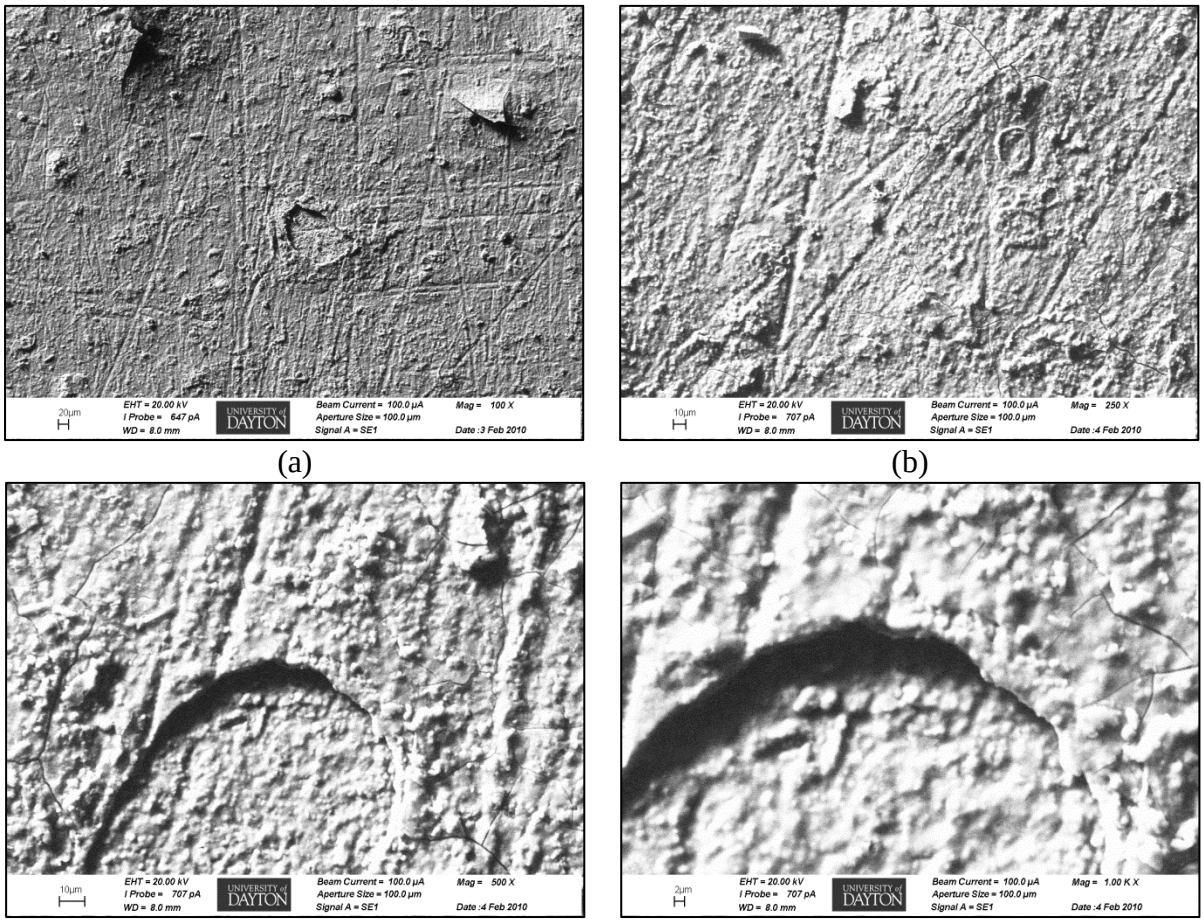

Figure C-29. SEM images of pure copper sample retrieved on 6 months exposure from Pt. Judith site. (a) 100X magnification (b) 250X magnification, (c) 500X magnification, and (d) 5000X magnification.

Distribution Statement A. Approved for Public Release.

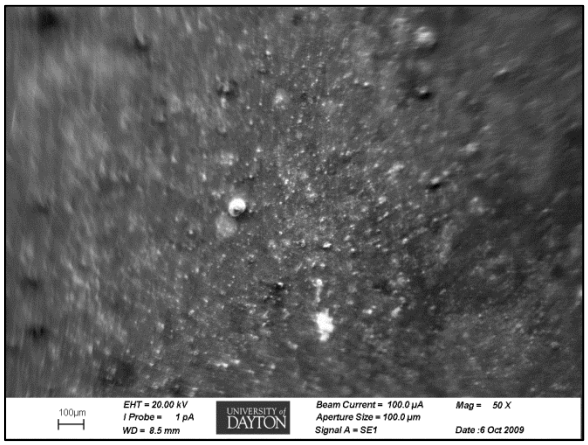

(a)

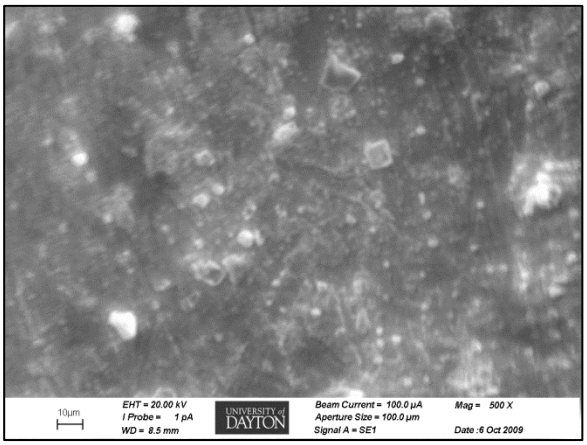

(b)

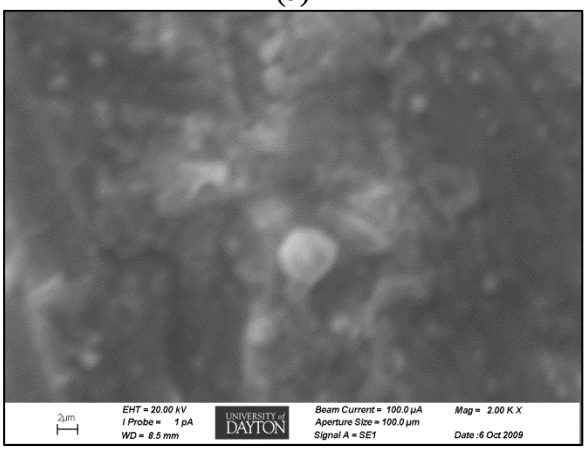

(c)

Figure C-30. SEM images of pure copper sample retrieved on 3 months exposure from Pt. Judith site. (a) 50X magnification (b) 500X magnification, and (c) 2000X magnification.

Distribution Statement A. Approved for Public Release.

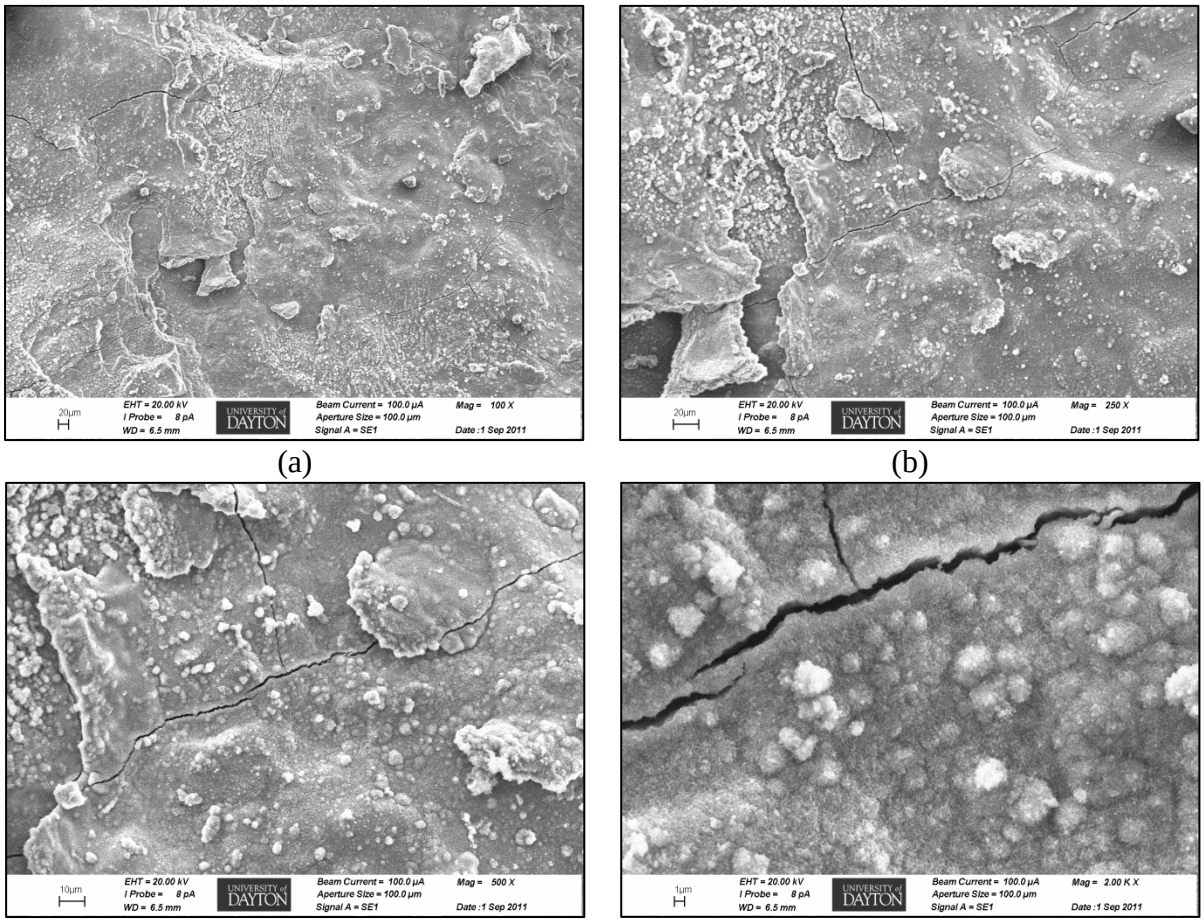

Figure C-31. SEM images of 1010 steel sample retrieved on 24 months exposure from Pt. Judith site. (a) 100X magnification (b) 250X magnification, (c) 500X magnification, and (d) 2000X magnification.

Distribution Statement A. Approved for Public Release.

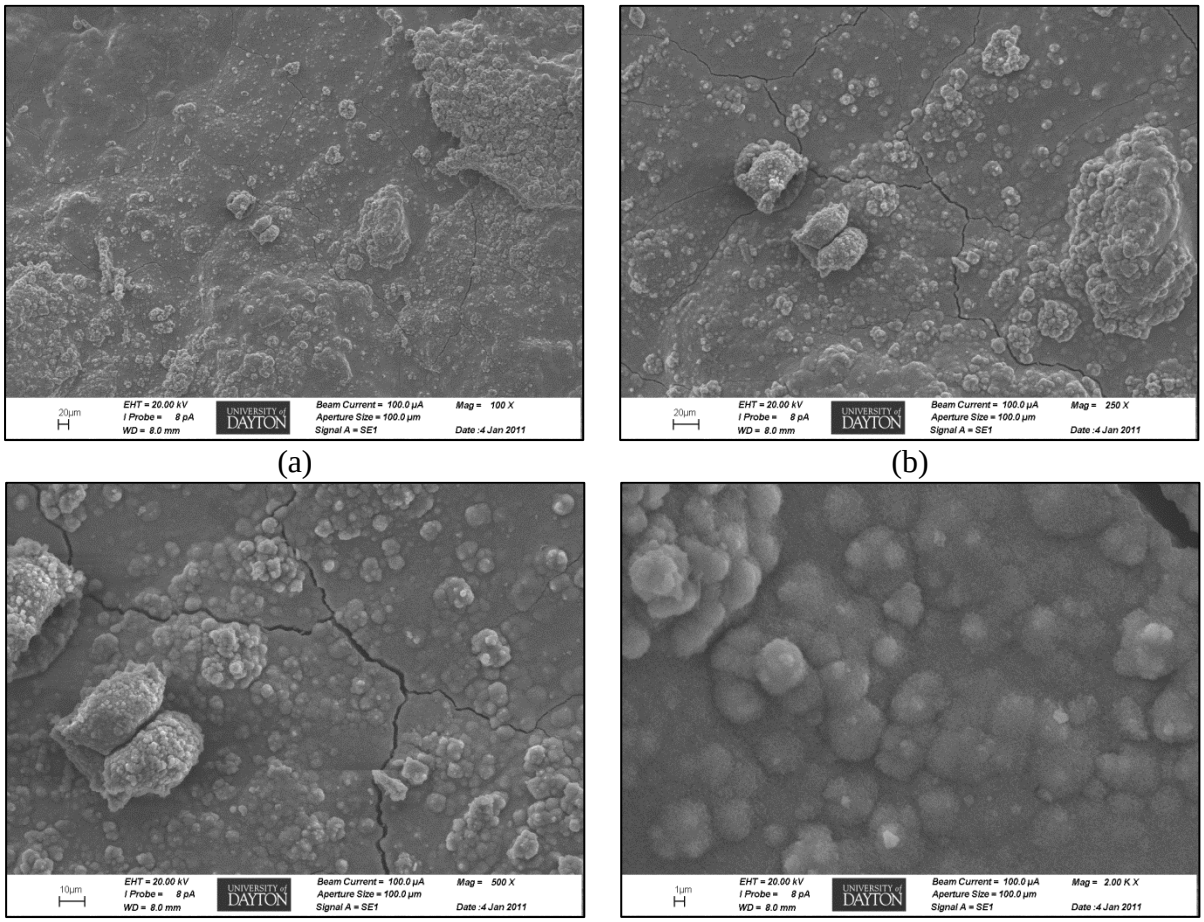

Figure C-32. SEM images of 1010 steel sample retrieved on 18 months exposure from Pt. Judith site. (a) 100X magnification (b) 250X magnification, (c) 500X magnification, and (d) 2000X magnification.

Distribution Statement A. Approved for Public Release.

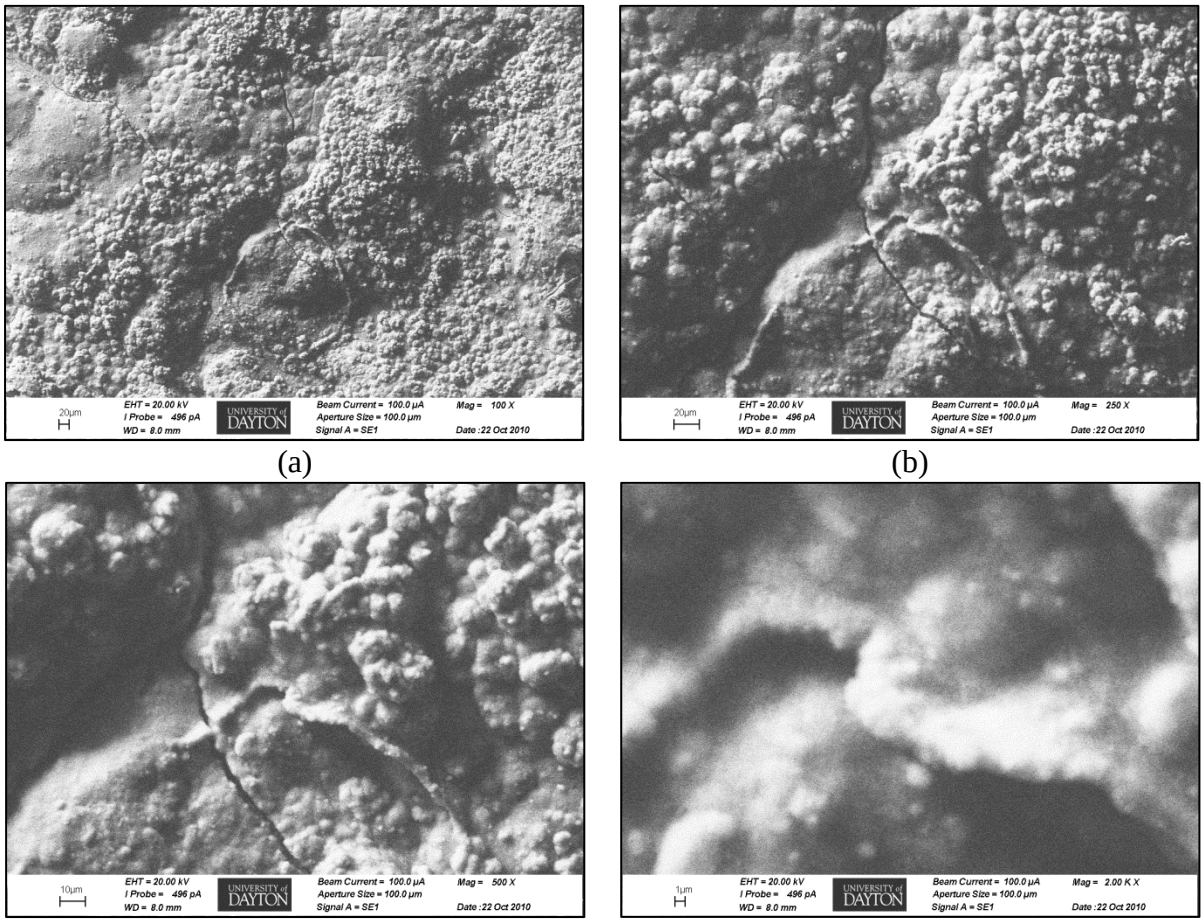

Figure C-33. SEM images of 1010 steel sample retrieved on 12 months exposure from Pt. Judith site. (a) 100X magnification (b) 250X magnification, (c) 500X magnification, and (d) 2000X magnification.

Distribution Statement A. Approved for Public Release.

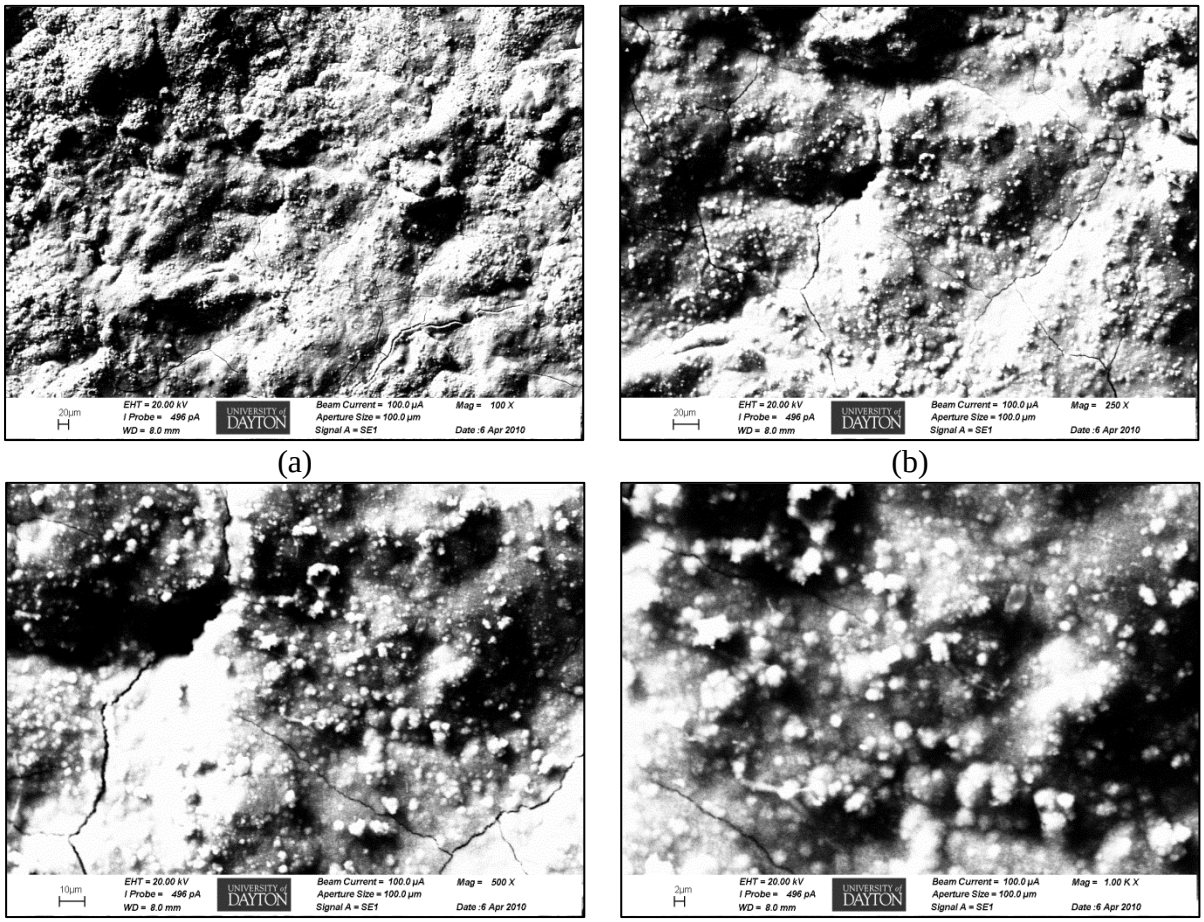

Figure C-34. SEM images of 1010 steel sample retrieved on 9 months exposure from Pt. Judith site. (a) 100X magnification (b) 250X magnification, (c) 500X magnification, and (d) 1000X magnification.

Distribution Statement A. Approved for Public Release.

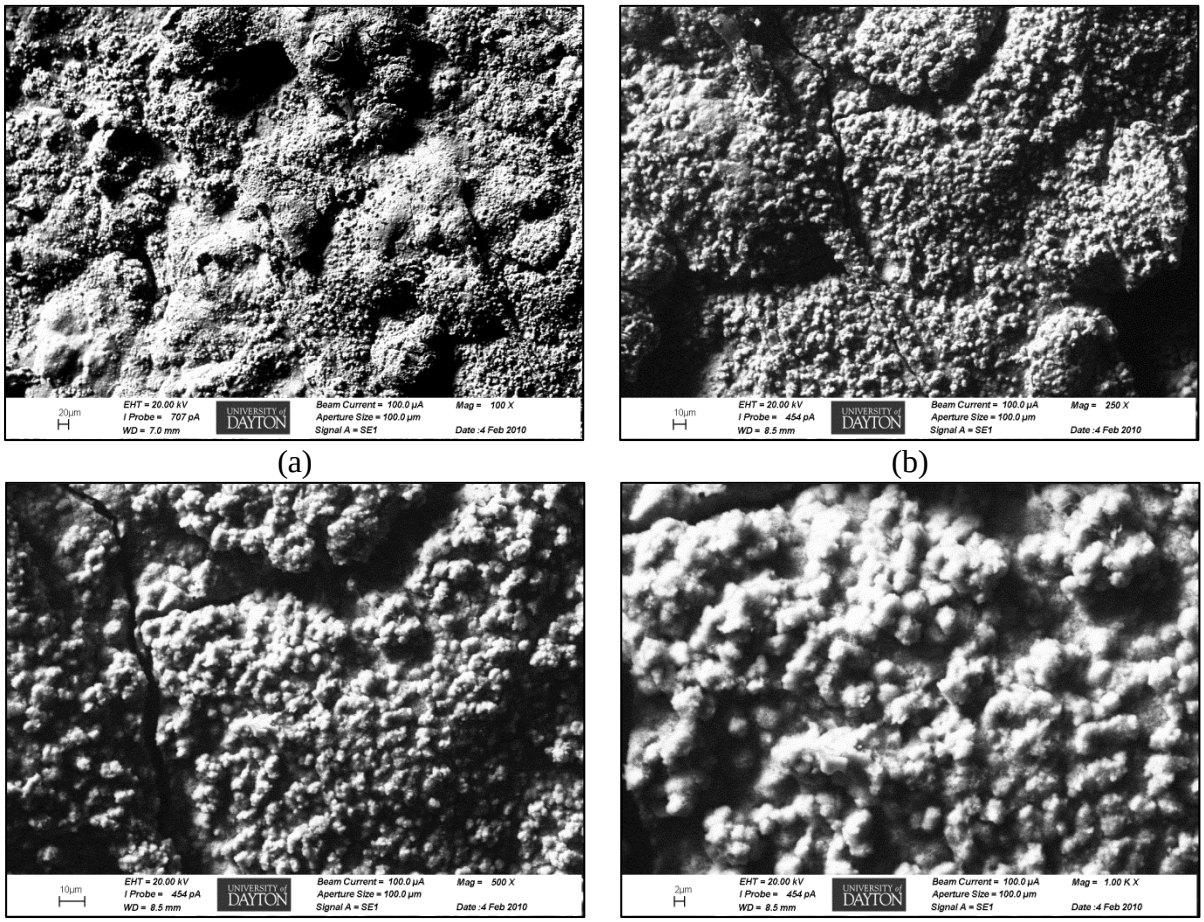

Figure C-35. SEM images of 1010 steel sample retrieved on 6 months exposure from Pt. Judith site. (a) 100X magnification (b) 250X magnification, (c) 500X magnification, and (d) 1000X magnification.

Distribution Statement A. Approved for Public Release.

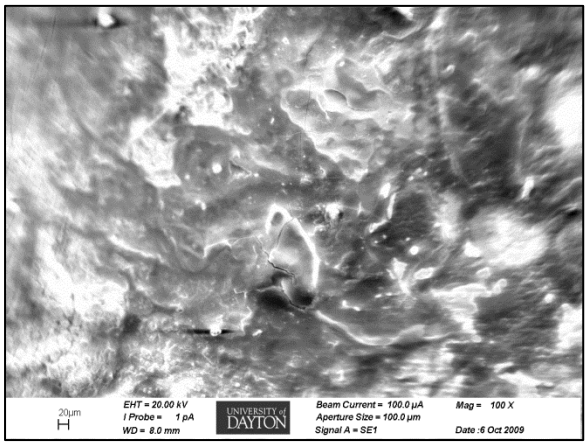

(a)

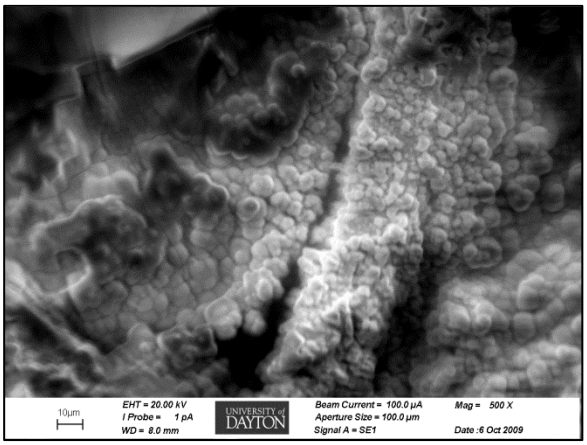

(b)

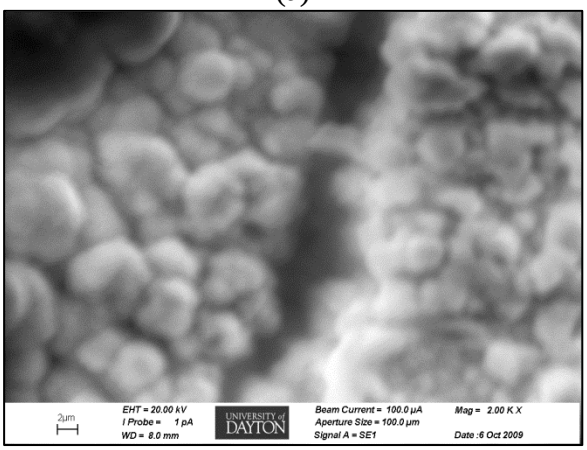

(c)

Figure C-36. SEM images of 1010 steel sample retrieved on 3 months exposure from Pt. Judith site. (a) 100X magnification (b) 500X magnification, and (d) 2000X magnification.

Distribution Statement A. Approved for Public Release.